What Controls Shallow Landslide Size Across Landscapes?

By

Dino Bellugi

A dissertation submitted in partial satisfaction of the

requirements for the degree of

Doctor of Philosophy

in

Earth and Planetary Science

and the Designated Emphasis

in

Computational Science and Engineering

in the

Graduate Division

of the

University of California, Berkeley

Committee in charge:

Professor William E. Dietrich, Chair

Professor Satish Rao

Professor Burkhard Militzer

Fall 2012

What Controls Shallow Landslide Size Across Landscapes?

Abstract

What Controls Shallow Landslide Size Across Landscapes?

by

Dino Bellugi

Doctor of Philosophy in Earth and Planetary Science

and the Designated Emphasis in Computational Science and Engineering

University of California, Berkeley

Professor William E. Dietrich, Chair

Shallow landslides that usually involve only the colluvial soil mantle, are a widespread phenomenon in the United States and the world. Often triggered by extreme precipitation events, they can be the primary sources of debris flows, and are generally a threatening source of hazards, causing loss of life, destruction of property, and affecting communities all across the nation. Shallow landslides also play an important role in landscape evolution, dominating erosion in steeper landscape, unleashing debris flows that carve valley networks, and delivering sediment to rivers. The two primary aspects affecting the impact of shallow landslides, both in terms of downstream hazard and their geomorphic significance, are their location and size.

Theoretical and observational research has provided some insight on the controls on the size of shallow landslides. It has been observed that landslide exhibit a smaller size in grasslands than in forested areas and that landslides were smaller in areas where root strength decreased as a result land use change. The parameters that are most relevant for the occurrence of rainfall-triggered shallow landslides are slope, pore pressure, root and soil strength, and soil depth. Theoretical analyses have suggested that a decline in root strength results in failures having lower minimum lengths and widths, while low gradients, low pore water pressures, or high soil friction result in failures having higher lengths and widths. However, few if any studies examine the controls on both landslide location and size across a landscape. I hypothesize that the co-organization of landscape properties, such as slope, soil depth, pore pressure, and root reinforcement, controls the size and location of shallow landslides.

We currently lack mechanistic models for specifically predicting shallow landslide size across landscapes, thus reducing the effectiveness of landslide hazard delineation, and inhibiting our ability to formulate and apply mechanistic models for landslide flux and surface erosion. One reason for this is the one-dimensional representation of slope stability, generally applied in existing regional scale applications. Such a representation cannot produce discrete landslides and thus cannot make predictions on landslide size. Furthermore, one-dimensional approaches cannot include lateral effects which are known to be important in defining instability. These limitations can be addressed by a three-dimensional slope stability model, but its application to a landscape is challenging. Whereas the one-dimensional slope stability at a location can be determined independently of its dimensions and surroundings, multi-dimensional analyses require the treatment of discrete shapes. As these shapes are not known *a priori*, a search algorithm is required. This is a non-trivial problem, whose naïve solution (i.e. an exhaustive search) is of

exponential complexity, rendering the problem effectively intractable at any relevant scale. Any new procedure must be sufficiently general to evolve with current understanding, but with a parsimonious parameterization in order to be compatible with available data. The procedure must be computationally efficient to be applicable at scales large enough to be relevant for geomorphological and hazard related questions, yet at sufficiently fine resolution to capture the fundamental mechanics of slope failure.

In this dissertation I develop a procedure which couples a novel slope stability model that captures the basic physics of shallow landsliding, with a new and efficient search algorithm based on spectral graph theory that can predict discrete shallow landslides. In order to apply this procedure at the regional scale, I define sub-models to produce the required data, when they are not available at the necessary resolution. These sub-models extract topographic attributes, compute the spatial distributions of soils, and estimate the root reinforcement and pore pressure fields. I define formal framework to evaluate the performance of the procedure, based on information retrieval theory. This procedure should advance our understanding and prediction capability, enabling me test the hypothesis that the co-organization of landscape properties, such as slope, soil depth, pore pressure, and root reinforcement, controls the size and location of shallow landslides. As these properties are mostly dictated by topography, I hypothesize that topography exerts a first order control on both location and size.

In chapter two, I present a multi-dimensional stability model framework that can be applied to landscapes at the regional scale. This slope stability model is mechanistic but not so mechanistic that its application becomes impracticable. It is fully three-dimensional in the treatment of the forces acting on a discretized slope element and it is statically determinate. The model considers the effects of root cohesion and pore pressures, and includes the effects of earth pressure in a manner that is compatible with natural slopes. Finally, this model is easily applicable to spatially gridded data, and requires only a modest parameterization facilitated by procedures defined to obtain spatially explicit parameter fields at the required resolution. The slope stability model allows for the characterization of the forces acting on all the boundaries resulting from the discretization of a landscape into slope element blocks (and thus the role of each block in the stability of the landscape). However, it requires a deterministic search procedure that is able to select discrete least-stable combinations of slope elements across a landscape to obtain meaningful shallow landslide predictions.

In chapter three, I define a procedure that can for the first time predict discrete landslides. Its foundation is a search algorithm based on spectral graph theory that can efficiently provide a good approximation for an otherwise intractable problem. This procedure relies on a slope stability model, as well as sub-models and data for, among others, topography, soil depth, and root strength, discussed in the previous chapter. However, the procedure is general, and is not confined by their choice: as better models and data emerge, the procedure can be easily modified to take advantage of such improvements. A formal framework is defined to evaluate the performance of the procedure, based on information retrieval theory. Applying the procedure to a synthetic landscape illustrates how landslide size and location are affected by the hetereogeneity of parameters such as root strength and pore pressure.

In chapter four, the procedure is applied to an instrumented catchment in the Oregon Coast Range using field-measured physical parameters, successfully predicting the size and location of the shallow landslide which destroyed the site during a storm in November, 1996. The procedure was then applied to a larger study area using modeled physical parameters, under a suite of

diverse hydrological scenarios. The application of the procedure results in, and is able to reproduce the distribution of sizes and locations observed during the ten years of research at the site. Performance is quantified using a set of information retrieval measures, performing significantly better than a random classifier, demonstrating the applicability of the procedure.

In chapter five, a sensitivity analysis is performed to explore the controls on shallow landslide size and location. Rainfall, vegetation, soil, and topographic characteristics are systematically varied, resulting in probability density functions of predicted landslide size and location. I find that increasing precipitation or soil depth results in an increased number of predicted landslides. In contrast, increasing soil strength through root reinforcement or friction angle results in a decrease in the number of predicted landslides. Increasing soil depth results in predicted landslides being preferentially located in locations with steep slopes, while increasing soil strength results in predicted landslides being preferentially located in locations with high drainage area. Precipitation affects characteristic landslide location differently: if lateral re-distribution of water is dominant, landslides are predominantly found in locations with high drainage area; in contrast, when vertical infiltration dominates they are predominantly found in areas with steep slopes. Predicted characteristic size increases with increased precipitation and with increased root strength. However, it decreases when the increased strength results from an increase of the soil friction angle. Under uniform soil thickness, characteristic size decreases with increasing soil depth. When soil thickness distributions are instead controlled by topography, increasing soil depth causes the predicted characteristic landslide size to first increase and then to decrease, after a critical value, reflecting the stabilization effect of very thick soils.

In chapter six the effects of the fine scale variability of root strength on slope stability are examined, using a method which could be extended to represent the impact of spatial variability of landslide-relevant parameters on landslide size, location, and abundance. A simple dynamic hydrological model is used in combination with a ten-minute rainfall intensity record for a landslide-triggering storm. When comparing with a map of debris flows which occurred during the storm, the procedure predicts landslides in the observed debris flow source areas. Although over-prediction is greatly reduced, there remain a considerable number of predicted landslides in areas which did not fail during the storm event. Regardless, this is a promising result, as it suggests that this procedure is capable of capturing the timing of landslides (as well as their size and location), given a sufficiently resolved characterization of the hydrology.

I find that the spatial structure of soil depth, pore pressure, and root strength determines the areas favorable to landsliding that can be exploited by rain storms, resulting in the characteristic size and location distributions of rainfall-triggered landslides. Varying these controlling properties, even uniformly, changes the spatial distribution of these areas in the landscape. This results in new characteristic distributions of landslide size and location, as landslides sample different parts of the landscape. This reveals the first-order control exerted by topography on shallow landslides. Furthermore, the general spatial pattern of landsliding did not fundamentally change with the introduction of stochastic variability in root strength or with variations in the mechanism of pore pressure generation. This highlights the fundamental role played by the topographically-controlled distribution of soil thickness in defining landslide location.

Understanding hazards posed by rainfall-triggered shallow landslides requires predicting *where* landslides will occur, *when* they will occur, *how big* will they be, *how fast* they will mobilize, and *how far* will they go. This research constitutes a significant step in this direction

by providing some of the first coupled predictions of where and how big landslides are, and demonstrating that capturing their timing is well within reach. By coupling this procedure with climate and vegetation models we can now explore the impact of climate and land use change on the landsliding regime. By integrating the procedure into a landscape evolution model we can then explore how, over longer time scales, landslides shape a landscape.

Contents

List of Figures

List of Tables

Acknowledgements

Throughout my 18-year career at U.C. Berkeley, first as a staff researcher and subsequently as a PhD student, I have been fortunate to interact with and receive support, help, and guidance from an interminable list of people. Many of them are now not just colleagues, but close friends who will always be a part of my life. Having just suffered from a major concussion, I will ask forgiveness if I can't remember all of you at this particular moment. But I know that you know who you are, even if I am not sure that I know who I am.

First and foremost, I would like to thank my advisor (and former boss), Bill Dietrich. Eighteen years ago I walked into his office wearing a green suit, smelling like cigarettes, and looking for a job. Now I'm walking out of here older, balder, without the suit, or the cigarette smell. More importantly, I walk out of here having grown academically and intellectually, excited about a strange world that lies at the intersection of earth science and computer science. This is thanks to Bill, who has opened my eyes and has been an inspiring mentor. He has taught me to be more curious and at the same time rigorous than I ever wanted to be. Bill has an unparalleled ability to pose interesting and challenging questions, and there has never been a time that I have come out of a meeting with him not having a different view or perspective on what I had previously thought I was sure about. Eighteen years is more than I have ever spent with anyone continuously. I am amazed we didn't end up in couple's therapy. It is not going to be easy to move on. During this time Bill and his wife Mary have become my friends and my family, sharing both joyful and sad moments, which in absence of another concussion, I shall never forget. Thank you both for all that you have given to me.

Many other professors and teachers here at U.C. Berkeley have had a considerable influence on my academic and intellectual growth. Michael Jordan, who at times unwillingly became my unofficial advisor, has over the years patiently listened to all my problems and given me invaluable advice on the way to and from our band's practice sessions, on social occasions, at the coffee shop, at his house, on vacation, and at any other time in which he was unfortunate enough to be in close proximity to me. Grazie Mike, sei un mito. Christos Papadimitriou showed me how much fun computer science theory can be, but also taught me that abstraction goes well beyond science and into the random walks of life. Satish Rao taught me to love graphs, that perspective is necessary to see the bigger picture, and that a factor of two is not important, especially when trying to predict the future. Thank you, Satish. Jitendra Malik was an inspiration to me, his lectures on vision and perception gave me the idea for the "landslide glasses" which ultimately led to this dissertation. Michael Manga, together with Doug Dreger, taught me to love teaching, at a time when I didn't know the ropes. Doug also became a partner in crime, whether it was on the motorcycle or at the tailgate on game day. Save me the Seahawks seat, Doug, it ain't over yet. Burkhard Militzer allowed me to take teaching to a whole new level by giving me the opportunity to design and teach a graduate course filled with many of the things I am excited about. This was an incredible experience, and I learned a lot from him in the process. Thank you, Burkhard for all your support. Big thanks to Inez Fung for always having her door open to me, and lovingly showing my nieces around. I am grateful to the members of my dissertation committee for reading (and signing!) my dissertation, and for providing a contructive review. And of course, many thanks to the additional qualifying examination committee members: Doug Dreger was the best chairperson one could wish for, Horst Simon encouraged me to pursue the designated emphasis in computational science and engineering, and Mary Power joined on

extremely short notice saving me a re-scheduling nightmare. Kathy Yelik and Horst Simon facilitated access to the National Energy Research Scientific Computing Center (NERSC), which provided invaluable computational resources and training. Outside of U.C. Berkeley, two people in particular provided funding, advice, resources, and friendship: Jim McKean (U.S. Forest Service, Rocky Mountain Research Station), and Efi Foufula, (University of Minnesota, National Center for Earth-surface Dynamics). I cannot thank the two of you enough.

My involvement in computer science was fortunately not limited to algorithms, graphs, machine learning, and programming. Whatever sanity I have kept (minimal) in these last few years is mostly due to the fact that a few nights a month the Positive Eigenvalues would gather round to play music and prepare gigs. As a founding member I can say that it has been a highlight of my time here in Berkeley. Mike, David, Christos, Erin, Pablo, Tomas, Lady X and I became the best of comrades, had a lot of fun, and we sure went out with a bang. Did I mention the electric ukulele? I am not sure the computer science department will ever be the same again.

All of my research has been a collaborative effort. I have been fortunate to have been surrounded by very talented people, all of whom contributed a piece of the puzzle. Many of them are also dear friends. I alphabetically list some names that persisted in spite of my concussion: Douglas Allen, Ron Amundson, Sayaka Araki, Pablo Arbelaez, Collin Bode, Christian Braudrick, Fred Booker, Mauro Casadei, Geoff Day, Ken Ferrier, Paul Hargrove, Arjun Heimsath, Leslie Hsu, Ionut Iordache, Brian Kazian, Jim Kirchner, Edwin Kite, Mike Lamb, David Milledge, Dave Montgomery, Peter Nelson, Jasper Oshun, Marisa Palucis, Daniella Rempe, Josh Roering, Daniele Rosa, Joel Rowland, Max Rudolph, Cristina Rulli, Kevin Schmidt, Michael Singer, Erik Sudderth, Paola Passalacqua, Taylor Perron, Rafael Real de Asua, Cliff Riebe, Josh Roering, Joel Rowland, Joel Scheingross, Jonathan Shewchuk, Leonard Sklar, John Stock, Kathleen Swanson, Ray Torres, Martin Trso, Elowyn Yager, Stefano Zanardo. In particular, Christian has been my (very patient) student mentor and the best G.S.I. ever. Daniella is the most helpful person in the world. David came through like a knight in shining armor when I needed help the most. As Gram Parson sung, “In my hour of darkness, in my time of need, oh Lord, grant me wisdom oh, Lord grant me speed”. I got both, and I could never have done it without your help. Aurelie Guilhem held my hand while teaching rocks and minerals, as well as while preparing for my qualifying exam. Bless your French soul, except during the World Cup. Sierra Boyd and Shan Dou made the second floor of McCone Hall much less lonely at night. And nothing at all could have happened without the help of Charley Paffenbarger. He kept every system running for me for over eighteen years, and has stepped in day or night whenever there was any problem. During this time Charley (and his wife Corinne) have become true friends, sharing art, music, and good company. Rock on, Chas. Finally, I owe the EPS staff (past and present) plenty of gratitude, with a special shout-out to Margie Winn, our graduate advisor.

I am blessed to have so many wonderful and supportive friends. In particular, my life here in Berkeley has revolved around the extended Reed College and Italian communities. It is an endless list, and all have become my chosen family. Here are just a few of the friends who accompanied me through this chapter of life: Adam, Alberto, “tall” Alessandro, “belli capelli” Alessandro, the other Alessandros, Alvise, Andre, Andrea, Anna, Annalisa, Arvydas, Barbara, Begum, Bonimba, Bridget, Bruno, Byron, Chazz, Chema, Cindy, Colter, Deborah, Demix, Denia, Dorothea, Dragan, Elizabeth, Elli, Eran, Fabio, Fabrizio, Firuzeh, Gina, Grant, Guillermo, Jane, Janet, Julie, Kristin, Lafcadio, Larry, Laurie, Leticia, Lisa, the other Lisas, Luca, JoAnne, Jon, Massimiliano, Massimo, Max, Melissa, Michael, Nicolo’, Nick, Paola, “little” Rebecca,

"gelato" Rebecca, Rob, Rutilio, Siobhan, Sloane, Tati, Tania, Tanja, Teresa, Till, Ursula. I also have to mention two slightly furrier friends that have been a fountain of affection. Little Beast (a.k.a. BeastyBeast) spent all of my first fifteen years in Berkeley with me. She taught me the importance of sticking to one's own agenda, and is now scratching at the window of Kitty Heaven. Biskit is now in Boston wondering what the white stuff falling from the sky might be, and why his supply of meat scraps and prosciutto ends came to a screeching halt last September. Any day now, any day now (I shall be released!).

I want to particularly thank my mother Vanna and my brother Duccio. We survived so much and made it so far due to our love and unconditional support. Vanna is a phenomenal and special person. Her intellectual drive, curiosity, tenacity, generosity, compassion, ethics, and love, have been a true inspiration. She has managed to be an incredible parent to my brother and me, while traveling through the battlefields of humanity to write about this world and make it better. We are bonded in a way that words cannot describe. Duccio is a loving, loyal, supportive, and fun brother who is next to me even when we are (as we are) across the world. Thank you both. I want to thank Alba Gaia and Galatea for being the light of my eyes, and Jette for being their mother and a sister to me. My siblings, Costanza, David, and Rob, their kids, their partners, their kids' partners, their kids' kids, and those about to enter the world (mitica Animals, se solo l'avesse saputo il babbo!) will always be my greatest gift. A big thank you to my adoptive family: Marion, Steve, Juliana, Peter, Gabe, Jim, Lily, Sam, Anabel, Dorian, Felix, Sadie, Emmet, and more soon to come. Thank you for making me feel at home even when home was continents away.

Two people in particular will not be reading these acknowledgments but have their place in these pages as well as in my heart. My father Piero passed away recently but even when battling sickness never stopped playing his music, teaching his students, and loving his children. Last winter break, I was in his apartment writing the application for what became my next appointment while he was constructing his last and perhaps most beautiful interpretation of Beethoven's sixth symphony. We exchanged notes, took breaks for coffee, and spent an unforgettable week together. A few months later, his last moments alive brought all his children together for the very first time. A procession of students, each touched in a different way, attested not only to his musicality, but to his generosity. He would have played music ad infinitum, the world is much poorer without him. Thank you Mara for taking care of him and allowing him to live in his music until the end, I will always be grateful to you. My friend Douglas is another hole in my heart the size of my heart. Douglas, you should have been here. There has not been a day of this PhD adventure that I have not looked down the hall for you. Rafa, Fred, and I (your Winers) still religiously go up to Tilden Park with a bottle, bread, cheese, and prosciutto. It's our way of saying that we miss you and love you, conscious that we are closer together thanks to you. We remind ourselves of what we (and you) lost when you left this world. This sweet ol' world.

And now, after looking back for three long pages, it is finally time to look forward. To new challenges, new problems, new colleagues, new friends, new places, new adventures. Mostly I look to forward to you, Arden and Celia. You are the coolest, funniest, grooviest girls in town. You are my life and you are my future. Thank you for all your love, help, and support. Most of all, thanks for sticking around and waiting for me to get through this hell. I know that it hasn't been easy. I am blessed to have you in my life and I love you more than words can say.

"If you are not long, I will wait for you all my life." - Oscar Wilde

To Arden and Celia

"Looking for another chance

for someone else to be

Looking for another place

to ride into the sun"

the Velvet Underground

Chapter 1

Introduction

1.1 Introduction

Shallow landslides that usually involve only the colluvial soil mantle (usually less than a few meters deep), are a widespread phenomenon in the United States and the world. Often triggered by extreme precipitation events, they can be the primary sources of debris flows, and are generally a threatening source of hazards, causing loss of life, destruction of property, and affecting communities all across the nation (figure 1.1). It is estimated that in the United States alone landslides result in 25 to 50 deaths and damages exceeding $2 billion annually [Spiker and Gori, 2003]. It is crucial to accurately assess such hazards, and to be able to predict them more accurately, particularly in light of expected climate and land use changes. Shallow landslides also play an important role in landscape evolution, dominating erosion in steeper landscape, unleashing debris flows that carve valley networks, and delivering sediment to rivers [Dietrich and Dunne, 1978; Benda, 1990; Benda and Dunne, 1997]. The two primary aspects affecting the impact of shallow landslides, both in terms of downstream hazard and their geomorphic significance, are their location and size. Location affects travel distance and bulking-up potential, while size affects the amount of sediment discharged, as well as the scale of local morphological change [Benda and Cundy 1990; Fanning and Wise 2001]. Moreover, the magnitude of shallow landslides (defined as the volume of material displaced) controls the extent of the hazard area, the intensity of impact within it and the vulnerability of elements at risk [Hungr et al., 2008]. Location and size together thus determine the downstream effects, particularly the potential hazard for people and property. While the advent of high resolution topographic data has enabled the application of slope stability models to determine locations with high landslide susceptibility (see review in Casadei et al., [2003a]), we currently lack mechanistic models for specifically predicting shallow landslide size across landscapes, thus reducing the effectiveness of landslide hazard delineation, and inhibiting our ability to formulate and apply mechanistic models for landslide flux and surface erosion [Dietrich, et al., 2003].

For the purpose of understanding and modeling landscape evolution, this limitation has been circumvented by incorporating the effects of landslides into non-linear, slope-dependent flux laws [Howard, 1994; Roering, et al., 1999], or by implementing grid-based infinite slope calculations in which each unstable grid cell is treated as an individual landslide [Tucker and Bras, 1998; Tucker et al., 2001]. Similarly, in landslide hazard delineation, calculations using a slope stability model and modeled local properties such as soil depth, root strength, and pore pressure are typically performed on a grid cell basis to map the spatial distribution of potential landslide areas [Montgomery and Dietrich, 1994; Casadei et al., 2003a; Tarolli and Tarboton, 2006; Bellugi et al., 2011]. These approaches for hazard delineation allow for reasonable physically-based predictions, but tend to over-predict landslide extent and do not provide information about individual discrete landslides.

Considerable attention has also been devoted to empirically characterizing landslide distributions. It has been observed that much like other natural hazards, landslides follow the concept put forth by Per Bak [1987] of *self-organized criticality* (e.g.: Turcotte, [1999]; Malamud and Turcotte, [1999]; Malamud et al., [2004a]; Malamud et al., [2004b]), and that frequency and landslide area are generally related by an inverse power law for at least a

truncated portion of their distribution (e.g. Stark and Hovius, [2001]; Brunetti et al., [2009]), a relationship that can be used empirically to approximate landslide-induced erosion rates [Hovius et al., 1997], or to infer the frequency of an event type in order to characterize regional landslide hazard [Guzzetti, et al., 2007]. These analyses have not distinguished between shallow landslides (typically smaller) and deep-seated ones involving the underlying bedrock. Empirical methods are also in use for landslide warning systems, in which historical landslide susceptibility is combined with precipitation thresholds (see reviews in Guzzetti et al., [2008], Baum and Godt, [2010]). Such approaches may be applied to a region, but certainly not to individual hillslopes as they do not enable spatially explicit predictions.

(a)

(b)

Figure 1.1. Shallow landslides in the San Francisco Bay area. a) Shallow landslides on hillslopes near Briones, California, showing a range of size and location (note that the unvegetated scars partly include the runout portion of the slide; scene width is about 300m), from [Dietrich, et al., 2008]. b) A landslide that struck Pacifica, CA, in 1982, destroying two residences and killing three children [photo: USGS].

Mechanistic and empirical approaches have been combined to constrain the problem of over-prediction and to make forecasts for individual storms [Stock and Bellugi, 2011]. While this approach is preferable to a purely empirical approach and applicable at the large scale [Bellugi et al., 2011], it cannot make a specific prediction about individual landslides and requires precipitation threshold data which are often not available in practice. Similarly, the power law relationship has been given a mechanistic foundation by Stark and Guzzetti [2009], combining an infinite-slope factor of safety analysis with a survival process approach in a probabilistic framework that expresses the likelihood that a failure will "survive" a series of random coin tosses simulating landslide rupture propagation, weighted by a limit-equilibrium analysis of the evolving rupture. This approach allows the exploration of the controls on the landslide size frequency distribution, but is not spatially explicit.

The understanding of landslide size and its sensitivity to controls such as slope angle, soil texture, and root reinforcement is currently an active area of research. Recent work by Lehmann and Or [2012] introduced a new hydro-mechanical modeling framework for simulating rainfall-induced rapid and shallow landslides. This framework is based on the fiber bundle paradigm, originally formalized by Daniels [1945] to analyze the strength of textiles, and more recently applied to quantifying root reinforcement by Schwarz et al. [2010], in which a load is incrementally and uniformly applied to a bundle of fibers until the weakest fiber breaks and its load is redistributed to remaining intact fibers. The fiber bundle paradigm is intimately tied to the concept of self-organized criticality, as the number of fibers failing during a load increment follows a power law [Hemmer and Hansen, 1992]. By coupling this paradigm to a hydrological model and an infinite-slope stability analysis, and applying it to many realizations of an artificial hillslope, the authors reproduce observed power law frequency-magnitude relationships arising from landslide inventory data. Although it has not been applied to natural landscapes, this framework has the potential for capturing the progressive nature observed in many failures.

Theoretical and observational research has provided some insight on the controls on the size of shallow landslides. Selby [1976] observed that landslide exhibit a smaller size in grasslands than in forested areas. Gabet and Dunne [2002] also observed that landslides were smaller in areas where root strength decreased as a result land use change. Reneau and Dietrich [1987] used a slope stability model that accounted for the effect of lateral root reinforcement and conducted a theoretical analysis illustrating how a decline in root strength results in failures having lower lengths and widths, while low gradients or high soil friction result in failures having higher lengths and widths. Casadei et al. [2003b] used a similar model to perform a sensitivity analysis illustrating that minimum width for failure increases with root cohesion and friction angle, and decreases with increasing slope or increasing relative saturation.

The methods reviewed above cover the range of what is used in current practice. The "next-generation" landslide prediction procedure needs to be broadly applicable at the regional scale and capable of providing quantitative information about individual landslides. A central issue is our lack of understanding of what controls not only the location, but also the size of individual landslides. For example, there are sufficient studies available to allow a reasonable prediction of runout length based on initial landslide volume, but the prediction of volume of first-time failures remains a problem [Crozier and Glade, 2005]. One of the key limitations is the one-dimensional representation of slope stability, generally applied in existing regional scale applications. Such a representation cannot produce discrete landslides and thus cannot make predictions on landslide size. Furthermore, one-dimensional approaches cannot include lateral

effects which are known to be important in defining instability (e.g. Arellano & Stark, [2000]; Schmidt et al., [2001]). These limitations can be addressed by a three-dimensional slope stability model, but its application to a landscape is challenging [Dietrich et al., 2008]. Whereas the one-dimensional slope stability at a location can be determined independently of its dimensions and surroundings, multi-dimensional analyses require the treatment of discrete shapes. As these shapes are not known *a priori*, a search algorithm is required. This is a non-trivial problem, whose naïve solution (i.e. an exhaustive search) is of exponential complexity, rendering the problem effectively intractable at any relevant scale. Given that the physics of slope failure are poorly understood, and that field data and observations are scarce and often incomplete, any new procedure must be sufficiently general to evolve with current understanding, but with a parsimonious parameterization in order to be compatible with available data. The procedure must be computationally efficient to be applicable at scales large enough to be relevant for geomorphological and hazard related questions, yet at sufficiently fine resolution to capture the fundamental mechanics of slope failure.

In this dissertation I develop a procedure which couples a novel slope stability model that captures the basic physics of shallow landsliding, with a new and efficient search algorithm based on spectral graph theory that can predict discrete shallow landslides. In order to apply this procedure at the regional scale, I will define sub-models that are able to produce the required data, when they are not available at the necessary resolution. These sub-models will extract topographic attributes, compute the spatial distributions of soils, and estimate the root reinforcement and pore pressure fields. A formal framework will be defined to evaluate the performance of the procedure, based on information retrieval theory. Such a procedure should advance our understanding and prediction capability, enabling to test the hypothesis that the co-organization of landscape properties, such as slope, soil depth, pore pressure, and root reinforcement, controls the size and location of shallow landslides. These properties are mostly dictated by topography, thus it is hypothesized that topography exerts a first order control on both location and size.

1.2 Dissertation Structure

In chapter two, I define a slope stability modeling framework that is suitable for a regional-scale application that is capable of predicting landslides of discrete size when coupled with a novel search algorithm (which in turn will presented in the following chapter). This requires the adoption of models that are sufficiently mechanistic with physically meaningful parameters which can be established and tested, yet not overly complex so that their application at the regional scale is impractical. In particular, I present a fully three-dimensional and statically determinate slope stability model that considers the effects of root cohesion and pore pressures, and that includes the effects of earth pressure in natural (inclined) slopes. This model is easily applicable to spatially gridded data, and parsimonious in its parameterization. However, it requires high-resolution spatial data of topography, soil depth, pore pressure, and root reinforcement. Thus to effectively apply it at the regional scale I also introduce a suite of sub-models that are able to produce these data, when they are not available at the necessary resolution. These sub-models extract topographic attributes, compute the spatial distributions of soils, and estimate the root reinforcement and pore pressure fields.

In chapter three I show how the problem of predicting landslides across a landscape can be reduced to the problem of finding the minimally-stable collection of cells in that landscape. I will

present a search algorithm that directly determines the initial shape and location of the most likely landslide, given the local conditions (e.g. topography, hydrology, and vegetation). While the exact solution of this problem could be obtained by applying a stability analysis and testing all possible combination of grid cells, such an approach would be intractable as the number of combinations grows exponentially with the number of cells. I thus build a search algorithm based on spectral graph theory that efficiently approximates the exact solution. Coupled with the slope stability model and the sub-models defined in chapter two, this search algorithm defines a novel general procedure for predicting discrete shallow landslides. This procedure retains a general structure so that as models and data improve they can be swapped in to improve performance. In this chapter I also define a formal framework based on information retrieval theory for evaluating the performance of the procedure.

The performance of the procedure is evaluated both qualitatively and quantitatively in chapter four. I will apply the procedure to a landslide-prone study area in the Oregon Coast Range using a dual approach. First, the slope stability model and the search algorithm is applied to a small catchment at the research site where an instrumental record of a rainfall-triggered shallow landslide allows the use of field-measured physical parameters such as hydrological conditions, soil depth, and root strength. Second, the procedure is applied across a larger area where repeat field mapping provides an inventory of all the shallow landslides that occurred over a 10-year period, and intensive research during the same period provides constraints on soil, vegetation, hydrological, and rainfall characteristics. The local characteristics of soil, vegetation, and hydrology are estimated using the sub-models defined in chapter two. The shallow landslide predictions resulting from the application of the procedure to both datasets is compared to the mapped observations, with emphasis on their location and size.

The sensitivity of landslide location and size to a variety of parameters is explored in chapter five. The procedure is applied to the landslide-prone study area and sensitivity analysis is performed by which soil, vegetation, rainfall, and topographic characteristics are systematically varied. Probability density functions of predicted landslide size and location are examined and general trends synthesized to illustrate the changes in landslide number, size, and preferred location in the landscape under varying conditions. In this process, parameter sets resulting in best performance with respect to the observed landslides are also examined.

In the sixth and final chapter, I examine the role of spatial and temporal variability of parameters with respect to shallow landslide location and size. I discuss the impact on the landsliding regime brought by temporal and spatial variations in rainfall and vegetation patterns which are expected to arise through climate and landuse change, and point to methods which may allow for their improved characterization. Finally, I conclude by discussing the implications of this research on landscape evolution and hazard prediction.

Chapter 2

Slope stability and shallow landslide size

2.1 Introduction

The increasing availability of high-resolution and LiDAR topographic data (e.g. www.opentopography.org; maps.csc.noaa.gov; lidar.cr.usgs.gov; www.nationalmap.gov; http://calm.geo.berkeley.edu/ncalm/dtc.html) and recent advances in climate model precipitation predictions (e.g. Anders et Al., [2007]; Dettinger et al., [2012]; Li et al., [2012]) allow for the design and application of mechanistic shallow landslide forecasting models that can predict failure timing and location at the regional scale [e.g. Casadei et al., 2003]. While the timing and location of shallow landslides is extremely important for hazard assessment at the regional scale, a fundamental attribute of landslides that is not predicted by any model at this scale is their size. Most models treat landslide size in an implicit fashion by either considering landslides as single grid cells or by grouping adjacent unstable cells. This results in arbitrary dimensions which depend strongly on grid resolution and on the accuracy of the digital data (e.g. Dietrich et al., [2001]; Claessens et al., [2005]). As the issue of landslide size is central to both hazards and geomorphic change [Dietrich et al, 2008], the ability to predict size is a necessary requirement for any advanced modeling effort. In this chapter I will define a slope stability modeling framework that is suitable for a regional-scale application that is capable of predicting landslides of discrete size using a novel search algorithm (which in turn will presented in the following chapter). This will require the adoption of models that are sufficiently mechanistic with physically meaningful parameters which can be established and tested, yet not overly complex so that their application at the regional scale is impractical.

The most common approaches used for mapping landslide hazard potential perform a limit-equilibrium analysis (i.e. the investigation of the static force equilibrium of the soil mass at the limit of stability) in which some form of the infinite slope equation is coupled with hydrological models to estimate the local pore pressure field, and with local estimates of root reinforcement and soil depth [e.g. Montgomery & Dietrich 1994; Iverson 2000; Casadei et al., 2003a; Tarolli and Tarboton, 2006; Baum et al., 2008]. These models are essentially one-dimensional in their physical setup, are principally concerned with landslide location rather than size, and by definition cannot account for lateral stress terms which can contribute considerable additional strength [Stark and Eid, 1998]. Limit-equilibrium also assumes a shape and location of the failure surface, typically considered to be slope-parallel and at the soil-bedrock interface. Further important assumptions include considering stresses to be uniformly mobilized over the whole length of the failure surface, and the soil mass to behave essentially as a rigid block.

The most common two-dimensional limit-equilibrium methods divide the soil mass above the failure surface into slices by vertical planes (e.g. the ordinary method of slices of Fellenius, [1927], boldly envisioned as implementable by a computer program by Whitman and Bailey, [1967]). The failure surface can be circular for rotational slides or planar for translational slides. These methods are theoretically statically indeterminate (i.e. more unknowns than equations, only solvable via optimization techniques), but can become determinate with some simplifying assumptions about the inter-slice forces. For example, Bishop's simplified method of slices [Bishop, 1955; Spencer 1967], assumes that the inter-slice forces are horizontal, obtaining a

statically determinate formulation. There is mutual support between slices, and the stability of the soil mass is determined by the net balance of driving and resisting forces, but the lateral resistances are generally ignored.

There also exist two-dimensional methods which use a continuum approach instead of a limit-equilibrium analysis. In such methods, implemented with finite-difference or finite-element deformable meshes which track the strains and stresses produced in the material body, the shear surface develops as a part of the solution. Continuum analysis provides clear advantages as few assumptions need to be made about shape or location of a failure surface (or about the inter-slice forces), but this comes at a high computational cost. No such model is in fact at the point where it could be applied at the regional scale. Continuum models vary in complexity: FLAC [Itasca Consulting Group, 2000], and [Griffiths and Lane, 1999] are examples of finite difference and finite element methods, respectively, with a prescribed water table height and uniform material properties; Griffiths and Fenton [2004] extends the latter method to probabilistically account for spatially-correlated, non-uniform cohesion; Borja and White [2010] extend the finite element approach in a different direction and couple a deformation model with a hydrologic model for flow in variably saturated soils. Being two-dimensional, none of these models consider the lateral resistances. Their three-dimensional equivalents (e.g. FLAC3D [Itasca Consulting Group, 2002]; Griffiths and Marquez [2007]) are an extension of the two-dimensional ones described above, and thus present even more challenging computational obstacles. Recent advances in massively-parallel computing hardware and software will allow these methods to be explored on larger scales in the not too distant future. In particular, software that can perform parallel adaptive mesh refinement on overlapping grids should be well suited to treat complex solid deformation and fluid flow problems under changing boundary conditions [Henshaw and Schwendeman, 2008].

In practice, three-dimensional stability analysis still relies on the limit-equilibrium approach. Hovland [1977] extends the two-dimensional method of slices to columns in three dimensions. All inter-column forces are ignored, and the normal and shear forces acting on the base of each column are derived as components of the weight of the column. The failure surface is assumed to be at the base of the columns, and the factor of safety is defined as the ratio of total available resistance to the total mobilized stress along this surface. Lateral resistances are also ignored. Chen [1981] incorporates the effect of friction on the sides of translational failures, and assumes a geometry consisting of a failure body bounded upslope and downslope by wedges used to quantify the effects of active and passive earth pressure (see figure 2.3). Such a three-block geometry with active wedges driving failure and passive wedges resisting failure of a central block has been in use since the 1960's in geotechnical engineering [e.g Terzaghi and Peck, 1967]. As in most engineering approaches, these wedges are assumed to be horizontal thereby limiting its applicability in natural slopes. Burroughs [1985] applies earth pressure at the lateral boundaries, but also incorporates the effects of root strength on these boundaries. His model requires a graphical solution using Mohr circles in the passive earth pressure calculation. Reneau and Dietrich [1987] and Casadei and Dietrich [2003b] ignore lateral friction and boundary pressure effects to estimate shallow landslide shape and size. Dietrich et al. [2008] take an approach similar to Burroughs [1985] but provide an analytical solution for earth pressure for geometries similar to those assumed by Chen [1981].

Few three-dimensional models have been applied to the catchment scale. Okimura [1994] computes a least stable cell using an infinite slope stability then explores potential rectangular

slide masses oriented downslope, finding good agreement between predicted locations and shapes and of observed failures over a limited area (and without any consideration of pore pressures, friction, and cohesion effects). Qiu et al. [2007] use a Monte Carlo approach to test potential ellipsoidal slip surfaces, using Hovland's method [Hovland, 1977] to compute their three-dimensional stability (thus without considering edge effects).

In this research I define a multi-dimensional stability model to be applied to landscapes at the regional scale in order to search for the least stable landslide sizes and shapes, by using a factor of safety approach and identifying areas that collectively would be expected to fail for a given hydrologic event. This is similar to the approach of Qiu et al. [2007], but here the search is deterministic rather than involving a random sample of possible shapes. The minimal requirements for such a slope stability model are that it is mechanistic but not so mechanistic to be impracticable, that it is fully three-dimensional and statically determinate, that it considers the effects of root cohesion and pore pressures, that it includes the effects of earth pressure in natural (inclined) slopes, that it is easily applicable to spatially gridded data, and that it requires minimal parameterization. While no *off the shelf* model matches all these requirements, many studies discussed here do include some of the necessary elements. In this chapter I will build on such previous studies to develop a slope stability framework which meets these requirements. New treatments will be added when needed, and particular attention will be devoted to defining procedures to obtain the necessary spatially explicit parameter fields at the required resolution, especially when these data are sparse.

2.2 Models and Sub-Models

In this section the physical model framework and the parameter choices used in this research are presented. The foundation is a mechanistic three-dimensional slope stability model that meets the requirements discussed in the previous section by appropriately considering resistances acting on all sides of a discretized hillslope element. To perform effectively, this model requires high-resolution spatial data of topography, soil depth, pore pressure, and root reinforcement. In order to apply this model at the regional scale, I define self-standing components, which will be hereafter referred to as *sub-models*, that are able to produce the required data, when they are not available from measurements at the necessary resolution. We thus present sub-models which extract topographic attributes, compute the spatial distributions of soils, and estimate the root reinforcement and pore pressure fields. These data are stored in spatial layers on which the slope stability model operates. In turn, the slope stability model computes the stability attributes (i.e. driving forces and resistances) associated with the discretized 3-D elements of the terrain. This framework will then be used to search for least stable combinations of discretized elements, using a novel algorithm presented in the next chapter.

2.2.1 Slope stability model

Because of its simplicity, generality, and applicability at the regional scale to grid-based spatial data, I adopt a method, which will be further described in [Milledge et al., in prep], that extends the simple three-dimensional force balance on an idealized slope element (figure 2.1), proposed by [Dietrich, et al., 2008], to account for lateral earth pressures on a sloping surface. This model does not consider progressive failure with strain softening, pore water pressure dynamics, or other unequal stress-strain behavior, effectively treating a potential failure as a rigid block. The rigid block assumption [e.g. Newmark, 1965] is likely incorrect in detail (see Iverson and Reid 1992), however it is useful with respect to our goal of determining the initial size and

shape of a failure. While mobilization can be induced by very different means, field evidence points to the fact that forces such as those acting on the boundaries of a rigid block may indeed set the scale for the initial failure, particularly when a large amount of multi-branched root material is present [Schmidt, et al., 2001]. The model is fully three-dimensional in its geometry (and multi-dimensional in terms of its parameterization), and follows the approach laid out by Hovland [1977], Chen [1981], and Arellano and Stark [2000]. It considers translational slides with non-circular failure surfaces and assumes that the failure plane is located at the soil-bedrock interface, which is likely the position of the sharpest shear strength contrast and a boundary for hydraulic conductivity. As a result of the three-dimensional discretization, similar to that used by [Hovland, 1977], complex failure surfaces are accommodated, in the sense that they will follow the shape of the soil-bedrock boundary.

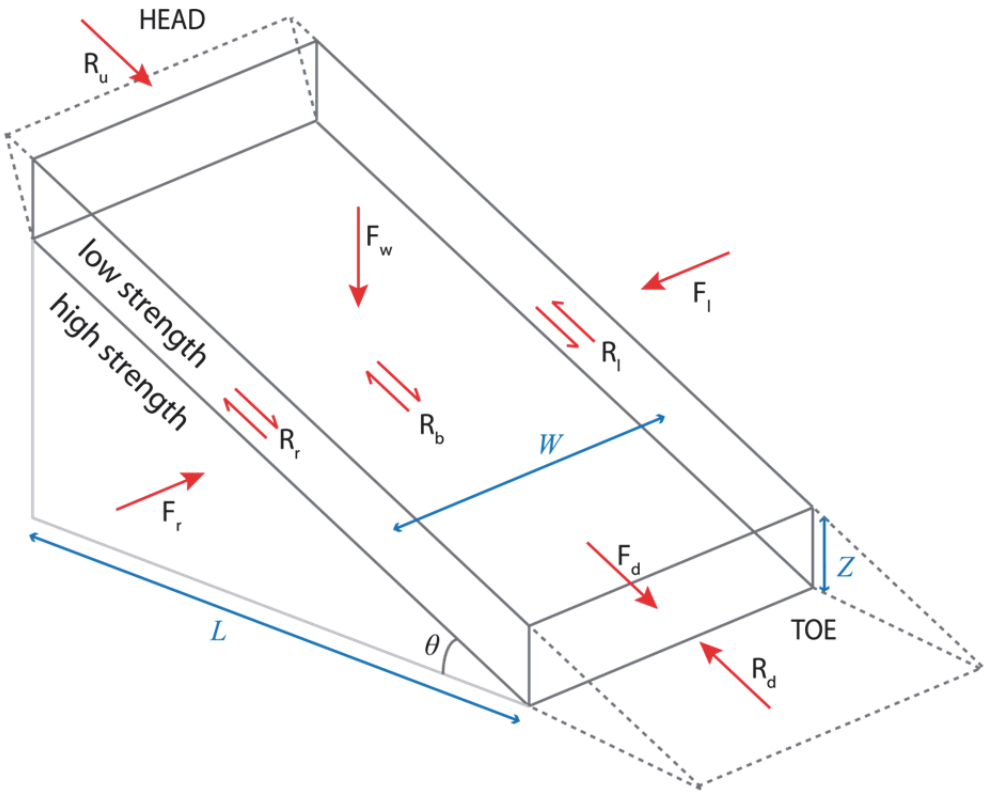

Figure 2.1. Three dimensional force balance stability analysis of a soil element on a slope. Force $\boldsymbol{R_b}$ on the element bottom boundary results primarily from the lithostatic force of the element $\boldsymbol{F_w}$. Forces $\boldsymbol{R_u}$ and $\boldsymbol{R_d}$ arise from active and passive earth pressure, respectively, while shear forces $\boldsymbol{R_l}$ and $\boldsymbol{R_r}$ result from the normal forces $\boldsymbol{F_l}$ and $\boldsymbol{F_r}$ that arise from at rest earth pressure on the element lateral margins. Adapted from [Milledge, et al., in prep].

The four lateral boundaries of a slope element are assumed to be vertical, while the base is assumed slope-parallel (figure 2.1). Length, width, and height of the slope element are measured in the three-dimensional Cartesian coordinate system of the elevation grid, with length and width measured horizontally on the *X*-*Y* plane and height measured vertically in the *Z* direction. The resistances along these boundaries are a combination of cohesion (soil and root cohesion) and friction, where the frictional resistances are the result of earth pressure acting normal to the boundary. For an element of width $\boldsymbol{W}$ (m), and length $\boldsymbol{L}$(m), corresponding to the grid spacing, with a vertical soil depth $\boldsymbol{Z}$ (m), and sloping in the $\boldsymbol{L}$ direction, the resistance $\boldsymbol{R_l}$ (N) and $\boldsymbol{R_r}$ (N) acting on the lateral boundaries of the element are defined as:

$$R_l = R_r = C_l Z L + \frac{1}{2} K_o g \left(\rho_s Z^2 - \rho_w h^2 \right) L \cos\theta \tan\phi \tag{2.1}$$

where C_l (Pa) is the total lateral cohesion from both soil and roots, h (m) is the saturated part of Z, ρ_s and ρ_w (kg/m^3) are the soil and water densities, θ and φ (degrees) are the slope and soil friction angles, g (m/s^2) is the force of gravity, and K_o is the *coefficient of at-rest lateral earth pressure* (discussed below) applied from the elements immediately to either side. The resistance R_d (N) acting on the downslope boundary is defined as:

$$R_d = \frac{1}{2} g K_p \left(\rho_s Z^2 - \rho_w h^2 \right) W \left(\cos\left(\phi' - \theta\right) - \sin\left(\phi' - \theta\right) \tan\left(\phi\right) \right) \tag{2.2}$$

where K_p is the *coefficient of passive lateral earth pressure* (discussed below) applied from the element immediately downslope, and φ' is the angle of friction at the boundary between the elements. The resistance R_u (N) acting on the upslope boundary is defined as:

$$R_u = \frac{1}{2} g K_a \left(\rho_s Z^2 - \rho_w h^2 \right) W \left(\cos\left(\phi' - \theta\right) - \sin\left(\phi' - \theta\right) \tan\left(\phi\right) \right) \tag{2.3}$$

where K_a is the *coefficient of active lateral earth pressure* (discussed below) applied from the element immediately upslope. The resistance on the base of the element is defined as:

$$R_b = C_b W L \sec\theta + \left(\rho_s Z - \rho_w h \right) g W L \cos\theta \tan\phi \tag{2.4}$$

where C_b (Pa) is the total cohesion from both soil and roots acting on the base of the element. Finally, the driving force F_d (N) is defined to be

$$F_d = \rho_s g Z W L \sin\theta \tag{2.5}$$

The theory of lateral earth pressure (K_o, K_a, and K_p) has been developed by Terzaghi [1941; 1943] within the context of earth-retaining structures, typically involving a wall, but can also be extended to discrete boundaries (such as those illustrated of the slope element of figure 2.1) by assuming these boundaries to be vertical, and not deforming [Eid et al., 2006]. The earth pressure coefficients are used to convert the vertical effective pressures, to which a soil element is subjected at some depth, to effective horizontal pressures acting on the lateral boundaries between soil elements. The case in which this boundary is static (i.e. it does not move towards or away from the soil element) is that of at-rest earth pressure (figure 2.2) in which the soil mass is in a case of static equilibrium. Following Arellano and Stark (2000) we assume that this is the case for the lateral boundaries (those parallel to the L direction of slope) of the geometry shown in figure 2.1. The conventional formulation for the at-rest coefficient is given by Lambe

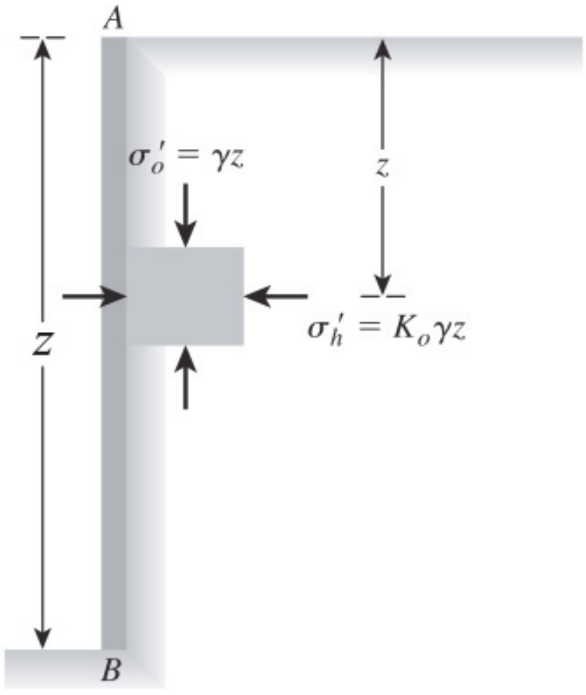

Figure 2.2. Lateral at-rest earth pressure: the coefficient Ko converts the effective vertical pressure to an effective lateral pressure. Adapted from [Das, 2010].

and Whitman, [1969] as:

$$K_o = 1 - \sin(\phi) \tag{2.6}$$

In contrast, the upslope and downslope boundaries of figure 2.1 (those parallel to the ***W*** direction) will move with respect to the upslope and downslope adjacent wedges, shown in the schematic cross-section in figure 2.3. At failure, the central block will move away from the boundary with the upslope (active) wedge, and towards the boundary with the downslope (passive) wedge. As illustrated in [Das, 2010], this causes the upslope wedge soil mass to fail along a basal curved surface (best represented as a *logarithmic spiral*), at the same time stretching outward and moving downward relative to the boundary (figure 2.4a). The downslope wedge soil mass will similarly fail along a basal curved surface, but the soil mass will in this case be compressed and move upward relative to the boundary (figure 2.4b). In both cases the earth pressure coefficients must take into account the friction along the block and the wedge (which offsets the direction of the lateral forces), as well as friction and soil and root cohesion along the curved failure surface [Soubra and Macuh, 2002].

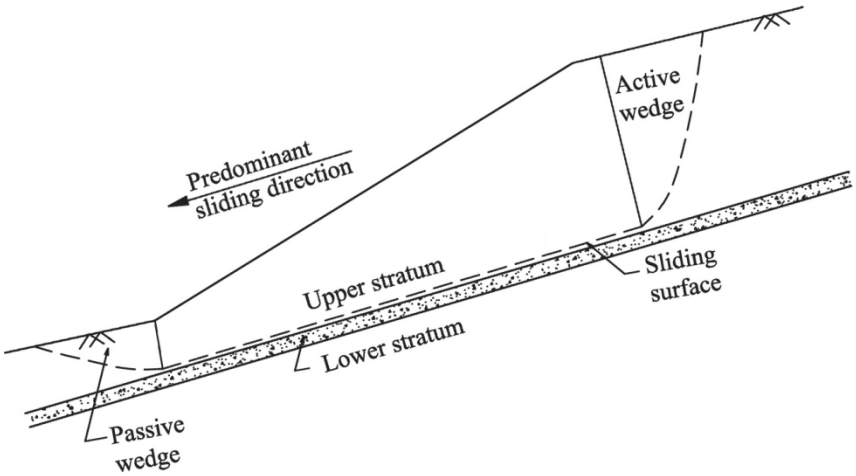

Figure 2.3. Active and passive earth pressure: the geometry of the upslope and downslope wedges. Adapted from [Eid et. al, 2006].

Terzaghi and Peck [1967] developed a procedure using *trial wedges* defined by different logarithmic spirals for evaluating the active and passive earth pressure coefficients in the case of a cohesionless soil mass: for various combinations of θ , φ , and φ', the log-spiral surface resulting in the *lowest* earth pressure force is selected, leading to the definition of the coefficient. Terzaghi's rationale is a direct consequence from Coulomb theory [Coulomb, 1773, 1776; Cullmann, 1875], in which the failure plane resulting in the most critical wedge is considered. Following this approach, Soubra and Macuh [2002] proposed an optimization procedure which minimizes the pressure force exerted by as soil mass of depth ***Z*** given θ , φ , φ', and γ (the unit weight of the soil, expressed in N/m^3) as a function of the two angles θ_0 and θ_1, which define a logarithmic spiral, accounting for soil and root cohesion ***C*** (*Pa*) along the logarithmic spiral boundary. They minimize the active and passive earth pressure forces P_a and P_p (*Pa*), defined as:

$$P_a = K_{a\gamma}\frac{\gamma Z^2}{2} + K_{ac}C \quad \text{, and } \quad P_p = K_{p\gamma}\frac{\gamma Z^2}{2} + K_{pc}C \tag{2.7}$$

where the coefficients $K_{a\gamma}$, K_{ac}, $K_{p\gamma}$, and K_{pc}, represent the effects of soil weight and cohesion for the active and passive cases, respectively. Once P_a and P_p are minimized then the active and passive earth pressure coefficients are given by:

$$K_a = K_{a\gamma} + 2K_{ac}\frac{C}{\gamma Z} \quad \text{, and } \quad K_p = K_{p\gamma} + 2K_{pc}\frac{C}{\gamma Z} \tag{2.8}$$

This method is adopted here in an offline fashion, whereby tables containing the active and passive earth pressure coefficients for binned values of ***Z, θ***, ***φ***, ***φ'***, and ***γ*** are pre-calculated. In order to limit the parameter search space ***φ'*** is set to ***φ*** (i.e. the soil friction angle is the same everywhere), and ***Z, γ***, and ***C*** are lumped into a single dimensionless parameter ***log(C/γZ)***, thereby producing three-dimensional tables defining K_a, and K_p for binned values of ***θ***, ***φ***, and ***log(C/γZ)***.

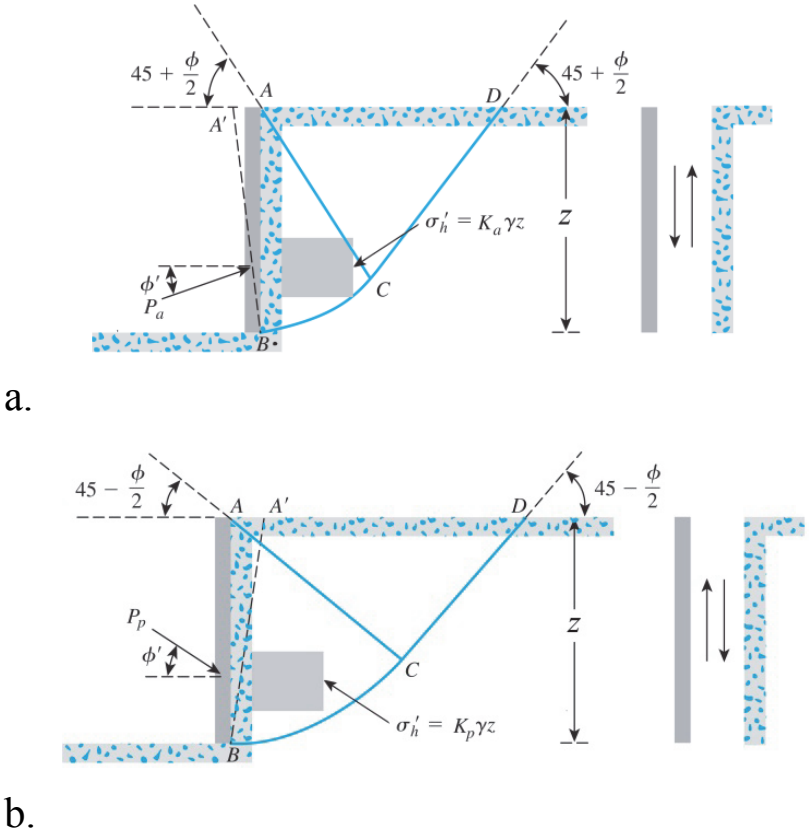

Figure 2.4. Schematic diagram of lateral active (a) and passive (b) earth pressure forces. The earth pressure coefficients Ka and Kp convert the vertical effective pressures to effective horizontal pressures acting on the upslope and downslope boundaries Adapted from [Das, 2010].

It is important to note that while the three-block landslide geometry shown in figure 2.3 is assumed here, the upslope and downslope wedges used to compute the earth pressure forces acting on the central block will not ultimately considered to be part of the landslides as delineated by the search procedure that will be presented in the next chapter. This procedure will indeed use the active and passive wedges to compute the forces acting on potential landslide boundaries, but because the length of these wedges is not fixed and is unknown a priori, the procedure will only return least-stable collections of *central* blocks (i.e. the blocks bounded upslope and downslope by the active and passive wedges, respectively).

With these assumptions and definitions, the *factor of safety* (***FS***) of a slope element can be calculated as indicated by Hovland [1977], as the ratio of total available shear force resistance, R_t, over the driving force, F_d:

$$FS = \frac{R_t}{F_d} = \frac{R_u + R_d + R_l + R_r + R_b}{F_d} \tag{2.9}$$

It should be noted that the slope direction of a slope element is not necessarily aligned with the grid reference frame. In this case the forces on each grid cell boundary are calculated as a combination of the two lateral forces acting on that boundary (i.e. the forces acting on the two sides of the slope element which intersect the grid cell boundary). These two forces are partitioned based on the orientation of slope element with respect to the grid reference frame (figure 2.5 a). Similarly, the driving forces contributed by a grid cell may not be pointing in the same direction as those contributed by another grid cell. Thus, when adding forces for a collection of cells the vector sum is used (figure 2.5 b).

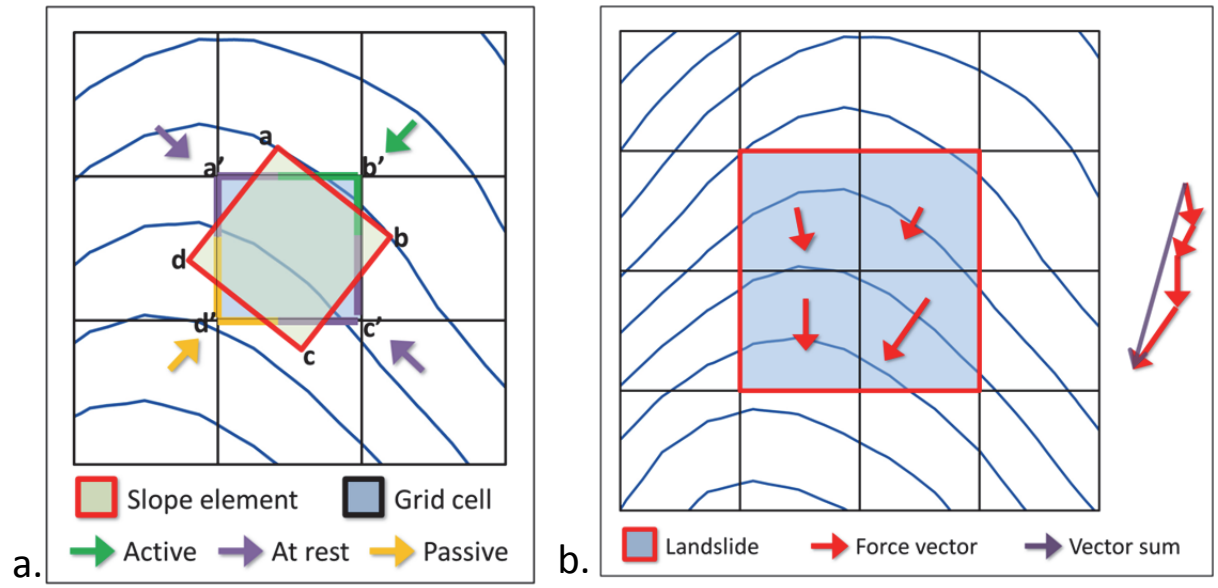

Figure 2.5. Force partitioning and re-orientation. a) Each edge of a slope element oriented parallel to the slope direction is subjected to one of the active, passive, and at rest earth pressure forces. When applied to the corresponding grid cell, which is not oriented in the slope direction, these forces must be re-distributed so that each edge of the grid cell receives a combination of forces. In this example, the slope element edges *a-b* and *a-d* experience active and at rest forces, respectively. The grid cell edge *a'-b'* (which intersects both *a-b* and *a-d*) experiences a combination of active and at rest forces proportionate to the amount of rotation between the slope element and the grid cell. b) A potential landslide consisting of a collection four grid cells. Each cell contributes a different amount of driving force to the collection. The total driving force for the landslide is equal to the vector sum of the four individual forces. Note that the length of the resulting vector is less or equal to the sum of the individual lengths.

The inputs required by this model are spatial layers of topographic slope, soil depth, soil saturation height, root cohesion (basal and lateral), and scalars indicating material properties (soil and water densities, soil cohesion and friction angle. While field-measured data is desirable, in practice it is rarely available, particularly at the required spatial resolution. This requires the adoption of other sub-models, which will be discussed in the following sections.

2.2.2 Topographic sub-model

Topographic data is typically made available in several forms. The most widely used models for topographic representation are *Digital Elevation Models* (DEM's), which consist of a matrix of elevations arranged into a regular grid or lattice. DEM's (also commonly referred to as *grids*) are always a product of some form of interpolation, as elevation data points are not collected at regular intervals. While this introduces another level of pre-processing, and thus a potential source for errors, the algorithmic advantages of regular grids, as well as modern resampling

techniques have made DEM's the dominant application choice for elevation data. Alternative representations include *Triangular Irregular Networks* (TIN's), in which each elevation data point is connected to two neighboring points, thus defining a triangular *facelet*, and Digital Line Graphs (DLG's), which consist of a vector-based map of *isolines* or *contours*. Of these, only TIN's created using a *Delauney triangulation* from a regular lattice (by which a circle passing through a triangle's vertices includes no other data point) offer a valid alternative to DEM's as the resulting *Voronoi diagram* consists of hexagonal cells that can provide similar benefits as the square cells of a DEM. Such TIN's have the advantage of being able to represent planar surfaces with fewer elements than DEM's, thus resulting in increased computational efficiency, but their generation is no simpler, and the potential for errors is similar when a lattice is required for their generation. DEM's are adopted for this research because they are the most readily available format for elevation data, and there is a trivial mapping from square grid cells to the idealized slope element of figure 2.1. Moreover, the adoption of a regular grid results in a mathematical representation of the forces acting on a landscape consisting entirely of symmetric matrices, whose computational advantages will become apparent in chapter three. However, it is pointed out that a regular Voronoi tessellation would achieve similar computational results.

While elevation data of almost the entire world is available at resolutions ranging from 10 to 90 meters, the advent of Light Detection and Ranging (LiDAR) technology has resulted in greater availability of high-resolution (from sub-meter to 3 meters) DEM's, which enable the accurate definition of topographic features relevant to geomorphologic and hydrologic modeling. This does not come without a cost, as such datasets contain orders of magnitude more entries than conventional data. For this reason the resolution is set equal to the scale of the smallest features of interest, and a 2 meter LiDAR-derived DEM is adopted. Elevations are pre-processed in ArcGis to remove depressions from the DEM, and the ArcGis ASCII format is adopted for greater interchangeability between other software packages.

Two fundamental topographic attributes must be derived from a DEM for modeling processes relevant to shallow landslides: slope and drainage area (also called contributing or upslope area). There are numerous methods to extract these attributes, and while the procedure that will be developed in the following chapter is independent of them, care should be used in their selection.

The two most widely used methods for computing slope on a DEM are those proposed by Zevenbergen and Thorne [1987] and by Horn [1981]. Both use a 3 cell by 3 cell moving window to assign a slope to the center cell, but differ in the number of adjacent neighbors used. The former method fits a quadratic equation to the window by using the four nearest cells (up, down, left, right), while the latter uses a third-order finite difference scheme which weighs the four closest cells more than the remaining four neighbors. While there is no established best method, it is common knowledge that in practice using four neighbors produces better results in smoother surfaces while using eight neighbors produces better results in rougher surfaces [Burrough and McDonnell, 1988]. As LiDAR-derived topographic data is generally rougher than conventional data, the method proposed by Horn [1981] is adopted. This is the same method used by many commercial GIS software packages, such as ArcGis (www.esri.com).

The three most common methods for routing flow and thus defining how drainage area is delineated are the steepest descent (D8) method, first introduced by O'Callaghan and Mark [1984], the multiple direction (MS) method, first introduced by Quinn, et al. [1991], and the single flow infinite directions (D∞) method first introduced by Tarboton [1997]. As with slope,

all the above methods rely on a 3 by 3 window to define flow direction from the center cell. The D8 method assigns flow to the single cell which results in the steepest descent out of the eight possible neighbors. This method concentrates flow and thus commonly used for routing flow in channels, but is most sensitive to grid orientation as it can only discriminate between directions that vary in multiples of 45 degrees. In contrast, the MS method assigns flow proportionally to slope to all downhill neighbors of the center cell. This results in a very dispersive flow, more descriptive of less convergent areas such as hillslopes, and is the least sensitive to grid orientation. The D∞ method attempts to bridge the other two methods by assigning flow to a single direction, but considering all possible directions and not just the eight defined by the immediate neighbors. In practice this results in flow being partitioned between two of the eight neighbors, slightly more dispersive than the D8 method but less than the MS method. While our procedure is general, in other words it does not depend on the choice of flow partitioning, in practice this choice can have a pronounced effect. Because sub-surface flow in hillslopes is the primary interest, the MS method is selected although the D∞ method could easily be substituted if sub-surface flow was deemed to be more concentrated.

Contributing area at a specific grid cell is simply the area of the collection of cells from which flow can reach this cell. Given a flow direction matrix, contributing area can be computed by recursively accumulating the contributing area of upslope cells, or conversely by handing off contributing area downslope from the highest elevations downwards. Regardless, it should be noted that, unlike slope, contributing area at a cell is a *non-local* operation as it may depend on cells which are a considerably removed. This can become problematic on very large datasets: because of this dependence, the data cannot easily be processed in separate *tiles*. For such cases Bellugi et al., [2011] developed a parallel algorithm based on the *partitioned global address space* (PGAS) parallel programming model and a graph representation of the landscape, which reproduces the results of standard serial implementations. Other algorithms based on numerical iterative approaches such as the *biconjugate gradient stabilized method* (BiCGSTAB), are under development [Richardson et al., 2011].

It is important to note that all flow-routing methods (and thus drainage area algorithms) assume that the DEM has been treated to remove *sinks* or *pits* (topographic depressions generally resulting from gridding topographic elevation data). This is generally achieved by the standard flooding approach described by Jenson and Domingue [1988] by which elevations of sinks are increased to those of their lowest neighboring outflow point, and the flow is directed towards this point. For this research all DEM's are pre-processed in this fashion using the tools packaged within the commercial software package *ArcGIS* (www.esri.com).

2.2.3 Soil depth sub-model

Based on the framework illustrated in Dietrich et al., [1995], soil depth is estimated by coupling an exponential soil production term [Heimsath, et al., 2001] with a non-linear diffusive term [Roering et al., 1999] in a finite-difference scheme, which is then run to match the generally sparse observations. Under the assumption that rivers efficiently transport away any material that is delivered, soil depth in channels is set to zero at each finite-difference iteration.

The rate of conversion of intact bedrock to mobile soil (typically due to biotic disturbance) declines exponentially with soil depth, and can be expressed as:

$$-\frac{\partial z_b}{\partial t} = \varepsilon e^{-\alpha h} \tag{2.10}$$

Here z_b (m) is the height of the soil-bedrock boundary above some datum, t is time, ε is the production rate (m/yr) at zero soil thickness, α (1/m) is the rate constant, h (m) is the soil thickness normal to the bedrock boundary. The annual transport across the entire hillslope is determined by the nonlinear flux equation:

$$\tilde{q} = \frac{K\nabla z}{1-(|\nabla z|/S_c)^2} \tag{2.11}$$

where q (m^3/m/year) is the flux, K (m^2/yr) is the diffusion coefficient, z (m) is the topographic elevation above a reference datum, and S_c (m/m) is the critical slope. For the model application described in chapter four, site-specific parameters that were calibrated for the Oregon Coast Range (the site of our application) are chosen. K is set to *0.0032* (*m^2/yr*) and S_c to *1.25* (*m/m*) based on Roering et al., [1999]; a is set to *0.0003* (*1/m*) and ε to *0.000268* (*m/yr*), based on Heimsath et al., [2001].

2.2.4 Hydrologic sub-model

Shallow sub-surface storm flow (*SSSF*) [Dunne and Black, 1970a; 1970b], plays a critical role in increasing soil water pore pressures, which in turn reduce the shear strength of soils, affecting the stability of hillslopes. SSSF is a very complex phenomenon involving, among many other factors, transient saturated and unsaturated flow, the interaction between surface water and ground water, the spatial heterogeneity of soils and their porous properties (including the distribution of macropores), the permeability and fracture density of the underlying bedrock, antecedent soil moisture conditions, as well the effects of vegetation. This complexity presents a formidable challenge to the definition, calibration, and validation of mechanistic hydrological models, suggesting that "their application is more an exercise in prophecy than prediction" [Beven, 1993]. There is thus a wide variety of approaches, all with a varying degree of simplifications, ranging from purely statistical approaches (e.g. Moore and Clarke, [1981]), to fully parameterized three-dimensional integrated surface and subsurface parallel codes designed to take advantage of modern high-performance computing platforms (e.g. Kollet and Maxwell, 2006]). Many studies have also focused on the hydrological triggering component of landslides, and their approaches also range from purely empirical (e.g. Caine, [1980]), to coupled, distributed hydrological-geotechnical models (e.g. Simoni et al., [2008]).

Most studies suggest that landslides result from development of positive pore water pressures resulting from a critical level of saturation (Iverson, 1997). The two dominant mechanisms that generate high pore water pressures at a point are topographically-steered subsurface flow (over timescales of days to weeks), and rapid vertical infiltration (over timescales of minutes to hours). An additional mechanism which can contribute to pore water pressure generation is flow into the soils from the underlying fractured bedrock. Partial or full saturation of soils can occurs in these exfiltration areas [Montgomery and Dietrich, 2002], directly contributing to landslide initiation [Mongomery et al., 2009]. However, due to the current inability to characterize flow to and from the bedrock, this mechanism is generally ignored. There is still much debate over which the dominant process is and how to parameterize it. For example, there are models that principally focus on the short-term vertical component (e.g. Iverson [2000], Baum et al., [2008]), others that favor the long-term lateral component (e.g. Montgomery and Dietrich [1994], Beven et al., [1995]), while others try to account for both short-term and long-term components (e.g. D'Odorico et al., [2005]).

In this research both topographically-steered subsurface flow and vertical flow will be considered, but they will be treated in the simplest way possible. This is because focus of this study is on developing a landslide search procedure (which is not dependent upon the choice of hydrological parameterization), and on understanding the controls on landslide size (in a fashion that is independent of specific parameterizations). The long-term subsurface flow is thus represented using the steady state hydrological model proposed by Montgomery and Dietrich, [1994]:

$$\frac{h}{z} = \frac{qa}{Tb\sin\theta} \tag{2.12}$$

where $\boldsymbol{h}$ (m) is the saturated fraction of the soil column $\boldsymbol{z}$ (m), $\boldsymbol{q}$ (m/day) is the *effective* precipitation (precipitation – evapotranspriration), $\boldsymbol{a}$ (m^2) is the upslope contributing area, $\boldsymbol{T}$ (m^2/day) is the transmissivity (m^2/day), $\boldsymbol{b}$ (m) is the grid cell size, and $\boldsymbol{\sin\theta}$ is the topographic gradient (figure 2.6). It should be noted that $\boldsymbol{T}$ is the integral of the saturated conductivity $\boldsymbol{k}$ (m/day) over the depth of the soil $\boldsymbol{z}$. Because $\boldsymbol{k}$ does not appear to vary with depth in the Oregon study site [Ebel, et al., 2007b], $\boldsymbol{T}$ can be effectively be approximated as $\boldsymbol{k*z}$. Thus the height of the saturated fraction of the soil column $\boldsymbol{h}$ can be expressed as:

$$h = \frac{qa}{kb\sin\theta} \tag{2.13}$$

Because of the steady-state assumption, after steady-state is reached time has no bearing in this model: a variation of the effective precipitation $\boldsymbol{q}$, causes an *instantaneous* change in $\boldsymbol{h}$. The short-term vertical component is modeled in a similar instantaneous fashion by setting the saturated fraction of the soil column $\boldsymbol{h}$ to a fixed amount of uniformly applied instantaneous pressure addition $\boldsymbol{p}$ (m) divided by the porosity $\boldsymbol{\eta}$:

$$h = \frac{p}{\eta} \tag{2.14}$$

where $\boldsymbol{\eta}$ is the dimensionless ratio of the volume of the voids to the total volume. It is assumed here that the precipitation depth $\boldsymbol{p}$ is the result of a short burst of rain in which there is no lateral re-distribution. When steady-state is obtained in the topographically steered model, an instantaneous vertical delivery can be also added to the laterally-dominated model. The short-term and the long-term components are thus combined by adding a fixed amount of pressure addition $\boldsymbol{p}$ to the long-term state:

$$h = \frac{qa}{kb\sin\theta} + \frac{p}{\eta} \tag{2.15}$$

It should be noted that throughout this study, if the application of equations 2.13 to 2.15 results in a local value of h that exceeds the local soil thickness z , h is assigned the value of z (i.e. h can never exceed z).

In this research shallow subsurface flow scenarios will be explored by varying the dimensionless parameter $\boldsymbol{q/k}$. For a specific value of $\boldsymbol{k}$, this ratio results in a precipitation rate having units of length per time. However this rate should not be compared with actual storm-induced rainfall rates as steady-state is rarely reached in reality. The results of these simulations will be compared with the vertical-only case obtained by just varying the parameter $\boldsymbol{p}$ (m). Additional simulations will also be performed to assess the effect of vertically dominated flow on antecedent conditions as represented by topographically-steered subsurface flow. In this case $\boldsymbol{p}$ will be varied for some fixed values of $\boldsymbol{q/k}$. These results will be presented in chapters four and five of this dissertation.

A transient version of the steady state model of equation 2.13 can be obtained by re-elaborating the model proposed by Rosso et al. [2006]: water table height at each cell and each time step during a storm sequence is a function of the local precipitation plus the fraction of water which may arrive from upslope area (modulated by an exponential decay which is in turn also a function of the topographic control and of the time step), minus a similarly computed fraction which can drain out of the cell. In essence water is instantaneously redistributed at each time step, and mass is conserved. The height of the saturated fraction $\boldsymbol{h_i}$ (m) of the soil column $\boldsymbol{z}$ (m), at a discrete time step $\boldsymbol{i}$ can be written as:

$$h_i = q_i * \frac{az}{Tb\sin\theta} * \left(1 - \exp\left(-\frac{1+e}{e-eS_r} * \frac{Tb\sin\theta}{az}\right) * t_i\right) + h_{i-1} * \exp\left(-\frac{1+e}{e-eS_r} * \frac{Tb\sin\theta}{az}\right) * t_i \quad (2.16)$$

where $\boldsymbol{q_i}$ (m/day) is the effective precipitation at time step $\boldsymbol{i}$, $\boldsymbol{h_{i-1}}$ (m) is height of the saturated fraction at time step $\boldsymbol{i-1}$, $\boldsymbol{t_i}$ (days) is the duration of time step $\boldsymbol{i}$, $\boldsymbol{e}$, and $\boldsymbol{S_r}$ are the void ratio (volume voids over the volume of solids), and degree of saturation of soils (volume of water over the volume of voids), respectively (dimensionless), and the other parameters are defined as above. When $\boldsymbol{T = k*z}$, this equation becomes:

$$h_i = q_i * \frac{a}{kb\sin\theta} * \left(1 - \exp\left(-\frac{1+e}{e-eS_r} * \frac{kb\sin\theta}{a}\right) * t_i\right) + h_{i-1} * \exp\left(-\frac{1+e}{e-eS_r} * \frac{kb\sin\theta}{a}\right) * t_i \quad (2.17)$$

This model will be explored in chapter six.

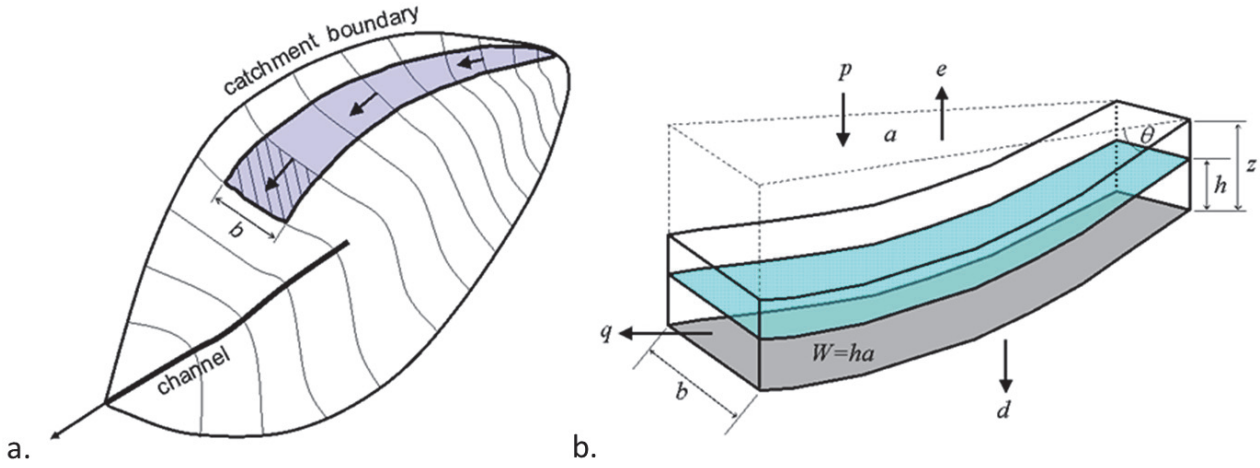

Figure 2.6. Shallow subsurface runoff model. Plan view (a) and cross section (b) of drainage area *a* draining across a contour length, *b*. In the cross section, the heavy line depicts the ground and water table surfaces. At steady state, *q* equals precipitation, *p*, minus evaporation, *e*, and deep drainage, *d*; *h* is the saturated fraction of the soil depth *z* (both measured normal to the ground surface). Adapted from [Dietrich et al., 1993].

2.2.5 Root cohesion sub-model

The characterization of the root reinforcement field is critical in landslide hazard assessment, as roots mechanically reinforce shallow soils in vegetated landscapes, promoting slope stability [Schmidt et al., 2001]. Species-specific spatial vegetation distributions thus play an important role in controlling the size of failures in landscapes [Roering et al., 2003]. As with soil depth, such data are often very sparse in most landscapes, and thus require a modeling approach. Commonly, root density declines exponentially with depth [Roering, 2008], and thus the contribution of roots to soil cohesion is often predicted as an exponential function of depth [e.g. Dunne, 1991; Benda and Dunne, 1997] of the form:

$$C_{rz} = C_{r0} e^{-zj} \tag{2.18}$$

where $\boldsymbol{C_{rz}}$ (Pa) is the amount of root cohesion at a depth $\boldsymbol{z}$ (m), $\boldsymbol{C_{r0}}$ (Pa) is a coefficient representing the maximum root cohesion value at the surface, and $\boldsymbol{j}$ (m^{-1}) is a coefficient which controls the depth at which $\boldsymbol{C_{rz}}$ approaches zero. Root cohesion can be integrated over the depth $\boldsymbol{z}$ to obtain the total root reinforcement:

$$R_{rl} = \int_0^z C_{r0} e^{-zj} dz = \frac{C_{r0}}{j}\left(1 - e^{-zj}\right) \tag{2.19}$$

where $\boldsymbol{R_{rl}}$ ($Pa\ m$) is the lateral reinforcement per unit perimeter length. Thus the root cohesion $\boldsymbol{C_b}$ (Pa) acting across the base at a depth $\boldsymbol{z}$ is equal to $\boldsymbol{C_{rz}}$, and the average lateral root cohesion $\boldsymbol{C_l}$ (Pa) acting on a unit perimeter length of depth $\boldsymbol{z}$ is $\boldsymbol{R_{rl}}$ averaged over $\boldsymbol{z}$:

$$C_b = C_{rz}, \text{ and } C_l = \frac{R_{rl}}{z} \tag{2.20}$$

The coefficients $\boldsymbol{C_{r0}}$ and $\boldsymbol{j}$ are typically obtained either from field data or literature-based estimates of the relationship between root strength, root density and depth. The approach chosen for our application is to extend the site-specific measurements reported by [Montogomery et al., 2009]. Using the methods described by Schmidt et al. [2001], they measured the spatial distribution of root type, size, and depth along the perimeter of the scarp of the landslide which occurred at the site. They report that the depth-averaged, spatially weighted apparent cohesion values due to roots is 4600 Pa, and they also report the apparent cohesion attributable to roots as a function of depth. By fitting an exponential function constrained to integrate to the reported average, values of $\boldsymbol{C_{r0}} = 21666\ Pa$, and $\boldsymbol{j} = 4.96\ m^{-1}$ are obtained. These values will be extended to the entire research area, but as root cohesion is not expected to remain constant, $\boldsymbol{C_{r0}}$ and $\boldsymbol{j}$ will be also halved and doubled in the simulations presented in chapters four and five. The contribution of vegetation surcharge to the normal and tangential forces is neglected, as on slopes nearing 45° they are nearly offsetting. This is confirmed by a sensitivity analysis showing that with respect to all the other variables, vegetation surcharge has minimal impact on slope stability [Borga et al., 2002].

Root reinforcement has thus far been treated as spatially uniform. In reality, one can expect root cohesion values to be somewhat spatially normally distributed and at the same time to exhibit some spatial correlation, according to some correlation length [Griffiths and Fenton, 2004]. This spatial correlation length determines the distance over which random values will be correlated: a short correlation length will result in a patchier root strength field, while a long correlation length will generate a smoother root strength field. To explore this effect a random grid is sampled from a Gaussian distribution with user-defined mean $\boldsymbol{\mu}$ and standard deviation $\boldsymbol{\sigma}$. A spatial correlation is obtained by repeatedly convolving the random Gaussian field with a two-dimensional symmetric Gaussian low-pass filter by which every cell in the Gaussian field is averaged (with Gaussian weights) with its neighbors. The resulting spatial root cohesion grid will approximately retain the mean value $\boldsymbol{\mu}$ and standard deviation $\boldsymbol{\sigma}$, but the number of iterations $\boldsymbol{n}$ will impose a spatial correlation. If we view this process as a random walk on a grid, it is intuitive that $\boldsymbol{n}$ determines how far information will travel from a specific cell and that the expected travel distance (and thus the correlation length) will be of the order of $\boldsymbol{n^{0.5}}$. The specific correlation length will of course also depend on the filter size and on the filter's standard deviation. Here this is simplified by choosing Gaussian filter of size 3 by 3 (which allows information only to travel one cell in any direction at each iteration), resulting in a correlation length of $\boldsymbol{b * n^{0.5}}$ where $\boldsymbol{b}$ (m), is the grid cell size. While this approach produces visually realistic

results, as shown in figure 2.7, it is only intended for exploratory purposes and is not representative of actual interactions between the landscape and the vegetation. The effect of spatially-correlated, normally distributed root reinforcement will be illustrated in chapter six.

2.2.6 Soil material properties sub-model

Additional parameters are required to describe the material properties of the colluvial soils which play a role in the slope stability calculation. These are the friction angle $\boldsymbol{\varphi}$ (*degrees*), the soil cohesion $\boldsymbol{C}$ (*Pa*), and the mean saturated bulk density $\boldsymbol{\rho_s}$ ($kg\ m^3$). Schmidt et al., [2001] report $\boldsymbol{\varphi}$ values of 40° obtained from tri-axial compression strength tests performed on five soil samples from two locations at the Oregon field site. Montogomery et al., [2009], report values of *39.1°* and *41°* obtained from similar tests performed on two undisturbed soil samples from the same site. Both Schmidt et al., [2001] and Montogomery et al., [2009] find the soils to be essentially cohesionless, with a saturated bulk density of *1600* ($kg\ m^3$). Here we treat soil parameters to be constant and set the soil material properties are treated as constant: $\boldsymbol{\varphi} = 40°$, $\boldsymbol{\rho_s} = 1600$ ($kg\ m^3$), and $\boldsymbol{C} = 0$ (*Pa*).

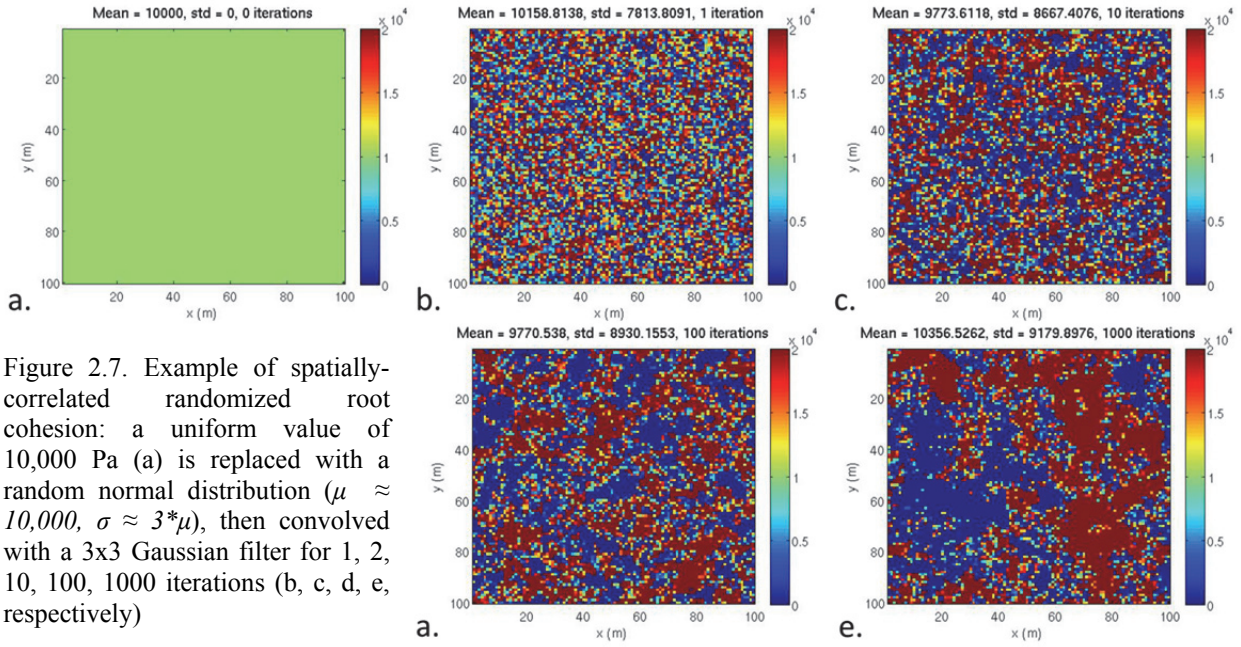

Figure 2.7. Example of spatially-correlated randomized root cohesion: a uniform value of 10,000 Pa (a) is replaced with a random normal distribution ($\mu \approx 10{,}000,\ \sigma \approx 3*\mu$), then convolved with a 3x3 Gaussian filter for 1, 2, 10, 100, 1000 iterations (b, c, d, e, respectively)

2.3 Discussion

In order to define the initial size and shape of a shallow landslide, the fundamental assumption is made that the potential failure mass behaves coherently as a rigid entity. In actuality, a failure may occur in a progressive fashion. For example, in cohesive soils failures have been observed to begin as small-scale cracks or deformations that ultimately coalesce into a continuous failure plane [Petley, et al., 2005]. Similarly, reduced internal strength and liquefaction can cause progressive failure, as suggested by the unusually small cross-sectional areas at the toe of some landslides [Lehre, 1982b]. Such complex behaviors are generally too challenging to be modeled at the regional scale. However the progressive nature of some failures can be represented with models which embrace the rigid block assumption. For example, Lehmann and Orr [2012] treat discretized soil columns as rigid blocks, but they remove them from the landscape and re-distributed their load to their neighbors once a failure threshold is

reached. This can cause neighboring columns to fail in both the upslope and downslope directions. There are challenges to this type of approach: inevitably it will be resolution-dependent as if the discretization is too fine no individual column may fail, yet if it is too large the progressive nature of some landslide events will be lost. It is possible that that a sufficiently fine discretization (i.e. very small rigid blocks) coupled with a search for the initial failure within an iterative approach that effectively removes (and possibly re-distributes) individual failed blocks from the landscape may offer a more faithful representation of observed dynamics.

Another significant assumption that was made here is that the failure plane of a shallow landslide lies at the interface between the colluvium (soil) and the (weathered) bedrock. While this is often the case [e.g. Reneau et al., 1986; Dietrich and Montgomery, 1998], many failures have been observed entirely within the colluvium [Reneau et al., 1984; Lehre, 1982b], generally below the root mass and at some textural, or permeability discontinuity. In the study area for this research all shallow landslides failed at or very near the soil-bedrock interface [Montgomery et al, 2000; Schmidt, 2012]. As an important focus of this research is the development of a regional-scale search algorithm for shallow landslide prediction, it is necessary to make the simplifying assumption of a fixed failure plane to limit the search space to the X-Y (horizontal) domain. Given this requirement and the landslide scar observations, it is thus assumed that the most likely failure location along the Z (vertical) axis is thus the soil-bedrock interface.

It is also assumed here is that a soil mass unit is of parallelepidal shape. Clearly this is not the case in reality as edges of an actual failure can be inclined and curved in the *X*, *Y*, and *Z* directions [Stark and Eid, 1998]. *Non-vertical* walls will cause earth pressures from adjoining cells to operate very differently. However, it is generally assumed that *vertical* walls will diminish the surface area on which lateral resistances operate resulting in a conservative underestimation of the factor of safety. In contrast, discretized *straight* walls (i.e. in the *X* and *Y* directions) will generally increase the perimeter length, thus overestimating the factor of safety. The issue of whether discretization is ultimately conservative is further complicated by the fact that on the X-Y plane the grid area is as likely to be an over estimate of the failure area than it is to be an under estimate. The discretization effects on the driving forces and on the basal resistance are thus unclear, although on average they should offset. In the limit, a finer discretization should remove this effect entirely resulting in a net conservative approach.

The method chosen to represent active and passive earth pressure relies on the Upper Bound Limit Theorem, commonly used in limit analysis [e.g. Chen 1975; Chen and Liu, 1990]. This theorem states that "the soil mass (of the upslope and downslope wedges) will collapse if there is any compatible pattern of plastic deformation for which the rate of work of the external loads exceeds the part of internal dissipation" [Drucker et al., 1952]. This means that the most critical solution (i.e. the one resulting in lowest of all possible upper bounds) corresponding to the assumed mechanism must be found. For the geometry shown in figure 2.3 this solution depends on the characterization of the wedge failure surface. As discussed in section 2.2.1, a log-spiral slip surface adopted here is an improvement over the classic Coulomb planar slip surface, as relaxing the planarity constraint allows for a more critical wedge to be found, and not yielding failure surfaces of infinite length (as produced by the Coulomb method when the slip surface is parallel to the bedrock surface). The two angles which define a log-spiral surface can be pre-computed (offline) by numerical optimization, thus not resulting in a higher computational overhead. It should be noted that while the log-spiral choice relaxes the (strict) planar assumption, it still imposes a constraint on the geometry of the failure. It is unlikely that a more

complex slip surface that results in a more unstable wedge would not exist. However, in order to numerically find a reasonable slip surface, it must be defined by relatively few parameters, so a compromise must be made. In practice, this may result in an over-estimation of the earth pressure term [Milledge et al., in prep].

A more conservative approach would be to find a lower bound solution (i.e. one that would guarantee stability, rather than instability). Such approaches are based on the Lower Bound Limit Theorem, also commonly used in limit analysis [e.g. Chen, 1975; Chen and Liu, 1990]. This theorem states that "If an equilibrium distribution of stress can be found which balances the applied load and nowhere violates the yield criterion, which includes c, the cohesion, and phi, the angle of internal friction, the soil mass will not fail, or will be just at the point of failure" [Drucker et al., 1952]. Rankine theory [Rankine, 1857] is a commonly used stress field approach to computing active and passive earth pressure for retaining structures. It assumes that the soil is cohesionless, the wall is frictionless, the soil-wall interface is vertical, the failure surface on which the soil moves is planar, and the resultant force is angled parallel to the backfill surface. Mazindrani and Ganjali [1997] extended Rankine theory to allow for a cohesive backfill and an inclined surface, but do not report results for surfaces inclined by an angle which is greater than the soil friction angle. Milledge et al., [in prep.] test this approach and indeed find that it is problematic at high slopes, and that at low slopes it generally results in an underestimation of the earth pressure.

The lower and upper bounds define an envelope in which the "true" earth pressure resides. These bounds rarely coincide when the surface is inclined, the soil is cohesive, and there is friction on the boundaries. As limit equilibrium analysis, commonly adopted for slope stability models (including the one used in this study) follows the approach and assumptions dictated by the Upper Bound Limit Theorem [Chen, 1975], the log-spiral method if not perfect is at least consistent. Finally, this method can be used and produces reasonable results over the range of conditions in which shallow landslides are common [Milledge, et al., in prep]. However, it should be pointed out that different characterizations of earth pressure may result in non-trivial slope stability differences, and thus more research is needed to develop a general method on which scientists can agree.

The soil depth sub-model chosen here produces a pattern of thin colluvium near ridges (and in divergent areas in general), and thick colluvium in hollows (and in convergent areas in general) which matches well field observations. However, because both soil production and downslope transport are not likely to vary significantly from one grid cell to the next, the predicted patterns are very smooth. In reality, greater local variations in soil depth are indeed observed in the field. This is probably due to the stochastic nature of soil production, which is mostly a result of small-scale (local) biotic events [Dietrich et al., 2003] such as tree throw and animal burrowing. Such events can be taken into account in a more probabilistic fashion. For example, Dietrich et al. [2008] propose that events such as tree throw in a specific location have a characteristic recurrence time N, initiate a stochastic soil production event with probability 1/N, and multiply the right hand side of equation 2.10 by the time elapsed since the last production occurrence. This approach produces more heterogeneous soil depth patterns, but recurrence times vary by orders of magnitude depending on the nature of the biotic event. Moreover, it is difficult to imagine that any single biotic event is mostly responsible for the conversion of rock to soil, suggesting that perhaps a distribution of types and recurrence of soil-producing events must be considered. While such a study is beyond the scope of this research, it should be noted

that the effect of soil heterogeneity on slope stability could be quite significant due to the interplay between soil, hydrology, and vegetation.

The parameters used to model soil depth in this research are region-specific. While similar data exist for some other regions (e.g. McKean et al., 1993; Heimsath, et al, 1997), this is generally not the case. In absence of soil production/transport parameters (or estimates from similar geologic settings) alternative methods must be established. For example, because soil depth is well correlated with topography, Ho et al. [2011] propose a simple relation between topographic index as defined by Kirkby [1975] and soil depth, with an empirically calibrated coefficient. Such methods, well guided by empirical observations may be sufficient to capture the topographically steered soil depth variations when better data are not available. It is important to notice that none of these approaches (including ours) accounts for the periodic evacuation of soil from hollows from shallow landslides and debris flows typical of these landscapes [Dietrich and Dunne, 1978]. Thus, any soil depth realization should generally be considered as an upper bound prediction, and that predicted deep pockets of soil may at times not correspond to reality.

We have adopted the three-block landslide geometry shown in figure 2.3, with the upslope and downslope wedges used to compute the earth pressure forces acting on the central block, in turn aiding or resisting its mobilization. The choice of only including the central block (or collections of central blocks) in the delineation of a landslide shape can have a significant impact on predicted landslide size. On slopes higher than the friction angle, the failure plane of the active or passive wedge can be arbitrarily close to the bedrock surface. The length of the wedges will thus extend beyond the upslope or downslope neighboring cells and it could be argued that these cells should in fact be considered part of the landslide. Rather than introducing rules for these cases, we choose to let the search procedure include the neighboring cells if the resulting factor of safety is decreased as a result. In some extreme cases, where very deep pockets of soils are predicted on slopes significantly higher than the friction angle, the force exerted by the active wedge on the central block may exceed the resisting force of the passive wedge. This could lead to abnormally small (e.g. single-cell) and deep (several meters) landslide predictions which are rarely observed. Pointing out that this is a limitation of earth pressure theory which often gives incorrect results for slopes exceeding the friction angle, we rely on the on the extremely low likelihood of such conditions in real landscapes (where deep soils are generally not found on very steep slopes) to avoid using an arbitrary rule to remedy the situation. Notwithstanding, a bias towards smaller landslides may result from these assumptions.

The treatment of hydrology is perhaps overly-simplistic in this study. This is because the aim here is only to capture the very essential elements of the landscape's response to landslide-triggering storms. The pore pressure response to such events is an extremely complex matter [e.g. Iverson, 1990], which depends among many other things on the abundance of macropores [e.g. Beven and Germann, 1982], and the amount of exfiltration from the underlying fractured bedrock [e.g. Montgomery et al., 1997; Montgomery and Dietrich, 2002]. There exist very complex three-dimensional distributed groundwater flow models [e.g. Ashby and Falgout, 1996; Jones and Woodward, 2001; Kollet and Maxwell, 2006] which can account for very heterogeneous media and preferential flow patterns. However, in practice their applicability is limited in natural settings as knowledge of the subsurface is generally limited [Beven, 1993] and model calibration is a daunting, if not impossible, task as parameter values cannot be measured in the field at the required scales [Beven, 1996].

While three-dimensional flow calculations have been performed over small areas [e.g. Ebel et al., 2007a, b], at the larger scale very crude simplifications of reality are required [e.g. Montgomery and Dietrich 1994; Beven et al., 1995; Iverson 2000] that will surely not hold everywhere. However, such approaches offer simplicity, inexpensive calculations, and a minimal number of parameters, with a quasi-physical interpretation to be estimated in representing the subsurface storage [Beven, 1997]. There is much debate on which are the essential mechanisms and the minimal parameters which must be taken into account for a quasi-mechanistic representation of hydrologic processes in the context of shallow landslide forecasting [e.g. Iverson, 2004; Montgomery and Dietrich, 2004]. Such debate is beyond the scope of this research, and in fact the approach taken here is to further relax mechanistic faithfulness by simply assuming that instantaneous topographically-steered or vertical flows (or both) contribute to the definition of landslide-triggering pore pressure fields. However, it is the hope that this research may shed some light on the signature of such processes on landslide size and location distributions. Iverson [2000] offers an elegant model for infiltration-based pore pressure development. This model only requires knowledge of initial conditions (i.e. location of the water table), and is thus compatible with the framework defined in this study: in infiltration dominated scenarios unsaturated initial conditions can be assumed, while in scenarios in which topographically-steered subsurface flow plays a dominant role initial conditions can be set to the output of the Montgomery and Dietrich [1994] model. The Iverson [2000] model will be included in subsequent research,

Following Schmidt et al. [2001], two simplifying assumptions are made in characterizing root reinforcement in the context of slope stability: that the tensile strength of individual root fibers is fully mobilized, and that all roots observed to be broken after the occurrence of a landslide failed simultaneously. It is acknowledged here that this is not always the case, and that models which use a fiber-bundle approach to represent progressive root failure (e.g. Schwarz et al., [2010]) are likely more realistic. However, for the scope of this research these simplifications are appropriate as the focus is on the initial landslide size sought over a regional scale. On such a scale a sufficiently fine discretization should capture the essential mechanics without unduly increasing the computational cost.

Root reinforcement is also assumed to decay exponentially with depth. This is supported by field observations in our research area: with the exception of the first few centimeters which don't have significant root presence the root mass noticeably diminishes with depth. This may not always be the case: for example, in a mature forest with a weaker understory the peak strength may occur lower in the soil column below the understory roots. In such cases a simple exponential decay may not be the most appropriate. It should also be pointed out that both the strength value and the exponential shape factor (controlled by the rooting depth) will vary with vegetation type. In an area with more complex vegetation than our study site, this may result in a different parameterization of root reinforcement. Most importantly, root reinforcement is spatially variable and not just with respect to soil depth. This variability is not trivial to characterize, as different vegetation species and ages will result in different correlation length across a landscape, which are not well characterized at present time.

Also neglected in this study is root strength deterioration following vegetation removal and root strength recovery following vegetation regrowth [e.g. Sidle, 1991; Sidle, 1992; Gerber, 2004; Dhakal and Sidle, 2003]. These effects are extremely important, but are outside the scope

of this research. For our purposes, the effects of root strength deterioration and recovery are captured by systematically varying the parameters C_{r0}, and j from equation 2.18.

Soil material properties such as friction angle and bulk density are held constant in this study. While these properties will change in different geologic settings, they do not vary considerably in the Oregon Coast Range. For example, reported values of the soil friction angle range between *35°* and *44°* [Yee and Harr 1977; Schroeder and Alto 1983; Burroughs 1985, Montgomery et al., 2009]. Considering the relatively few number of measurements and the margin of error involved in soil tests, this assumption is not unreasonable.

2.4 Conclusion

In this chapter I presented a multi-dimensional stability model framework that can be applied to landscapes at the regional scale. This slope stability model is mechanistic but not so mechanistic that its application becomes impracticable. It is fully three-dimensional in the treatment of the forces acting on a discretized slope element and it is statically determinate. The model considers the effects of root cohesion and pore pressures, and includes the effects of earth pressure in a manner that is compatible with natural slopes. Finally, this model is easily applicable to spatially gridded data, and requires only a modest parameterization facilitated by procedures defined to obtain spatially explicit parameter fields at the required resolution. While this framework allows for the characterization of the forces acting on all the boundaries resulting from the discretization of a landscape into slope element blocks (and thus the role of each block in the stability of the landscape), a deterministic search procedure that is able to select discrete least-stable combinations of slope elements across a landscape must be defined in order to obtain meaningful shallow landslide predictions. No such procedure exists, and its development will be the focus of the next chapter.

Chapter 3

Searching for the optimal landslide: a new efficient method for shallow landslide prediction

3.1 Introduction

In a discretized landscape, one can imagine a shallow landslide as a collection of elements (e.g. grid cells), which behave coherently, mobilizing together in accordance to some physical properties and conditions which characterize their instability (i.e. their propensity to mobilize into a landslide). One can also imagine that for a particular discretized landscape and a particular criterion to quantify the instability of a collection of cells, there is one such collection which is less stable than any other. If one further imagines that under such conditions this minimally-stable configuration is the most likely to mobilize first, then the problem of predicting landslides across a landscape can be reduced to the problem of finding the minimally-stable collection of cells in that landscape, and iterating to find the next distinct collection of cells until no more unstable collections are found. This is precisely the goal: I wish to directly determine the initial shape and location of the most likely landslide, given the local conditions (e.g. topography, hydrology, and vegetation). I shall refer to this minimally-stable collection of grid cells as the *most favorable* or *optimal* landslide. The exact solution of this problem could be obtained by testing *every* combination of grid cells and applying a stability analysis such as those discussed in the previous chapter. However, such a *brute-force* approach would be intractable, as the number of possible combinations of cells grows exponentially with the number of cells $\boldsymbol{n}$ in the grid, resulting in $\boldsymbol{O(2^n)}$ complexity. As an example, using brute force to find the least stable landslide across a small $1\ km^2$ landscape discretized into a square grid composed of *1000* by *1000* cells (as one would obtain using modern LiDAR data) could result in exploring a number of different combinations of cells of the order of $\boldsymbol{O(2^{1,000,000})}$, a number so vast that the task would be unfeasible even using the world's most powerful computers.

In this chapter I will examine the computational complexity of this problem, and show that it is as hard as most problems known to computer scientists today. I will then build an algorithm based on spectral graph theory that efficiently approximates the exact solution. I will insert this algorithm into a novel general procedure for finding shallow landslides. This procedure will rely on models and data such as those discussed in the previous chapter, but will not be confined by them: as our models and data improve they can be swapped in to substitute the current choices. I will lay the groundwork for a real-world application, to follow in the next chapter, by devising metrics to assess the procedure's performance. Finally I will conclude by discussing the quality, complexity, implementation, and possible improvements for this procedure.

3.2 A hard problem

Let us examine the problem of finding landslides from a *computational complexity theory* view point. If we state the problem as *"given a discretized landscape, produce the most unstable collection of cells contained in it"*, what can we say about its complexity? In order to discuss this, a succinct review of complexity theory is necessary. Some of the material presented in this section derives from text books by Papadimitriou, [1994], Cormen et al., [2001], Dasgupta et al., [2006], and Arora and Boaz, [2009]. For further details and definitions I refer the reader to these

texts. Some of the examples used here are inspired by lectures given in the Computer Science department at U.C. Berkeley by Christos Papadimitriu, Satish Rao, and Umesh Vazirani.

In computational complexity theory there are several classes of problems, the simplest of which is denoted by the letter ***P***, representing the set of all *decision* problems (i.e. problems having a *yes* or *no* answer) for which a solution can be obtained *efficiently*. Here an *efficient* solution means a *polynomial time* solution, i.e. that there is an algorithm that solves the problem and whose running time can be upper-bounded by a polynomial expression which is a function of the input size. For example, it is easy to verify that a naïve sorting algorithm which compares every element to every other element of a list in order to produce a sorted list will have a running time of at most $k*n^2$, where ***n*** is the number of elements in the list, and ***k*** is some constant which will depend on how much time the algorithm takes to compare any two elements in the list. Thus, the problem of determining whether some list is sorted belongs to the set ***P***.

The next class of computational problems is denoted by ***NP*** (which stands for *non-deterministic polynomial time*), and it consists of all the decision problems for which no such polynomial time algorithm is known, but for which a candidate solution could be quickly verified. A classic example of such a problem is the simplified version of the *traveling salesman* problem: given a set of cities and their pairwise distances, is there a route of length less than ***k*** which passes through all the cities exactly once? The problem could potentially require exploring all possible orders in which to visit the cities, resulting in an exponential time upper bound. However, given a candidate solution, it is easy to add up the distances of the proposed city order and verify whether it is less than ***k***. Clearly the set ***P*** is a subset of ***NP***. However it should be noted that determining whether $P = NP$ or $P \neq NP$ is perhaps the most notable unsolved problem in computer science [Cook, 1971]. Another subset of ***NP*** is the set of ***NP-complete*** problems: these are the problems that are in ***NP*** and whose solution could solve any other problem in ***NP***. The first such problem to be discovered was the *satisfability* problem (also known as ***SAT***): that of determining if the variables of a given Boolean formula can be assigned in such a way as to make the formula evaluate to *TRUE* [Cook, 1971]. To this day, no algorithm which can efficiently solve this problem is known. Since Cook's seminal paper, the list of ***NP***-complete problems has grown exponentially. This is because the task of proving that a candidate problem is ***NP***-complete simply requires that a solution can be easily verified and that an algorithm which efficiently solves an ***NP***-complete problem can be easily transformed to solve the candidate problem. For example, it turns out that the traveling salesman problem described above is in the ***NP***-complete set.

Now consider the stricter version of the traveling salesman problem: given a set of cities and their pairwise distances, find the shortest a route which passes through all the cities only once. Firstly this is not a *decision* problem to which there is a yes or no answer, rather a *search* problem. Secondly, it is easy to imagine that like its decision equivalent the search traveling salesman problem could require an exponential time algorithm to find a solution. Thirdly, this search version of the problem is at least as difficult as the decision version. In other words, if a search algorithm could find a minimal path between the cities, then it could also answer questions about the existence of a path of some arbitrary length. This means that the decision version of the traveling salesman problem is *reducible* to the search version of the same problem. Problems such as this one which are as least as difficult as ***NP***-complete problems but to which an ***NP***-complete problem can be reduced are called ***NP-hard***.

This particular nomenclature is somewhat misleading, as not every ***NP***-hard problem is in the set ***NP***. The simplest example of an ***NP***-hard problem which is not in ***NP*** is perhaps the *halting* problem: given a program and its input, will it halt? While this is a decision problem, if the program were to loop indefinitely for some particular input, then the running time could not be bounded at all, implying that the halting problem does not belong to ***NP***. In contrast, every ***NP***-complete problem is also ***NP***-hard, leading to the alternative definition that a problem is ***NP***-complete if and only if it is in both sets ***NP*** and ***NP***-hard.

The requirement of a problem to belong to the class of decision problems is also misleading. For example, the search version of the traveling salesman problem can be solved by repeatedly calling the decision version and doing a binary search: if ***n*** is the number of cities and ***m*** the maximal pairwise distance between any of them, we initialize the current minimum length to be ***0*** and the current maximum length to be ***m*n***. We initialize the current path length ***k*** as we would in any binary search, halfway between the minimum and the maximum. Then we call the algorithm which solves the decision version of the problem, and check if there is a path between the cities of length less than ***k***. If the answer is yes, we replace the current maximum length with ***k***, and if the answer is no we replace the current minimum length with ***k***. We re-initialize ***k*** halfway between the new maximum and new minimum lengths and repeat the process until the current minimum length is equal to the current maximum minus one. After at most ***log(m)*** iterations we obtain the length ***l*** of the minimal path. Now one must find a path of length ***l*** which touches each city only once: beginning from any city ***a,*** we select a road to another city ***b*** that we have not seen before. Knowing that ***d*** is the distance between ***a*** and ***b***, we ask the decision algorithm the following question: if the distance between ***a*** and ***b*** were ***l*** instead of ***d*** would we still have a minimal path of length ***l***? If the answer is yes, then going from ***a*** to ***b*** cannot be part of the desired minimal path. To make sure we never go from ***a*** to ***b*** we forever pretend that the distance from ***a*** to ***b*** is indeed ***l*** and not ***d***. If in contrast the answer is no, we move to ***b***. From ***b*** we repeat the process towards another city ***c***, and so on. Eventually we will get back to ***a*** having excluded all the choices which will not result in the minimal path length ***l***. As there are ***n*** cities, this process will take at most n^2 iterations. As the total number of iterations is $log(m)+ n^2$, a polynomial running time, we can conclude that the search version of the traveling salesman problem is also ***NP***-complete.

This theory can be applied to our problem of finding the minimally-stable collection of cells in a discretized landscape. Much like the search for the minimal path for the traveling salesman, ours is a search problem. There are many search problems that ask for an optimal solution among a great number of them. Some are easy, and some are hard. For example, consider the *minimum spanning tree* problem which could be illustrated as follows: an electric company has to service a new residential development. They have to service every house, and the wires need to be buried underground, which imposes a high cost that can vary with length of each section. Thus, the company wants to find the shortest such path which touches all the homes in order to minimize their costs. While at first glance this may appear to be the same problem as the traveling salesman problem, in fact it is a very easy problem. It was solved in 1926 by Otakar Boruvka to construct an efficient electricity network for the region of Moravia in the Czech Republic [Nesetril, 2001]. For an example of a minimum spanning tree, see figure 3.2.e. So we ask, is our problem more like the traveling salesman or like the minimum spanning tree? Is it easy or is it hard? It turns out that it is very hard, and we will see later in this chapter that indeed it is ***NP***-hard as the solution of it will solve an ***NP***-complete problem. In practice what is done in such situations is to devise an algorithm which *approximates* the exact solution efficiently, and then

demonstrate that approximation error is bounded. This is the path I shall follow in the next sections.

3.3 An alternative approach: spectral clustering

If finding the exact solution to the minimally-stable collection of cells problem is *NP*-hard, perhaps we can devise a tractable way to *approximate* the exact solution. For example, we could imagine there should be some contrast between elements of the minimally-stable collection of cells and elements outside of it. It thus seems intuitive that delineating the boundary of the minimally-stable collection of cells entails maximizing the similarity of the elements in the collection and at the same time maximizing the contrast between these elements and the neighborhood not in the collection, and that that collections having such a boundary would produce ideal candidates for potential landslides. Some of the material presented in this section derives from text books by Chung [1997], Kogan, [2007], Hastie, et al., [2009], Cvetković et al., [2010], and from review papers by Mohar, [1991], Jain et al., [1999], and Von Luxburg [2007]. Some of the examples used here are inspired by lectures given in the Computer Science department at U.C. Berkeley by Michael Jordan, Satish Rao, Umesh Vazirani, and Jitendra Malik.

3.3.1 Clustering

Such a goal is a classic example of a *clustering* problem. Clustering is a fundamental data analysis task with broad (and seemingly disparate) applications in fields such as data mining, machine learning, pattern recognition, image analysis, bioinformatics, information theory, control and signal processing, and psychology, just to name a few, in the context of *unsupervised classification*. In essence, it is the process of finding a structure in otherwise unlabelled data by dividing them into *clusters* such that objects in a the same cluster are *similar* to each other and *dissimilar* from objects in other clusters. This can be done in a *hard* fashion, by which objects can only be assigned to one cluster, or in a *fuzzy* fashion, so that objects are assigned a probability of belonging to each cluster. A typical clustering process requires the following steps [Jain et al., 1999]:

(1) *Pattern representation*: determining the number of classes, and the number, type, and scale of the features available to the clustering algorithm. An important part of this task involves *feature selection* and *feature extraction*, which are the processes of identifying the most effective subset of the original features available and to apply transformations to these features to produce new salient ones, respectively.

(2) Definition of a *similarity measure* appropriate to the data: typically such a measure takes the form of a *distance function* which must obey distance axioms (e.g. the *triangle inequality*), although more perception-based measures related to the *saliency* of features may be used.

(3) *Clustering* (also called *grouping*): the application of an algorithm which divides data into *clusters*. There are two basic classes of such algorithms: *non-parametric* methods typically recursively merge or split data clusters, depending on how similar they are, while *parametric* methods attempt to minimize a cost function or an optimality criterion which associates a cost to each instance-cluster assignment.

(4) *Data abstraction*: the process of extracting a simple and compact representation of the clustered data for further processing tasks. This could be as simple as the centroid of each

cluster, although typical applications require more information such as a geometrical and/or statistical description.

(5) *Output assessment*: the evaluation of a clustering procedure's output. This analysis can be performed by selecting a specific (and often subjective) criterion of optimality, or by applying more objective statistical methods, depending on the application.

The definition of these steps is critical and at the same time application-dependent, as illustrated in figure 3.1.

Clustering is not a new problem, as it has been traced all the way back to Aristotle [Hansen and Jaumard, 1997]. Consequently, it is not suprising that many algorithms have been developed over time. *Hierarchical* methods which group or divide data based on their similarity, generally resulting in a *binary tree* whose *root* is the entire dataset, and whose *leaves* are the individual data objects. In contrast, *partitional* methods such as *K-Means* assign data into a pre-defined number of clusters, with no hierarchical structure. *Probabilistic* or *mixture* methods instead assume that objects in different clusters are generated according to different probability distributions, and thus algorithms such as the *expectation-maximization* or *EM* algorithm can be used to estimate distribution parameters. An extensive review of many clustering algorithms can be found in [Hastie, et al., 2009].

Figure 3.1. Four different object pairings illustrating the difficulty of defining a clustering process. A few questions for the reader: should the two objects in each pairing be in the same or different clusters? What would be an appropriate similarity measure? What would the objective of a clustering procedure be in this case? Clearly the answers depend on the application. Inspired by [Kogan, 2007].

3.3.2 Spectral Clustering

In recent years, clustering algorithms inpired by *spectral graph theory*, the study of the eigenvalues of graphs, best described by Chung [1997], have become increasingly popular as they often can outperform the traditional approaches, and can take advantage of the computational efficiency of modern linear algebra software. As with computational complexity theory, discussed in section 3.2, I provide here only a minimal introduction to spectral clustering methods, as such a general discussion is beyond the scope of this study. Rather I shall focus on essential notions which are needed for the shallow landslide prediction problem. For more technical details the reader may refer to spectral clustering reviews such as Von Luxburg [2007].

As with traditional clustering methods, *spectral clustering* relies on the same main five steps described above. The pricipal difference is is that the objects (or data points) are represented as a *graph*, an abstract representation of a collection of objects, some of which are linked together. The graph could be *connected*, in which case there is a path from any object to any other object, *fully connected*, in which case each object is connected to all other objects, or *partially connected*, in which case there are objects which are not connected to each other. There are some fundamental characteristics of a graph, which are defined based on these connections. *Undirected* graphs are such that if an object ***a*** is connected to an object ***b***, then ***b*** is also connected to ***a***. In contrast, a *directed* graph may have one-way connections. For example, if our objects were all the people at a party, the people who were introduced to each other would form an undirected graph, while the people who know other party guests would form a directed graph, as knowing someone is not necessarily a mutual relationship. Both for simplicity and of relevance to our application I shall only focus on undirected graphs. The other fundamental characteristic is whether a these connections have weights associated to them. To stay with our example, the party guest who have been introduced to each other would be represented as an *unweighted* graph. However, if we said that two guests, once introduced to each other, were more connected if they were closer in age, then one would have to use a *weighted* graph to be able to capture this distinction. Examples of such graphs are shown in figure 3.2. Without loss of generality one can assume that all the weights of the graph are positive, as one can always add a constant to them. For simplicity, I will also restrict the weight values to real numbers, although it should be noted that these methods can be used with complex numbers.

In the construction of a graph, one has to decide what criteria to use to determine which objects are connected, and how these objects are connected. In the previous example any guest could be connected with any other guest, as long as they had been introduced. Suppose however that they then sat at a formal dinner, so that they could only interact with people seated at their vicinity, then the graph would be a *k-nearest neighbor* graph, where *k* would be the number of people seated next to or directly across from each guest. The connection in this case is determined by spatial constraints, and the weight associated to that connection may be dependent on their age. Suppose instead that guests were at a standing buffet dinner, while their teenage kids were to be seated at a separate little table were they could all interact. In this case the teenagers would form an ε-*neighborhood* graph, where the ε is solely based on belonging to the same age group. In this case, adding weights to these connections may not add much to the descriptive power of this graph, particularly if the teens were roughly of the same age.

Another particularity of graphs is that they define a series of special matrices. The party guests who have been introduced in the previous example could be listed as entries of an ***n*** by ***n*** matrix, where ***n*** is the number of guests: if guest ***i*** has been introduced to guest ***j***, then the entry

(i,j) of the matrix would be set to ***1***, and to ***0*** otherwise. Such a matrix is called an unweighted *adjacency* matrix. This entry could further encode the age difference of the guests in which case the matrix is weighted. This is the general case we shall use, and we will denote this matrix by ***W***. A *degree* matrix ***D*** is also a ***n*** by ***n*** matrix, but where the number of connections of each object is encoded, for example how many people each guest has been introduced to. In this case the matrix is strictly diagonal, as each guest ***i*** is represented by the entry ***(i,i)***. Perhaps the most important matrix defined by a graph is the *Laplacian* matrix ***L***, which in its un-normalized form is simply the degree matrix minus the adjacency matrix: $\boldsymbol{L = D - W}$. The most important properties of the Lapacian matrix are that it is *symmetric*, and *positive semi-definite*. This means that for any vextor ***x***, $\boldsymbol{x^T L x \geq 0}$. It also means that all the eigenvalues of ***L***, which form the *spectrum* of ***L***, are real-valued and $\geq \boldsymbol{0}$. The reader is reminded that for a square ***M*** of size ***n*** by ***n***, a non-zero vector ***v*** of size ***n*** is an *eigenvector* of ***M*** if it satisfies the set of linear equations defined by $\boldsymbol{Mv = \lambda v}$, with the scalar $\boldsymbol{\lambda}$ being the *eigenvalue* associated with ***v***.

While incredibly simple in its construction, the Laplacian matrix can tell us much about the graph through its eigenvalues. One example that is particularly relevant for clustering applications is concerned with the number of *connected components* of a graph, i.e the number of groups of objects which are connected to each other and disconnected from the rest of the graph. In our dinner party example, these would be the groups of guests who have all met each other within their group but did not meet other groups of guests, perhaps because they came later. It may seem almost magical that the number of such connected components is exactly the number of zero-valued eigenvalues in the spectrum of ***L***! For an example of the connected components of a graph, see figure 3.2.d. An overview of many such properties of the Laplacian matrix can be found in Mohar [1991]. The *normalized* Laplacian matrix is the Laplacian matrix defined above, normalized by the degree matrix: $\boldsymbol{L_n = D^{-0.5} L D^{-0.5}}$. It has the same exact properties of the standard Laplacian, but can be more useful for some clustering applications. Intuitively, normalizing by the degree matrix can be seen as taking an average of each object's connection. In practical applications this diminishes the effects of noise, and prevents some small isolated clusters from accidentally forming. An in-depth review of normalized graph Laplacians and their properties can be found in Chung [1997]. I will exploit the spectral properties of graphs to find our optimal landslides.

3.3.3 Spectral Clustering and Shallow Landslides

In the next sections will introduce an efficient spectral clustering search procedure specifically developed for next-generation shallow landslide prediction. In order to define such procedure, I first make an important assumption: the initial landslide shape is the result of an optimization of the forces acting on a cluster of grid cells, locally resulting in the minimal factor of safety, defined as the ratio of the driving and resistive forces. I also impose what is perhaps the only constraint of the search algorithm, namely that the landscape is represented as an undirected graph. As we will see later in this chapter, this enables us to exploit properties of symmetric matrices, and of their spectra. We define a weighted, undirected *k*-neighborhood graph with *k* set to *4* in the case of a regular square grid (or *k* set to *6* in the case of a regular Voronoi tessellation), requiring grid cells to be connected only to their neighbors. In essence, the classical factor of safety analysis is recast as a graph partitioning problem, where the nodes are annotated with the landslide mobilizing forces, the edges with the resistive forces, and their ratio (the factor of safety) is the objective function to be minimized. In other words, we want to find a partition of the graph such that the edges between different groups have a very low weight

(which means generally that points in a landslide cluster are dissimilar from points outside of a landslide cluster, and specifically that there is little resistance holding the landslide cluster connected to the non-landslide cluster) and the edges within a group have high weight (which means generally that points within a landslide cluster are similar to each other, and specifically that high resistance between them will allow them to mobilize coherently). The approach used here is a spectral method reminiscent of the *normalized cut*, introduced by Shi & Malik [2000] in the context of image segmentation, which computes the cut cost as a fraction of the total edge connections to all the nodes in the graph using the spectrum of the normalized Laplacian described above. The principal differences in our method, aside from the very different application, lie mainly in the definition of the graph (ε-neighborhood in their case), and in the construction of the matrices (our matrix is only Laplacian-like, and the normalization is non-standard). As a result our algorithm is better suited for landslide prediction.

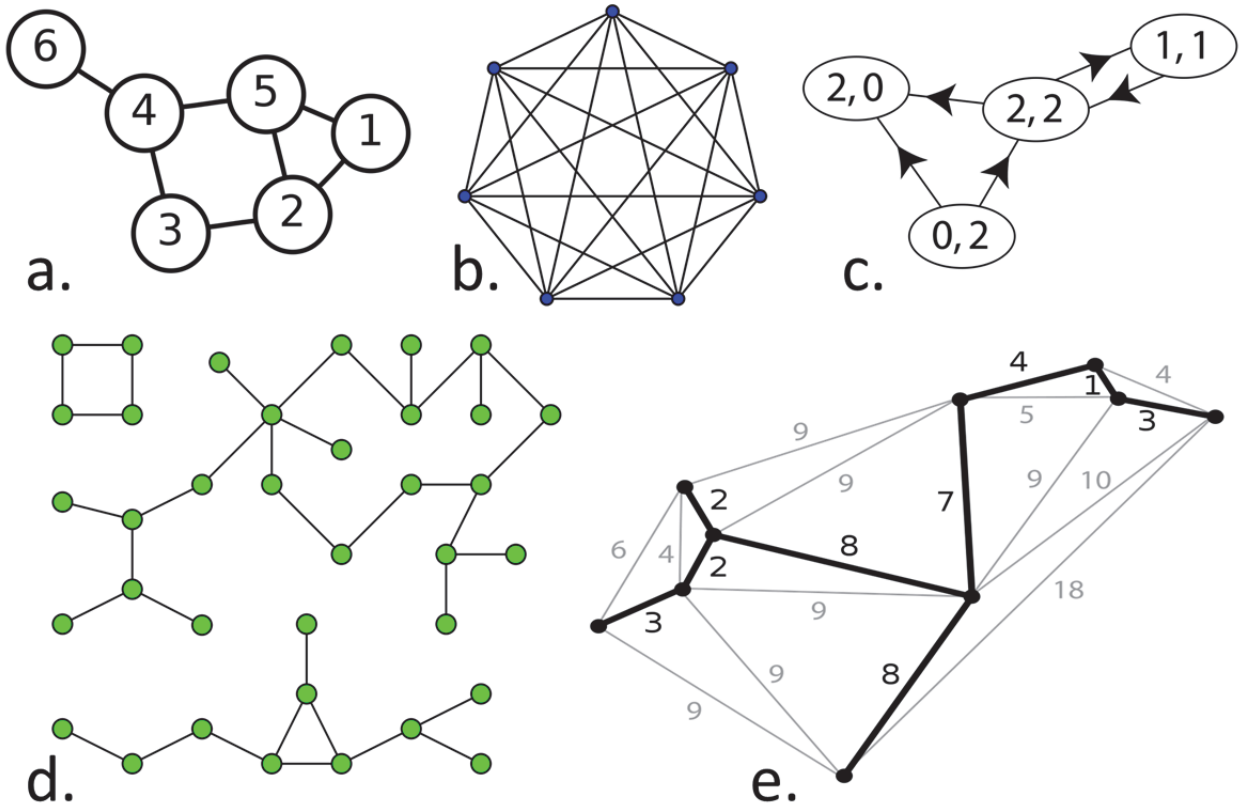

Figure 3.2. Five examples of graphs. a) an un-weighted connected undirected graph with 6 vertices and 7 edges; b) an un-weighted fully-connected undirected graph with 7 vertices, each having degree 6; c) a un-weighted directed graph showing both the in-degree and the out-degree of each vertex; d) an un-weighted partially connected undirected graph with 3 connected components; e) a weighted connected undirected graph and its minimum spanning tree. Source: www.wikipedia.org.

The search procedure is general, in the sense that it does not rely on a particular definition of the driving and resistive forces involved in landslide mobilization, but it requires a slope stability model to characterize the stability of a soil mass. As discussed in chapter 2, any such model in turn will require a series of input data and sub-models (e.g. slope, soil depth, root strength, material properties, pore pressure), thus defining feature selection step for the clustering algorithm. These features are then transformed into features that describe boundary forces and resistances salient for the clustering process, thus defining the feature extraction step. In the

following chapters I will show the effects of different parameterizations of a physical slope stability model, particularly with respect to the choices of sub-models. and point to the most significant unknowns. But in developing the search I will remain as abstract as possible, in order not to impose limitations which could make the procedure not applicable in the future, as better data and sub-models become available.

3.4 A novel procedure

The shallow landslide land prediction procedure is conceptually illustrated in figure 3.3. At the base lie a series of models which are used to describe the physical attributes of the landscape, the hydrological processes, and the distributions and characteristics of soils and vegetation. These models produce spatially explicit layers on which a slope stability model can be applied. The foundation of the procedure, and the principal original contribution of this work, is the search for the optimal landslide, given knowledge about the local conditions of topography, hydrology, precipitation, and soil characteristics. As mentioned in the previous section, I base the otherwise intractable search on spectral graph theory [Chung, 1997]. The goal is to represent and analyze the attributes of the landscape that are relevant to shallow landsliding as abstractly as possible, in order to separate the search algorithm from specific physical representations or specific physically-based models, which all come with advantages and disadvantages. To achieve this goal, I choose as the principle instrument a *graph*, a mathematical abstraction representing a set of objects where some pairs of the objects are connected to each other. The objects in turn are represented by mathematical abstractions called *vertices* or *nodes*, and the connections between some pairs of vertices are called *edges*. Typically, we depict a graph (in diagrammatic form) as a set of dots for the vertices, connected by lines (or curves) for the edges. In this framework, delineating a landslide is equivalent to *partitioning* such a graph into a set of vertices labeled "landslide" and another set labeled "not a landslide". The collection of edges separating these two vertex sets is referred to as a *cut*, which in this case represents the forces acting on the perimeter of a potential landslide. The collection of vertices within the cut represents the forces acting on the base of a landslide, as well as the gravitational forces which collectively influence mobilization. In the next sections I describe how to build such a graph, how to evaluate the goodness of the (exponentially numerous) possible cuts, and how to

3.4.1 Graph representation

The landscape and all its spatial attributes are discretized into a regular grid (i.e. with square grid cells). The attributes of landscape relevant to a mobilizing process (in this case shallow landslides) are represented as a *weighted graph* $\boldsymbol{G=(V,E)}$, where the *vertices* (or *nodes*) $\boldsymbol{v \in V}$ of the graph represent the vertical soil columns corresponding to the original discretized grid cells. An *edge* $\boldsymbol{e_{ij} \in E}$ is formed between every pair of vertices $\boldsymbol{v_i}$ and $\boldsymbol{v_j}$ whose corresponding cells were adjacent in the original grid. These edges represent the forces that act between the vertical soil columns. An example of such a graph is shown in figure 3.4. Any graph $\boldsymbol{G}$ can be represented as an adjacency matrix $\boldsymbol{A}$, where an entry $\boldsymbol{A_{ij}}$ is nonzero if and only if there is a connection between $\boldsymbol{v_i}$ and $\boldsymbol{v_j}$ in $\boldsymbol{G}$. While in an *unweighted graph* these entries are binary, in a *weighted graph* these entries encode the weights $\boldsymbol{w_{ij}}$ which can be seen as the strength the connection represented by edge $\boldsymbol{e_{ij}}$. Note that if the original grid is of size $\boldsymbol{n}$ by $\boldsymbol{m}$, then $\boldsymbol{A}$ will be of size $\boldsymbol{nm}$ by $\boldsymbol{nm}$. However, $\boldsymbol{A}$ will contain mostly zero values as there are only connections between nodes and their immediate neighbors, and thus will be extremely sparse. This is important computationally, as it introduces little memory overhead, when compared to the original grid. It should also be

noted that, safe for the 1-cell wide boundary along the edges of the grid, all cells have the same number of neighbors, and thus $\boldsymbol{G}$ is *k-regular* (4-regular in the case where only the upslope, downslope, left, and right neighbors are considered) and $\boldsymbol{A}$ is symmetric.

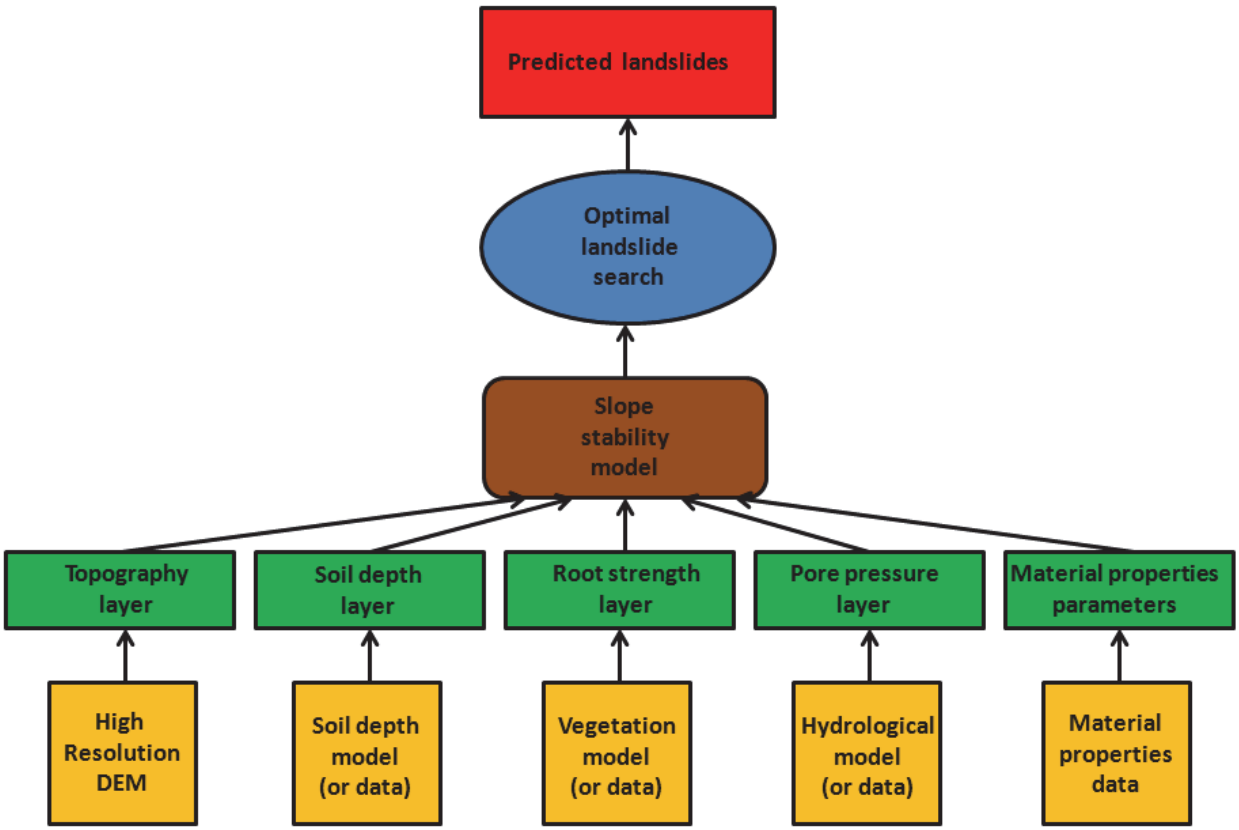

Figure 3.3. Diagram of the shallow landslide predicting procedure. Sub-models and/or data (represented in orange) produce the features (represented in green) which are selected by the slope stability model. This model in turn produces the criteria used by the search algorithm (represented in blue). The output of the search is a list of shallow landslide predictions (represented in red).

The nodes of this graph are annotated with the forces that each individual column contributes: the gravitationally driven downslope mobilizing forces and the frictional resistive forces acting on the base of the column. To remain within the confines of an undirected graph, only the magnitude of the forces is encoded. In practice, this will result in an over-estimation of the driving force, as in a non-planar slope some forces contributed by individual grid cells may partially offset each other. However, it should be noted that this is a conservative approach, in the sense that more potential landslides are sought. Furthermore, when candidate landslides are presented to the search algorithm the factor of safety is correctly computed by summing the *east-west* and *north-south* components of the forces separately (see section 3.4.4). Similarly, the edges of the graph are annotated with the forces that play a role between a grid cell and its neighbors: these are mostly resistive (e.g. root strength, earth pressure), but may include a gravitational "push" from upslope neighbors. Hereafter I will refer to all the mobilizing forces simply as *forces*, and to all the resistive forces as *resistances*. Such forces and resistances can also be encoded in two $\boldsymbol{nm}$ by $\boldsymbol{nm}$ matrices $\boldsymbol{F}$ and $\boldsymbol{R}$. The force matrix $\boldsymbol{F}$ is only associated with the vertices of G, and thus will be zero everywhere except for the diagonal:

$$F_{ii} = F_{d_i} \tag{3.1}$$

where F_{d_i} is the force contributed by vertex v_i. Being a diagonal matrix, F is symmetric by construction (figure 3.5). The resistance matrix R is similarly constructed, but here the resistances are associated with both the vertices and the edges of G. The diagonal of R is:

$$R_{ii} = R_{b_i} + \sum_{i \neq j}^{m*n} w_{ij} \tag{3.2}$$

where R_{b_i} is the basal resistance contributed by vertex v_i, and the w_{ij} term is the sum of the edge weights leaving the given vertex v_i (i.e. the sum of all the resistances between v_i and its neighbors). It should be pointed out that the diagonal of R differs from that of a general Laplacian matrix, as it also encodes the R_b terms. Another difference results from the fact that the resistive forces are not symmetrical, as illustrated in figure 3.4. In order to obtain an undirected graph, these forces are first *symmetrized*: the off-diagonals entries of R, visualized in figure 3.6, contain the negated average of the weights along a given edge:

$$R_{ij} = R_{ji} = -\frac{w_{ij} + w_{ji}}{2}, i \neq j \tag{3.3}$$

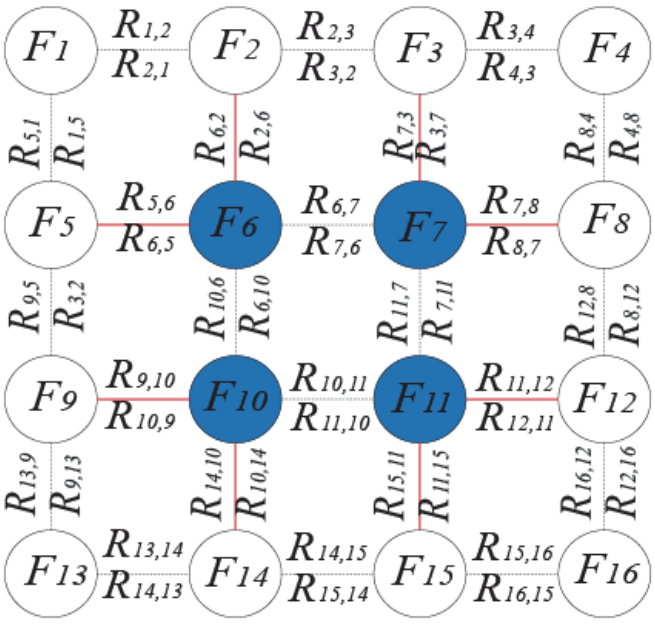

Figure 3.4. Graph of a discretized landscape, consisting of 16 grid cells. The nodes, labeled ***F1-F16***, are associated with the mobilizing forces, as well as the frictional forces contributed by each grid cell. The edges represent the resistive forces between grid cells: the edge labeled $R_{i,j}$, encodes the resistance that node F_i imposes on node F_j. Note that as defined, $R_{i,j}$, is not necessarily equal to $R_{j,i}$. For the blue nodes to form a landslide, their mobilizing forces must exceed the resistive forces of the red edges combined with their frictional forces.

In order to verify that the symmetric formulation (eq. 3) is correct, let a potential landslide S be a subset of V, and let x be an indicator vector of length $n*m$ (the number of rows and columns of the original grid). Each component $x_k \in \{0,1\}$ indicates whether vertex v_k is part of S or not: if $x_k=1$ then $v_k \in S$, and if $x_k=0$ then $v_k \notin S$. Note that the index k, where $0 \leq k < n*m$, corresponds to the position of a grid cell in a linearized representation of the grid, i.e. $k=i*m+j$ for each cell (i,j). For each pair of neighboring vertices v_i and v_j, the lateral resistance should only take the values shown in table 1 below, according to the values of x_i and x_j.

$v_i \in S$	$v_j \in S$	x_i	x_j	Lateral resistance
no	no	0	0	0
yes	no	1	0	w_{ij}
no	yes	0	1	w_{ji}
yes	yes	1	1	0

Table 3.1: Possible values of lateral resistance between neighboring vertices v_i and v_j.

It is easy to verify that equation 3.3 is consistent with table 1, and thus R is a symmetric matrix by construction. The reader may notice that R and F are constructed in a way that is similar to

the *affinity* and *degree* matrices of a graph, and that $\boldsymbol{F^{1/2}RF^{1/2}}$ is thus similar to the normalized *Laplacian* matrix of a weighted graph [Chung, 1997]. $\boldsymbol{G}$ is now fully represented as an undirected graph.

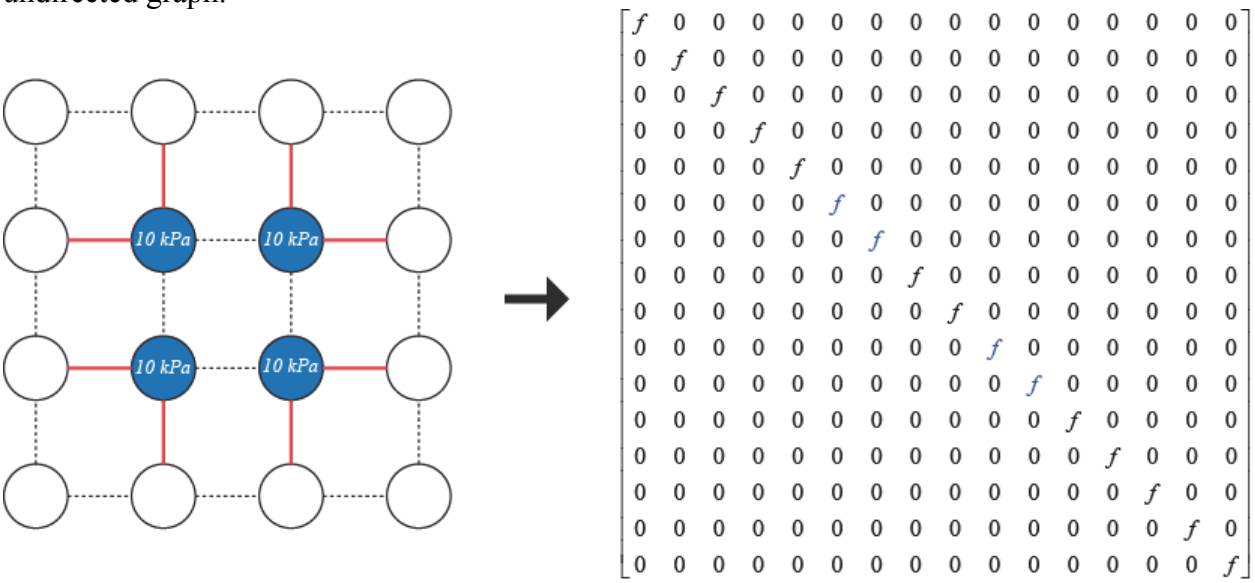

Figure 3.5. Discretized landscape graph with 16 nodes and the corresponding 16 by 16 force matrix $\boldsymbol{F}$. The diagonal of $\boldsymbol{F}$ encodes the magnitude of the gravitational mobilizing forces contributed by each grid cell. The blue nodes in the graph correspond to the blue entries in the matrix. Note the extreme sparsity of $\boldsymbol{F}$, which is generally $\boldsymbol{n}$ by $\boldsymbol{n}$, but only has n entries.

3.4.2 Graph partitioning

Having defined an indicator vector $\boldsymbol{x}$ which allows labeling a subset $\boldsymbol{S \in V}$ a landslide or not a landslide, we now need to define a general criterion for instability to partition V, the vertices of $\boldsymbol{G}$, into $\boldsymbol{S}$ and its complement, which we will call $\boldsymbol{S'}$. In all mechanistic slope stability analysis methods with a foundation in Coulomb theory [Coulomb, 1773], the *limit-equilibrium* is considered to be moment when the sum of mobilizing forces acting on a mass exactly balances the sum of the resistive forces acting on the same mass [Terzaghi, 1950]. Thus, a common criterion for instability is if the ratio of resistances over the forces. If this ratio drops below unity, then the mass is unstable. This ratio is typically referred to as the *factor of safety* (FS), and the common (although not formal) view is that a lower FS implies a greater probability of failure. The FS can be adopted as the similarity measure (also referred to as an *objective* or *cost function*), noting that up to now nothing more has been specified other than a stability analysis will involve forces that aid or resist landslide mobilization, in other words benefits and costs to be used in the context of an optimization. The cost function $\boldsymbol{C(x)}$ of any partition $\boldsymbol{S}$ can be written as:

$$C(x) = \frac{x^T Rx}{x^T Fx} \tag{3.4}$$

An example of a partition and its factor of safety (FS) is illustrated in figure 3.7. Based on these definitions, the *optimal* partition $\boldsymbol{S^*}$ is determined by the indicator vector $\boldsymbol{x^*}$ which minimizes $\boldsymbol{C(x^*)}$. We now have to find $\boldsymbol{x^*}$. Unfortunately, finding $\boldsymbol{x^*}$ in the discrete case (i.e. $\boldsymbol{x^* \in \{0,1\}}$) is not only intractable, but NP-complete. A formal proof by Christos Papadimitriou is presented in appendix 1 of Shi and Malik, [2000]. Fortunately, there exist efficient methods to find very good approximations to this class of problems.

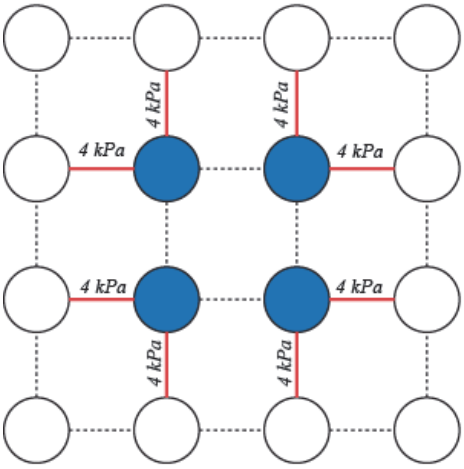

$$\begin{bmatrix}
0 & w & 0 & 0 & w & 0 & 0 & 0 & 0 & 0 & 0 & 0 & 0 & 0 & 0 & 0 \\
w & 0 & w & 0 & 0 & w & 0 & 0 & 0 & 0 & 0 & 0 & 0 & 0 & 0 & 0 \\
0 & w & 0 & w & 0 & 0 & w & 0 & 0 & 0 & 0 & 0 & 0 & 0 & 0 & 0 \\
0 & 0 & w & 0 & 0 & 0 & 0 & w & 0 & 0 & 0 & 0 & 0 & 0 & 0 & 0 \\
w & 0 & 0 & 0 & 0 & w & 0 & 0 & w & 0 & 0 & 0 & 0 & 0 & 0 & 0 \\
0 & w & 0 & 0 & w & 0 & 0 & 0 & 0 & 0 & 0 & 0 & 0 & 0 & 0 & 0 \\
0 & 0 & w & 0 & 0 & 0 & 0 & w & 0 & 0 & 0 & 0 & 0 & 0 & 0 & 0 \\
0 & 0 & 0 & w & 0 & 0 & w & 0 & 0 & 0 & 0 & w & 0 & 0 & 0 & 0 \\
0 & 0 & 0 & 0 & w & 0 & 0 & 0 & 0 & w & 0 & 0 & w & 0 & 0 & 0 \\
0 & 0 & 0 & 0 & 0 & 0 & 0 & 0 & w & 0 & 0 & 0 & 0 & w & 0 & 0 \\
0 & 0 & 0 & 0 & 0 & 0 & 0 & 0 & 0 & 0 & 0 & w & 0 & 0 & w & 0 \\
0 & 0 & 0 & 0 & 0 & 0 & 0 & w & 0 & 0 & w & 0 & 0 & 0 & 0 & w \\
0 & 0 & 0 & 0 & 0 & 0 & 0 & 0 & w & 0 & 0 & 0 & 0 & w & 0 & 0 \\
0 & 0 & 0 & 0 & 0 & 0 & 0 & 0 & 0 & w & 0 & 0 & w & 0 & w & 0 \\
0 & 0 & 0 & 0 & 0 & 0 & 0 & 0 & 0 & 0 & w & 0 & 0 & w & 0 & w \\
0 & 0 & 0 & 0 & 0 & 0 & 0 & 0 & 0 & 0 & 0 & w & 0 & 0 & w & 0
\end{bmatrix}$$

Figure 3.6. Discretized landscape graph with 16 nodes and the corresponding 16 by 16 resistance matrix $\boldsymbol{R}$. The diagonal of $\boldsymbol{R}$ includes the frictional resistive forces contributed by each grid cell. The off-diagonal entries of $\boldsymbol{R}$ encode the symmetrized resistive forces acting between grid cells. The blue nodes in the graph correspond to the blue entries in the diagonal of $\boldsymbol{R}$, while the red edges correspond to the red off-diagonal entries of $\boldsymbol{R}$. Note that $\boldsymbol{R}$ is also very sparse, as it is generally $\boldsymbol{n}$ by $\boldsymbol{n}$, but only has $\boldsymbol{5*n}$ entries on average.

3.4.3 Spectral Relaxation

In order to find the minimizing solution to equation 3.4, we need to relax the condition that $\boldsymbol{x}$ is discrete. We thus allow $\boldsymbol{x}$ to take on any real value (i.e. $\boldsymbol{x} \in \{0,1\}$) and follow an approach similar to that adopted by Shi and Malik [2000]. If we let $\boldsymbol{y} = \boldsymbol{F}^{1/2}\boldsymbol{x}$, the resulting cost function becomes:

$$C(y) = \frac{y^T F^{-1/2} R F^{-1/2} y}{y^T y} \tag{3.5}$$

We note that the cost function defined by equation 3.5 is the *Rayleigh* quotient: as $\boldsymbol{F}$ and $\boldsymbol{R}$ are both symmetric real-valued square matrices, the inner product of $\boldsymbol{F}^{-1/2}\boldsymbol{R}\boldsymbol{F}^{-1/2}$ is also symmetric and thus *positive semi-definite*. It is well known that the minimizing solution to the Raleigh quotient is the eigenvector pointed to by the smallest nonzero eigenvalue of the linear system defined by:

$$F^{-1/2} R F^{-1/2} y = \lambda y \tag{3.6}$$

This eigenvector, that we call $\boldsymbol{y}^*$, is retained to extract the most salient partition $\boldsymbol{x}^*$, after reversing the change of variable used above by letting $\boldsymbol{x}^* = \boldsymbol{F}^{-1/2}\boldsymbol{y}^*$. One can think of $\boldsymbol{x}^*$ as a continuous indicator vector, representing the fraction of each node that contributes to the optimal partition $\boldsymbol{S}^*$. In addition, conscious of the fact that $\boldsymbol{x}^*$ is only an approximation of the original discrete $\boldsymbol{x}$, we do not limit ourselves to the first eigenvector, rather we take the first $\boldsymbol{k}$ eigenvectors, where $\boldsymbol{k}$ can be a function of the eigenvalues of equation 3.6 or, more simply, selected by the user on the basis of the computational constraints at hand.

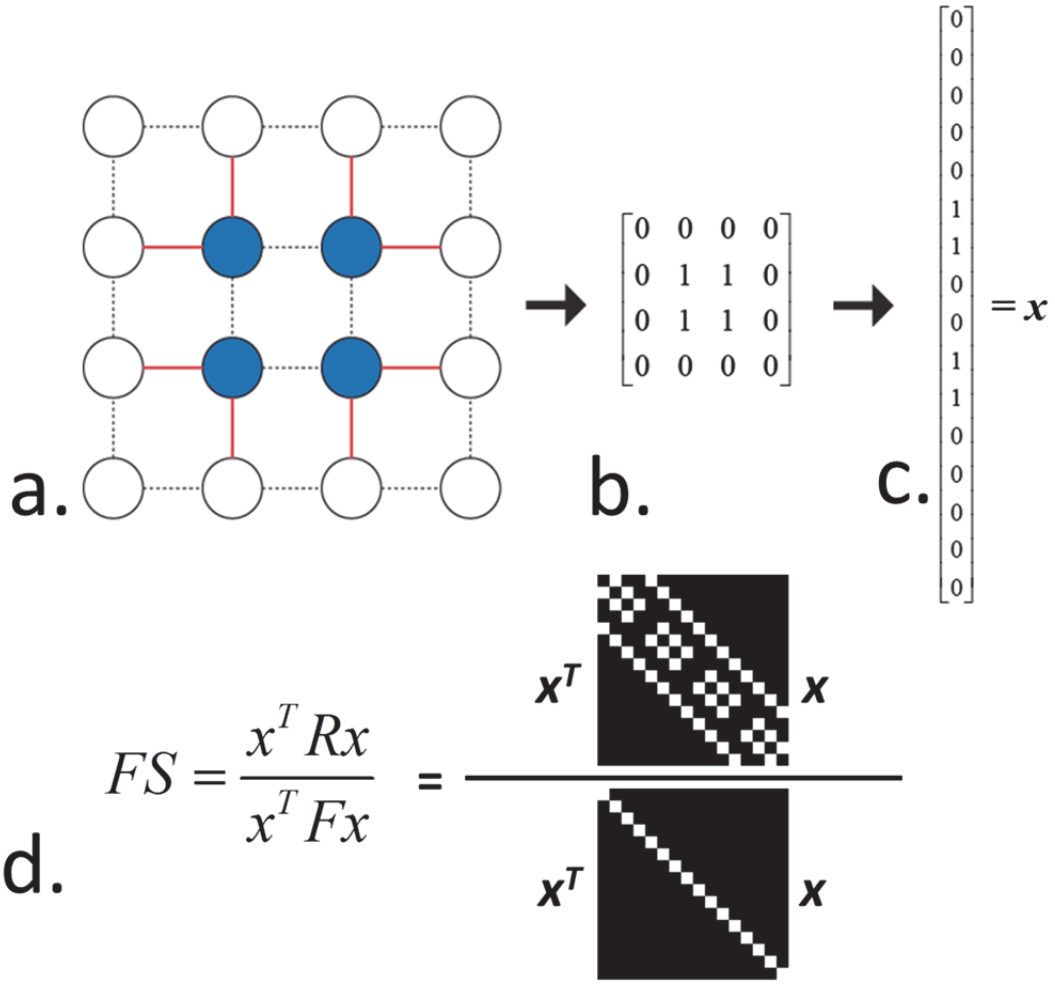

Figure 3.7. Factor of safety of a graph partition. a) Example of a graph partition dividing the graph into a set of blue vertices and a set of white vertices. The cost is associated with the red edges (the cut), which model the resistive forces acting on the perimeter of a landslide. The benefit is associated with the blue vertices, which model the driving gravitational forces acting in the interior of the slide. The blue and white vertices are inside and outside the potential landslide, respectively; b) The binary matrix corresponding to the partition where the blue vertices take the value of 1 and the white vertices take the value of 0; c) The indicator vector $\boldsymbol{x}$ corresponding to this partition, obtained by linearizing the matrix; d) A visual illustration of the objective function corresponding to the factor of safety. The best cut is that which has the minimal value for *FS*.

3.4.4 Recovering the discrete solution

An approximation to the discrete solution $\boldsymbol{x}$ can be obtained by thresholding the continuous vector $\boldsymbol{x}^*$. As $\boldsymbol{x}^*$ is also of length $\boldsymbol{nm}$, all $\boldsymbol{2*nm-1}$ possible interesting threshold values are used. All $\boldsymbol{x}_i$'s for which the corresponding $\boldsymbol{x}_i^*$ are greater than the candidate threshold $\boldsymbol{t}_i$ are set to $\boldsymbol{1}$, and the rest of $\boldsymbol{x}$ is set to $\boldsymbol{0}$. In other words, $\boldsymbol{x}^*$ can be visualized as a landscape where each threshold is a contour elevation value, and the regions at threshold $\boldsymbol{t}_i$ are the projection on the Cartesian plane of the points with elevation higher than $\boldsymbol{t}_i$. In general, any threshold $\boldsymbol{t}_i$ may give rise to disconnected discrete regions. In particular, a region $\boldsymbol{r}_i$ at threshold $\boldsymbol{t}_i$ must either have not existed at threshold $\boldsymbol{t}_{i-1}$, or be an expansion (or contraction) of a region $\boldsymbol{r}_{i-1}$' at threshold $\boldsymbol{t}_{i-1}$, or be the result of the merging of regions $\boldsymbol{r}_{i-1}$' and $\boldsymbol{r}_{i-1}$" at threshold $\boldsymbol{t}_{i-1}$. At any threshold, regions are labeled using a connected-component analysis, as described in Haralick and Shapiro [1992]. These connected components represent candidate landslides. The evolution of the regions

throughout the thresholding process gives rise to a *contour tree*. In such a tree T_c, nodes represent the events of birth, merge, and death of regions, while edges represent the extension or contraction of an individual region, as illustrated in figure 3.8.

We are interested in finding the minimal values of $C(x)$ (the factor of safety of a collection of cells represented by x) of all edges in T_c. The connected components at each threshold can be compared with those which were present at the previous threshold. This gives rise to three possible outcomes:

1) A component that was not present at the previous iteration appears in the current iteration. This is the case of the leaves of T_c. In this case the component is initialized as a new candidate landslide in the *active* set of components, and its $C(x)$ value is stored, along with its bounding box and indicator vector x.
2) A component is found in the current iteration which overlaps with one active component from the previous iteration. This is the case of the edges of T_c. In this case the cost of the two components is compared and the active component is updated with the value, geometry, and indicator vector of the one with the minimal value of $C(x)$.
3) A component is found in the current iteration which overlapped with two distinct active components in the previous iteration. This is the case of the non-leaf nodes of T_c. We consider this as a new component to be initialized as in the first case. At the same time the two components from the previous iteration are placed in the *inactive* list of components.

This process is then repeated for the negative of x^*, which is equivalent to inverting the x^* landscape and generating a new contour tree T_c'. At the end of both these passes the active and inactive component lists contain all the minimal values along the edges of T_c and T_c'. These connected components represent the candidate landslides, and as these are discrete partitions their factor of safety can now be correctly evaluated by taking into account both the magnitude and orientation of the gravitationally driven forces, by computing their vector sum. It should be noted that taking into account the direction of the gravitational forces addresses the under-estimation of the factor of safety discussed in section 3.4.1. The subset of this collection of regions having the value of $FS < 1$ represents the potential landslides approximated by the continuous solution x^*. As x^* is only one of the many eigenvectors examined, this process is repeated. It's worth noting that since the eigenvectors are independent of each other, the thresholding process is trivially parallelized. As individual landslide predictions may be derived from different thresholds of a single eigenvector, as well as from a different eigenvector, they may very well overlap. When this is not desired (see discussion), a final step is then required to prune the overlapping predictions in order to retain only a subset of them. The overlap ratio O_r is defined for two regions r' and r'':

$$O_r = \frac{r' \cap r''}{r' \cup r''} \tag{3.7}$$

If $O_r > l$, where l is a dimensionless user-defined threshold, the region with the highest $C(r)$ is discarded. Thus, when $l = 0$, no overlap is allowed, while when $l = 1$ no regions are discarded. The resulting collection of regions constitutes our landslide prediction given the input conditions defined for the landscape. Finally, the data abstraction for this collection of regions consists of an array of structures (one per predicted landslide) containing a logical mask identifying the landslide cells, their factor of safety, as well as their geometric properties such as area, perimeter, centroid, major and minor axes of the best fitting ellipse, and their orientation. An ArcGis-

compatible raster coverage containing all the predicted landslide cells labeled with their factor of safety is also output for easy visualization in a GIS environment.

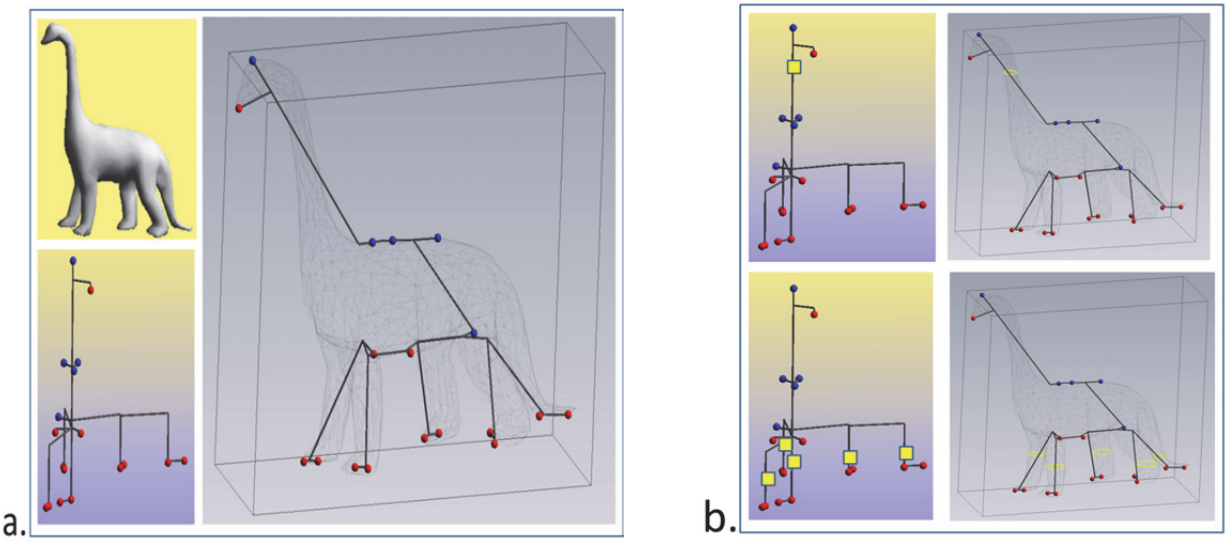

Figure 3.8. Contour trees and level sets. a) Clockwise from top left: A dinosaur, its mesh, and its contour tree. Births, and deaths are represented in red, and blue, respectively. Edges represent the evolution of the *level sets*. b) Left: slicing the tree at two different thresholds, marked in yellow. Right: the corresponding level sets outlined in yellow, illustrating how the thresholding process gives rise to different regions. Source: www.pascucci.org.

3.4.5 Evaluation of the search procedure

Generally, there are two types of methods for evaluating clustering results. An *internal evaluation* usually assigns the best score to the algorithm that produces clusters with high similarity within a cluster and low similarity between clusters. In contrast, in an *external evaluation*, clustering results are evaluated based on data that was not used for clustering, such as known external benchmarks. I will define here how both approaches will be used for evaluating the procedure. In this chapter I will define the methodology while the results of an actual evaluation applied a real-world case will be presented in the next chapter.

3.4.5.1 Internal evaluation

The search procedure is evaluated internally in a graph-theoretical context by comparing all the discrete graph partitions obtained from the thresholding process (the landslide predictions) to the real-valued solutions defined by equation 3.5. I have shown that the optimal solution to the relaxed factor of safety equation is given by the eigenvector associated with the smallest nonzero eigenvalue of the linear system defined by equation 3.6. We also know that that all the other distinct sub-optimal solutions to equation 3.5 are given by the other eigenvectors associated with the spectrum of equation 3.6. By sorting this spectrum in ascending order one can plot the factor of safety of all the real-valued solutions as a function of the eigenvalue number, in ascending order. Each of these eigenvectors will also have generated a set of discrete solutions to equation 3.4. It cannot be proven that one can ever obtain a *complete* set of discrete solutions, as enumerating all the discrete solutions is not a tractable task. However, we can populate the domain of the previous plot with the factor of safety of discrete solutions, and observe the behavior of the search procedure. An example of a plot of the discrete and continuous solutions is shown in figure 3.9.

The expectations of this evaluation are the following:

1) All the discrete solutions (blue dots in the example of figure 3.9) should plot below the ***y = 1*** line, as they are presumed to be unstable configurations. This is guaranteed as the procedure does not by default return configurations that are stable. It is noted that the user can optionally relax this requirement, should one wish to observe the set of predictions with a factor of safety less than ***k***.

2) All the discrete solutions should plot close to the real-valued solutions (red dots in the example of figure 3.9). Because real-valued solutions do not constitute feasible landslides, it would be desirable to have the discrete solutions (i.e. the feasible landslides) have similar factors of safety.

3) No discrete solutions should plot below the first real-valued solution (left-most red dots in figure 3.9). This would violate the Raleigh quotient principle invoked in solving equation 3.6, and would indicate a faulty behavior of the algorithmic implementation. Similarly, as the eigenvalue number increases, the real-valued solutions should increase in value.

4) As the eigenvalue number increases, the discrete solutions will approach (and possibly surpass) the real-valued solutions as the real-valued solution, a function of the entire eigenvector, deteriorates. This is unavoidable: the eigenvectors are all orthogonal to each other and they define subspaces that are progressively less "meaningful", a concept that is the basic principle of principal component analysis. In the meantime, the discrete solutions are a function of only part of the eigenvector and are thus not subject to the orthogonality constraint.

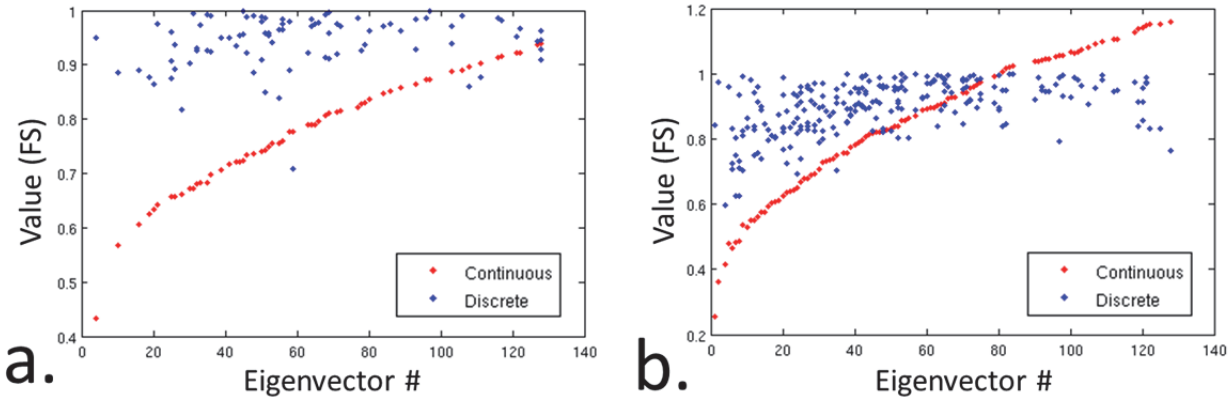

Figure 3.9. Continuous and discrete cost values. Example of from a simulation where root strength is held constant: low pore pressure (a) and high pore pressure (b). Note that the discrete solution can be lower than the continuous solution at high eigenvector numbers. The *y*-axes do not have the same scale.

In the next chapter I will apply this evaluation methodology, present the results, and discuss their implications. It is also noted that the algorithm has multiple consistency checks embedded in the search process. The most notable is that each prediction is subject to an automated back-analysis in a post-processing step. If the factor of safety, or any of the individual resistive or driving forces, do not match those returned by the search procedure, an error is thrown and the procedure aborts.

3.4.5.2 External evaluation

For the external evaluation I will exploit two unique datasets collected on and in the vicinity of the Mettman Ridge field research site in the Oregon Coast Range, near Coos Bay, OR, which will be described in detail in the next chapter. As for the internal evaluation case, the results and their implications will also be discussed in the next chapter; here I will focus solely on the methodology.

The first dataset consists of an instrumental record of a rainfall-triggered shallow landslide that occurred at the research site [Montgomery et al., 2009]. Here all the physical parameters such as hydrological conditions, soil depth, and root strength were measured. In particular, the rainfall intensity and duration, as well as the pore pressure field were being monitored in situ when the event occurred, and the landslide was mapped onto high-resolution topographical data. This dataset allows for testing the slope stability model and the search procedure without using a hydrological or a soil depth model. Moreover, there are precise constraints on how to characterize the effect of root strength as a function of soil depth. This allows using the input data to make a prediction, and verifying that the output of the procedure matches the dimensions and the location of the observed landslide. Furthermore, by varying the treatment of earth pressure and root strength in the slope stability model their effects on the accuracy of the prediction can be quantified. I shall refer to this dataset and its location as ***CB-1***.

The second dataset consists of repeat mapping of a 0.5 km^2 area surrounding the Mettman Ridge site, which documents all the shallow landslides that occurred over a 10-year period [Montgomery, et al., 2000]. As for the Mettman Ridge landslide, these maps have been registered onto high-resolution LiDAR-derived topographical data. While the precise local characteristics of soil, vegetation, and hydrology, at the time and location of these events is unknown, subsequent research in the area constrained parameters governing the rate at which bedrock is converted into soil [Heimsath et al., 2001], the rate at which soil is transported downslope [Roering et al., 1999]; similarly, the characterization of root strength was extensively studied [Schmidt et al., 2001; Roering et al., 2003], and the hydrological and material properties of the soils were also extensively documented [Montgomery, 1991; Torres et al., 1998; Ebel et. al, 2007a, 2007b; Montgomery et al., 2009]. The entire procedure can thus be applied, and results can be compared with observations under a variety of possible conditions determined by parameters $\boldsymbol{q/K}$ (the effective precipitation divided by the hydraulic conductivity, defined in chapter 2), and $\boldsymbol{C_0}$ (the intercept of the root strength vs. soil depth function, also defined in chapter 2). I shall refer to this dataset and its location as ***CB-MR***.

But how do we compare the predictions with observations? The challenge is that we have a dataset of observations spanning a ten-year period, while the recurrence interval of an individual shallow landslide at a specific location is much greater. This is mostly controlled by the time required for a failed location to infill with soils, which is in the order of thousands of years [Reneau et al., 1986]. Should we thus be quantitative or qualitative? A quantitative approach would take into consideration the *hits* and *misses*, while a qualitative approach would take into consideration whether what is returned by the search procedure *looks* like a landslide, meaning it has the right size, the right shape, and is in a reasonable location. I will define metrics for both approaches in this section.

Rating the effectiveness of the landslide search procedure is very similar to rating a search engine's ability to find documents which are relevant to a query. The relevant documents are in our case the grid cells which are labeled as *"landslide"*, the irrelevant documents are those which are labeled *"non-landslide"*, and the query corresponds to the conditions under which we

ask the procedure to return a set of grid cells. We can thus apply concepts from *information retrieval theory*, of which we will provide only essential elements, derived from the information retrieval textbook by Van Rijsbergen, [1979]. For further details and definitions about the materials covered in this section, we refer the reader to this text. A *true positive* (***TP***) is defined as a grid cell which is labeled "landslide" in both the predicted and observed data sets, a *false positive* (***FP***) is a cell which is labeled "landslide" in the predicted but not in the observed data set, a *true negative* (***TN***) is a cell which is labeled "non-landslide" in both the predicted and observed data sets, and a *false negative* (***FN***) is a cell which is labeled "not landslide" in the predicted but is labeled "landslide" in the observed data set. The accuracy of a prediction can thus defined to be:

$$accuracy = \frac{TP + TN}{TP + TN + FP + FN} \tag{3.8}$$

This is very intuitive, as we want to maximize the amount of correctly labeled cells *TP*+*TN*. However, suppose that in the observed dataset only 5% of the cells were labeled as "landslide". A procedure that always returned all cells as labeled *"*non-landslide*"* would paradoxically have 95% accuracy. One thus needs to consider the number of predicted *"*landslide*"* cells which are actually landslides in the observations, and the number of landslide cells in the observations which are in turn predicted. In information retrieval, *precision* is defined to be the fraction of retrieved instances that are relevant to a query, while *recall* is the fraction of relevant instances that are in fact retrieved. They are defined as:

$$precision = \frac{TP}{TP + FP} \text{ , and } recall = \frac{TP}{TP + FN} \tag{3.9}$$

where *TP*, *FP*, and *FN*, are defined as above. Precision and recall have a straight-forward probabilistic interpretation: if ***l*** is the instance label (i.e. the observation), ***z*** the instance assignment (i.e. the prediction), and + means that the instance is relevant (i.e. a landslide cell), then:

$$precision = P(l = + \mid z = +) \text{ , and } recall = P(z = + \mid l = +) \tag{3.10}$$

It's important to notice that in order to have 100% precision, it would be sufficient to just return one cell which was correctly labeled *"*landslide*"*. Similarly, 100% recall could be obtained by returning all the landscape labeled as *"*landslide*"*. A good procedure thus should maximize both precision and recall, although which is more important will depend on the application. For example, in military applications precision may be favored in order to limit civilian casualties, while in diagnostic medical applications recall may be favored in order to screen a greater number of potential cancer patients. Regardless, precision and recall must be considered together, and they typically form the bases of a 2-dimensional *precision/recall* curve (***PR***), in which each data point is a query, the *y*-axis represents precision and the *x*-axis represents recall. Ideally to maximize both precision and recall, a procedure should plot close to the upper right corner of such a plot, although empirically precision tends to diminish as recall increases. A commonly used alternative to precision and recall is called a *receiver operating characteristic* (***ROC***) curve, a legacy term from World War II radar engineers. In an ***ROC*** curve, the *true positive rate* (***TPR***) is plotted against the *false positive rate* (***FPR***):

$$TPR = \frac{TP}{TP + FN} \text{, and } FPR = \frac{FP}{FP + TN} \tag{3.11}$$

where the ***TPR*** measures the fraction of "landslide" cells which are correctly labeled (exactly as recall), and the ***FPR*** measures the of "non-landslide" cells which are misclassified as "landslide". A good score in ROC space should be close to the upper-left corner. While there is a

one-to-one correspondence between the two curves [Davis and Goadrich, 2006], ***ROC*** curves have the property that they are insensitive to changes in class distribution, such as when the number of negative instances is increased by orders of magnitude [Fawcett, 2006]. They also can be easily used to compare the performance of a classifier to a *random classifier* (represented by the ***1:1*** line in the ***ROC*** space). In contrast, ***PR*** curves can better discriminate between classifiers when changes in class distribution are small. Examples of ROC and PR curves are shown in figure 3.10.

Often it is desired to compare the performance of a classifier against some parameter used in generating the data distribution. For example, one may wish to compare precision and recall as a function of the amount of precipitation. A common way to perform such an evaluation is to encode precision and recall into a single number F_β:

$$F_\beta = (1+\beta^2)\frac{precision * recall}{(\beta^2 * precision) + recall} \tag{3.12}$$

where β is a positive real number which represents the relative importance of recall to precision [Van Rijsbergen, 1979]. As β is generally not known, it is common practice to assume that it is equal to 1, in which case equation 3.12 reduces to:

$$F_1 = 2\frac{precision * recall}{precision + recall} \tag{3.13}$$

where F_1 is the *harmonic mean* of precision and recall, ranging between ***0*** and ***1***, with the latter representing a perfect prediction. While widely used, this measure does not take into account the true negatives, as the term ***TN*** does not appear in either precision or recall. An alternative measure, often used to evaluate binary classifiers in machine learning, is the *Matthews correlation coefficient* [Matthews, 1975] which is defined as:

$$MCC = \frac{TP * TN - FP * FN}{\sqrt{(TP+FP)(TP+FN)(TN+FP)(TN+FN)}} \tag{3.14}$$

The ***MCC*** is essentially a correlation coefficient between the observed and predicted binary classifications, ranging from -1 to $+1$. A MCC of $+1$ represents a perfect prediction, a ***MCC*** of ***0*** is equal to a random prediction, and a ***MCC*** of -1 indicates complete disagreement between predictions and observations. Like accuracy, it encodes all the TP, FP, TN, FN, terms into a single number, and like F_1 it is balanced. As there is no absolute agreement on the effectiveness of all these measures, in chapter 4 I will present ***ROC***, ***PR***, F_1, and ***MCC*** plots for a variety of simulations performed under diverse assumed conditions on the ***CB-MR*** site.

An important and objective test is to compare the predicted results, as expressed by these metrics, to a *random model*. At the single grid cell or pixel scale this can be done in ***ROC*** space. The null hypothesis in this case is that the classifier labels each pixel at random, in which case its ***ROC*** curve will follow the ***1:1*** line in ***ROC*** space [Fawcett, 2006]. If instead the classifier produces ***ROC*** curves which consistently fall above the ***1:1*** line, this hypothesis can be rejected. A slightly different approach to a random model comparison is the feature-based method suggested by Dietrich et al., [2001]. As a null hypothesis they propose that shallow landslides (and not just individual landslide pixels!) do not obey their proposed mechanistic criteria. To test this hypothesis, they compare the performance of their model (Shalstab) applied to an observed landslide catalog to the performance on an equivalent but randomly distributed catalog. They found that the Shalstab model outperforms the random model, rejecting the null hypothesis, but that once recall is increased to capture all the landslides the results don't differ greatly from the

random model. I will also test this second null hypothesis by replacing the observed landslides with an analogous but randomly positioned datasets. These random datasets will have constraints on number, size and shape, all derived from the observed landslide distribution, but none on their position other than that they must be distinct. Specifically, random landslides will be represented as ellipses having the ratio of major and minor axes equal to the ratio of the average axes of the observed landslides. In a fashion similar to the method presented by Spowart et al., [2001], their size will be sampled from a normal distribution with mean and standard deviation obtained from the observed dataset, while their position and orientation will be sampled from the uniform distribution. In order not to introduce biases, the number of random landslides will reflect the ratio of observed landslide area to the size of the study area. In this random test a true positive is obtained when there is overlap between the predicted and the observed/random sets, while a false positive is obtained when there is no overlap. It should be noted that true negatives and false negatives are undefined, thus with the exception of precision the above-discussed information retrieval measures cannot be used. The comparison indicated by Dietrich et al. [2001] is adopted instead. They plot the cumulative percent of observed landslides captured as a function of steady state precipitation, and compare to a random dataset. They also plot the cumulative percent of the landscape area comprised in the predictions. The results of these tests applied to the ***CB-MR*** site will be presented in chapter 4.

For a more qualitative assessment of the procedure, I will compare the predictions to the observations using *probability density functions* (***PDF***), *cumulative distribution functions* (***CDF***). For a continuous random variable $\boldsymbol{X}$, $\boldsymbol{f_x}$ is the ***PDF*** of $\boldsymbol{X}$ when:

$$P\left[a \le X \le b\right] = \int_a^b f_x(x)dx \tag{3.15}$$

where $\boldsymbol{P}$ is the probability function, and $\boldsymbol{a}$ and $\boldsymbol{b}$ represent an interval in which $\boldsymbol{f_x}$ is evaluated. This function describes the *relative likelihood* that $\boldsymbol{f_x}$ falls in the interval defined by $\boldsymbol{a}$ and $\boldsymbol{b}$. The ***CDF*** in turn describes the probability that $\boldsymbol{X}$ will have a value less or equal to $\boldsymbol{x}$:

$$F_X = P\left[X \le x\right] \tag{3.16}$$

The ***PDF*** and the ***CDF*** are intimately related as:

$$F_X(x) = \int_{-\infty}^{x} f_x(t)dt \tag{3.17}$$

I select three random variables $\boldsymbol{X_i}$ which capture the essence of size, shape, and location of the predicted and the observed landslides. As a proxy for size I will use *planimetric area*, the area of each landslide in the ***x-y*** coordinate plane; as proxy for shape I will use the *aspect ratio*, defined as the ratio of the major and minor axes of the best-fitting ellipse for each landslide; as a proxy for location I will use the median *topographic index*, of each landslide:

$$I_T = \frac{A}{b\sin(\theta)} \tag{3.18}$$

where $\boldsymbol{A}$ is the drainage area (m^2), $\boldsymbol{b}$ is the grid cell size (m), and $\boldsymbol{\theta}$ is the slope angle [Dietrich et al., 1992]. This index increases when the area term dominates, and decreases when the slope term dominates. In essence, the median topographic index records whether landslides occurred preferably in convergent hollows or in less convergent but steeper parts of the landscape. Each simulation will result in three ***PDF*** and three ***CDF*** curves which will be compared the respective curves derived from the observed dataset. To assess the similarity of the predicted and observed distributions I will employ the widely-used *Kolmogorov-Smirnov* test, commonly referred to as

the ***K-S*** test [e.g., Conover, 1971; Borradaile, 2003; Corder, 2009]. The ***K-S*** test is a nonparametric test for the equality of continuous, one-dimensional probability distributions. It can be used to compare a sample with a reference probability distribution (*one-sample* ***K-S*** test), or to compare two samples to each other (*two-sample* ***K-S*** test). I will use the two-sample K-S test to pairwise examine each predicted and observed ***CDF*** type (size, shape, location), and determine the likelihood that they come from the same underlying distribution. The ***K-S*** test statistic is the maximum difference between the two cumulative distribution curves:

$$KS_{n,m} = \sup\left|F_{1,n}(x) - F_{2,m}(x)\right| \tag{3.19}$$

where $\boldsymbol{KS_{n,m}}$ is the test statistic, $\boldsymbol{F_{1,n}}$ and $\boldsymbol{F_{2,m}}$ are the two normalized cumulative distributions, with ***n*** and ***m*** observations, respectively, and ***sup*** designates the *supremum*. The null hypothesis is that $\boldsymbol{F_{1,n}}$ and $\boldsymbol{F_{2,m}}$ come from the same distribution. This hypothesis is rejected at a significance level $\boldsymbol{\alpha}$ if:

$$\sqrt{\frac{nm}{n+m}}KS_{n,m} > KS_{\alpha} \tag{3.20}$$

where $\boldsymbol{KS_{\alpha}}$, the critical values for level $\boldsymbol{\alpha}$, can be extracted from published tables [e.g. Pearson and Hartley, 1972]. In chapter 4 I will present ***PDF***'s, ***CDF***'s, as well as their ***KS*** statistics, derived from a variety of simulations performed on the ***CB-MR*** site.

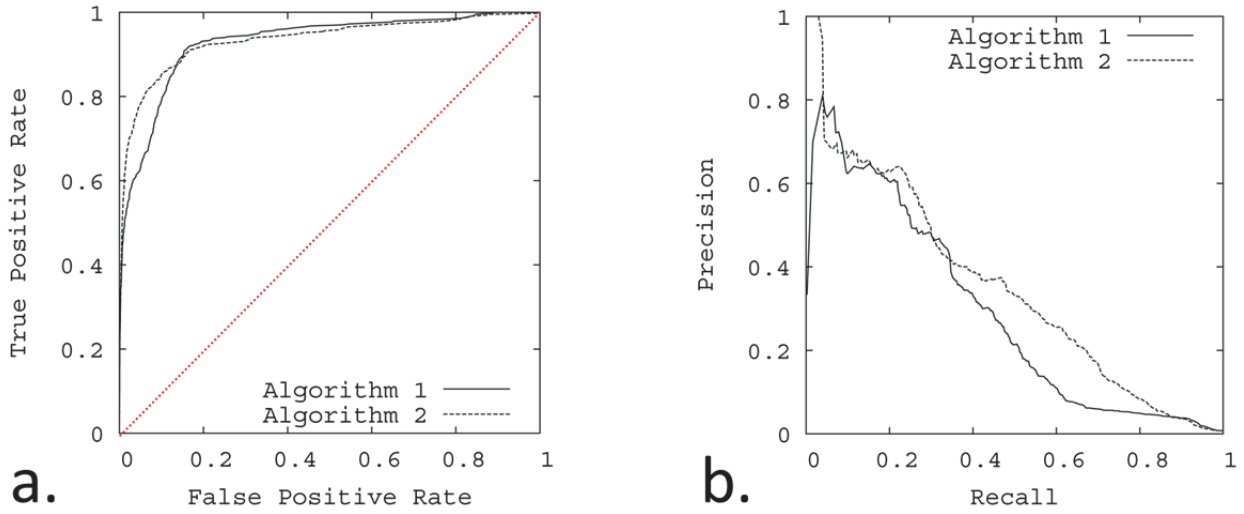

Figure 3.10. Examples of *ROC* curves and *PR* curves. a) Comparison of two binary classifiers in *ROC* space; the red dotted line is a random classifier for comparison. b) Comparison of two binary classifiers in *PR* space; the performance of the two algorithms is more distinguishable. Adapted from [Davis and Goadrich, 2006].

3.4.6 Implementation

The search procedure has been implemented and tested on a 64-bit Dell Precision T5500 Workstation with two quad-core Intel Xeon E5620 processors, equipped with *24 Mb* of cache, and running at a clock speed of 2.40 GHz. System random access memory (RAM) consists of *24 Gb*, with a maximum bandwidth of *25 Gb/s*. In order to test under different operating systems, the system was configured in dual-boot mode, running *64-bit* CentOs Linux (v. 2.6.18-308.1.1.e15), as well as 64-bit Windows 7 Ultimate (Service Pack 1). The software is written in Matlab R2012a (v. 7.14.0.739), and runs indifferently under both operating platforms. Two versions have been developed and tested: a standard serial version, and a parallel

implementation. The latter version uses the Matlab Parallel Computing toolbox, and can take advantage of up to twelve processor cores, with a nearly-linear speedup.

Input spatial layers are read from disk, and are expected to be in ArcGis ASCII Raster format. The output consists of an ArcGis ASCII raster containing a layer with all the predicted shallow landslides encoded with their factor of safety value. Individual landslide information is summarized in a comma-separated ASCII text file (CSV) containing the following fields: id, x-centroid, y-centroid, factor of safety, volume, surface area, area, perimeter, major axis length, minor axis length, eccentricity, orientation of major axis, topographic index. Supplemental landslide information including a bit-map and bounding box of each prediction is enclosed in a Matlab data file (.mat). Optional output includes individual ArcGis ASCII rasters for each landslide, mapped to the input reference frame.

3.4.7 Complexity

The complexity of the search algorithm will vary with the iterative method used to extract the eigenvectors and eigenvalues of the above-defined linear system. In our case, this is determined by the Matlab implementation of the function ***eigs*** which in turn relies on the software package ***ARPACK*** [Lehoucq et al., 1998]. We have bounds on these methods, as they won't be faster than linear and are cubic in the worst case (for dense matrices). Typically though they are of sub-quadratic complexity, $\sim O(d^{3/2})$, where d is the dimension of the Laplacian-like matrix.

Connected component analysis has logarithmic complexity $O(|V|\log|V|)$, where $|V|$ is the number of vertices in the graph (i.e., the number of grid cells). The union-find algorithm instead has complexity $O(r\log(r))$, where r is the number of regions contributed by each eigenvector ($|V|$ in the worst case). Pruning overlapping regions is quadratic in the naïve case, although a more appropriate data structure (such as a *quad-tree*) could reduce the cost to $O(l\log(l))$, where l is the total number of regions having $FS < 1$ (note that $l << kr$ in practice).

In order to keep the problem size small, the procedure is windowed over the input layers. Let N be the number of windows necessary to cover the landscape, and n the number of cells in each window. It should be noted that in order to avoid edge effects the windows must have significant overlap in both the x and y directions. Thus $n*N$ is in practice approximately 25% greater than the number of cells of the landscape grid. Let k be the number of eigenvectors to extract per window, r the maximum number of regions allowed to be contributed by each eigenvector, and l the total number of regions having $FS < 1$. The total complexity is then approximately:

$$complexity = O(N(n^3 + k*\log(n) + n*\log(r)) + l^2) \tag{3.21}$$

The n^3 term arises from the fact that for n grid cells, the Laplacian-like matrix is of size n^2. This term dominates, although in practice for small sparse matrices such as in our application this should be considered a worst case scenario. Regardless, this results in a huge reduction from the intractable $O(N2^n)$ complexity of a brute force method. To allow the procedure to run even on modest hardware, an optional limit to the maximum number of connected components r and the maximum number of eigenvectors k can be set by the user.

3.5 A synthetic example

The procedure can be better illustrated with simple examples involving two synthetic landscapes. Figure 3.11 shows the first synthetic landscape, consisting of a simple *20 m* by *20 m* planar surface with a *75%* slope (*36.9°*). On this surface (discretized into *1 m*^{2} grid cells), a group of *16* grid cells is assigned a soil depth of *1.5 m*, while another group of *16* grid cells is assigned

a soil depth of *1 m*. Water saturation levels for these two groups are set to *100%* and *75%*, respectively. The rest of the cells are assigned *0.5 m* of unsaturated soil. At the two *16*-cell locations lateral cohesion values are lowered from *4600 Pa* to *100 Pa*, and basal cohesion values are lowered from *1000 Pa* to *100 Pa*, simulating local gaps in the root strength field. The soil friction angle is set to a value just below the slope angle on the entire hillslope, namely 35°. Soil and water bulk densities are set to *1600 kg* m^{-3}, and *1000 kg* m^{-3}, respectively. In essence, an artificial hillslope is created in which sharply contrasting local conditions are imposed such that the slope stability model would predict that the two *16*-cell blocks should fail while the rest of the hillslope would not. Furthermore, the local conditions are such that one of the *16*-cell blocks will have a lower factor of safety than the other due to increased soil mass and saturation ratio.

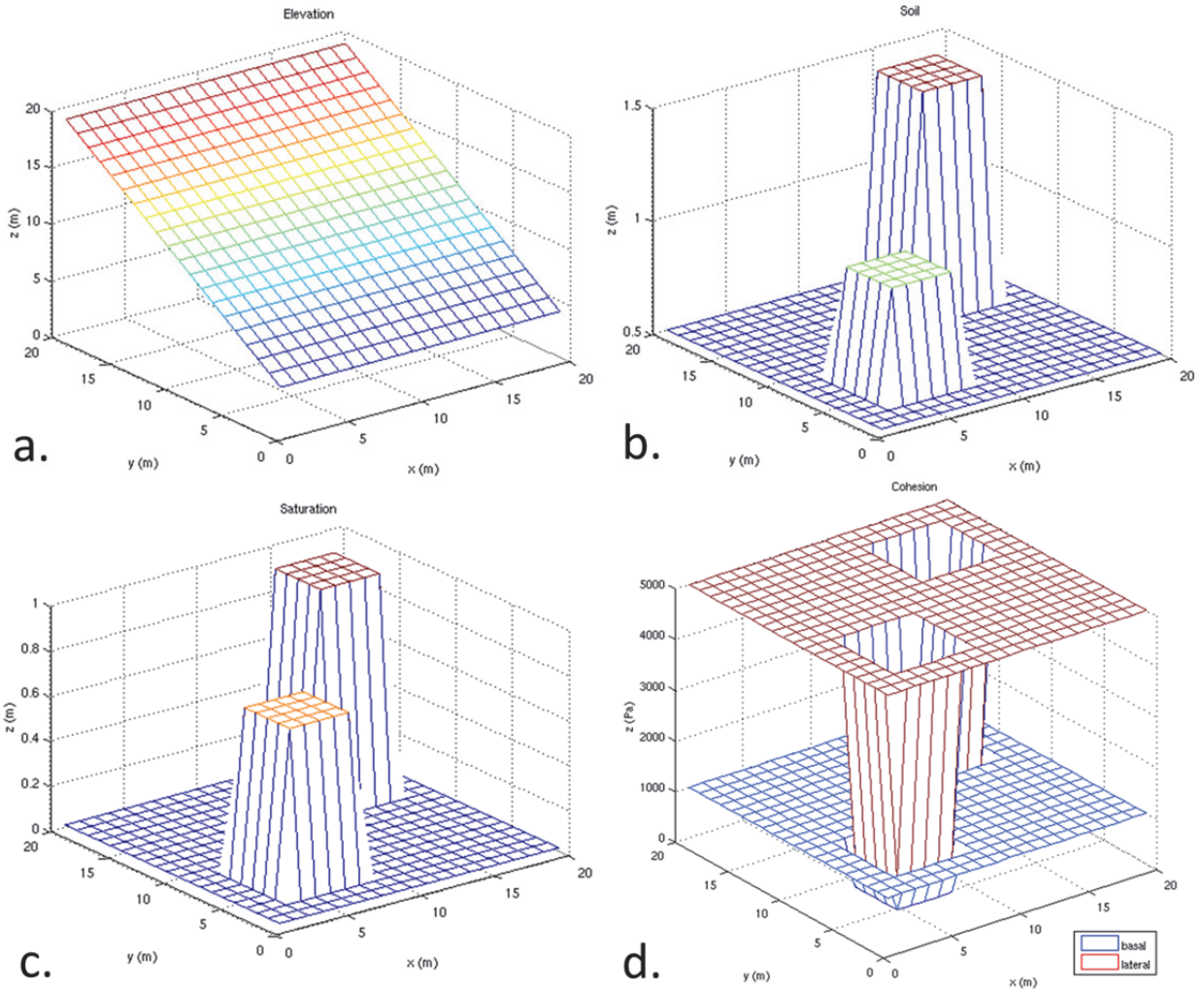

Figure 3.11. Synthetic landscape 1. A planar *75%* slope (a) in which two groups of *16* grid cells are assigned a soil depth of *1.5 m* and *1 m*, respectively, while the soil in remaining cells is *0.5 m* thick (b); the saturation ratio (*h/z*) is set to *1* and *0.75* for the two groups of cells, respectively, while the rest are unsaturated (c); cohesion values are lowered for the same group of cells, simulating a gap in the root strength field.

The procedure is then applied to this synthetic hillslope. The force matrix ***F*** and Laplacian-like resistance matrix ***R*** are assembled, as defined by equations 3.1 and 3.2-3.3, respectively, and the cost function of equation 3.5 gives rise to the linear system defined by equation 3.6. Figure 3.11 (a and b) shows the eigenvectors associated with the two smallest eigenvalues of this linear

system, reshaped to the size of the original *20* by *20* grid. The thresholding process is analogous to taking *399* slices (parallel to the *x*-*y* plane) of these curved surfaces, and setting the discrete values of each cell to be one if the eigensurface is above the slice at that cell or zero if not. The factor of safety of the resulting discrete shapes is evaluated using the slope stability model, and the shapes having the minimal factor of safety are retained. As shown in figure 3.11 (c and d), these shapes correspond exactly to the locations of the perturbed *16*-cell blocks, with the thicker, more saturated block resulting in a lower factor of safety than the other block.

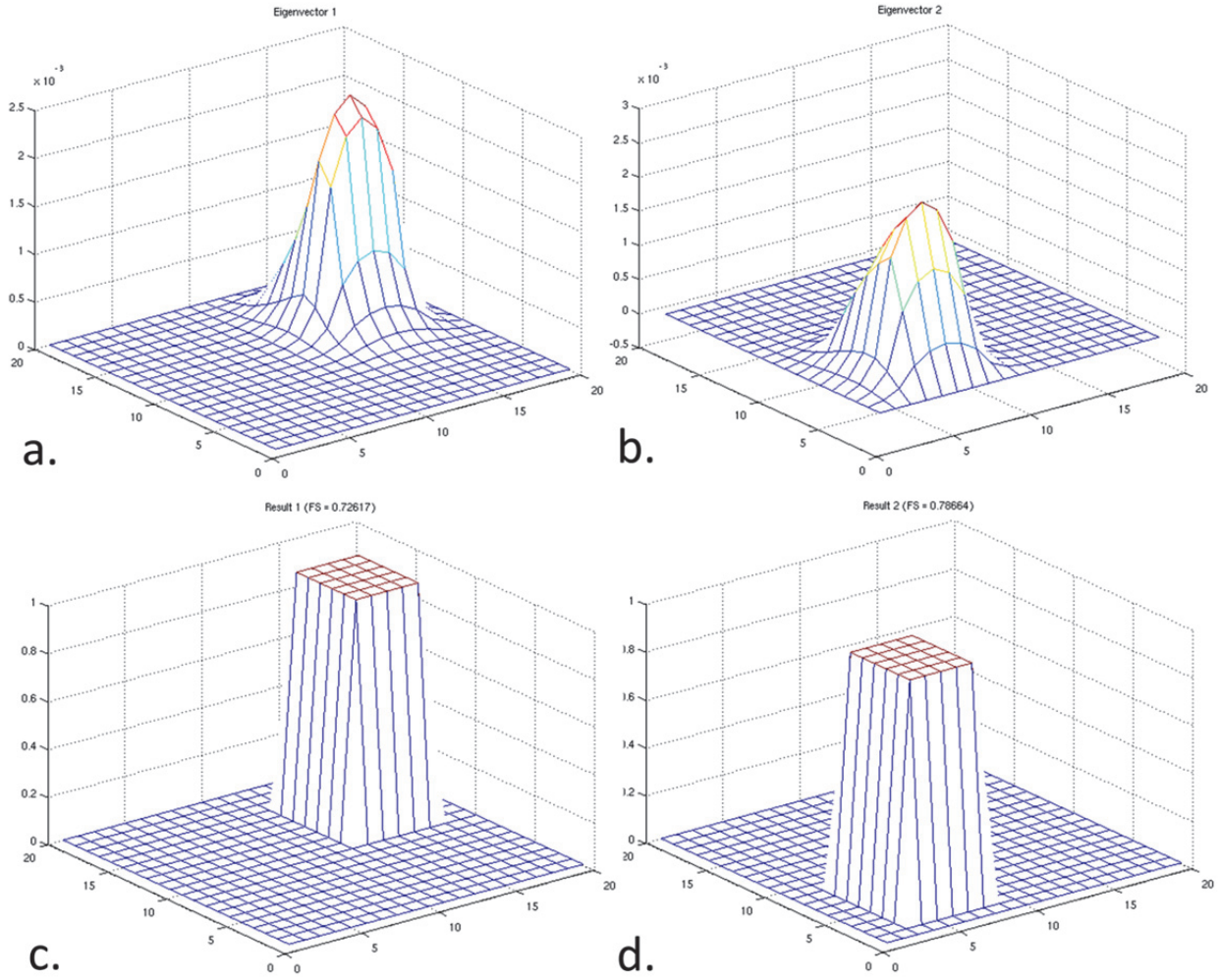

Figure 3.12. Synthetic landscape 1: continuous vs. discrete solutions. The first (a) and second (b) eigenvectors associated with the two smallest eigenvalues of the linear system defined by equation 3.6; the discrete landslide predictions resulting from thresholding the first (c) and second (d) eigenvectors. The predicted landslides correspond exactly to the 16-cell blocks of figure 3.11, with the first predicted landslide having a lower factor of safety than the second, as would be expected.

This synthetic experiment illustrates the workings of the landslide prediction procedure, and supports the hypothesis formulated in chapter one that a physically-based model coupled with an efficient search procedure can be used to predict shallow landslides. A similar experiment can be performed to illustrate the other hypothesis put forth in chapter one, namely that the heterogeneity of parameters such as root strength and pore pressure controls the size of shallow landslides. On a second synthetic landscape consisting of a larger but similarly critically-inclined surface, the procedure is applied first with uniform conditions, then with conditions varying

downslope, and finally with conditions varying both downslope and cross-slope. In all cases a *100 m* by *100 m* planar surface is inclined at *45°* with uniform soil depth (*0.5 m*), friction angle (*35°*), and soil and water densities (*1600 kg* m^{-3}, and *1000 kg* m^{-3}, respectively). The boundary of the surface is fixed to a no-failure condition (figure 13.3 a).

The first case is shown in figure 3.13: the saturation ratio ***h/z*** is uniformly set to *0.75*, and root strength is uniformly set to *4600 Pa*. The procedure is applied and, not surprisingly, the least stable shape found encompasses the whole surface (excluding the boundary). If any group of cells can fail (and they can under the specified conditions), then adding more cells which have identical properties can only increase instability. This is intuitive as the driving forces increase with volume while the resistive forces increase with surface area.

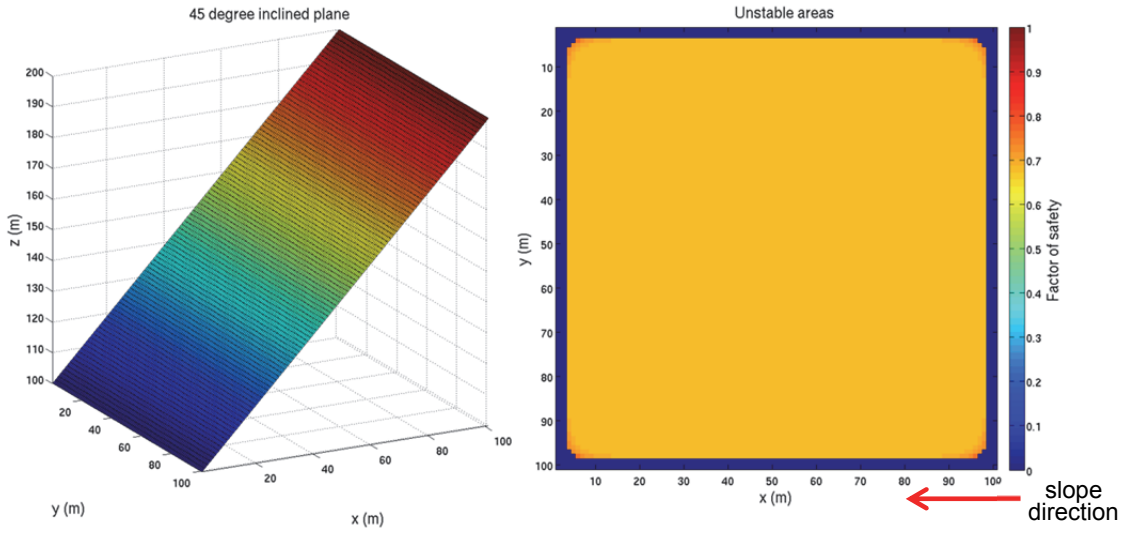

Figure 3.13. Synthetic landscape 2: uniform conditions. (a) *100 m* by *100 m* planar surface with *45°* slope, *0.5 m* soil depth, *35°* friction angle, *1600 kg* m^{-3} soil densitiy, and *1000 kg* m^{-3} water density. (b) Overlapping unstable shapes with FS < 1 recovered by the landslide prediction procedure, extending to the fixed boundary. Overlapping shapes are distinguished by a change of color.

In the second case, shown in figure 3.14, the setup is exactly the same, except for the saturation ratio. Here ***h/z*** increases downslope according to equation 2.12 (with *log(**q/T**) = -2*), simulating the application of rainfall (figure 3.14 a). This implies that with all other conditions remaining constant, the factor of safety of individual cells decreases downslope. The procedure is applied and the least stable shape no longer encompasses the whole surface, rather it has a discrete length (figure 3.14 b). Even though the grid cells in the downslope row are the least stable, there is a benefit to "*growing*" larger. However, once the saturation ratio drops significantly this benefit is lost, resulting in a discrete least-stable shape which extends only half way upslope.

In the third case, shown in figure 3.15, the setup is the same as in the previous example, but now instead of root strength being uniform the surface is assigned two patches of high root strength and two of low root strength (figure 3.15 a). The high strength patches are assigned a value of *10,000 Pa*, while the low-strength ones are assigned a value of *100 Pa*, simulating the patchiness vegetation. Thus conditions vary both downslope and cross-slope, and the least stable shape found by the procedure is constrained in both directions (figure 3.15 a). As in the previous case the landslide "grows" while h/z is sufficiently high, but only in areas of low root strength. As a result only a quarter of the inclined surface can fail.

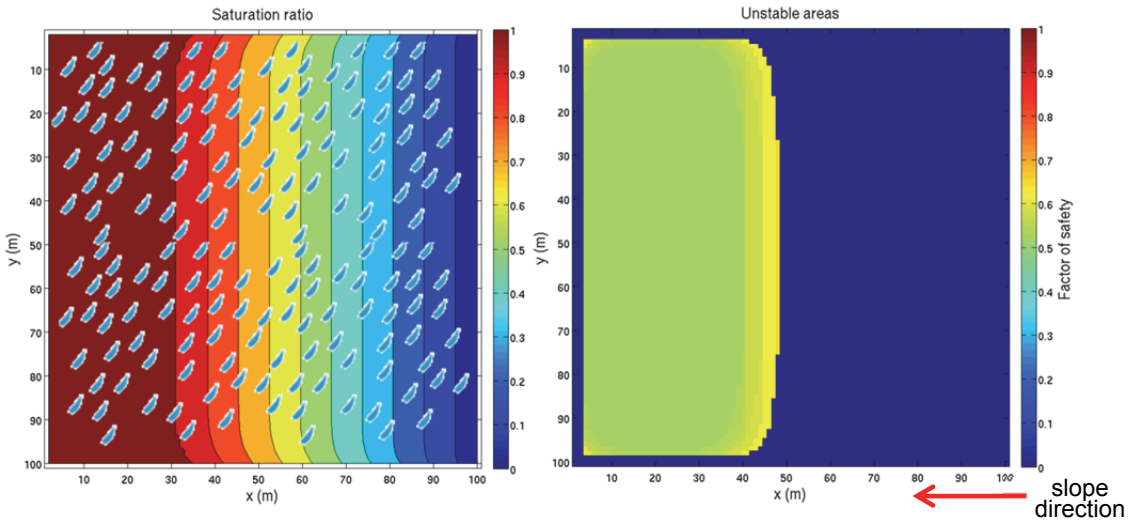

Figure 3.14. Synthetic landscape 2: variable saturation ratio. (a) The saturation ratio *h/z* as determined by equation 2.12 applied to the surface of figure 3.13a for $log(q/T) = -2$, simulating rainfall conditions. (b) Discrete overlapping (as distinguishable by their color) unstable shapes with FS < 1 recovered by the landslide prediction procedure, extending only part way upslope.

This second synthetic experiment further illustrates the behavior of the landslide prediction procedure under several very simple cases. In these extremely simplified scenarios the procedure behaves sensibly, and lends support to the hypothesis formulated in chapter one that heterogeneity of parameters such as root strength and pore pressure control landslide size. What occurs in more complex situations will be explored in the following chapters.

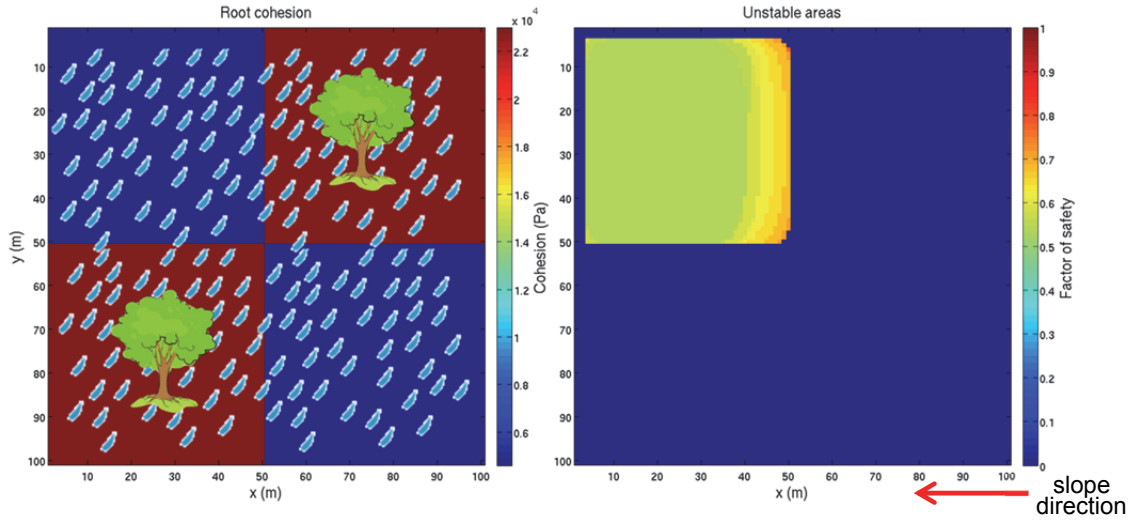

Figure 3.15. Synthetic landscape 2: variable saturation ratio and root strength. (a) Two high-strength (*10,000 Pa*), and two low-strength (*100 Pa*) patches applied to the scenario of figures 3.13a and 3.14a, simulating varying vegetation conditions. (b) Discrete overlapping (as distinguishable by their color) unstable shapes with FS < 1 recovered by the landslide prediction procedure, extending only part way upslope and part way cross-slope.

3.6 Discussion

The problem of searching for least-stable shallow landslides among a potential exponential number of them requires finding a suitable and efficient approximation. This is because all the possible unstable regions in a landscape cannot be enumerated unless strict limits are imposed to

both the size of examined landscapes and potential landslide shapes. The nature of approximating such complex searches implies limiting the searchable space in a way that does not greatly reduce the likelyhood of finding the optimal (or near-optimal) solution. This goal is achieved by accepting the *"guidance"* of the continuous solution of equation 3.5. Notwidthstanding the lack of guarantees of such an approach, the goal was to make minimal assumptions in order to keep the search as general as possible, and for the search to be independent from the slope stability model and all the sub-models. This is mostly motivated by the fact that not only do we expect models and data to improve in the coming years, but we believe that the ability to predict discrete landslides will play a fundamental role in indicating what models should be explored in greater depth, and what data is opportune to collect in order to make predictions more accurate. Ultimately, only one fundamental assumption was made, namely that the landscape and the forces acting on it can be represented using an *undirected graph*. This choice was made because we know how to find good approximate solutions to a linear eigenvector/eigenvalue problem, while an unconstrained nonlinear problem presents many more difficulties.

A spectral graph partitioning method defines potential landslides on the basis of a global optimization (i.e. the optimization is performed on the matrix containing information about all nodes and edges). This means that the force balance is solved instantaneously and globally. This is consistent with the rigid block assumption within the slope stability model introduced in chapter two, but does not allow modeling progressive failure in the current form of the algorithm. Representing progressive failure would require an iterative approach in which the least stable shapes defined by our method are removed (and possibly re-distributed) across the landscape.

The transformation between directed and undirected graph occurred both in the representation of the edges and of the nodes. I have demostrated that the symmetrization of the edges does not misrepresent the boundary between a potential landslide and its surroundings. We have noted that encoding in the nodes the magnitude of the force rather than the force vectors results in an over-estimation of the forces and thus a lower factor of safety (section 3.4.1). This will result in more candidate landslides found during the discretization process. The factor of safety of this over-populated candidate landslide set is in turn examined with a correct force formulation (see section 3.4.4), and those regions which as a result of using force vectors instead of magnitudes become stable are pruned from the list. We have not, however, demonstrated that encoding the magnitude of the forces instead of the force vector does not result in differently shaped eigenvectors which, when thresholded, may give rise to entirely different regions which may not overlap with those currently produced. Unfortunately this is not demonstrable, as it cannot even be shown that with any formulation some unstable regions will not be missed. In practice though, we can say that that this is extremely unlikely because of the following reasons:

a) An over-estimation of the forces results in a lower value for the continuous solution ***C(y)***, defined in equation 3.5. The eigenvector surfaces will thus have either *"fatter"* peaks, or fatter valleys, or both. We threshold each eigenvector and its complement, which is equivalent to starting from single pixels corresponding to the peaks and *"growing"* the regions while the threshold decreases, then starting from the valley single pixels and growing the regions while the threshold increases. This implies that in one direction or the other we will likely end up examining more areas than we would with *"skinnier"* peaks or valleys.

b) We examine a large number of eigenvectors over a small window that is moved over the landscape. As the eigenvector number increases the continuous solution deteriorates, resulting in progressively *"bumpier"* surfaces. Thus the number of peaks and valleys also quickly increases, generating a larger distribution of "seeds" from which regions are grown

Where we run into problems is that it is not hard to imagine that there may exist cases where, in a topographic setting in which valleys are longer than they are wide, the hypothetically correct eigenvectors are not only skinnier, but as also more *"oblung"*. This is because the forces along the valley axis are much less likely to cancel each other out than those perpendicular to the valley axis. This means that when using our *"rounder"* eigenvector surfaces, while it is true that we start looking at single pixels and grow to regions that necessarily have to be larger than the theoretically most unstable region, it is also possible that there are some skinny shapes that may never be seen in the process. While we can remind ourselves that we may never see all unstable shapes, as there are too many of them, it is important to consider that in some topographic settings there could be a bias toward rounder shapes.

The issue of overlapping landslide predictions (i.e. different discrete predicted landslide shapes which have grid cells in common) is dealt by the procedure with the parameter defined by equation 3.7 which can be set by the user. The reason for this approach is that whether overlap should be allowed depends on the application. If the goal is to inform the user of all possible landslides for a type of event, then no unstable shape should be discarded. In contrast, if the user is interested in the most likely landslide (*likely* here is synonimous with the *least stable*), then for two virtually identical shapes are predicted, it is intuitive to discard the most stable of the two. While these are clear end-member examples, the question of what is a sensible amount of overlap to permit is a difficult one to answer: a significant amount of overlap may result in over-prediction, while insufficient overlap may result in under-prediction. Generally, all overlapping landslides will be reported in this study. However, when the objective is to match a single specific event, the least stable of the overlapping landslides is retained. The influence of overlapping landslide predictions will be further examined in the next chapter in the context of a specific application.

The order in which the eigenvectors are examined is irrelevant to the final outcome. This is what is commonly referred to as an *embarassingly parallel* problem in the parallel computing literature: this phase of processing can be run in parallel as there are no dependencies between these tasks. As a result, practically linear speed up can be obtained with minimal communication. In a very similar way, the processing order of the windows is not important for the results. This suggests a dual level of parallelization, appropriate for today's typical high-performance computing (***HPC***) hardware. Typical ***HPC*** systems have a distributed architecture in which a system has many nodes, each with multiple many-core processors and shared memory. The natural way for the application to exploit this architecture is to parse out windows to each node, and have the many cores in each node take on the eigenvector thresholding process. This can be achieved with minimal modifications to the current code, but it would require the use of the Matlab Distributed Computing Toolbox.

We defined metrics that can be used to evaluate the performance of our procedure, but we did not explicitly state how we plan to demonstrate that this performance is satisfactory. In many areas of computer science (e.g. computer vision, machine learning, information retrieval, etc.) a plethora of benchmark datasets are available to the entire community so that improvement in algorithm development can be more precicely quantified; unfortunately, no such things exist for

shallow landslide prediction. Furthermore, while it would be essential to have publicly available databases of accurately mapped shallow landslides, it also critical to understand the conditions under which they occurred. I will thus present mostly an evaluation of the procedure as a function of condition of occurrence, with a particular focus on those which can change more rapidly. The intent is not solely to gage under what scenarios do we have a greater precision/recall, rather also that of understanding of what conditions can create a particular shallow landslide response.

In the first synthetic experiment presented here, the procedure recovered *exactly* the landslides which were "*planted*" on an artificial surface with very sharp contrasting conditions. This was expected, as in such cases the cost of the optimal graph partition is significantly lower than when using alternative graph cuts. In other words, in this example adding or removing even a single cell to the predicted shape will drastically change its factor of safety. In more complex scenarios exact performance cannot be expected, as parameters will vary quite differently, particularly in a real topographic setting. As already discussed, in such cases we must accept the approximation provided by the continuous solution which by definition cannot provide all possible results, including at times the optimal one.

In the second synthetic experiment, we observed that on a critically-inclined surface under uniform conditions the largest possible landslide is predicted to be the least stable. As soon as a single parameter (the saturation ratio) is allowed to vary, the emergence of discrete landslide sizes is observed. This observation is further reinforced when variation of a second parameter (root strength) is introduced. This illustrates how growing or shrinking relates to cost and benefit, as defined by the search algorithm. Figures 3.14b and 3.15b also illustrate the distinction (and size difference) between a *critical* size and an *optimal* size: the former is the size at which the factor of safety falls below 1, while the latter is the size resulting in the minimal factor of safety. Furthermore, this example shows that even in extremely simple scenarios many different outcomes are possible.

3.7 Conclusion

In this chapter I have presented a procedure that can for the first time predict discrete landslides. Its foundation is a search algorithm based on spectral graph theory that can efficiently provide a good approximation for an otherwise intractable problem. This procedure relies on a slope stability model, as well as sub-models and data for, among others, topography, soil depth, and root strength, discussed in the previous chapter. However, the procedure is general, and is not confined by their choice: as better models and data emerge, the procedure can be easily modified to take advantage of such improvements.

I presented two simple synthetic examples which illustrate how the procedure searches for landslides, and how their size can be affected by the hetereogeneity of parameters such as root strength and pore pressure. I laid the groundwork for a more complex real-world application, which will be presented in chapter four of this dissertation, in which the metrics defined here will be used to assess the procedure's performance. I hypothesize that the ability to predict discrete landslides can play a fundamental role in understanding the response of the shallow landslide regime to heterogeneous conditions, a topic that will be explored in chapter five. It will also help us understand the response of the shallow landslide regime to the type of changes which we can expect in the not too distant future, a topic that will be examined in chapter six.

Chapter 4

Evaluating the procedure: a case study in the Oregon Coast Range

4.1 Introduction

The initial working hypothesis of this research was that we could build a model which captures the basic physics of shallow landsliding across landscapes and couple it with an efficient search algorithm to improve our prediction capability and advance our understanding of shallow landsliding controls. In chapter two I introduced a mechanistic framework that computes the stability of discrete elements of a landscape using field-measured or modeled data, which is mechanistic in its definition but not so mechanistic that it cannot be applied to landscapes. In chapter three I defined an efficient search algorithm which can select least stable combinations of these elements to produce discrete shallow landslide predictions. To test the first part of the initial hypothesis, namely the ability of the new model to improve predictions, the procedure will be applied in this chapter to a landslide-prone study area in the Oregon Coast Range. Our site was selected because of two unique datasets deriving from over a decade of research at this site. First, an instrumental record of a rainfall-triggered shallow landslide that occurred in a small catchment at the research site [Montgomery et al., 2009] allows for the application of the slope stability model and the search algorithm using field-measured physical parameters such as hydrological conditions, soil depth, and root strength. Second, across a larger area (0.5 km^2) repeat field mapping provides an inventory of all the shallow landslides that occurred over a 10-year period [Montgomery, et al., 2000]. Also during this 10-year period intensive research was conducted in the area, providing detailed information on soil, vegetation, hydrological, and rainfall characteristics. This dataset thus presents a unique opportunity to apply all the sub-models which estimate the local characteristics of soil, vegetation, and hydrology (see review in Ebel et al., 2007a and 2007b). Given the volume and quality of the data from this site, it has been a benchmark for many landslide models [e.g. Montgomery and Dietrich, 1994; Rosso et al. 2006; Borja and White, 2010]. The procedure will be applied to both datasets, and the resulting shallow landslide predictions will be compared to the mapped observations, with particular emphasis on the size and location of failures. In this chapter, the performance of the procedure will be evaluated both qualitatively and quantitatively using the methods described in chapter three.

4.2 Study area

The study area is located on the Mettman Ridge, about *15 km* north of Coos Bay, Oregon (figure 4.1a). It consists of steep, highly dissected soil-mantled hillslopes and steep channels typical of the Oregon Coast Range where the maritime climate delivers approximately *1500 mm* of annual precipitation [Montgomery and Dietrich, 1994]. The study area burned in the late nineteenth century, was clear-cut logged in 1987, and was replanted in 1988 with Douglas fir seedlings [Montgomery and Dietrich, 1994; Montgomery et al., 2009]. The Mettman Ridge is mostly underlain by Eocene sandstone and the resulting colluvial soils are well-mixed, gravelly sands with sandstone clasts [Montgomery et al., 2000; Schmidt et al., 2001]. Soils thickness ranges from roughly *0.1 m* to *0.5 m* on topographic noses to greater than *2 m* in topographic hollows, with bedrock outcrops in many areas where the slope exceeds *45°* [Montgomery and

Dietrich, 1994]. The colluvium has a friction angle of *40°*, and is essentially cohesionless [Schmidt et al., 2001]. Roots produce an apparent cohesion via root fiber reinforcement (referred to as root cohesion or root reinforcement) promoting slope stability in shallow soils [Schmidt et al., 2001]. Many channels begin at small landslide scars [Montgomery and Dietrich, 1998], and shallow debris flows periodically deliver the colluvial soils to the downslope channel system. The average slope is of the study area is *36°*, with maximum slopes exceeding *60°* in many locations.

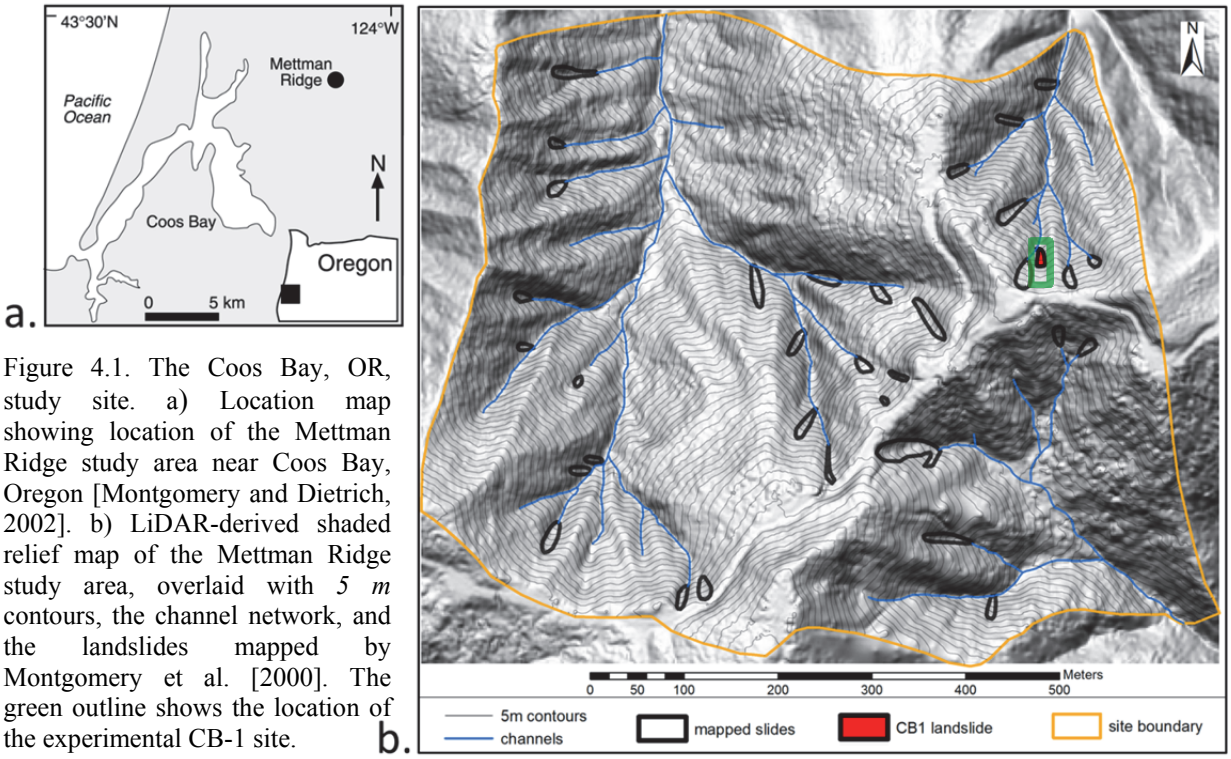

Figure 4.1. The Coos Bay, OR, study site. a) Location map showing location of the Mettman Ridge study area near Coos Bay, Oregon [Montgomery and Dietrich, 2002]. b) LiDAR-derived shaded relief map of the Mettman Ridge study area, overlaid with *5 m* contours, the channel network, and the landslides mapped by Montgomery et al. [2000]. The green outline shows the location of the experimental CB-1 site.

To investigate the mechanisms responsible for pore-water pressure development and shallow subsurface runoff generation, an experimental monitoring site (CB-1) was setup in a small north-facing catchment of the Mettman Ridge study area (figure 4.3 a). CB-1 was selected because it was small enough to enable detailed monitoring of hydrologic response, yet large enough to include the entire source area of a small first-order stream. Recent logging infrastructure provided access and allowed for water storage for use in artificial sprinkling experiments. Most importantly, unlike many similar sites it had not experienced landsliding after being clear-cut. The experimental site was equipped with rain gages, piezometers, sprinklers, wells, tensiometers, weirs, lysimeters, and a weather station (figure 4.2). The CB-1 catchment area is *860* m^2, and the average slope is *43°*. Soil depths measured throughout the catchment range from a few centimeters on the divergent side slopes to a little less than *2 m* in the thicker part of the hollow (figure 4.4 a).

Landslides are common in the steep Coast Range terrain, are usually triggered by intense rainfall events, and are typically found on steep slopes *(> 35°)* in areas which can focus storm runoff such as topographic hollows and roads. Non-road associated failures are typically *7 m* wide, *13 m* long, and less than *1 m* deep, while road associated failures can be four times larger in volume [Robison et al., 1999]. Their occurrence increased dramatically following widespread

timber harvesting and road construction [Montgomery et al., 2000], with the most significant incidence found in areas where disturbance is less than 10 years old [Robison et al., 1999]. Many channels begin at small landslide scars [Montgomery and Dietrich, 1988], and these landslides commonly mobilize as debris flows which cut the channel network draining the landscape, suggesting the fundamental role played by landslides in shaping the landscape.

As in the surrounding Coast Range, landslides are ubiquitous in the Mettman Ridge area. All shallow landslides which occurred there during the decade of research at the CB-1 site were mapped by Montgomery et al. [2000]. Of the 34 scars shown in figure 4.1b, nearly all were mapped by walking the study area and a few were mapped from low-altitude aerial imagery. Of these landslides 16 occurred in the first two years after the 1987 clear-cutting of the area, 30 occurred in topographic hollows that define the axis of unchanneled valleys, and 10 were also associated with drainage from a logging road [Montgomery et al. 2000].

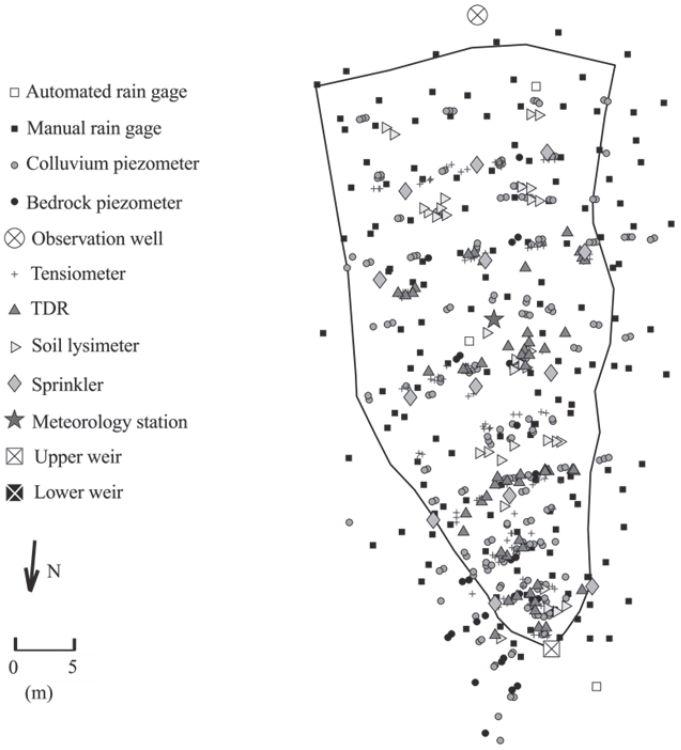

Figure 4.2. Location of the CB-1 instrumentation. From Ebel et al., [2007a].

In November 1996 a rainstorm delivered the largest recorded 24-hour rainfall to the Oregon Coast Range, triggering widespread landsliding in many areas and causing extensive damage and loss of lives [Robison et al., 1999]. Over the period of November 16–18, the CB-1 rain gauges measured *225 mm* of rain with a maximum daily intensity of *145 mm/day* and a 48-hour average intensity of *85 mm/day* [Montgomery et al., 2009]. The 24-hour total of *160 mm* of rainfall recorded at the North Bend, OR, airport was *27 mm* greater than the previous daily maximum recorded since 1931. Five landslides occurred in the Mettman Ridge study area during this storm. Most significantly, during the evening of November 18th, about one hour after the peak rainfall, the slope failed at the CB-1 site. The colluvium from the CB-1 hollow mobilized as a debris flow, destroying most of the infrastructure at the experimental site (figure 4.3). The debris flow left a *156* m^2 scar that was on average *5 m* wide and *26 m* long, with depths ranging from *0.3* to *1 m*. A detailed forensic investigation led to the conclusion that the initial landslide only comprised the upper part of the scar, with an area of approximately *58* m^2 [Montgomery et al. 2009]. In the upper part of the scar, the colluvial soil was excavated to the bedrock, and root exposed in the headscarp and lateral margins were uniformly snapped, suggesting full engagement of their tensile strength during initial failure [Montgomery et al., 2009]. Figure 4.4b shows the debris flow scar, the initiation area, and the pore pressure field measured by the installed piezometers. While this event effectively shut down research operations at the site, the CB-1 measurements possibly represent the most complete data set available for any catchment that underwent slope failure [Ebel et al., 2007a].

Figure 4.3. The north-facing CB-1 experimental catchment. (a) before and (b) after the November 1996 storm. Photos courtesy of William E. Dietrich.

4.3 Application to a single catchment with field-measured data

Here we apply the shallow landslide prediction procedure to the *860* m^2 CB-1 experimental catchment. The data used for this application consists of spatial 1 m resolution grids containing elevation, soil depth, and pore pressure values used in the re-analysis of the failure performed by Montgomery et al., [2009]. The fundamental difference between the Montgomery et al., [2009] re-analysis and this application is that no failure shape is prescribed here, allowing the search algorithm to find the least stable failure configuration. Another difference between this application and the 2009 re-analysis consists of the treatment of root strength which is assumed here to be exponentially decaying with depth (rather than uniform). Root reinforcement values are obtained by fitting an exponential function to the published data, as described in chapter two. Thus average root strength values vary spatially with soil depth, although they are constrained to reflect the average values reported by Montgomery et al. [2009]. Finally, the treatment of pore pressure values differs slightly in that no adjustment was made to the original data (rather than a 10 cm adjustment to some of the grid cells, reported by Montgomery et al. [2009]). Table 4.1 lists the parameters used for this simulation.

h [m]	z [m]	phi [deg]	C_{r0} [Pa]	j [m^{-1}]	ρ_s [kg/m^3]	P_w [kg/m^3]
measured (0-1.245)	measured (0.005-2.172)	40	21,666	4.96	1,600	1,000

Table 4.1. Parameters used for the application of the procedure to the CB-1 site.

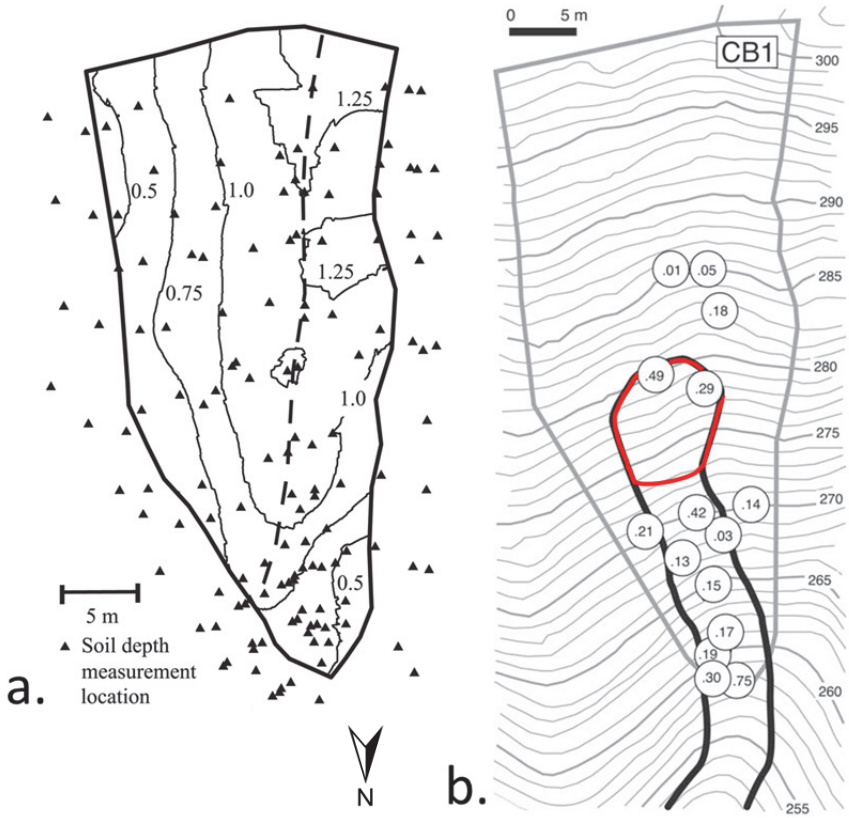

Figure 4.4. CB-1 field measurements. a) Map of the CB-1 catchment showing the locations of soil depth measurements collected by [Schmidt, 1999] and the resulting *0.25 m* soil depth contours. b) Map of the pore pressure ratio. Circles indicate the locations of the piezometer nests used, and the resulting *h/z* values; the red outline indicates the initial failure area, while the black outline indicates the subsequent debris flow. Adapted from Montgomery et al., [2009].

The continuous and discrete solutions resulting from the application of the procedure to the CB-1 site are shown in figure 4.5, while a topographic map with the predicted landslide is shown in figure 4.6. Under the conditions measured during the November 1996 storm event, the procedure predicts failure at the same location and of similar size as the actual landslide which occurred at the CB-1 site. The predicted landslide differs from the observed landslide only in that it extends a couple of meters further upslope, resulting in an area *9* m^2 larger than the observed failure. The factor of safety of the predicted landslide is *0.89*, a value very close to that of *1.0* computed with the slope stability model CLARA-W [Hungr et al., 1989] by Montgomery et al., [2009].

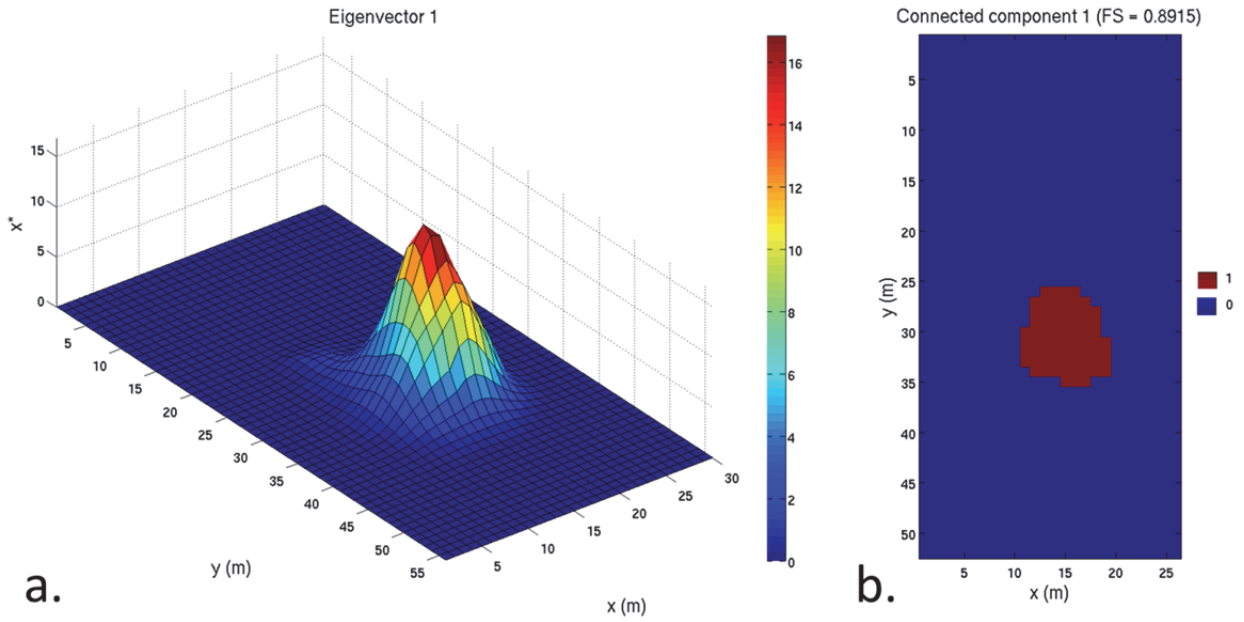

Figure 4.5. Continuous and discrete solutions at CB-1. a) The continuous indicator vector $\boldsymbol{x}^*$, representing the fraction of each node that contributes to the optimal partition $\boldsymbol{S}^*$ (see section 3.4.3), found by applying the procedure to the CB-1 site. b) The discrete indicator vector $\boldsymbol{x}$ obtained from thresholding $\boldsymbol{x}^*$ (see section 3.4.4), resulting in the partition having the minimum FS.

4.4 Application to a landscape with modeled data

Here we apply the shallow landslide prediction procedure to the *0.5* km^2 Mettman Ridge study area (CB-MR). Topographic data used for this application consists of a *2 m* resolution grid containing LiDAR-derived elevations with an original average data point spacing of *2.3 m* [Roering et al., 1999]. In contrast with the CB-1 application, soil depth, water table height, and values for the lateral and basal root strength fields will be modeled here using the methods described in chapter two. The aim is to demonstrate the applicability of the procedure, and evaluate its performance. This does not involve an exhaustive search of the best-performing parameters, rather a suite of scenarios is selected. In steep upland topography, and in the Oregon Coast Range in particular, field investigation suggests that "slowly-changing" variables such as soil depth, root strength, and soil friction angle can be crudely estimated [e.g. Dietrich et al., 1995, Montgomery et al, 2000, Schmidt et al., 2001]. In contrast, hydrologic conditions are far from continuously varying and are not due to a single event. In the context of demonstrating the procedure, here soil depth and root strength parameters will be held constant, while several hydrologic scenarios will be investigated. In the following chapter a full suite of simulations involving all the principal variables will be presented. Two different approaches will be used for performance evaluation. First, the properties (i.e. size, shape, location) of predicted landslide populations will be compared to the observed dataset. In terms of size, this form of validation has been used, among many others, by Stark and Guzzetti [2009], where the general power-law characteristics of an observed landslide dataset were reproduced. Here, I will statistically compare predicted and observed distributions, using the methods defined in section 3.4.5.2. Second, the observed dataset will also be used to test the procedure's ability to capture individual

observed landslides. A similar comparison has been suggested by Dietrich et al. [2001], who compare the percent of observed landslides captured with the percent of the landscape predicted to be unstable. Here this comparison will also be evaluated using information-retrieval measures, described in section 3.4.5.2.

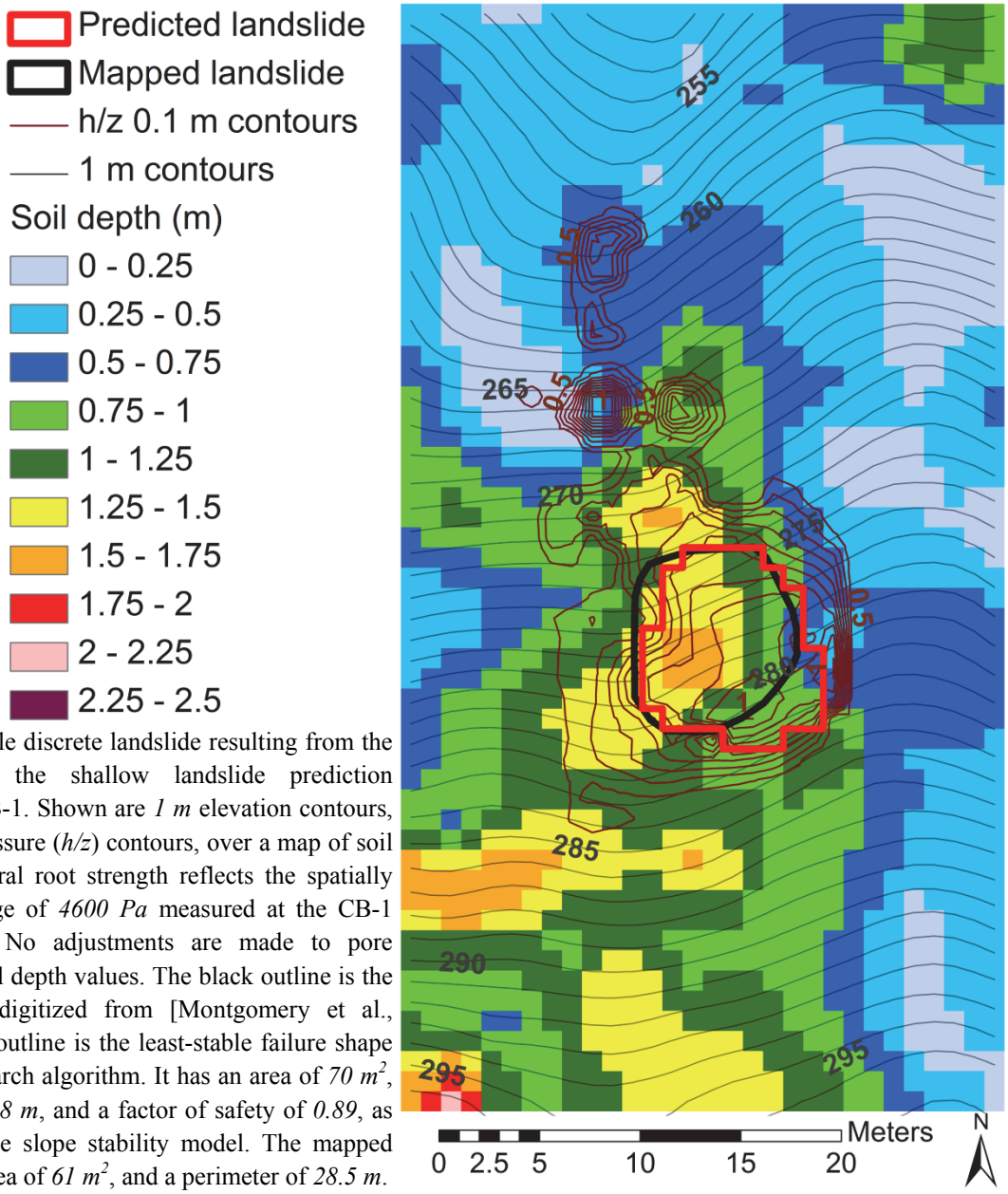

Figure 4.6. Single discrete landslide resulting from the application of the shallow landslide prediction procedure to CB-1. Shown are *1 m* elevation contours, *0.25 m* pore pressure (*h/z*) contours, over a map of soil depth (*m*). Lateral root strength reflects the spatially weighted average of *4600 Pa* measured at the CB-1 landslide scar. No adjustments are made to pore pressure and soil depth values. The black outline is the actual failure, digitized from [Montgomery et al., 2009]. The red outline is the least-stable failure shape found by the search algorithm. It has an area of *70* m^2, a perimeter of *38 m*, and a factor of safety of *0.89*, as computed by the slope stability model. The mapped failure has an area of *61* m^2, and a perimeter of *28.5 m*.

4.4.1 Parameters and simulations

The soil depth model parameters will be fixed to the calibrated parameters published by Roering et al., [1999], and Heimsath et al., [2001], listed in table 4.2. Initial soil thickness was set to a uniform low value of *10 cm* and the model was run for *6,000 years*. Under the assumption that rivers efficiently transport away any material that is delivered, soil was not allowed to accumulate in channel locations. Figure 4.7 shows the predicted soil depth values for CB-MR, illustrating the pattern of thicker soils in convergent hollows and thinner soils in

divergent slopes. The spatial pattern of water table height is similar, as it is a function of slope and contributing area (i.e. a linear function of the topographic index) which tends to be high in hollows. This results in interplay between soil depth (z), water table height (h), and relative saturation (h/z). Figure 4.8 shows the relationship between soil depth and the topographic index (equation 3.18), which will be used in this study as a proxy for location in the landscape. Figure 4.8 shows that soil depth increases with the topographic index, as does its variance. This illustrates the covariance of soil depth and water table height. As discussed in chapter two, actual soil depths likely express a greater degree of local variability than those adopted here. However, the degree of variability is not expected to change over the ten years of landsliding data examined at CB-MR. Thus, as a first approximation, we hold the soil depth pattern constant over time. As pointed out in chapter two, no mechanism that explicitly accounts for prior shallow landsliding is included in the soil depth model. Each location in which one would expect landsliding to play a role is *fully-loaded* with soil. Thus the soil depth realization shown in figure 4.7 should be considered an upper bound, as at any moment in time some areas which experienced recent landsliding may be considerably thinner.

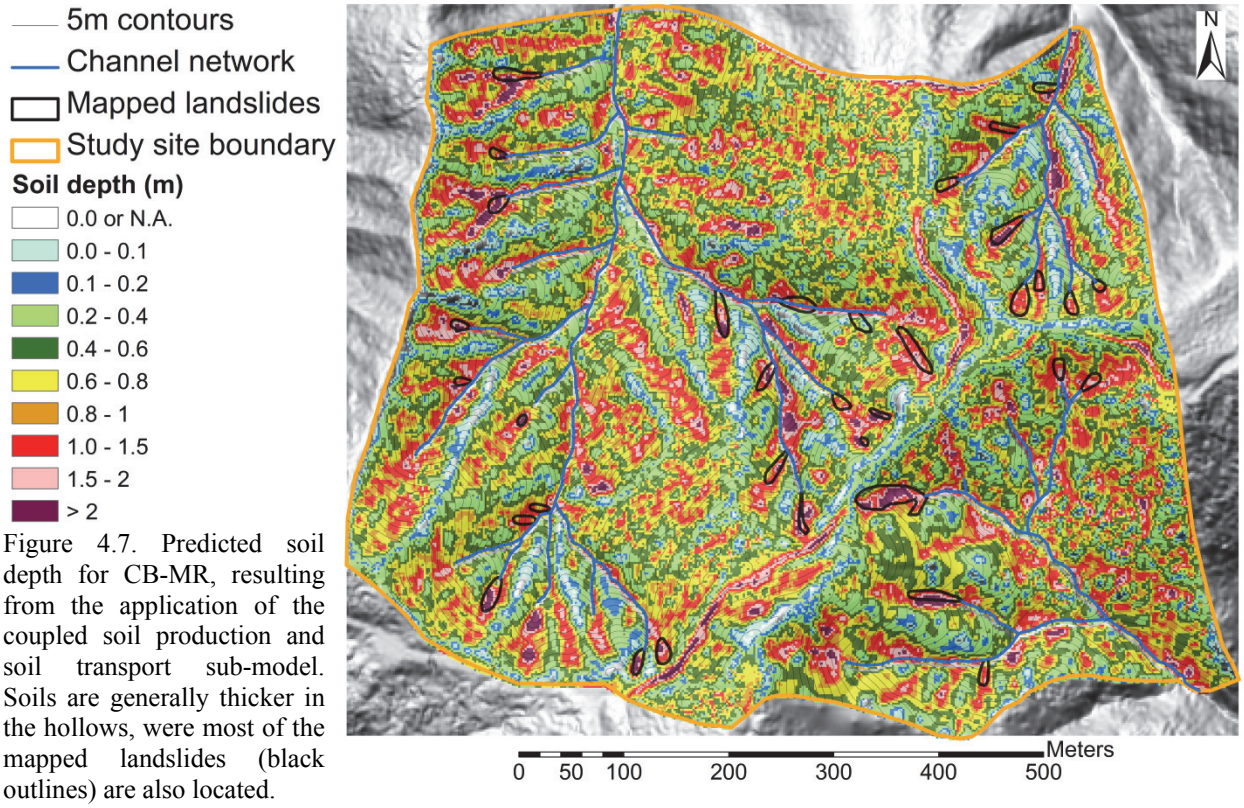

Figure 4.7. Predicted soil depth for CB-MR, resulting from the application of the coupled soil production and soil transport sub-model. Soils are generally thicker in the hollows, were most of the mapped landslides (black outlines) are also located.

Also as a first approximation the root strength field parameters (C_{r0} and j) will be held constant in this application, using the values measured at the CB-1 site listed in table 4.2. The resulting spatially varying lateral and basal root reinforcement values are shown in figure 4.9. The Mettman Ridge area was clear-cut at the same time, and thus spatially averaged root strength values are not expected to vary significantly across the site. In contrast to soil depth, root strength can vary over a ten-year interval [Schmidt et al., 2001], and these effects will be explored in the next chapter. Local (meter-scale) variations can be very significant, but to be captured detailed information of vegetation type, age, and location is required. The alternative probabilistic approach outlined in section 2.2.5 will also be explored in the following chapters.

The treatment of the hydrologic response to rainfall events is perhaps the most problematic of the modeling efforts. For example, hydraulic conductivity at the CB-1 site can vary significantly [Ebel et al., 2007b]. Furthermore, evidence of fracture flow at CB-1 [Torres et al., 1998; Ebel et al., 2007b, Montgomery et al., 2009] suggests an extremely complex hydrological response that is unlikely to be captured by any hydrological model. Moreover, the exact rainfall conditions and the timing of failure are only known for the CB-1 landslide. For the purpose of demonstrating an application of the shallow landslide prediction procedure, a much simpler approach is taken. The instantaneous hydrological models described in section 2.2.4 are applied using a wide range of effective precipitation values (representing cases for low, moderate, high, and extreme precipitation), and the procedure will be applied using the resulting spatial fields of water table heights. These models represent the two end-member scenarios of shallow sub-surface flow, namely the purely lateral (topographically-steered, slope-parallel) and purely vertical (infiltration-dominated, no topographic control) cases. The former model can be viewed as representative of long-duration, low-intensity rainfall, while the latter can be viewed as representative of high-intensity, short-duration bursts of rain. The two models will also be combined; this is mostly for illustrative purposes (i.e. no extensive search for the best combination of the two will be performed). Combining shallow subsurface and vertical flows can be viewed as representing short, intense burst of rain over wet antecedent conditions. Table 4.1 lists the parameters used for all the simulations presented in this section.

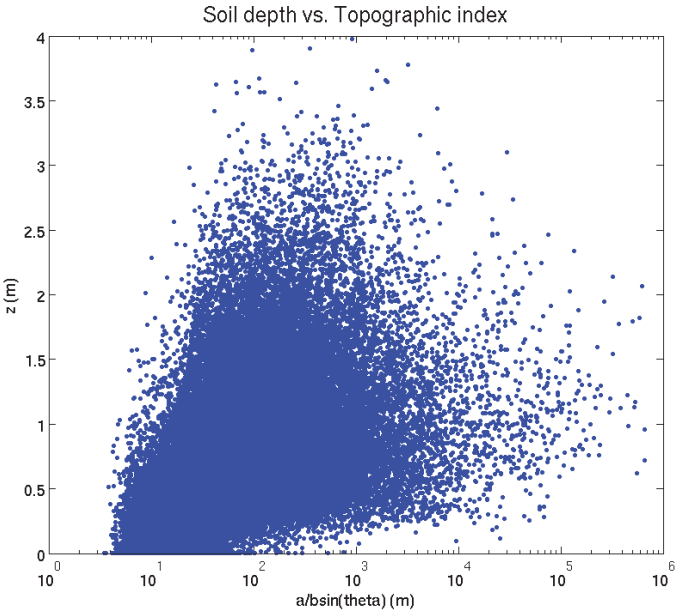

Figure 4.8. Soil depth and topographic index. Predicted soil depth for CB-MR, plotted against the topographic index $a/b\sin\theta$ (equation 3.18). As topographic index increases soil depth also increases, and the variance becomes much larger. This illustrates the covariance of soil depth with the water table height, a linear function of the topographic index.

First the topographically-steered (also referred to as lateral hereafter) model (equation 2.13) is be applied in simulations 1-4 with values of *log(q/K)* ranging of *-3.1*, *-2.8*, *-2.5*, and *-2.2*, respectively. Assuming the average value of $\boldsymbol{k} = 67$ *m/day* reported for the CB-1 site by Ebel et al. [2007b], these values correspond approximately to effective steady-state precipitation of *50 100*, *200*, and *400 mm/day*, respectively. These values should not be compared to real precipitation values as they reflect steady-state precipitation rarely attainable during actual storms. Rather, they should be considered indicative of a relative change in precipitation rates. Figure 4.10 (a-d) illustrates the expansion of the "wetness" (*h/z*) predicted by this model for these *log(q/K)* values. It can be observed that saturated areas expand outwards from topographically convergent areas, and that at the value of *log(q/K)* of *-2.2* almost all of the observed landslides overlap with some fully-saturated grid cells.

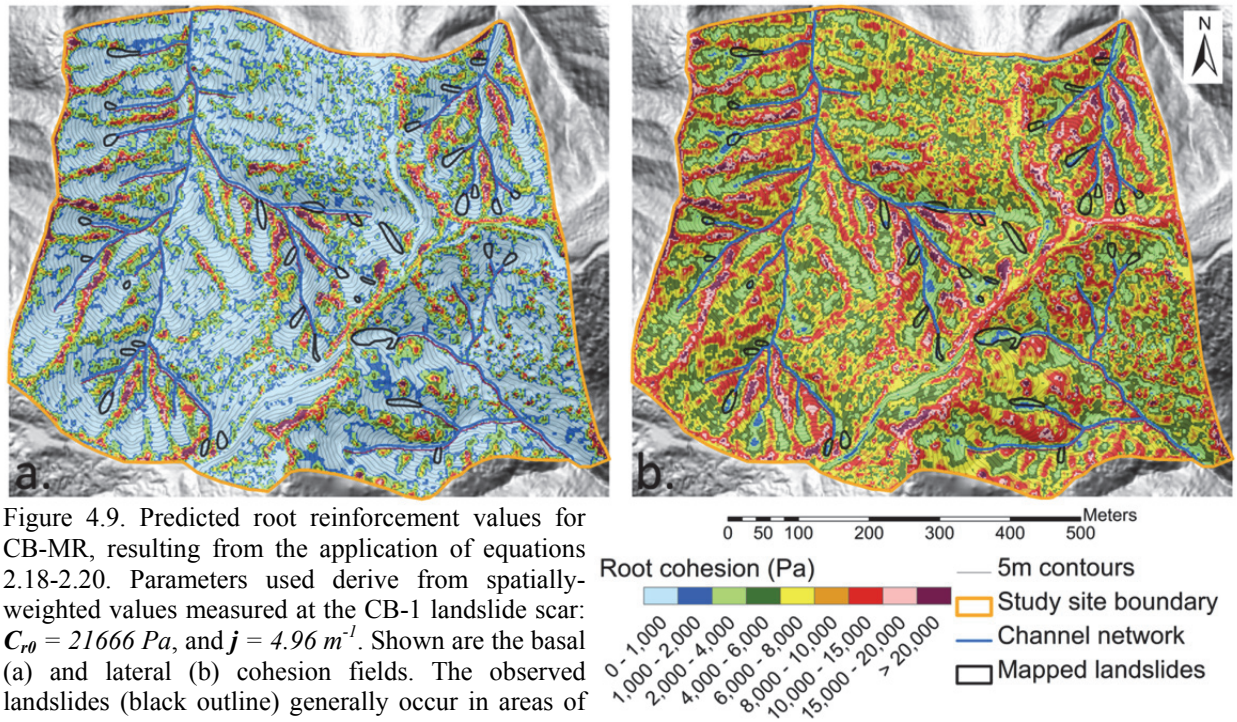

Figure 4.9. Predicted root reinforcement values for CB-MR, resulting from the application of equations 2.18-2.20. Parameters used derive from spatially-weighted values measured at the CB-1 landslide scar: $C_{r0} = 21666\ Pa$, and $j = 4.96\ m^{-1}$. Shown are the basal (a) and lateral (b) cohesion fields. The observed landslides (black outline) generally occur in areas of low predicted root cohesion.

The purely vertical model (equation 2.14) will be applied with a similar range of instantaneous precipitation values in simulations 5-8, assuming the average soil porosity value of $\eta = 0.50$ measured by Montgomery et al., [1997] at the CB-1 site. Figure 4.11 (a-d) illustrates the expansion of the "wetness" predicted by this model for values of p of *50*, *100*, *200*, and *400 mm*, respectively. As in the lateral model, these values represent an instantaneous addition of water to the water table, and thus are not comparable to actual precipitation rates. In contrast to the purely lateral model, here we see the expansion of the saturated areas initiating from topographically divergent areas, due to thinner soils present in these locations.

simulation #	log(q/k) []	p [mm]	C_{r0} [Pa]	j [m^{-1}]	phi [deg]	k [m/day]	ρ_s [kg/m^3]	ρ_w [kg/m^3]	α [m^{-1}]	ε [m/yr]	K [m^2/yr]	Sc []
1	-3.1	0	21,666	4.96	40	67	1,600	1,000	0.0003	0.000268	0.0032	1.25
2	-2.8	0	21,666	4.96	40	67	1,600	1,000	0.0003	0.000268	0.0032	1.25
3	-2.5	0	21,666	4.96	40	67	1,600	1,000	0.0003	0.000268	0.0032	1.25
4	-2.2	0	21,666	4.96	40	67	1,600	1,000	0.0003	0.000268	0.0032	1.25
5	-Infinity	50	21,666	4.96	40	67	1,600	1,000	0.0003	0.000268	0.0032	1.25
6	-Infinity	100	21,666	4.96	40	67	1,600	1,000	0.0003	0.000268	0.0032	1.25
7	-Infinity	200	21,666	4.96	40	67	1,600	1,000	0.0003	0.000268	0.0032	1.25
8	-Infinity	400	21,666	4.96	40	67	1,600	1,000	0.0003	0.000268	0.0032	1.25
9	-3.4	100	21,666	4.96	40	67	1,600	1,000	0.0003	0.000268	0.0032	1.25
10	-2.8	25	21,666	4.96	40	67	1,600	1,000	0.0003	0.000268	0.0032	1.25

Table 4.2. Parameters used in the simulations performed on the CB-MR site (described in section 4.3).

To compare the relative performance of these end-member hydrological models, the mixture model of equation 2.15 is also tested. In this case, the water table height is fixed at average value measured at CB-1 (figure 4.4), which for the assumed porosity $\eta = 0.50$ is equivalent to an instantaneous addition of *125 mm* of water. For simulations 9-10, two combinations of p and q are then chosen to match this total. In the first case (simulation 9) the vertical contribution (*100 mm*) is four times the lateral, while in the second case (simulation 10) the vertical contribution (*25 mm*) is a fourth of the lateral (figure 4.12). While p and q are not intended to represent actual

precipitation values, this exercise allows the exploration of simultaneous vertical and lateral contributions to the water table height. In both cases the fully saturated areas develop in the most convergent parts of the landscape, but the resulting spatial distribution of *h/z* differs significantly, particularly in thin-mantled divergent areas. This is because vertical flow increases the water table height in a spatially uniform manner, while the lateral flow is topographically steered.

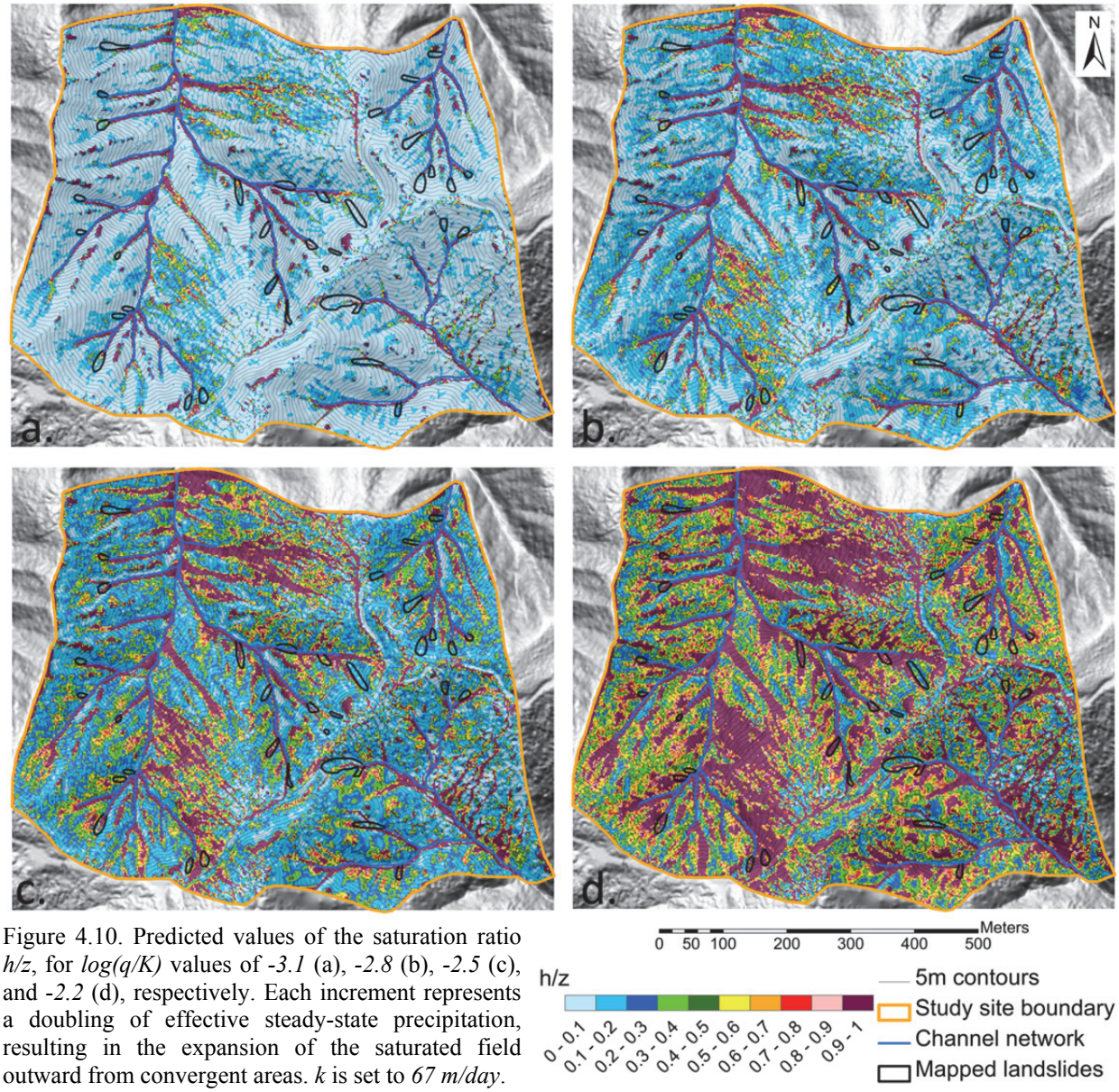

Figure 4.10. Predicted values of the saturation ratio *h/z*, for *log(q/K)* values of *-3.1* (a), *-2.8* (b), *-2.5* (c), and *-2.2* (d), respectively. Each increment represents a doubling of effective steady-state precipitation, resulting in the expansion of the saturated field outward from convergent areas. *k* is set to *67 m/day*.

Under the scenarios described, the procedure is applied on the *350* by *427 2*-meter resolution CB-MR DEM. As described in section 3.4.7, several options are available to reduce the problem size and thus increase computational performance. For the hardware described in section 3.4.6 a moving window size of *125* by *125* cell is used, and after each iteration the window is shifted in the *x* or *y* direction by *100* cells, resulting in a *25*-cell overlap and a total of *20* iterations. At each iteration the number of eigenvectors examined is set to 128, and thresholding is performed for each distinct eigenvector value. In each thresholding step a maximum of 25 regions are retained, resulting in a theoretical maximum number of examined regions of *1,000,000,000*

(*20*128*125*125*25*). While this appears to be a large number, it should be pointed out that it is less than 2^{30}, thus a critical reduction from the $2^{350*427}$ possible cell combinations.

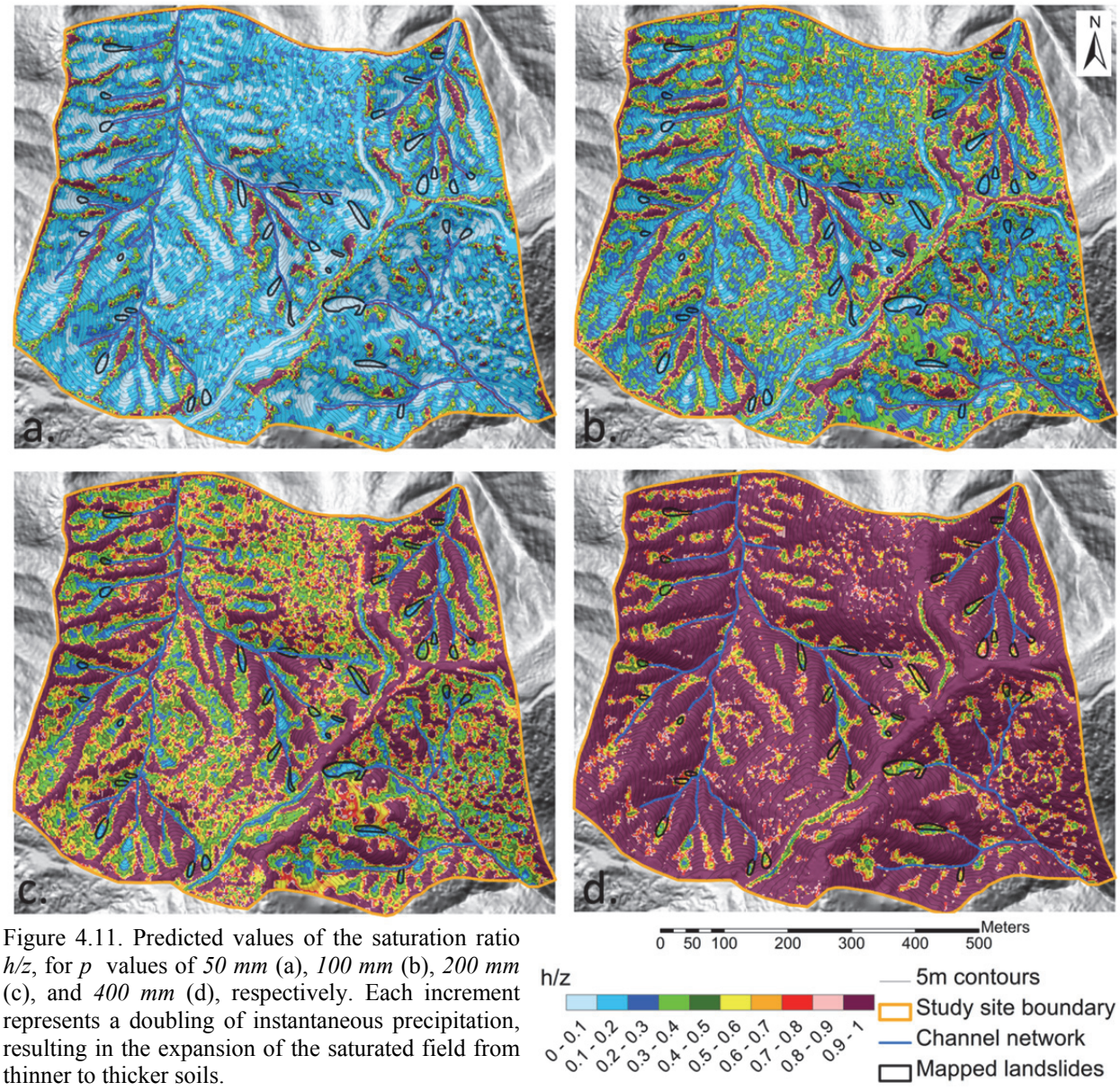

Figure 4.11. Predicted values of the saturation ratio *h/z*, for *p* values of *50 mm* (a), *100 mm* (b), *200 mm* (c), and *400 mm* (d), respectively. Each increment represents a doubling of instantaneous precipitation, resulting in the expansion of the saturated field from thinner to thicker soils.

4.4.2 Simulation results

In this section the results of simulations 1-10 are presented, separated according to the hydrologic model used.

4.4.2.1 Shallow sub-surface (lateral) flow simulations

Figure 4.13 (a-d) shows a map of shallow landslide predictions produced by the procedure in four steady-state shallow subsurface flow scenarios (simulations 1-4 in table 4.2). A few important observations can be made just from these maps. The first striking observation is that these predictions consist of *discrete* landslides having size, shape, and location comparable to the observations. As commonly observed, they are generally longer than they are wide, and their

number increases with increasing precipitation. More specifically, two things happen as precipitation increases: existing landslides become less stable, and new ones appear. The second observation is that a large number of landslides are predicted, and that many outcomes (i.e. overlapping predictions) are possible in all scenarios. The number of observed landslides captured by each simulation (*hits* or *true positives*) also increases with precipitation: some of the observed landslides are captured with a modest steady-state precipitation of *50 mm/day*, many are captured with *100 mm/day*, most are captured with *200 mm/day*, and virtually all are captured with *400 mm/day*. With the number of hits, the number of predicted landslides which are not supported by the 10-year record of observations also increases (*false positives*). We note that during the ten years of record it is unlikely that the soil was ever fully loaded or that precipitation was in fact in steady state. However, it can be remarked that the location and size of the false positives is consistent with the pattern of the true positives. Notwithstanding, for lack of better information all predictions which do not overlap with observations will be considered as false positives when assessing the performance of the procedure. The third observation is that landslides are predicted almost exclusively in convergent areas, where both soil and water tend to accumulate. In fact, predicted landslides rarely extend out of the thickest parts of the hollows, as would be suggested by the ten-year records for this location. These observations also suggest that the sub-models used in these simulations (and their parameterization) capture the essential characteristics of this landscape.

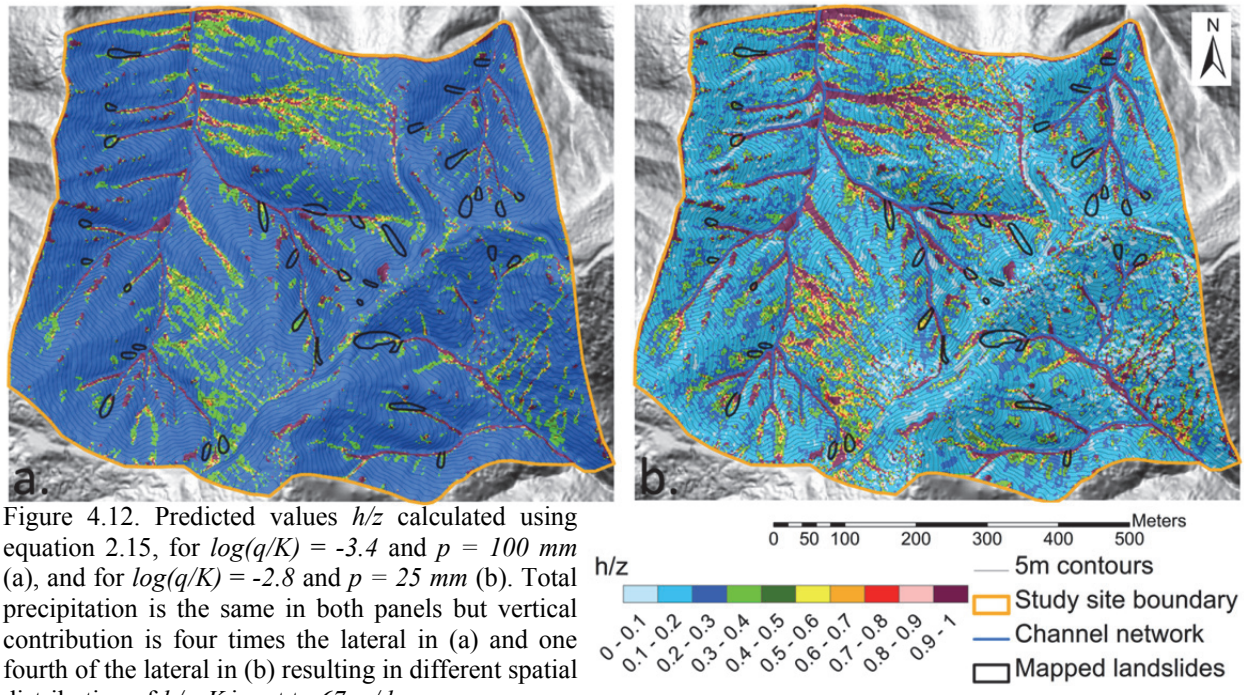

Figure 4.12. Predicted values *h/z* calculated using equation 2.15, for *log(q/K) = -3.4* and *p = 100 mm* (a), and for *log(q/K) = -2.8* and *p = 25 mm* (b). Total precipitation is the same in both panels but vertical contribution is four times the lateral in (a) and one fourth of the lateral in (b) resulting in different spatial distribution of *h/z*. *K* is set to *67 m/day*.

When specifically comparing the predicted size distributions (*probability density functions* or PDF's) to the observed size distribution (figure 4.14a), the results indicate that while the predicted PDF's resemble the observed, predicted size appears smaller than observed for these four steady-state precipitation scenarios. In fact, the *Kolmogorov-Smirnov* (K-S) test, which uses a measure of distance between the empirical *cumulative distribution functions* (CDF's, shown in figure 4.28 for all the simulations in this section) to determine if they may derive from the same distribution, confirms that only the PDF of the results of simulation 4 (*log(q/K) = -2.2*) belongs

to the same distribution as the observations (table 4.3). In similar experiments (presented in the next chapter), simulations with *log(q/K) =-1.9* to *-2.3* also produced size distributions which did not fail the K-S test. Figure 4.14a also shows that the PDF's shift to the right (towards larger sizes) with increasing precipitation, a topic that will be discussed in the next chapter.

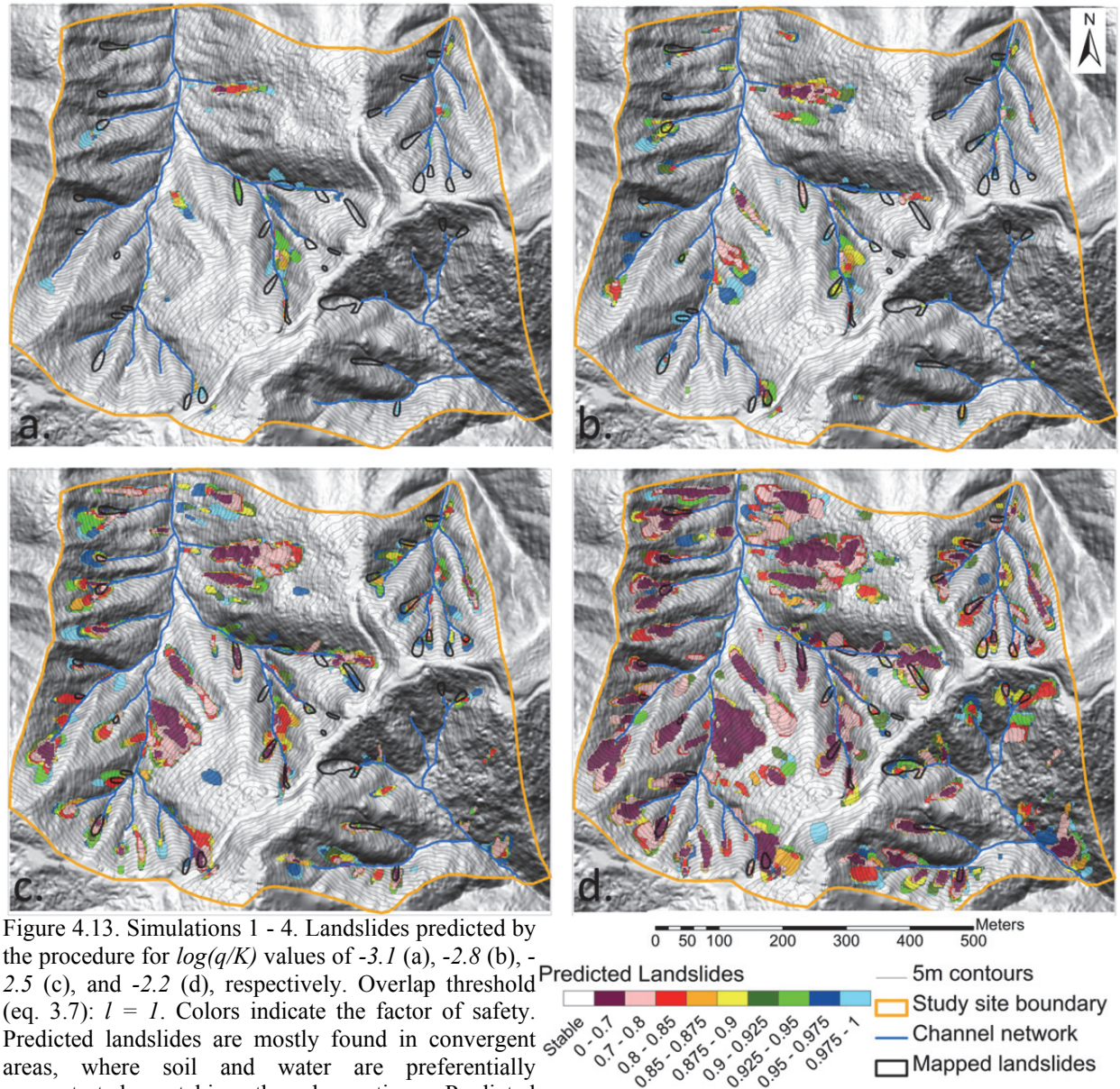

Figure 4.13. Simulations 1 - 4. Landslides predicted by the procedure for *log(q/K)* values of *-3.1* (a), *-2.8* (b), *-2.5* (c), and *-2.2* (d), respectively. Overlap threshold (eq. 3.7): *l = 1*. Colors indicate the factor of safety. Predicted landslides are mostly found in convergent areas, where soil and water are preferentially concentrated, matching the observations. Predicted size is generally smaller than observed.

The median *topographic index* $\boldsymbol{I_T}$ (equation 3.18) of a landslide is used in this study as a proxy for location. This index is essentially the ratio of drainage area and slope, thus a low index indicates landslide location to be in steep non-convergent areas, while a higher index places them further down the valley axis where drainage area increases and slope decreases. Figure 4.14b shows the PDF's of the median topographic index of landslides predicted in simulations 1-4 as well as of the observed distribution.

a.

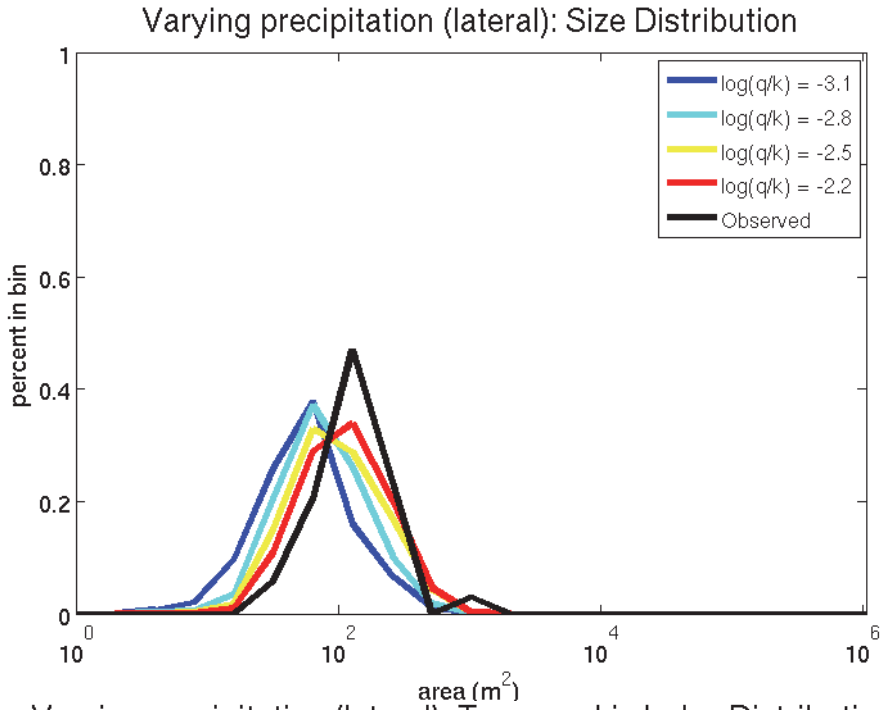

b.

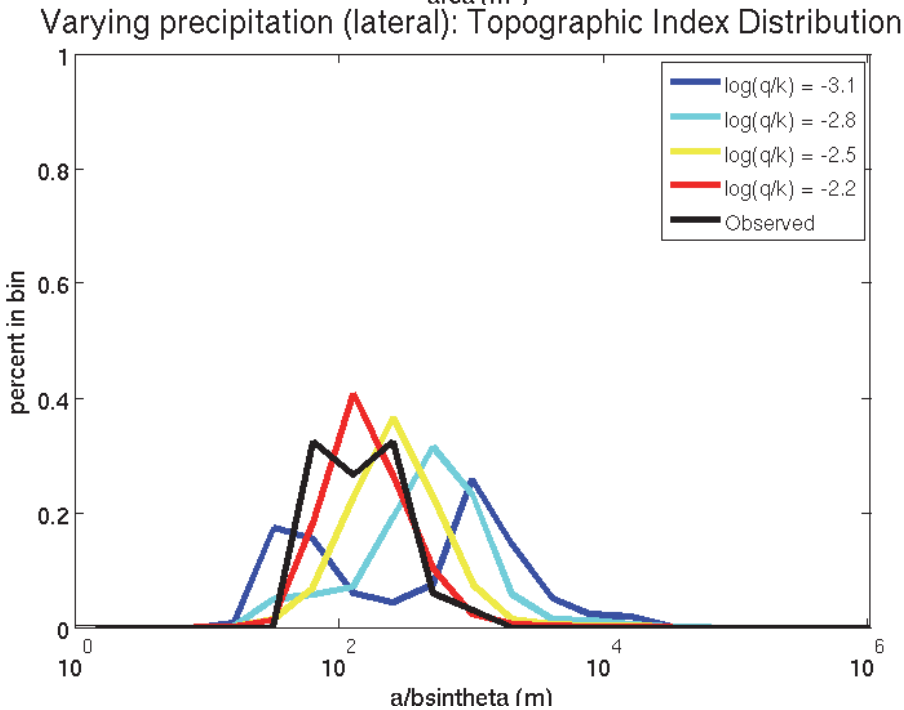

Figure 4.14. Simulations 1 - 4 distributions, for *log(q/K) = -3.1 to -2.2*, equivalent to *q = 50-400 mm/day*. a) Predicted size distributions resulting from the application of the procedure using the lateral hydrological model: as precipitation increases, the size distribution shifts to the right (larger size), until it matches the observations when *log(q/K) = -2.2*. b) Predicted topographic index distributions resulting from the application of the procedure using the lateral hydrological model: as precipitation increases, the size distribution goes from bi-modal (high slope or high area) to uni-modal, matching the observations when *log(q/K) = -2.2*.

As with size, the K-S test indicates that only the distribution resulting from simulation 4 belongs to the same distribution as the observations (table 4.3). This value is not unique, as in similar experiments (presented in the next chapter), simulations in which *log(q/K) = -2.1* to *-2.3*

also produced distributions which did not fail the K-S test. Figure 4.14b also reveals that with moderate precipitation, the distribution is bi-modal: landslides can either occur on steep slopes or in highly convergent areas. As precipitation increases the distribution tightens to match the observations with a single mode. These results will be discussed in greater detail in the following chapter.

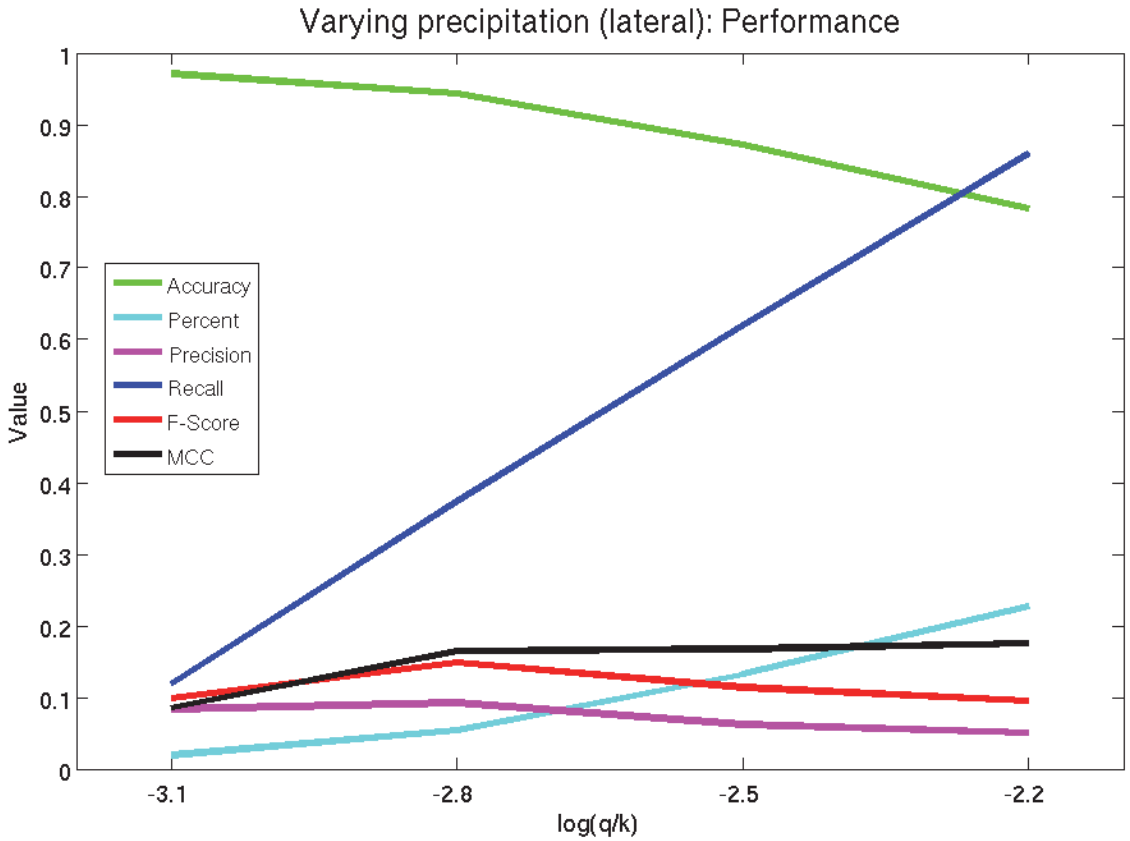

Figure 4.15. Simulations 1 - 4 performance measures. As precipitation increases, recall (dark blue) increases much faster than the percent landscape predicted unstable (light blue); at the same time accuracy (green) decreases, and after an initial slight increase precision (magenta) follows; the F-score (the harmonic mean of precision and recall, red) reaches a peak when $log(q/K) = -2.8$, at which point the MCC (the correlation between predicted and observed, black) only slightly continues to improve.

As a proxy for landslide shape, the *aspect ratio* is used here. It is defined as the ratio of the major and minor axes of the ellipse which best fits the shape of the landslide. For example, landslide which is twice as long as it is wide will have an aspect ratio of two, while a circular landslide will have an aspect ratio of 1. Figure 4.29 shows the PDF's and CDF's of aspect ratio for all the simulations presented in this chapter. The observed distribution has mean and median aspect ratios of 2.8 and 2.5, respectively. The mean aspect ratios for simulations 1-4 range from 1.9 to 2, while the median values range from 1.7 to 1.8. No discernible trends emerge, and no predicted distribution passes the K-S test. This signifies that while predicted landslides are indeed significantly longer than wide, they do not belong to the same statistical distribution. The distributions vary little with varying precipitation, and in fact they vary little in any of the simulations presented in this chapter, as shown in figure 4.29.

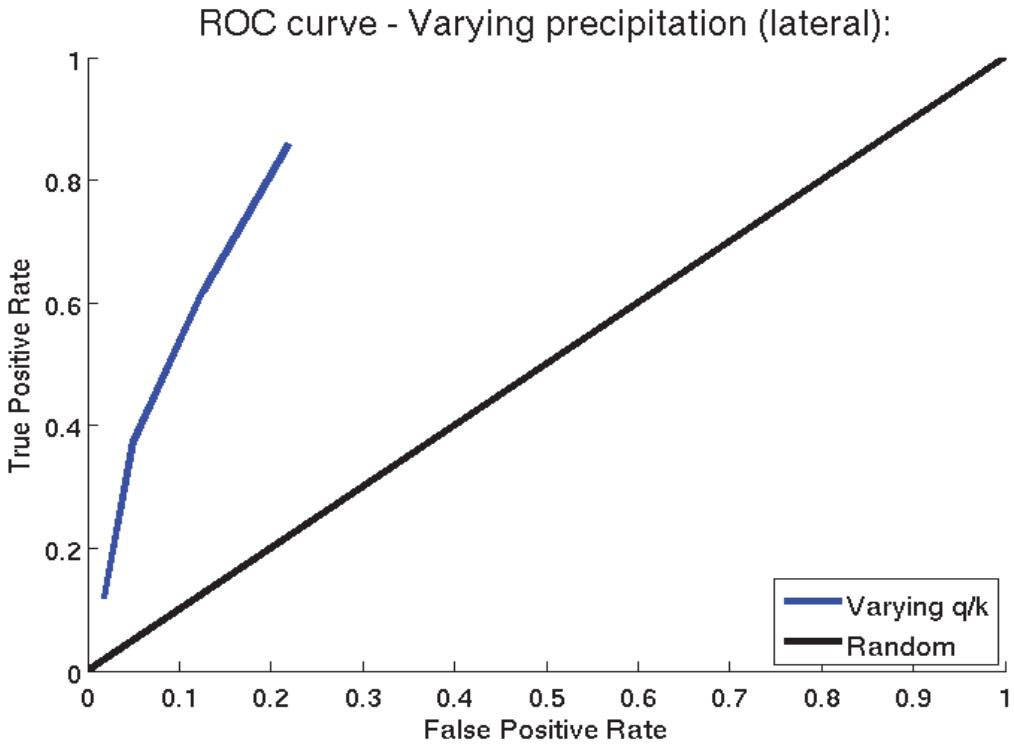

Figure 4.16. Simulations 1 - 4 ROC curve. A sharp contrast can be observed between modeled and random performance; peak true positive rates (TPR) of *86%* are obtained in correspondence of a false positive rate (FPR) of 22% when *log(q/K) = -2.2* (and recall is highest); in contrast the ratio of TPR to FPR is maximal when *log(q/K) = -2.8* (not the lowest recall rate).

In order to evaluate performance, several measured were defined in chapter 3, both at the grid cell (or pixel) scale as well as at the landslide scale. Figure 4.15 summarizes the pixel-scale measures for simulations 1-4. One can observe that *recall* (the probability that an observed landslide is predicted, equations 3.9 and 3.10) increases with increasing precipitation. After an initial increase, *precision* (the probability that a predicted landslide is observed, equations 3.9 and 3.10) decreases with increased precipitation. This is to be expected, as there is generally an inverse relationship between precision and recall [Van Rijsbergen, 1979]. However, the actual value of precision is never high. The probability of predicting an observed landslide cell never surpasses 10%. While certainly not a good result, this is somewhat misleading as the ratio of observed landslide cells to the entire landscape is extremely low. This effect is even more apparent with accuracy (the probability of a cell being correctly labeled, equations 3.8): with the least precipitation, very few landslides are predicted and thus accuracy is almost *100%*. The F-score, the harmonic mean of precision and recall (equation 3.13) reaches its peak of *15%* (of the maximum possible value of *1*) at a *log(q/K)* value of *-2.8*. The MCC measure (the correlation between observed and predicted classification values, equation 3.14) also has a sharp inflection at the same *log(q/K)* value, after which it stays stable around a value of *17%* (of the maximum possible value of *1*), i.e. the degree of correlation no longer improves, but neither declines. It should be noted that the MCC value never approaches zero nor it is ever negative, values typical for random predictions or anti-correlated predictions, respectively. It should also be noticed that with increasing precipitation the percentage of the landscape predicted to be unstable (labeled simply as *percent* in figure 4.15) increases. However, this increase is considerably slower than the increase in recall, suggesting the procedure can indeed discriminate between landslide pixels and non-landslide pixels. A summary of the results shown in figure 4.15 is given in table 4.4.

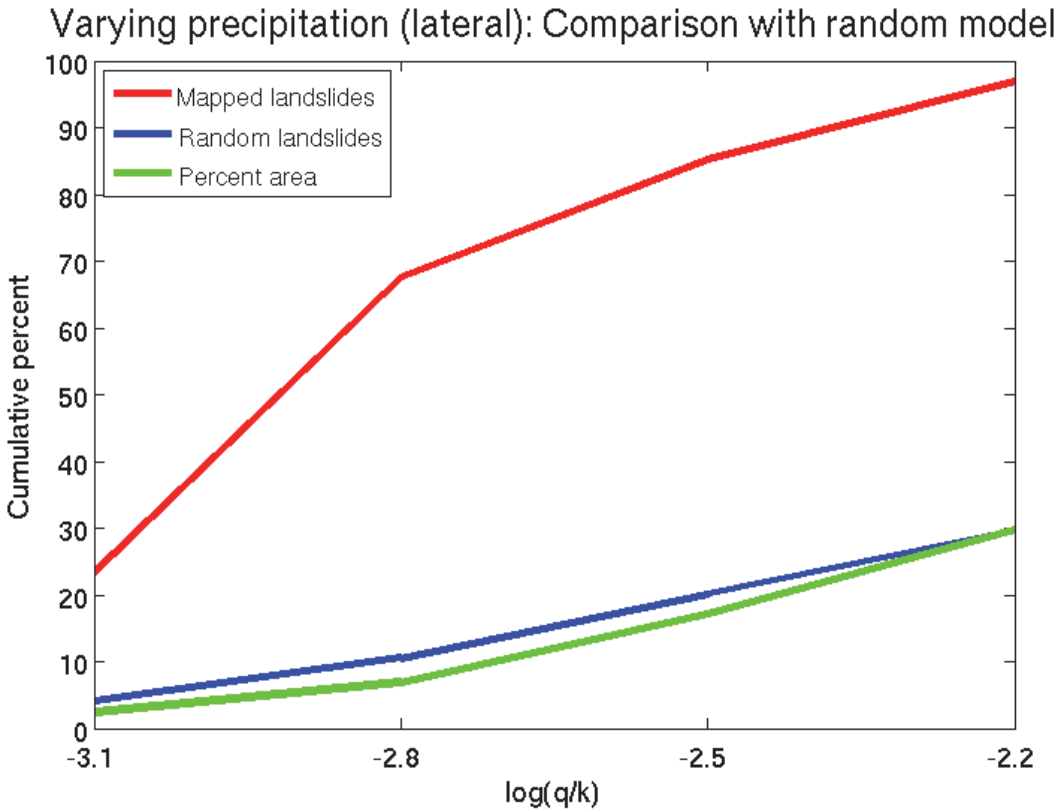

Figure 4.17. Simulations 1 - 4, comparison with random model and with percent landscape predicted unstable. The percent of captured observations (red) increases steadily and much faster than the percent of the landscape predicted as unstable (green); the ratio between the two is maximal when *log(q/K) = -2.8*; generally the random (non-mechanistic) blue curve increases at the same rate as the percent unstable green curve, illustrating the discriminatory capability of the mechanistic model.

The *receiver operating characteristic* (ROC) curve (the *true positive rate* plotted against the *false positive rate*, equation 3.11) is shown in figure 4.16. For these four simulations the procedures reaches a maximal true positive rate (TPR) of *86%*, at the price of a false positive rate (FPR) of *22%* (the theoretical optimum is a *100%* percent true positive rate with a *0%* false positive rate). A four-fold to almost seven-fold increase of TPR to FPR could be considered to be an excellent result, but as with the previous measures caution should be used because of the skew between landslide pixels and non-landslide pixels present in this dataset. Regardless, the sharp contrast between the predictions and random results (represented by the 1:1 line in figure 4.16) leave little doubt about the discriminatory power of the procedure. A summary of the results shown in figure 4.16 is given in table 4.4.

At the landslide scale (i.e. considering landslide predictions as a whole and not just landslide pixels), the null hypothesis that landslides do not behave according to the proposed mechanistic criteria defined in the previous chapters is tested (see section 3.4.5.2 for details). Figure 4.17 shows the percent of the observed landslides captured versus the percent of randomly distributed landslides sampled from the same size distribution, for simulations 1-4. There is a macroscopic divergence between the two plots, which allows the null hypothesis to be rejected. One can observe that while the two plots keep diverging, the divergence rate (the ratio of the slopes of the lines) reaches a peak at a *log(q/K)* value of *-2.8*. Very different trends can also be observed in the comparison to the percent of the landscape predicted to be unstable, also shown in figure 4.17.

This result also suggests the discriminatory power of the mechanistic assumptions adopted here. A summary of the results shown in figure 4.17 is given in table 4.4.

4.4.2.2 Vertical (non-topographically steered) flow simulations

Figure 4.18 (a-d) shows a map of shallow landslide predictions produced by the procedure in four instantaneous vertical flow scenarios (simulations 5-8 in table 4.2). Again, one can observe discrete predicted landslides having size and shape comparable to the observations, albeit somewhat larger. As in the previous set of simulations, they are generally longer than they are wide; their number increases with increasing precipitation, with landslides becoming less stable as new ones appear. A large number of landslides are predicted (with many overlapping predictions), indicating the many possible outcomes. The number of observed landslides captured by each simulation (*hits* or *true positives*) also increases with precipitation, but considerably fewer are hit for low and moderate precipitation values (*50 mm*, and *100 mm*), as compared to the lateral simulations. With the number of hits, the number of false positives also increases. Another important difference from the lateral simulations can be observed in the location of the predictions: while the majority predicted landslides are still in areas with some convergence (often aligned with the valley axes), they are located much further upslope. This is an intuitively satisfying finding, as upslope in the hollows the soils are thinner and thus preferentially saturated by the uniformly-distributed water table, yet thick enough to overcome the effects of cohesion and friction. Only when the precipitation becomes extreme (*400 mm*) does one observe a significant prediction population in more divergent areas where soils are generally extremely thin, resulting in a considerable increase of false positives. Although many observed landslides are captured with high precipitation (and all are captured with extreme precipitation), the spatial pattern of the predictions would suggest that vertically-dominated flow is less suited to capture the essential hydrologic characteristics of this landscape.

Figure 4.19a shows the size distributions resulting from these simulations. At low and moderate precipitation values the size is shifted to the left (smaller) than the observed distribution, while at high and extreme values it is shifted to the right (larger). None of the corresponding CDF's (shown in figure 4.28 for all the simulations in this section) come from the same distribution as the observed landslides, according to the K-S test (table 4.3). This does not imply that purely vertical flow never results in correct size predictions. In fact, in similar experiments (shown in the next chapter), simulations in which $p = 15$ and 17.5 *mm* (i.e. $h = 30$ and *35 mm*) produced a size distribution which did not fail the K-S test. However, the observed topographic index distribution associated with landsliding was never reproduced using solely vertical flow.

Figure 4.19b shows the PDF's of the median topographic index of landslides predicted in simulations 5-8 as well as of the observed distribution. As with size, the K-S test indicates that none of these distributions belong to the same distribution as the observations (table 4.3). Furthermore, in similar experiments with a wider range of p values than those presented in this chapter, no topographic index distribution was produced which passed the K-S test. The tightness of the distributions shown in figure 4.19b also supports the expectation that with a uniformly-distributed water table the range of locations where soils are thick enough to overcome cohesion and friction, yet thin enough to be highly saturated imposes a control on location. These controls will be explored in greater detail in the following chapter.

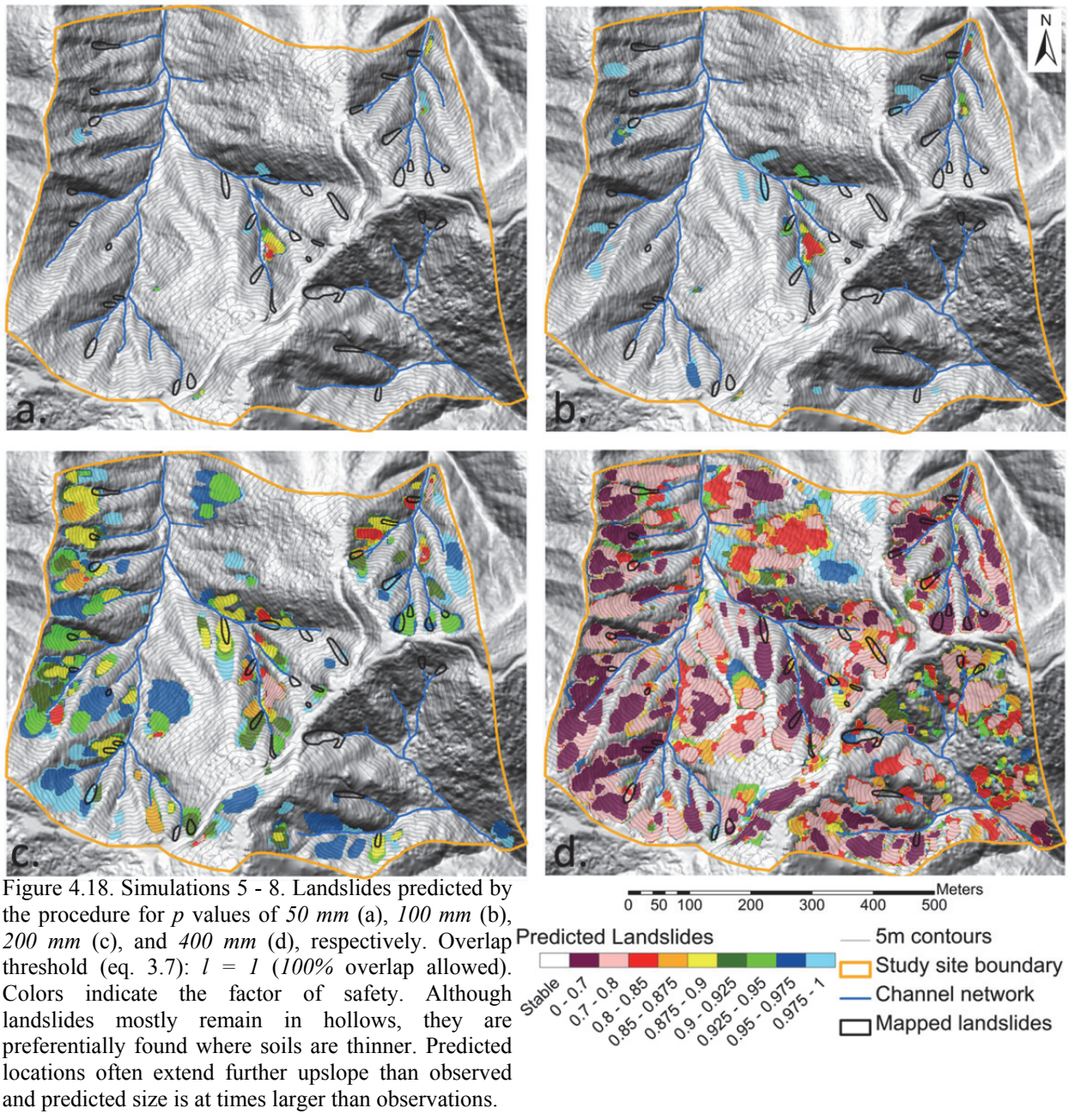

Figure 4.18. Simulations 5 - 8. Landslides predicted by the procedure for *p* values of *50 mm* (a), *100 mm* (b), *200 mm* (c), and *400 mm* (d), respectively. Overlap threshold (eq. 3.7): *l = 1* (*100%* overlap allowed). Colors indicate the factor of safety. Although landslides mostly remain in hollows, they are preferentially found where soils are thinner. Predicted locations often extend further upslope than observed and predicted size is at times larger than observations.

Figure 4.20 summarizes the pixel-scale measures for simulations 5-8. As in the lateral simulations, recall increases with increasing precipitation, and after an initial increase, precision decreases with increased precipitation. However, the precision value is always lower than in the previous simulations, reaching a maximum of *6%*. Similarly, the decline in accuracy with increased precipitation is considerably faster than in simulations 1-4. The maximum F-score and MCC values are also lower, at *8%* and *12%*, respectively. It should be noted that these two peaks occur at very different h values, suggesting that the MCC value is less sensitive to false positives than the F-score. The percentage of the landscape predicted to be unstable increases with precipitation, but reaches a much higher value than with the lateral model. Comparing this increase with the increase in recall suggesting the using this hydrological model the procedure

has more limited discriminatory capability, particularly with values of p greater than *200 mm* ($h > 400\ mm$). A summary of the results shown in figure 4.20 is given in table 4.4.

a.

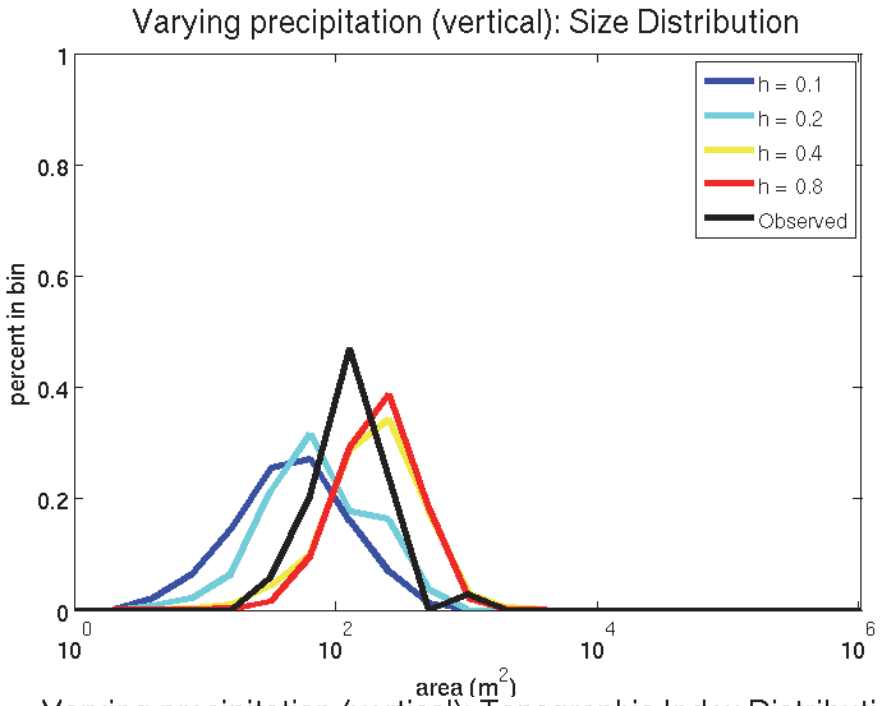

b.

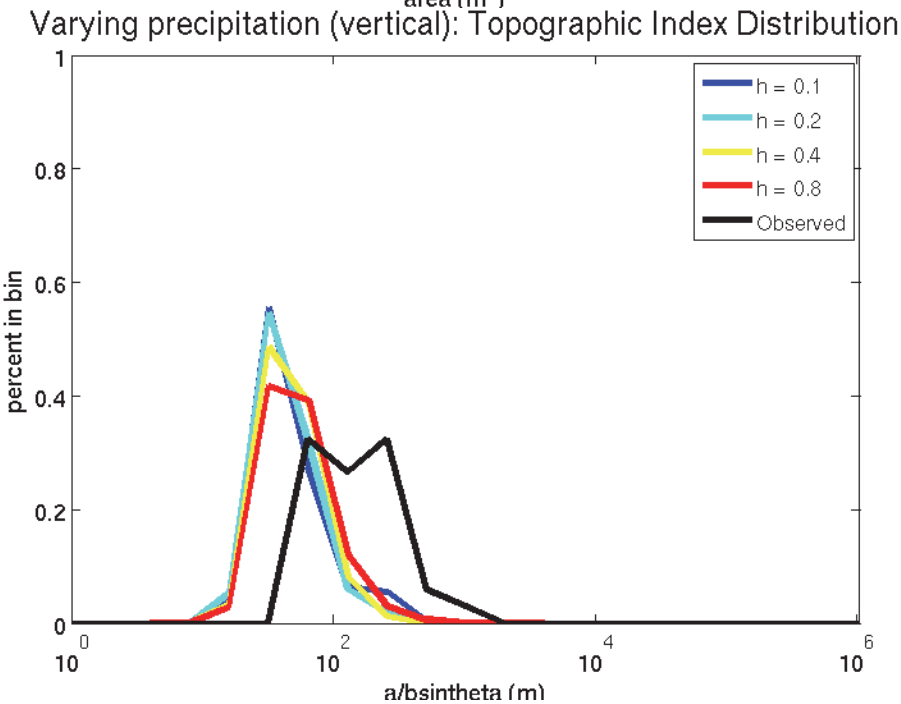

Figure 4.19. Simulations 5 - 8 distributions, for $h = 0.1$ to $0.8\ m$, equivalent to $p = 50$ to $400\ mm$. a) Predicted size distributions resulting from the application of the procedure using the vertical hydrological model: as precipitation increases, the size distribution shifts to the right (larger size), until it reaches a maximum when $h = 0.8\ m$; size is at first smaller, then larger than observations; intermediate distributions with $h = 0.3\ m$ and $h = 0.35\ m$ (shown in chapter 5) do match the observations. b) Predicted topographic index distributions resulting from the application of the procedure using the vertical hydrological model: as precipitation increases, the topographic index distribution slightly shifts to the right (less slope, more area), until it reaches a maximum when $h = 0.8\ m$, well to the left of observations which are never reproduced.

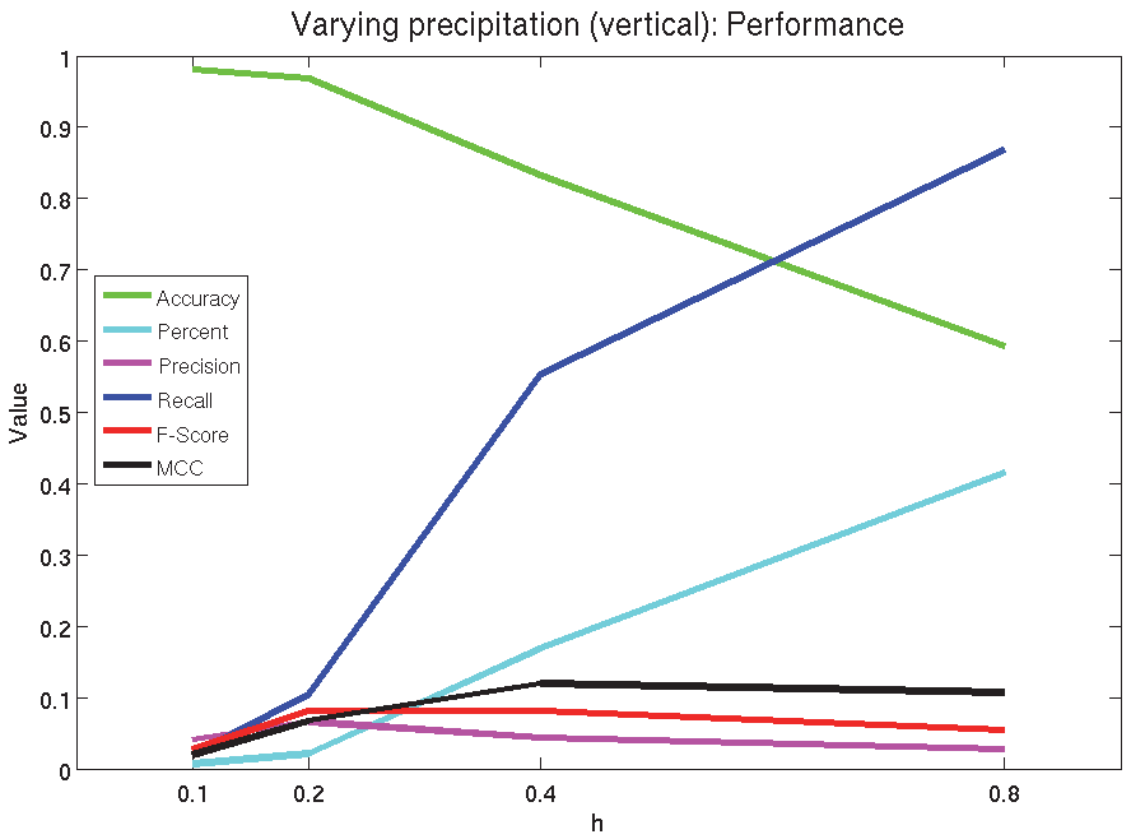

Figure 4.20. Simulations 5 - 8 performance measures. As precipitation increases, recall (dark blue) increases much faster than the percent landscape predicted unstable (light blue) until $h = 0.4\ m$, then increases at a similar rate; at the same time accuracy (green) decreases, and after an initial increase precision (magenta) follows; the F-score (red) reaches a peak when $h = 0.2\ m$, while the MCC (black) is maximal when $h = 0.4\ m$.

The *receiver operating characteristic* (ROC) curve for simulations 5-8 is shown in figure 4.21. The maximum true positive rate is just higher than for simulations 1-4 (*87%*), but at the cost of a much higher false positive rate (41%). All four simulations produce ROC values that are closer to the 1:1 line. A similar performance decrease with respect to simulations 1-4 can be observed at the landslide scale in figure 4.22: while the percent of the observations captured can be higher (and reach *100%* in the extreme precipitation case), this is at the cost of a much higher percent of the landscape being predicted as unstable. In fact the percent captured and percent unstable lines no longer diverge when p is greater than *200 mm*. Classification is better than if the null hypothesis were adopted, but direct comparison between the two simulation groups using the randomly generated datasets is less meaningful, as a new random dataset is generated for each simulation. A summary of the results shown in figure 4.21 and 4.22 is given in table 4.4.

4.4.2.3 Mixed topographically steered (lateral) and vertical flow simulations

Figure 4.23 (a-b) shows a map of shallow landslide predictions produced by the procedure using two different combinations of both hydrologic models (simulations 9-10 in table 4.2). The total effective precipitation is held constant but in 4.23a vertical contribution is four times the lateral, while in 4.23b the vertical contribution is a fourth of the lateral. No attempt was made to find optimal combinations of the two models, nor should the chosen precipitation rates be compared to actual storm scenarios.

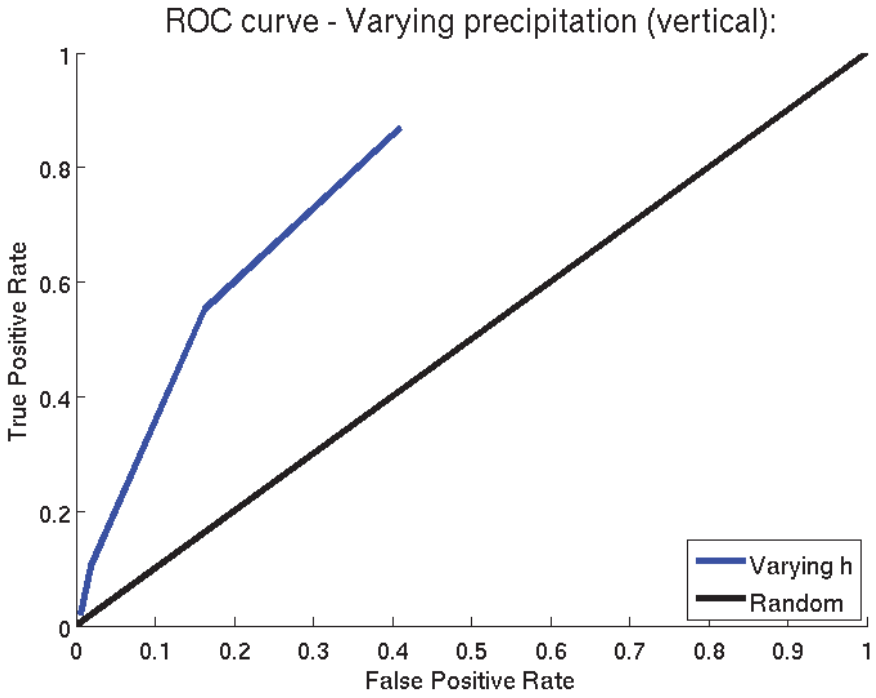

Figure 4.21. Simulations 5 - 8 ROC curve. A contrast can be observed between modeled and random performance, although significantly less than for simulations 1-4 (figure 4.16); peak true positive rates (TPR) of *86.8%* are obtained in correspondence of a false positive rate (FPR) of 41% when $h = 0.8$ (and recall is highest); in contrast the ratio of TPR to FPR is maximal when $h = 0.1$ (and recall is lowest).

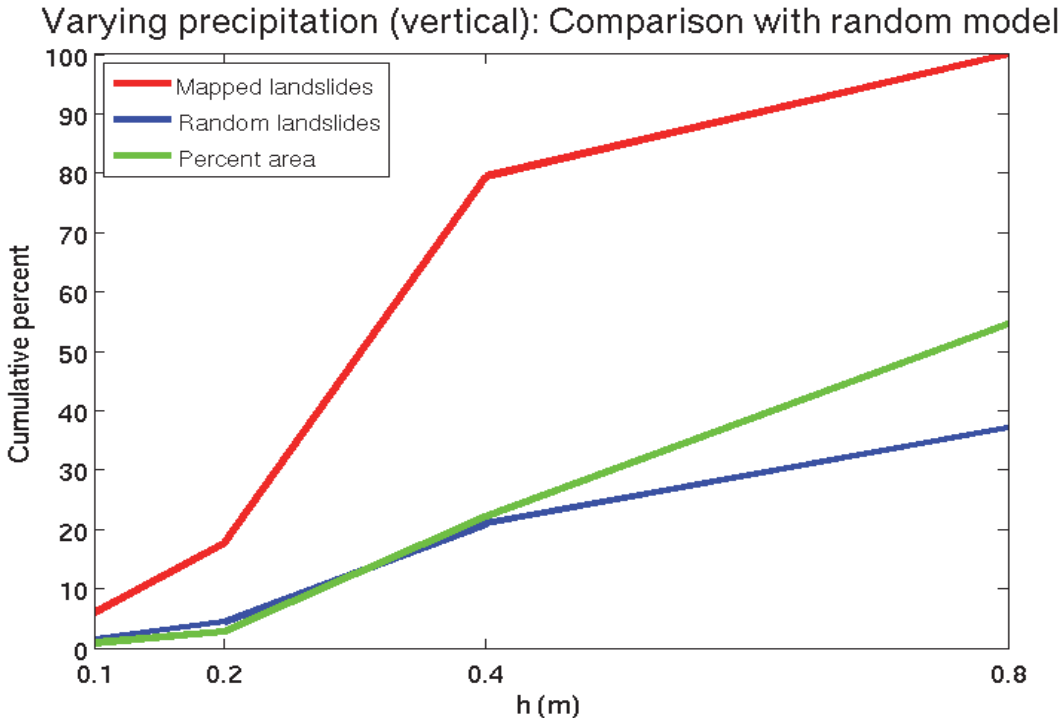

Figure 4.22. Simulations 5-8, comparison with random model and with percent landscape predicted unstable: the percent of captured observations (red) increases most rapidly and much faster than the percent of the landscape predicted as unstable (green) until $h = 0.4$ *m*, then increases at a lesser rate; the ratio between the two is maximal when $h = 0.1$ *m* (and recall is lowest); generally the random (non-mechanistic) blue curve increases at a rate consistent with percent predicted unstable green curve, illustrating the discriminatory capability of the mechanistic model even in decreased performance scenarios.

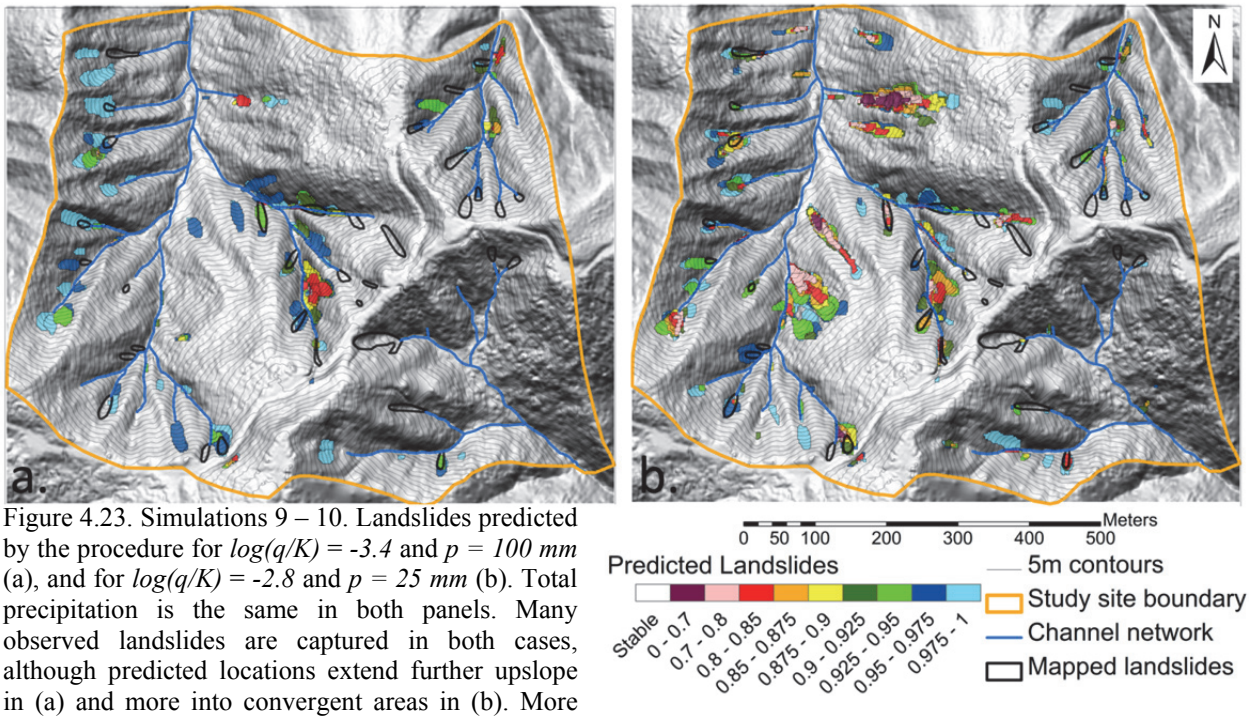

Figure 4.23. Simulations 9 – 10. Landslides predicted by the procedure for *log(q/K) = -3.4* and *p = 100 mm* (a), and for *log(q/K) = -2.8* and *p = 25 mm* (b). Total precipitation is the same in both panels. Many observed landslides are captured in both cases, although predicted locations extend further upslope in (a) and more into convergent areas in (b). More observed landslides are captured in (b).

The results shown here are meant to be merely an indication of how performance may vary with different characterizations of the hydrology where both simultaneous vertical and lateral additions contribute to the water table height. In both panels the discrete predicted landslides have size and shape comparable to the observations, capturing many of the observed landslides. There are many similarities between the two maps, but there are also a few noticeable differences. When vertical flow dominates and thus the water table is more spatially uniform, predicted landslides are located further upslope, often appearing disconnected from the channel network. This is rarely the case when the subsurface flow is mostly topographically steered, as in the case where the lateral model dominates. In this case a greater number of overlapping predictions is also observed, illustrating the wider range of convergent locations where landsliding is likely to happen. Principally as a result of this difference in preferred predicted locations, more observed landslides are captured when using the topographically-steered model.

The size distributions resulting from these simulations are shown in figure 4.24a. While the two distributions are not strikingly different, the vertically-dominated simulation exhibits in slightly "fatter" distribution with wider tails and a larger mean than the laterally-dominated one. In contrast, the topographic index distributions shown in figure 4.24b are almost symmetrical (with the vertically-dominated being centered upslope and the topographically-steered being focused in higher drainage areas), suggesting that a different mixture of vertical and lateral contributions. None of the distributions resulting from the two mixtures pass the K-S test (table 4.3), and the difference in the CDF's is illustrated in figure 4.28.

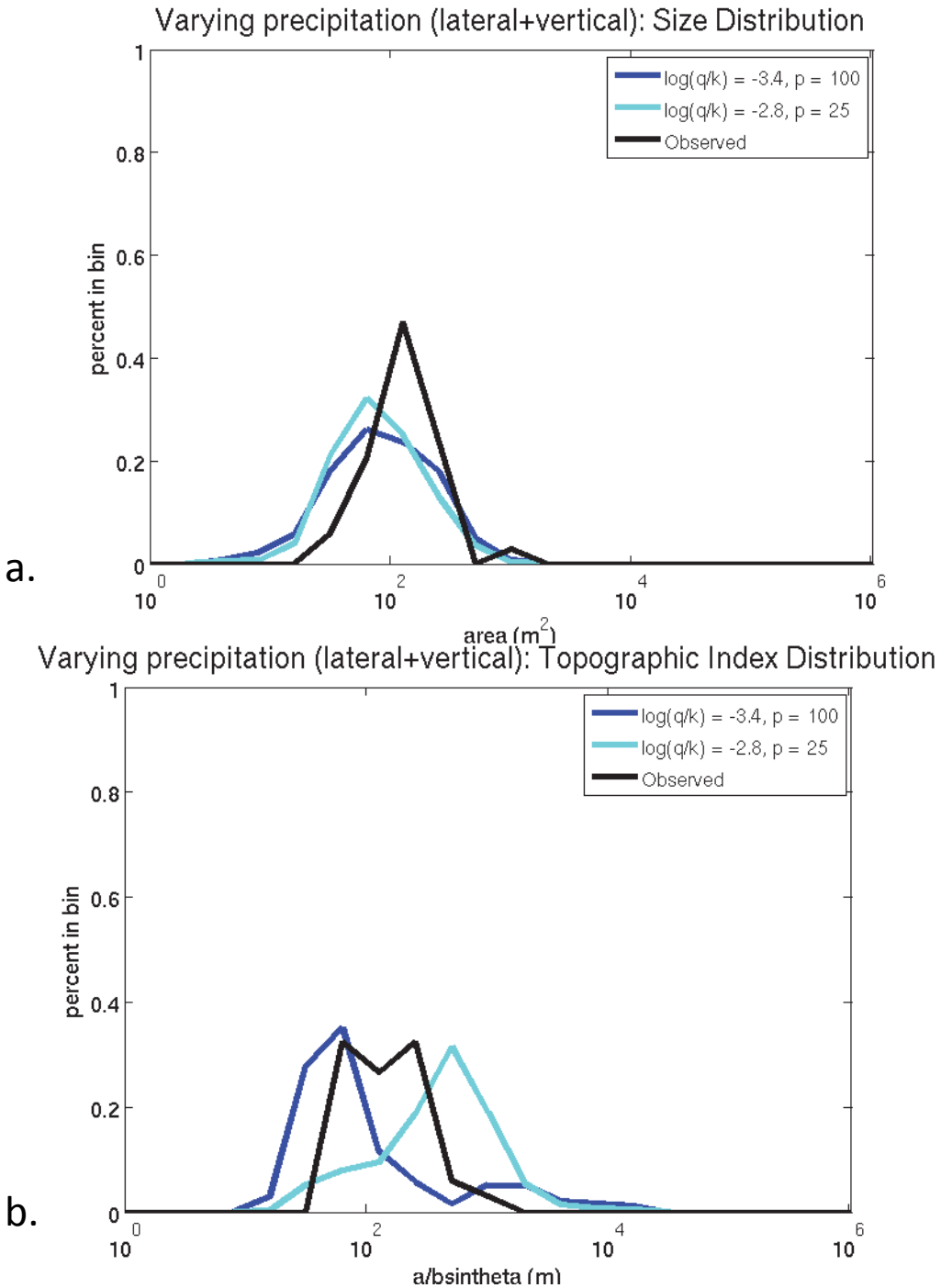

Figure 4.24. Simulations 9 - 10 distributions for *log(q/K) = -3.4* and *p = 100 mm*, and for *log(q/K) = -2.8* and *p = 25 mm*, resulting in similar total precipitation (*~125 mm*) from a different combination of the lateral and vertical hydrological models. a) Size distribution: increased relative vertical contribution slightly increases size and similarity to observations. b) Topographic index distribution: increased relative vertical contribution shifts location towards steep areas while increased relative lateral contribution shifts locations towards higher drainage areas. Observed landslide distribution lies in between the two distributions.

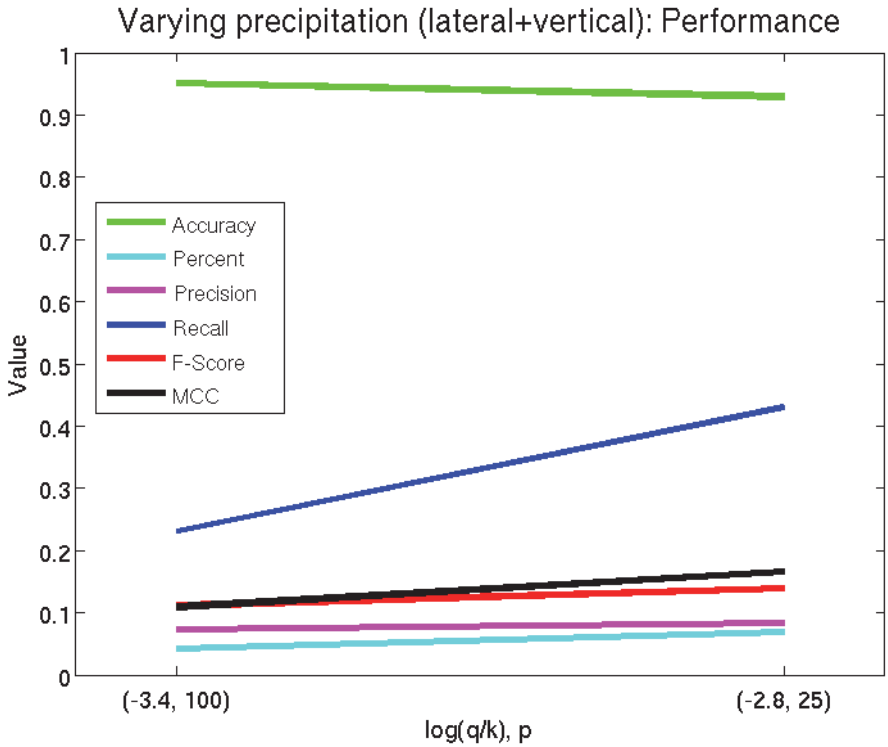

Figure 4.25. Simulations 9 - 10 performance measures. As relative lateral contribution increases, recall (dark blue) increases significantly and much faster than the percent landscape predicted unstable (light blue); at the same time accuracy (green) decreases, but precision (magenta) slightly increases; both the F-score (red) and the MCC (black) improve with increased relative lateral contribution.

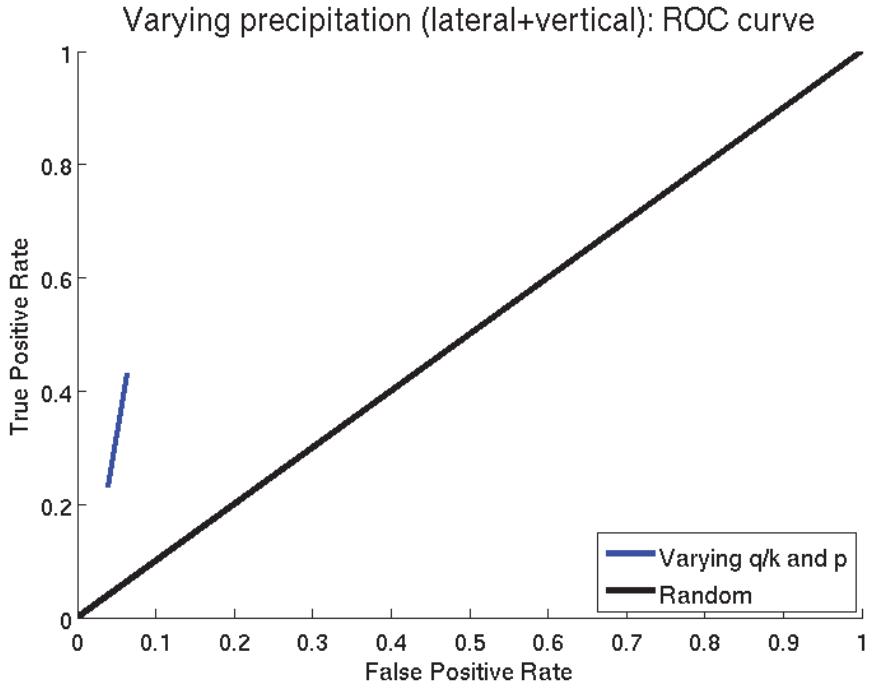

Figure 4.26. Simulations 9 - 10 ROC curve. A clear distinction can be observed between modeled and random performance; peak true positive rates (TPR) of *43.7%* are obtained in correspondence of a false positive rate (FPR) of *6.4%* when $log(q/K) = -2.8$ and $p = 25$ *mm* (when the relative lateral contribution is greater); the ratio of TPR to FPR is also maximal in this case, indicating a better performance with respect to the vertically-dominated case.

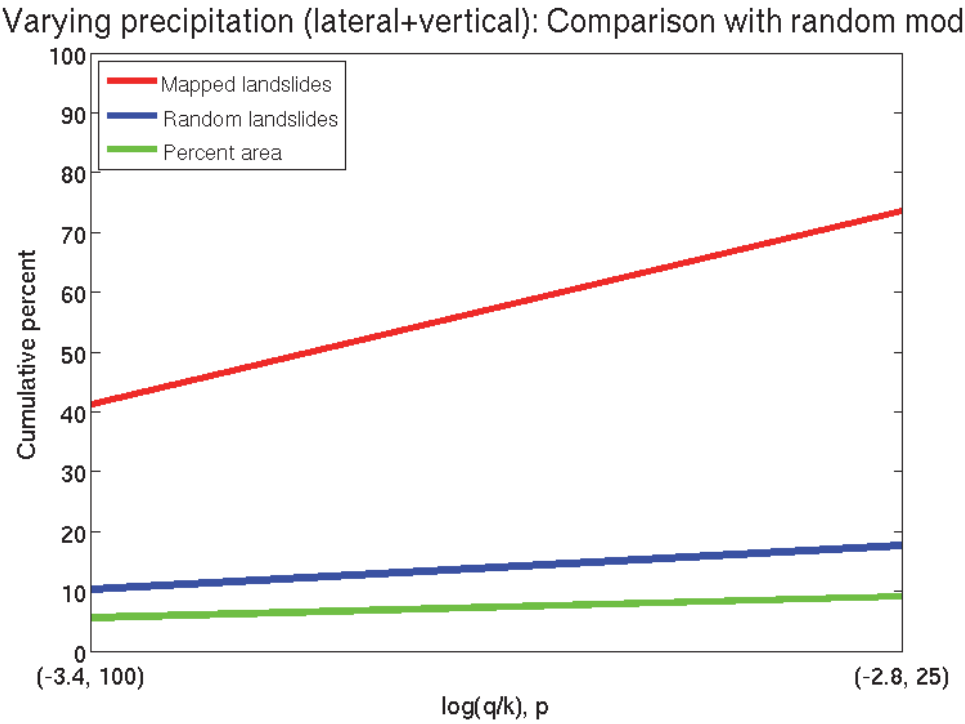

Figure 4.27. Simulations 9 - 10, comparison with random model and with percent landscape predicted unstable: the percent of captured observations (red) is significantly higher when the relative lateral contribution is greater (*log(q/K) = -2.8* and *p = 25 mm*); while in this case the percent of the landscape predicted as unstable (green) is slightly higher, the ratio between the two is maximal; the improvement of the laterally-dominated case when compared to the random (non-mechanistic) blue curve is also apparent, illustrating the improved performance with respect to the vertically-dominated case.

simulation #	K-S Test (size)	K-S Test (top. Ind.)	K-S Test (aspect)
1	fail	fail	fail
2	fail	fail	fail
3	fail	fail	fail
4	pass	pass	fail
5	fail	fail	fail
6	fail	fail	fail
7	fail	fail	fail
8	fail	fail	fail
9	fail	fail	fail
10	fail	fail	fail

Table 4.3. Kolmogorov-Smirnov (K-S) test results for simulations 1-10. Only the size and topographic index distributions resulting from the application of the shallow sub-surface flow hydrologic model (with *log(q/K) = -2.2*) pass the K-S test. Among results that will be shown in chapter 5, simulations using the lateral hydrologic model with *log(q/K) = -2.1 to -2.3* result in size and topographic index distributions which pass the K-S test, while simulations with *log(q/K) = -1.9* only pass the test for the size distribution. Similarly, simulations using the vertical hydrologic model with *p = 15* and *17.5 mm* result in size (but not topographic index) distributions which pass the K-S test. This indicates that several different parameterizations can reproduce observed size and location distributions. However, the aspect ratio is never reproduced.

Simulation number	Recall	Precision	Accuracy	F-score	MCC	TPR	FPR	Percent landscape (pixel)	Percent captured (model)	Percent captured (random)	Percent landscape (landslide)
1	11.9 %	8.5 %	97.1 %	9.8 %	8.5 %	11.9 %	1.8 %	1.9 %	23.5 %	4.4 %	2.5 %
2	37.4 %	9.2 %	94.3 %	14.9 %	16.5 %	37.4 %	4.9 %	5.4 %	67.7 %	12.6 %	7.0 %
3	61.9 %	6.2 %	87.1 %	11.3 %	16.7 %	61.9 %	12.5 %	13.2 %	85.3 %	22.7 %	17.3 %
4	85.9 %	5.0 %	78.2 %	9.5 %	17.5 %	85.9 %	21.9 %	22.7 %	97.1 %	30.9 %	29.9 %
5	2.0 %	4.0 %	98.1 %	2.6 %	1.9 %	2.0 %	0.6 %	0.6 %	5.9 %	1.5 %	0.8 %
6	10.4 %	6.6 %	96.8 %	8.0 %	6.7 %	10.4 %	2 %	2.1 %	17.6 %	4.4 %	2.8 %
7	55.3 %	4.4 %	83.3 %	8.1 %	11.9 %	55.3 %	16.3 %	16.8 %	79.4 %	20.9 %	22.1 %
8	86.8 %	2.8 %	59.4 %	5.4 %	10.6 %	86.8 %	41.0 %	41.6 %	100 %	37.1 %	54.6 %
9	23.1 %	7.3 %	95.1 %	11.1 %	10.9 %	23.1 %	3.9 %	4.2 %	42.2 %	10.3 %	5.5 %
10	43.7 %	8.3 %	92.9 %	13.9 %	16.6 %	43.7 %	6.4 %	6.9 %	73.5 %	17.6 %	9.1 %

Table 4.4. Summary of performance measures for simulations 1 to 10.

In terms of performance, the topographically-dominated simulations surpass the vertically-dominated in every measure (figure 4.25) with the exception of accuracy which shows a slight decrease possibly due to the increased recall (accuracy decreases with increased recall in every simulation shown in this chapter). The performance advantages of the topographically-dominated case are also visible in the ROC statistic, in which the increase of the TPR is not matched by a similar increase of the FPR (figure 4.26). An even greater difference is evident in the landslide-scale comparison, in which a significantly greater percent of observations are captured by the topographically-dominated simulation with only a slight increase of the percent of unstable landscape being predicted (figure 4.27). The topographically-dominated model also shows a much better performance when compared to the random null hypothesis. A summary of all the performance measures is given in table 4.4.

It is not clear, based on the results summarized in table 4.4, whether for this type of landscape a mixed model dominated by topographically-steered hydrology but with an added vertical component (simulation 10) performs better than a pure shallow subsurface flow (with simulation 2 being the most similar in terms of total precipitation). In contrast adding some topographically-steered flow to a vertically dominated hydrology (simulation 9) does show a clear improvement over the purely vertical case (here simulation 6 is the closest analogue in terms of total precipitation). While only two mixtures of relative lateral and vertical contributions were presented here, a continuum of mixtures will be explored in the next chapter.

4.4.3 Internal validation

Shown in figure 4.30 are the discrete and the continuous cost function values for simulation 2. The former, shown in blue, are the result of evaluating equation 3.4 using the predicted landslides as the indicator vector $\boldsymbol{x}$. The latter, shown in red, are the result of evaluating equation 3.4 using the transformed eigenvector $\boldsymbol{x}^*$ for the first *128* eigenvalues of equation 3.6. The discrete indicator vector $\boldsymbol{x}$ is a binary representation of the unstable shapes, while the continuous indicator vector $\boldsymbol{x}^*$ could be thought of as the fractional contribution of each grid cell to the theoretical unstable shapes (see section 3.4.3). As discussed in sections 3.4.1 and 3.4.4, to make the search problem tractable only the magnitude is encoded in the matrix representation of the driving forces. While the values plotted in figure 4.30 are closely related to the factor of safety, in fact they will always be slight under-estimates. This is corrected during the thresholding process (section 3.4.4) by individually evaluating the true factor of safety for each of the

predicted shapes. Here we wish to compare the discrete and continuous solutions of equations 3.4 and 3.5 in a consistent manner, and thus the values resulting from the matrix product are used.

One can observe that all the requirements outlined in section 3.4.5.1 are met:

- All the discrete solutions plot below the $\boldsymbol{y = 1}$ line (in fact they plot slightly lower as they are under-estimates).
- All discrete solutions plot close to the real-valued solutions. The difference between the two is largest for the first (optimal) eigenvector number, and it reduces as the eigenvector number increases.
- No discrete solution plots below the first (left-most) real-valued solution. In fact, no solution plots below the first real-valued solution, supporting its optimality.
- As the eigenvector number increases, the discrete solutions approach, and often surpass, the real-valued solutions. As discussed in section 3.4.5.1, the discrete solutions are not subject to the same orthogonality constraints as the eigenvectors defined by a linear system.

The same observations have been made for all the simulations presented in this chapter, but are not shown here for succinctness. As part of model development and testing similar plots have been generated for a diverse range of conditions, and violations to the above requirements have never been encountered. The software implementing the procedure contains many consistency checks throughout the code (e.g. alerts are generated for non-symmetric matrices, division by zero, complex numbers, etc.). In particular, all the final (matrix-derived) results are re-computed by an independent module on a pixel by pixel basis, and the results are both written to file and output to screen. This guarantees error-free operation in a manner equivalent to "hand-checking" the results.

4.5 Discussion

The application of the procedure under the conditions measured during the November 1996 storm event, resulted in a predicted failure at the same location and of similar size as landslide which occurred at the site during the storm. While this is an excellent result, it should be noted that topographic constraints of the site imply that if something can fail, it will be inevitably centered on or around the maximal values of pore pressure and soil depth. In other words, location alone is not a very strict test. More telling is perhaps the combination of size and factor of safety results. There were no free parameters in this application, as soil depth, pore pressure, root strength, and soil friction angle were measured. However, a choice was made to model the decline of root strength with depth, rather than to treat the measured value as uniform. While this treatment resulted directly from the published data, one could imagine that uniform values would lead to higher strength of the material and thus a higher factor of safety. Consequently, either a much larger size would fail, or none at all, highlighting the good performance of the procedure.

The predicted landslide has an area that is 9 m^2 larger than the observed failure, extending a couple of meters further upslope. This is likely due to the small-scale parameter variations that exist in natural landscapes which cannot be captured even in a site as well studied as CB-1. In particular, we note that the spatial arrangement of the piezometer nests used to measure the pore pressure values (figure 4.4) will inevitably result in the extension upslope of the highest values (the peak measurement is straddling the upslope border of the landslide and no other piezometers are in the immediate vicinity to constrain the pore pressure field). Notwithstanding, the reader is

again reminded that the procedure involves a variety of simplifications and relies on an approximation method, and thus can never guarantee a perfect result. It should also be remarked that the CB-1 landslide (both observed and predicted) precisely straddles the area of high pore pressure and thicker soils. This lends support to the hypothesis that the co-organization of these parameters controls the size of shallow landslides, and suggests that our procedure localizes favorable areas well.

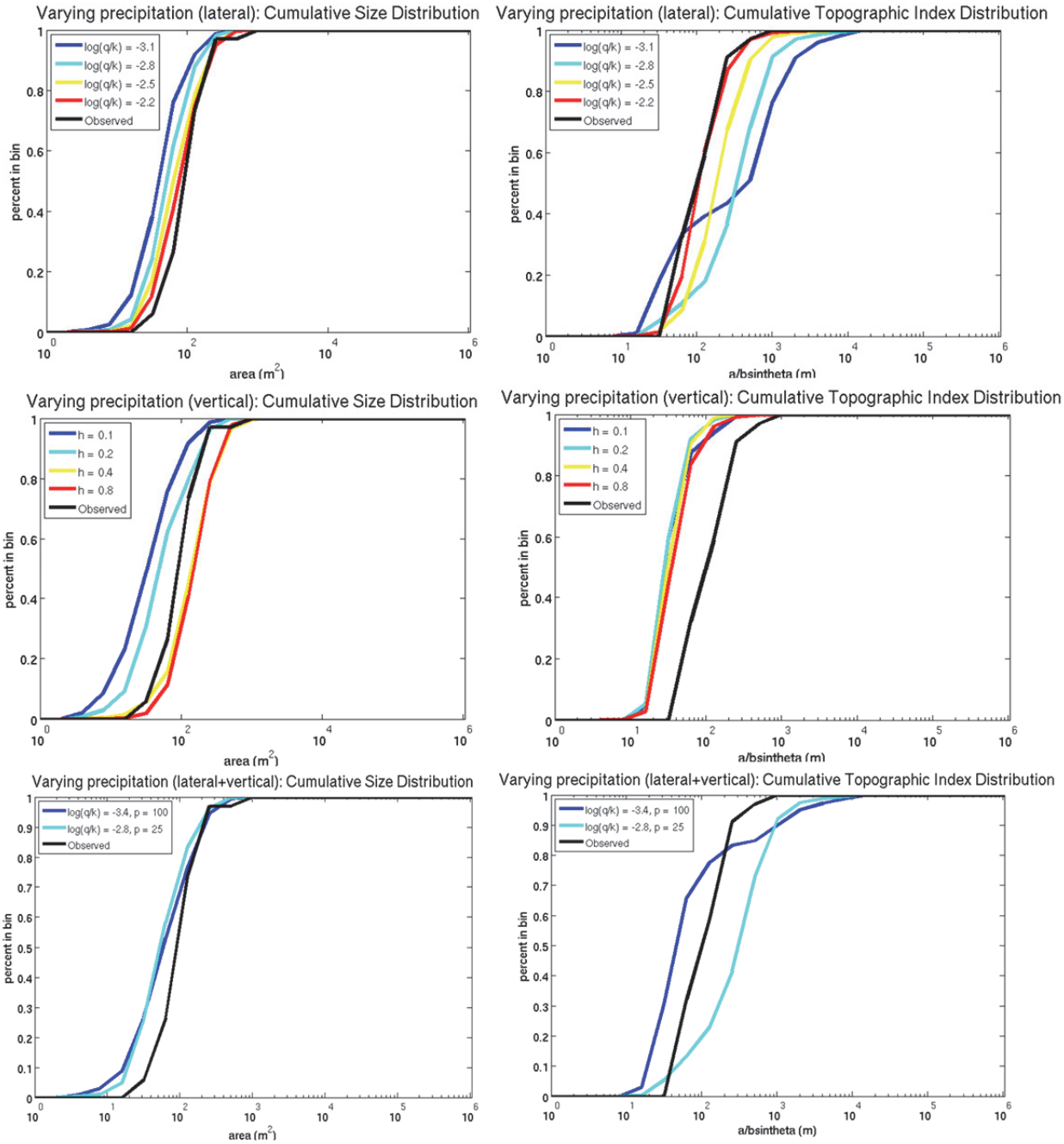

Figure 4.28. Simulations 1 - 10 CDF's. Size and topographic index distributions for all ten simulations. The distributions for *log(q/K) = -2.2* (top row, red lines) appear visually similar to the observations and in fact pass the K-S test. All other distributions appear visually dissimilar to the observations and in fact fail the K-S test.

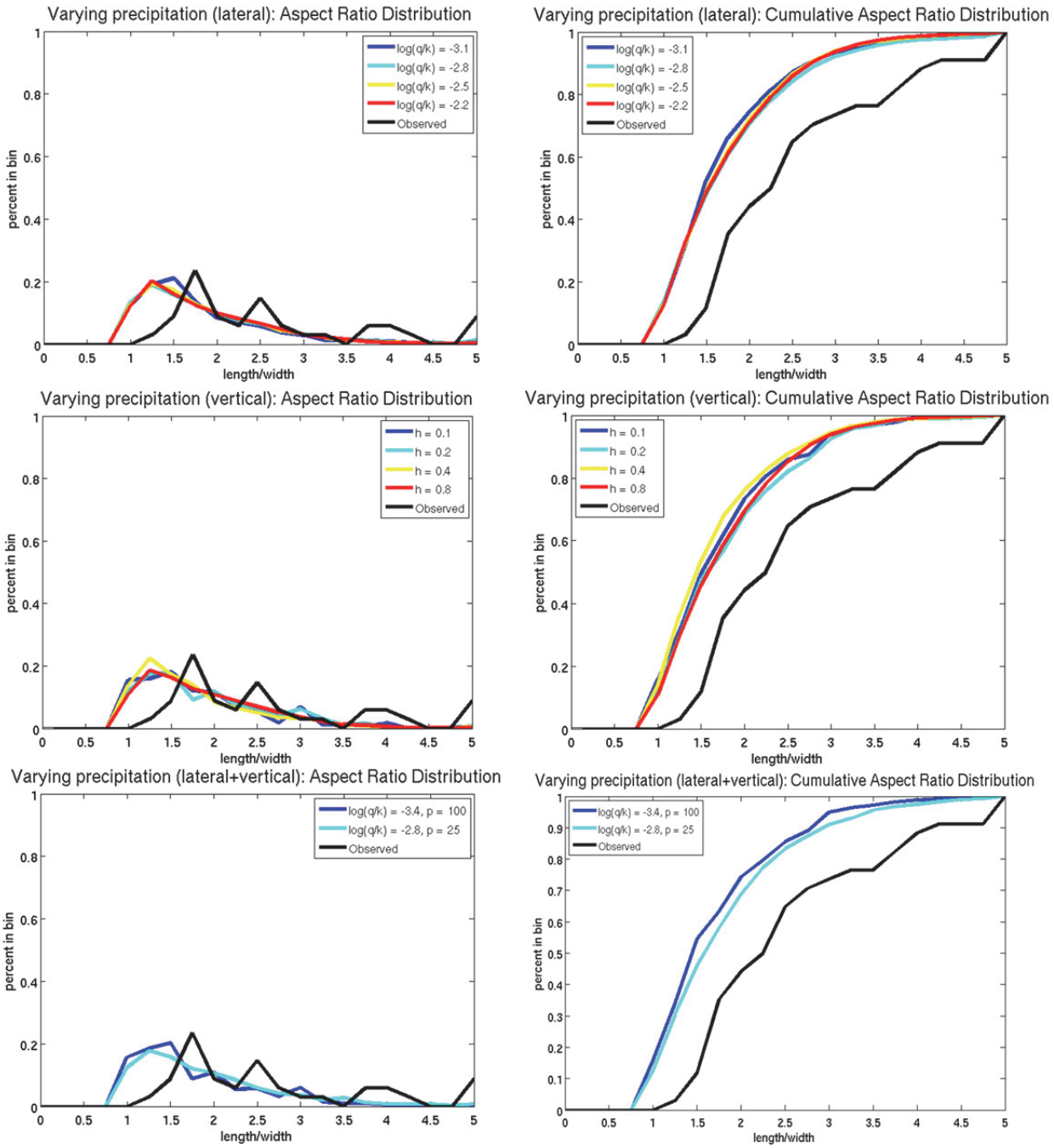

Figure 4.29. Simulations 1 - 10 aspect ratio distributions. PDF's (left) and CDF's (right) of the aspect ratio distributions for all ten simulations. Notwithstanding the different hydrological models and their parameters, no discernible trend emerges from these distributions. The difference between predicted and observed distributions is particularly evident in the CDF's.

When the model is applied to the CB-MR site, discrete landslide predictions emerge, often with comparable sizes and locations as the observations. Many, if not most, of the predictions are in areas where landslides have not been observed. The mapped landslide dataset was adopted because it is useful to compare predictions with observations, however it must be noted that the observations were collected in a ten-year period. Over a longer period, landslides should appear

in many other locations, as is suggested by the dissected landscape. Furthermore, we know that these landscapes experience cycles of soil infilling due to creep, and soil evacuation due to landsliding. The soil depth sub-model adopted here does not account for landsliding, with the result that all the hollows are *fully-loaded*. The combination of these two factors will inevitably result in over-prediction. However, it should be remarked that predicted landslide (whether or not observed) coincide with areas of high pore pressure and thicker soils (where the effect of root strength is less significant). Again, this gives confidence in the ability of procedure to accurately localize favorable areas.

In the application of the model to CB-MR, many overlapping landslides are observed. This indicates that many outcomes are possible for any scenario, suggesting that subtle variations in local conditions could determine which outcome will ultimately be realized. As discussed in section 3.6, by varying the parameter $\boldsymbol{l}$ (equation 3.7) the user has a choice on how much overlap to allow. However, this choice is arbitrary and thus here it was chosen not to limit overlap in any way ($l = 1$). The result is that many locations are predicted as being part of more than one landslide, which does not happen in reality. While generally one can assume that the least-stable prediction is the most likely, this is not always the case: for example, a rapid rise in pore pressure may result in the theoretically least-stable shape to be "skipped" in favor of a larger one. It should be noted that overlap restrictions (using equation 3.7) will inevitably affect the size and location distributions. While the bias introduced by varying the parameter l was not explored, close examination of the spatial maps resulting from simulations 1-10 (figures 4.13, 4.18, 4.23) suggests that selecting only the least-stable shape among overlapping ones would bias the size distribution towards smaller sizes.

The focus of this chapter is on evaluating the performance of the procedure under a suite of selected scenarios. For this purpose, two different approaches were taken, namely comparing the properties (i.e. size, shape, location) of predicted landslide populations and testing the procedure's ability to capture individual observed landslides.

When comparing predicted and observed distributions we can capture size and location. However, in this application this requires a high steady-state precipitation rate. This rate should not be compared to actual precipitation rates as steady-state conditions are rarely attained in reality. This is because the time scale necessary for establishment of steady state conditions may be significantly larger than the duration of most rainstorms [Iverson 2000]. Nonetheless, the unrealistic rates used in the best-performing simulations may be pointing to (and compensating for) deficiencies in the overly-simplified hydrological models. For example, as precipitation is varied through the ratio of the effective precipitation to the saturated conductivity q/K, high values of q may be a result of an over-estimation of K. Measurements of hydraulic conductivity vary significantly at the CB-1 location [Ebel et al., 2007b], thus a spatially uniform treatment of K may be too simplistic. Perhaps more significantly, it has been observed that a large fraction of the flow is not confined to soils but involves the underlying bedrock [Torres et al., 1998; Ebel et al., 2007b, Montgomery et al., 2009]. It could thus be argued that a value of K based entirely on soil measurements may in fact be inappropriate. The over-prediction of shallow landslides observed in several of the simulations presented here may in part due to the unrealistic steady-state precipitation rates. A dynamic hydrological model that captures the transient response of the landscape to rainfall may produce more realistic results and reduce over-prediction. One such model will be explored in the final chapter of this dissertation.

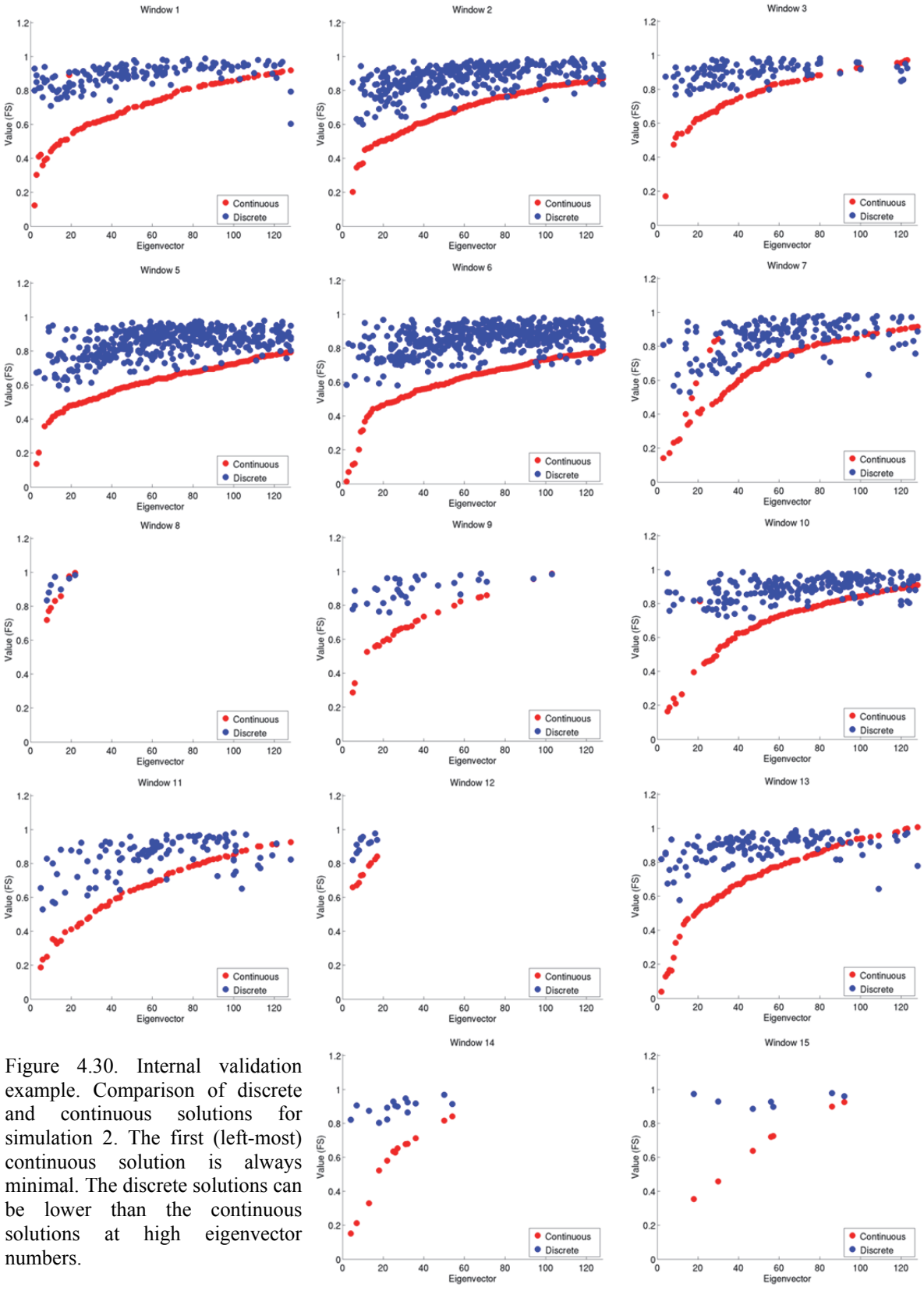

Figure 4.30. Internal validation example. Comparison of discrete and continuous solutions for simulation 2. The first (left-most) continuous solution is always minimal. The discrete solutions can be lower than the continuous solutions at high eigenvector numbers.

In most cases, the predicted size distribution is smaller than observed. A mechanistic explanation whereby size is rarely captured could derive from the imprecision of attributing correct parameter values throughout the site: for example one could expect that with higher root cohesion a larger size would be needed to overcome increased resistance on the margins. Similarly, the fact that the observed aspect ratio distribution is never captured might also be explained mechanistically: for example, a different distribution of the lateral forces (i.e. a stronger downslope boundary, or a weaker cross-slope boundary) should result in larger aspect ratios, all else being constant. Another potential explanation for the mismatch in size and shape could be due to the difficulty of establishing the true initial geometry of landslides in the field. For example, in the base map (fig 4.1), the CB-1 landslide is mapped as having a considerably larger size and longer shape than subsequently estimated through forensic post-failure investigation. The same may be true at other locations, resulting in observations having a bias towards larger sizes and longer shapes.

When testing the procedure's ability to capture individual observed landslides, the performance is significantly better than that of a random classifier. This can be observed from both pixel-based and feature-based comparisons (described in section 3.4.5.2), as shown in the ROC and MCC results and in the null-hypothesis test (e.g. figures 4.15 - 4.17). These results give some degree of confidence in the model's prediction, and the performance measures defined here provide a mean to tune or constrain model parameters. In other fields such as image classification or information retrieval, the scores obtained in this study from these performance measures (e.g. precision/recall, F-score) would be considered low. These fields have benefited from decades of research and development and in particular from the widespread availability of well-designed training datasets (e.g. www.vision.caltech.edu/Image_Datasets/Caltech256/). Such benchmarks provide opportunities for newly-developed algorithms to be applied, tested, and compared, resulting in the incremental but continuous advancement of the field. Viewed in this light, the results presented here are a very good initial step, but landslide identification could greatly benefit from similar community-based research efforts.

4.6 Conclusion

In this chapter I applied the procedure which couples a mechanistic slope stability model that computes the stability of discrete elements of a landscape with a search algorithm which can select least stable combinations of these elements to produce discrete shallow landslide predictions. This procedure was applied to the instrumented CB-1 catchment using field-measured physical parameters, successfully predicting the size and location of the shallow landslide which destroyed the site during the 1996 storm. The procedure was then applied to the larger CB-MR study area using modeled physical parameters, under a suite of diverse hydrological scenarios.

First, the discrete landslide predictions were evaluated by comparing the properties of predicted landslide populations with a dataset of observed landslides collected over ten years of research at the site. The application of the procedure to the larger CB-MR study area resulted in, and was able to reproduce the distribution of sizes and locations observed during the ten years of research at the site.

Second, the CB-MR landslide dataset was used to test the procedure's ability to capture individual observed landslides. At the pixel scale, performance was quantified using a set of information retrieval measures based on true and false positives and negatives. At the feature

scale, the percent of observed landslides captured by the predictions was compared to the percent of the landscape predicted as unstable. In both cases the performance is significantly better than a random classifier.

For a simulation that reproduced both the observed size and location (as represented by a topographic index) distribution, we captured more than *97%* of observed landslides, with less than *30%* of the landscape being predicted as unstable. The same simulation had a true positive rate of almost *86%* and a false positive rate of less than *22%*. These results demonstrate the applicability and give confidence in the shallow landslide prediction procedure. We can now use it to ask important questions such as what controls the size and location of shallow landslides. These questions will be the focus of the next chapter.

Chapter 5

What controls shallow landslide size and location: experiments on Oregon Coast Range topography

5.1 Introduction

The size, location, and frequency of shallow landslides define both the hazard potential they present and their geomorphic influence on landscape evolution. As reviewed in chapter 1, at present there exist mechanistic and empirical methods that can broadly define potentially unstable areas. Empirical relationships based on landslide inventories can characterize the probability distribution of landslide size in specific areas (e.g. Stark and Hovius, [2001]; Brunetti et al., [2009]). Similarly, empirical relationships can characterize the probability of landslide occurrence given rainfall characteristics (e.g. Guzzetti et al, [2007, 2008]; Brunetti et al. [2010]). Current spatial predictions do not provide information on landslide size, while empirical size distributions do not provide information on landslide location. Furthermore, empirical relationships do not allow for predictions to be made under changing conditions caused by landuse and climate change.

In the previous chapters I defined a slope stability method and coupled it with an efficient search algorithm to select least-stable combinations of grid cells to produce discrete shallow landslide predictions across a landscape. This procedure was tested on an instrumented small catchment where parameters were well constrained and on a larger landscape where a detailed landslide inventory is available. The results of these tests provide confidence that the procedure can effectively predict size and location of shallow landslides. We are now able to address questions such as what controls how big landslides are, where do they happen, and when (or how frequently) do they happen. Of these questions, the one we know least about is what controls landslide size. In this chapter, the sensitivity of landslide size to a variety of parameters will be explored. In this process the question of location will also be addresses, while in the next chapter I will point to a framework that can help address the question of when and how often shallow landslides may occur. Addressing these questions may also help with back-analysis of observed landsliding events, and identify the signatures of the dominant processes involved.

As discussed in the previous chapters, the parameters that are most relevant for the occurrence of rainfall-triggered shallow landslides are slope, pore pressure, root and soil strength, and soil depth. The hypothesis that was formulated in chapter one is that the co-organization of these parameters, mostly dictated by topography, controls the size and location of shallow landslides. This was supported by experiments on a synthetic landscape in which the intersection of a high pore pressure and low root strength fields limited the size of landslides (section 3.5). In the first application to a real landscape (chapter 4) we also observed the impact of the spatial distributions of pore pressure on landslide size: the landslide that occurred at the small instrumented catchment (CB-1) straddles the high pore pressure field and on the larger study area (CB-MR) predicted landslides grew larger as the pore pressure field expanded.

Observations also suggest that landslide size and abundance is affected by the root reinforcement provided by diverse vegetation cover. In New Zealand, Selby [1976] observed that for the same rainfall conditions landslides exhibited a smaller size (but were more numerous) in

grasslands than in forested areas, Reneau and Dietrich [1987] compare their data on landslide width in hardwood forests with that reported by Lehre [1982a;1982b] for grasslands and brush, showing that the forests slides were 1.6 times wider than the grasslands. Similarly, Gabet and Dunne [2002] documented that landslides were smaller (and more numerous) in areas where root strength decreased as a result of coastal vegetation to grassland pastures. Using a slope stability model that accounted for the effect of lateral root reinforcement but not the full three-dimensional effects in the model presented in chapter two, Reneau and Dietrich [1987] proposed that a decline in root strength would lead to failures of lower lengths and widths; in contrast, low gradients or high soil friction would require failures to have higher lengths and widths. They emphasized the role of colluvium thickness in slope stability: thick colluvium reduced the effect of root strength but could also reduce the likelihood of destabilizing pore pressure. Using a similar model, Casadei et al. [2003b] performed a sensitivity analysis in which they showed that minimum width for failure increases with root cohesion and friction angle, and decreases (nonlinearly) with increasing slope or increasing relative saturation. Both of these studies focused on how the theoretical *critical* width of shallow landslides (i.e. the minimal width required for instability) is expected to vary under uniform conditions, and inferred that spatial extent of controlling properties (i.e. colluvium thickness, root strength, and local pore pressure) set an upper limit on size. These predictions are intriguing, but depend strongly on the assumptions in their simple models. With these assumptions, controls on landslide width were proposed, but both width and length, and, hence, size, could not be predicted.

Experiment number	Number of simulations	log(q/k) []	p [mm]	C_{r0} [Pa]	j [m^{-1}]	phi [deg]	Soil depth multiplier	Soil depth addition (m)	Smoothing filter size (m)	Description
Base case	1	-2.8	0	21,666	4.96	40	1	0	0	Steady-state shallow subsurface (lateral) flow, field-constrained
1	37	-5.5 – -1.9	0	21,666	4.96	40	1	0	0	Vary steady-state shallow subsurface (lateral) flow
2	20	-Infinity	2.5 – 500	21,666	4.96	40	1	0	0	Varying uniform instantaneous (vertical) pressure addition
3	11	-2.8 – -3.8	10.8 – 106.4	21,666	4.96	40	1	0	0	Vary proportion of vertical to lateral flow contribution
4	15	-2.8	0	10833 – 43332	2.48 – 9.92	40	1	0	0	Vary root strength base value and exponential decay function
5	11	-2.8	50	21,666	4.96	35 – 45	1	0	0	Vary soil friction angle
6	8	-2.8	0	21,666	4.96	40	0.25 – 2	0	0	Vary soil depth (proportionately)
7	20	-2.8	0	21,666	4.96	40	0	0.25 – 8	0	Vary soil depth (uniformly)
8	7	-2.8	0	21,666	4.96	40	1	0	0 – 110	Vary topographical smoothing filter size

Table 5.1. Description and parameterization of the experiments presented in chapter 5. In experiments 1-8 parameters are varied relative to a *reference case* scenario, which uses the best-performing field-constrained parameterization presented in chapter four.

In a real landscape, critical size for failure and actual size of failure may be rather different, as conditions are rarely uniform. With the ability to spatially predict discrete landslides under varying conditions on a real landscape, it now becomes possible to explore the controls not just on critical size, but on *probable* landslide size (i.e. the most likely as indicated by a *probability density function*). Spatial discrete landslide prediction capability also allows exploring how probable location varies with varying parameters. The question of what controls landslide size and location across a landscape will be the focus of this chapter.

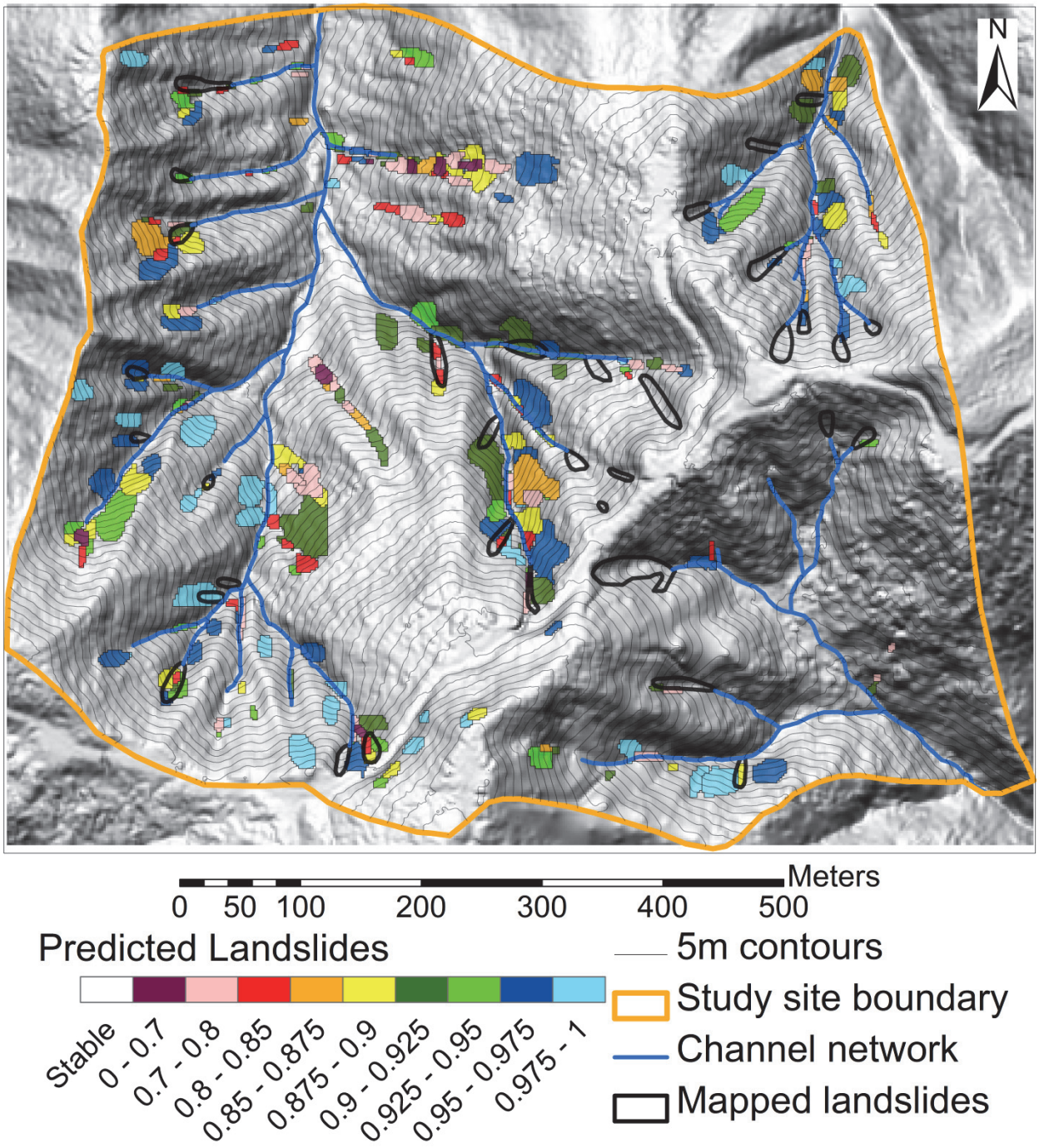

Figure 5.1. Landslides predicted by the procedure for the *reference case* scenario. The "slow-changing" parameters consist of the best field-constrained estimates presented in section 4.4.1. The hydrologic parameter $log(q/K) = -2.8$ used for this scenario reflects the best-performing value from experiments presented in chapter four. Overlap threshold (eq. 3.7): $l = 1$. Root strength parameters are $C_{r0} = 21{,}666\ Pa$, and $j = 4.96$. Colors indicate the factor of safety. Predicted landslides are mostly found in convergent areas, where soil and water are preferentially concentrated.

To explore the controls on landslide size and location, the procedure will be applied to the landslide-prone study area in the Oregon Coast Range (CB-MR) presented in chapter four, where repeat field mapping provides an inventory of all the shallow landslides that occurred over a 10-

year period [Montgomery, et al., 2000], and intensive research in the area provide constraints on soil, vegetation, hydrological, and rainfall characteristics. A sensitivity analysis will be performed by which these characteristics will be systematically varied, and the resulting probability density functions of predicted landslide size and location (as represented by a topographic index) will be examined. As topography plays an important role on the spatial organization of these parameters, the effect of smoothing the landscape on landslide distributions will also be explored. Finally, I will summarize general trends such as increase or decrease in number or size of predicted landslides as the parameters are systematically varied, and comment on which parameter sets result in best performance.

5.2 Methods

The shallow landslide prediction procedure will be applied to the 0.5 km^2 Mettman Ridge study area (CB-MR), where 2 meter LiDAR-derived topographic data is available. Similarly to the approach taken in chapter four, a wide range of hydrological scenarios will be explored. The two end-member (laterally and vertically dominated) steady-state hydrological models introduced in chapter two will be adopted, and as hydrological conditions are the least constrained, an extreme range of precipitation values will be used. Within a range of realistic precipitation values, a mixture of the two models will also be explored. In contrast to chapter four, the "slowly-changing" variables such as soil depth, root strength, and soil friction angle will be varied. As the magnitude of these variables is more constrained, only the range of realistic values will be explored. It is important to note that these characteristics are varied on the entire landscape. As a result, the spatial distribution of areas favorable for landsliding which can be exploited by storms (or in this case by applied steady-state precipitation) changes with each parameterization, resulting in a difference in characteristic landslide size and/or location.

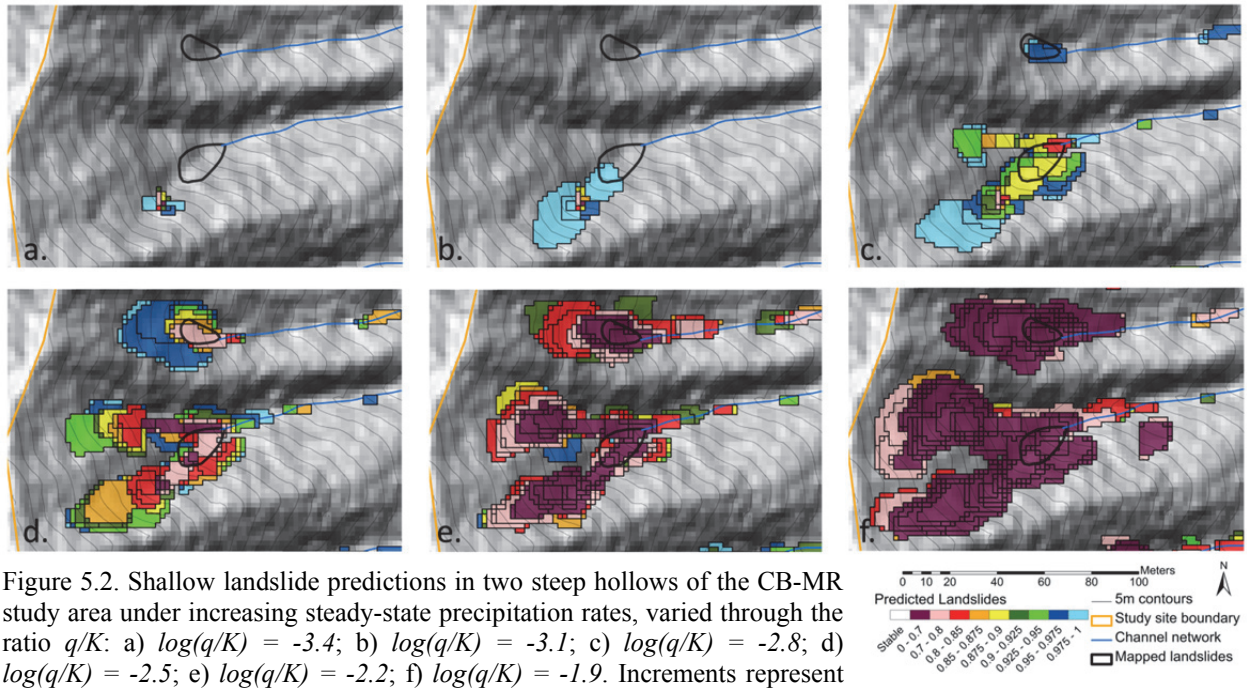

Figure 5.2. Shallow landslide predictions in two steep hollows of the CB-MR study area under increasing steady-state precipitation rates, varied through the ratio q/K: a) $log(q/K) = -3.4$; b) $log(q/K) = -3.1$; c) $log(q/K) = -2.8$; d) $log(q/K) = -2.5$; e) $log(q/K) = -2.2$; f) $log(q/K) = -1.9$. Increments represent doubling of q. Landslides begin upslope in the hollow, and as these expand with relative saturation new landslides emerge downslope. Final extent of landsliding is limited by the topographic characteristics of the hollows.

While many of these parameters co-vary in actuality, here they will be treated as independent. In each experiment one parameter will be allowed to vary, and the others will be assigned the most likely value based on field studies. When the hydrological characterization is held constant, the precipitation value which gave the best performance score in the simulations of chapter four will be adopted. Two parameters that are included in the slope stability framework will be held constant in this study: the saturated hydraulic conductivity $\boldsymbol{k}$ (*m/day*) and the soil density $\boldsymbol{\rho_s}$ (kg/m^3); uniformly varying the former is equivalent to varying the effective precipitation $\boldsymbol{q}$ (*m/day*), while the latter (which varies little in the relatively thin colluvial mantle) is considered to have little impact on slope stability [Borga et al., 2002]. It is also assumed that the CB-MR soils are essentially cohesionless [Schmidt et al., 2001] with a roughly constant porosity of 50% [Montgomery et al, 1997]. The parameters used in all the experiments presented in this chapter are summarized in table 5.1. It should be noted that experiments 1 to 8 vary parameters relative to a *reference case* scenario, which uses the best-performing field-constrained parameterization presented in chapter four. As in the experiments presented in chapter four, no restrictions on overlapping predictions will be applied here (i.e. all predicted unstable outcomes will be presented). Throughout the experiments, the water table height h is not allowed to exceed the soil thickness z. Probability density functions (PDF's) of predicted landslide size and of predicted median topographic index (a proxy for location, equation 3.18) will be generated from each parameterization and these PDF's will be compared to each other and to the observed distributions. Aspect ratio distributions will not be examined here, as they were found to be invariant under the range of parameter choices presented in this chapter, and essentially unchanged from those presented in chapter four of this dissertation.

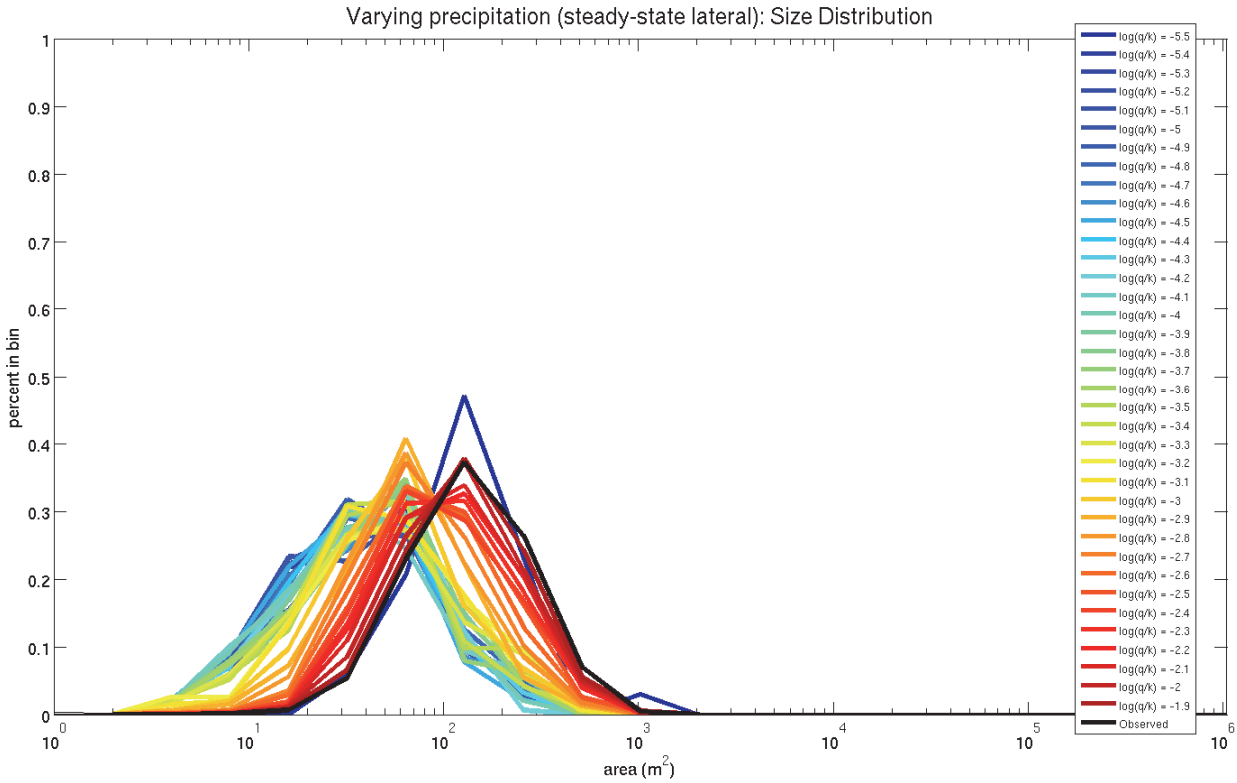

Figure 5.3. Size distributions predicted using the lateral hydrological model. As precipitation increases, the size distribution shifts to the right (larger size) until it matches the observations when *log(q/K) = -2.3* to *-1.9*.

In experiment 1 to 3, the hydrological parameters are varied while root strength, friction angle, and soil depth are held constant. In experiment 1 the steady-state shallow subsurface flow hydrologic model (equation 2.13) is used with a ratio of effective precipitation to saturated conductivity ***log(q/K)*** varying from -5.5 to -1.9. For a value of ***k*** = *67 m/day* [Ebel et al., 2007b], this is equivalent to steady-state precipitation ranging from approximately *0.2 mm/day* to *843 mm/day*. In experiment 2, the purely vertical hydrologic model (equation 2.14) is used instead, with a range of *uniformly applied instantaneous pressure addition p* ranging from *0* to *500 mm*. In experiment 3 the mixture model (equation 2.15) is adopted and the relative contribution of the lateral and vertical components is varied while the total amount of precipitation (i.e. the sum of *p* and *q*) is held constant. The chosen value of *117 mm* represents the precipitation depth (*p*) necessary to reproduce the average saturation levels measured at CB-1 during the landslide-causing storm of November 1996. The ratio of vertical to lateral contribution is then varied from 0.1 to 10.

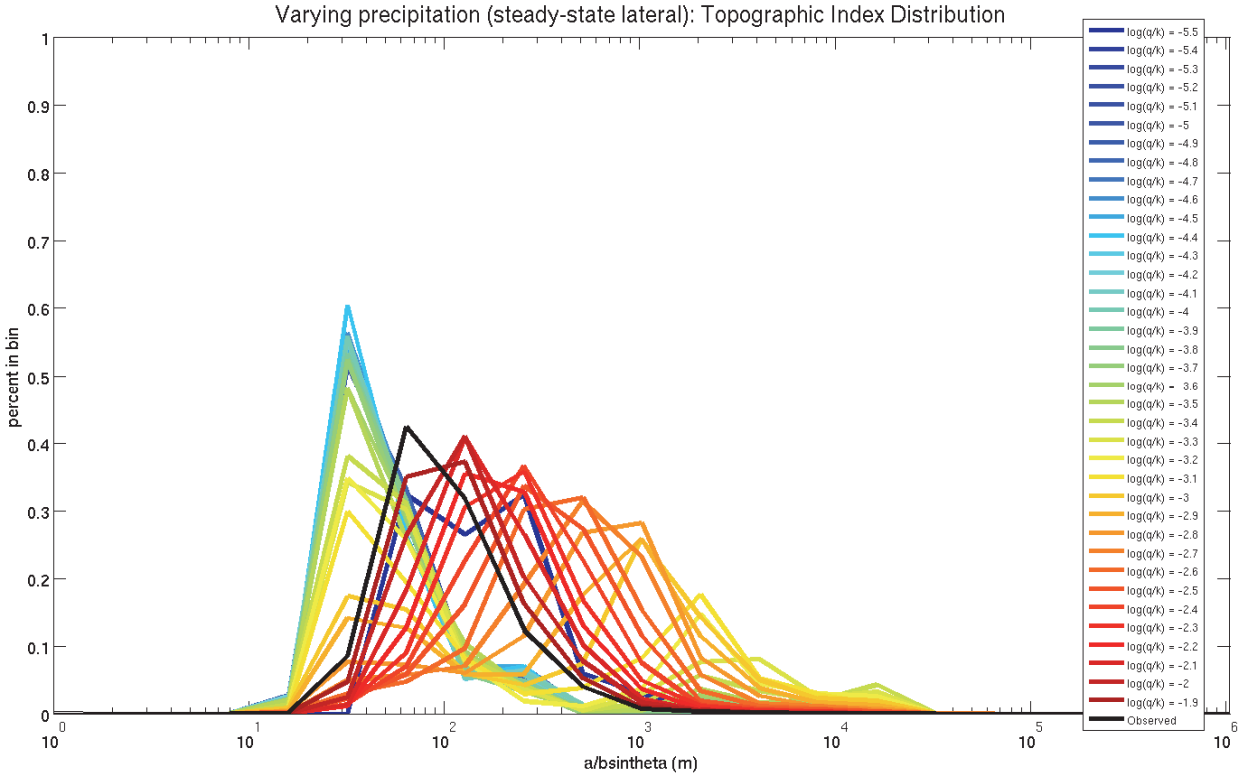

Figure 5.4. Topographic index distributions predicted resulting using the lateral hydrological model. Initially the distribution is skewed to the left (high slope); as precipitation increases, the size distribution becomes bi-modal (high slope or high drainage area); as precipitation further increases the distribution is uni-modal again, matching the observations when *log(q/K) = -2.3* to *-2.1*.

In experiments 4 to 6, the hydrological parameters are held constant while root strength, friction angle, and soil depth are individually varied. In experiment 4 both parameters defining root strength (equations 2.19 and 2.20) are varied from half to twice the base values measured at the CB-1 landslide where lateral and basal root strength were estimated to be *4,600* and *100 Pa*, respectively. For the CB-1 landslide, which has an average depth of almost *1 m*, this range corresponds to lateral root strength values of *1,100 Pa* to *16,500 Pa* and basal root strength values of *1 Pa* to *4,000* Pa. In experiment 5 the friction angle is varied from *35°* to *45°*. In experiment 6 the soil depth is varied proportionally to the modeled CB-MR values (which range

from *0* to *540 cm* with a mean of *70 cm*, figure 4.7), resulting in spatially variable soil depths. Here values are multiplied by a factor of *0.25* to *2*. In experiment 7 the soil depth is varied uniformly (soil is spatially invariant) with a range from *25* to *800 cm*.

Finally, the effect of varying the degree of roughness and dissection of the landscape is explored in experiment 8. The original LiDAR-derived topography is progressively smoothed using a Gaussian filter of size varying from *0* to *110 m*. After each level of smoothing the soil depth is re-calculated using the model described in sections 2.2.3 and 4.41. While average soil depth remains roughly constant throughout this exercise, the spatial distribution of soil thickness becomes progressively more uniform as filter size increases. Also as a result of smoothing, the mean slope of the landscape progressively declines while the mean drainage area progressively increases.

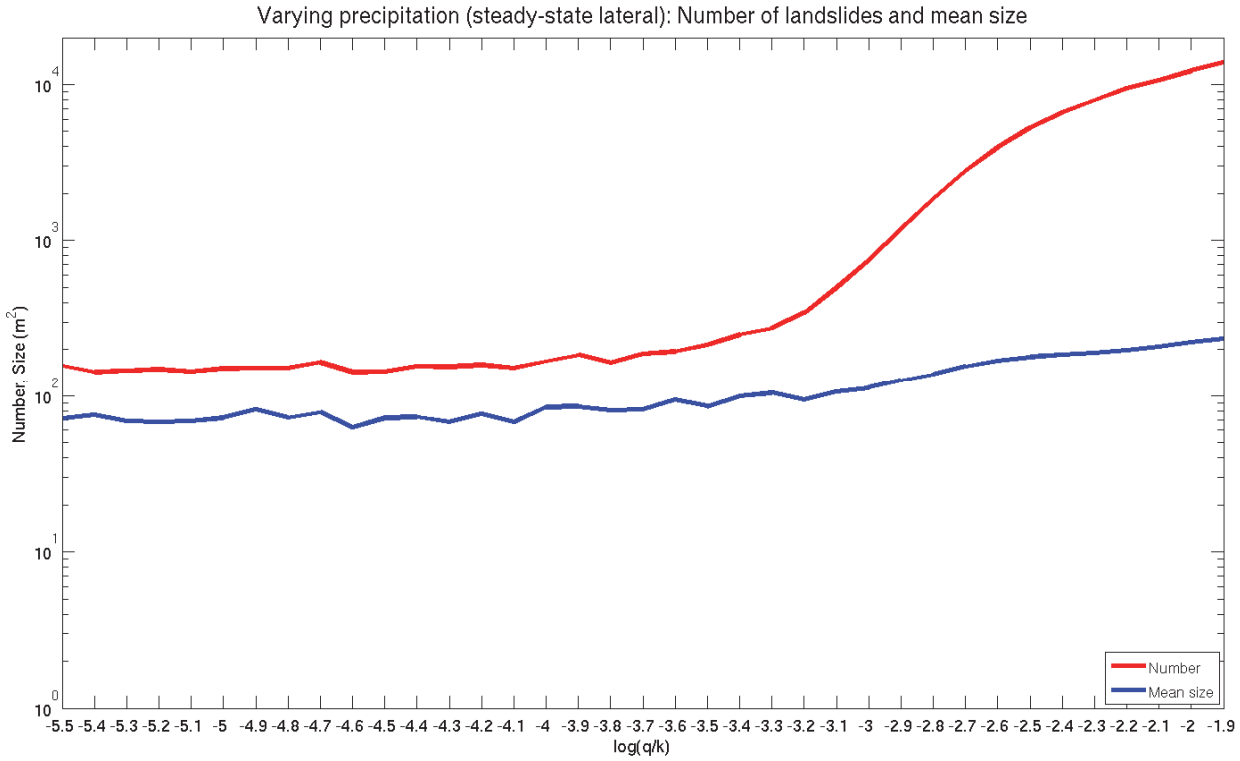

Figure 5.5. Number of shallow landslide predictions and their mean size under increasing steady-state precipitation rates, varied through the ratio *q/K*: mean predicted size generally increases, and a more rapid increase in number of predicted landslides is observed when *log(q/K)* exceeds *-3.2*.

5.3 Results

We have observed in chapter four that failures can only occur in locations where there is sufficient soil to overcome the resistive forces provided by root strength. The spatial pattern of soil thickness is determined by the divergence of the soil flux with convergent areas generally exhibiting thicker soil cover than divergent areas. Thus in general hollows have thicker soils than noses, and soil thickness increases down a hollow axis. The soil mass contributes to both the driving (slope-parallel) and normal forces, proportionally to the slope angle. An increase in soil mass will increase the factor of safety when the slope angle is low, as the normal component of the gravitational force (and thus the frictional force acting on the base) increases faster than the shear component. In contrast, when the slope angle is high an increase in soil mass will decrease

the factor of safety as the shear component of the gravitational force (and thus the slope-parallel driving forces) increases faster than the normal component. In other words, an increase of the soil mass will make a sub-critical slope (i.e. a slope such that the driving forces are less than the resistive forces) less critical and a critical slope more critical. The cohesive component of these soils is principally due to the effects of root reinforcement which decreases exponentially with soil depth. Thus increasing soil depth diminishes the root strength contribution, also resulting in decreased stability. In contrast, shallow soils offer a lower driving force contribution and much higher root strength, resulting in increased stability. As a result, landslides should occur preferentially in deeper soils.

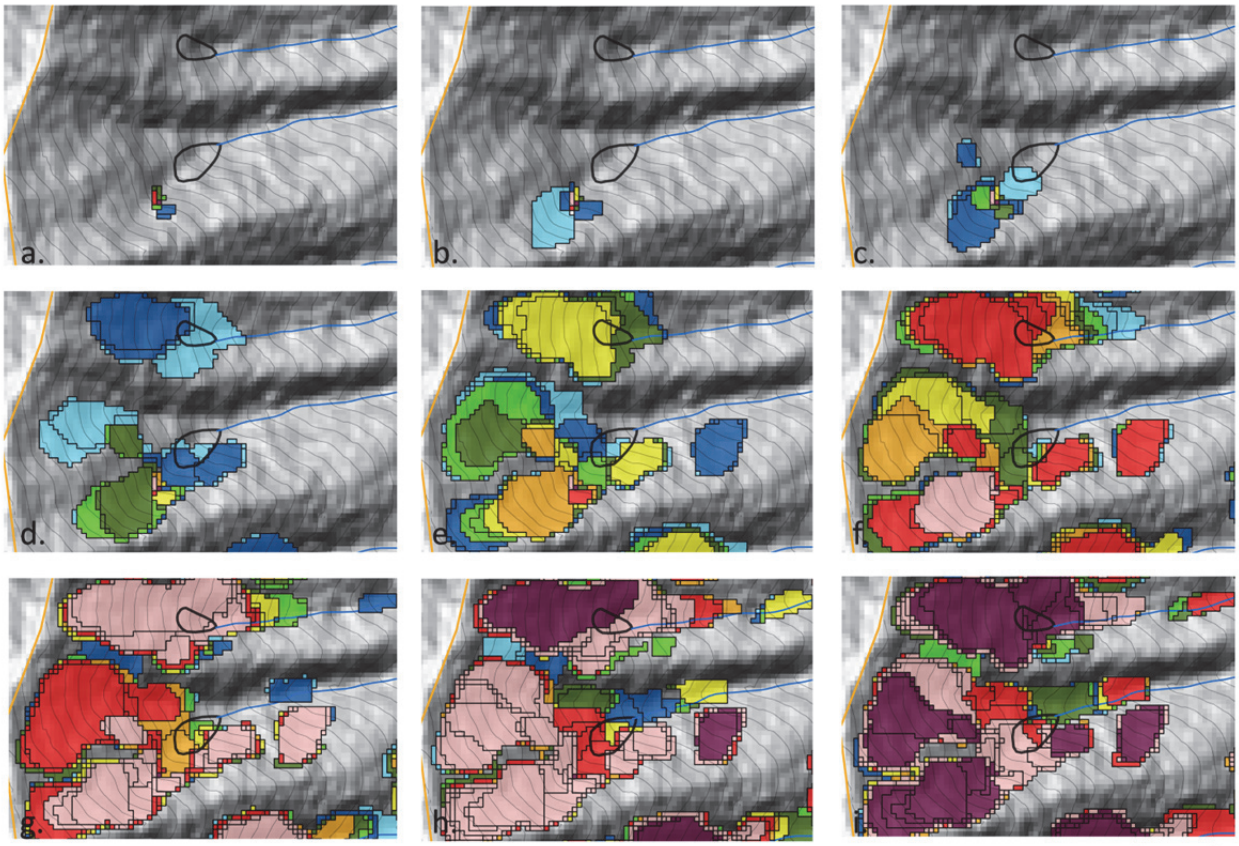

Figure 5.6. Shallow landslide predictions in two steep hollows of the CB-MR study area under increasing instantaneous vertical addition to the water table height *h*, varied through the parameter *p*: a) *p = 2.5 cm*; b) *p = 5 cm*; c) *p = 10 cm*; d) *p = 15 cm*; e) *p = 20 cm*; f) *p = 25 cm*; g) *p = 30 cm*; h) p = 35 cm; i) *p = 40 cm*. Landslides begin upslope in the hollow, and as relative saturation is higher in thinner soils they generally expand upslope only when *p* becomes very large. New landslides emerge downslope. Final extent of landsliding is limited by the topographic characteristics of the hollows.

The spatial pattern of relative saturation is both a function of water table height and soil depth. In the absence of spatial variability of the water table height (e.g the case of purely vertical infiltration-dominated flow), relative saturation decreases with soil depth, increasing stability. When instead the subsurface flow is topographically steered (e.g the case of shallow subsurface flow), relative saturation increases in convergent areas, resulting in decreased stability. In other words, under the vertically-dominated scenario, soil depth increases in hollows (due to transport convergence) but relative saturation decreases (*h/z* decreases as *z* increases), while under the laterally-dominated scenario both soil depth and relative saturation increase

(both h and z increase due to transport convergence). Thus the spatial pattern of relative saturation and the water pathways leading to elevated pore pressure should control where landslides occur along the hollow axis. In the absence of any other control, larger landslides are expected to be less stable (see section 3.5). However, as landslides get larger the spatial variability in the parameters (particularly slope, soil depth and relative saturation) should constrain the area over which landslides may occur (as inferred by Reneau and Dietrich [1987] and Casadei et al. [2003b]). This section presents the results of experiments in which landscape characteristics drive spatial differences in relative saturation, root strength, soil friction, soil depth, and topographic roughness across the CB-MR study area.

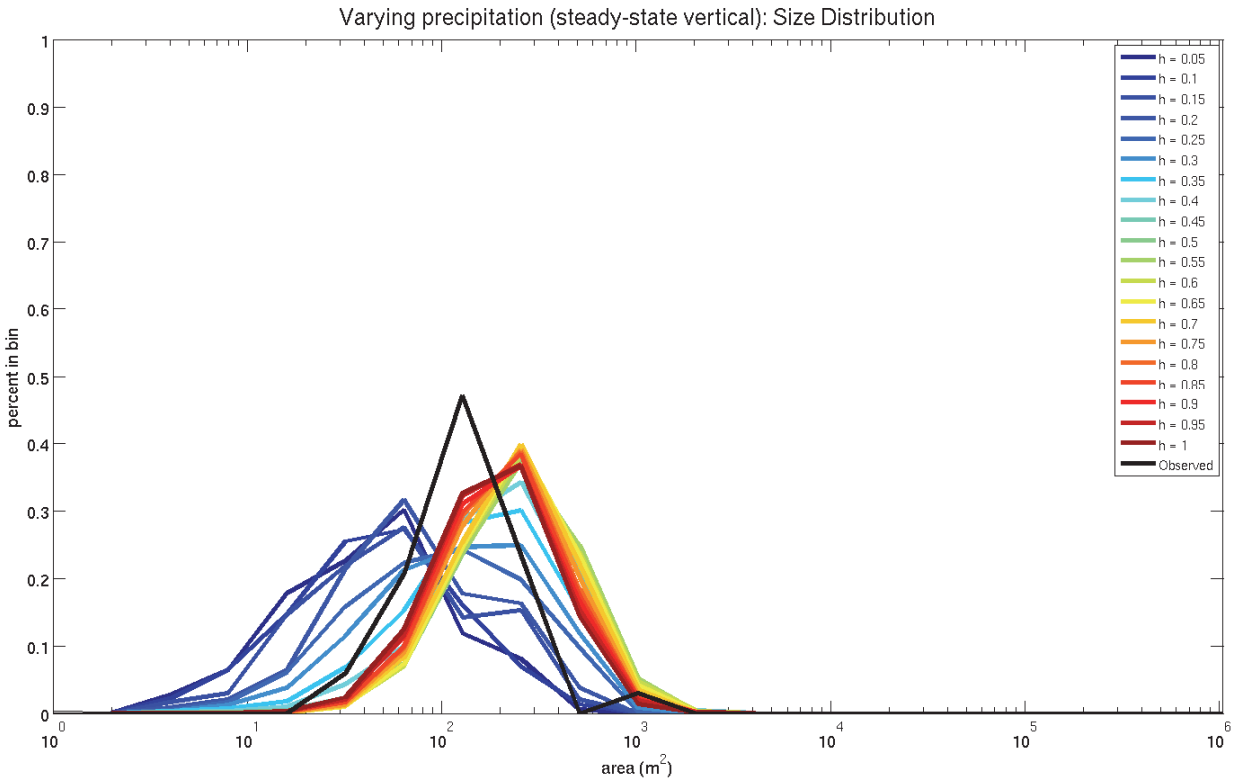

Figure 5.7. Size distributions predicted using the vertical hydrological model. As precipitation increases (and the water table height h increases), the size distribution shifts to the right (larger size), until it reaches a maximum when $h = 0.55$ *m,* after which only smaller landslides are added to the distribution; size is at first smaller, then larger than observations; intermediate distributions with $h = 0.3$ *m* and $h = 0.35$ *m* do match the observations. Note that $h = p/\eta$ when $h < z$, and $h = z$ otherwise.

Results will be presented as spatial maps of shallow landslide predictions for the CB-MR study site, as well as for a small portion of the map area to show the details of changing size, location and numbers with changes in driving variables. These will followed probability density functions of predicted landslide size and location (using the median topographic index as a proxy for location)), and by plots of size and number as a function of driving variables for the entire map. The aspect ratio of predicted landslides was essentially invariant in almost all the experiments, and thus will generally not be discussed. In section 5.3.1, I will first present the results of the application of the procedure under variable hydrologic controls. This will be followed by the effects of variable root and soil strength (sections 5.3.2, and 5.3.3, respectively). Results of varying the soil depth will be presented in section 5.3.4, while the impact of smoothing the topography will be shown in section 5.3.5. In a separate section (5.3.6) general

trends emerging from the experiments, as well as the influence of parameter choices on performance, will be presented. As there is much uncertainty around the parameter choices (particularly the hydrological parameters), it is perhaps more useful to view the results presented here as changes relative to a reference case scenario.. In this scenario, the steady-state shallow subsurface flow hydrological model is used with an effective precipitation to saturated conductivity ratio $log(q/K) = -2.8$, together with the best estimates (field-constrained) of parameters for root strength, friction angle, and soil depth (see section 4.41). This scenario was chosen because in the experiments of chapter four it produced the best compromise between precision and recall, as defined by the F-score. A spatial map of shallow landslide predictions resulting from this parameterization is shown in figure 5.1.

5.3.1 Hydrological controls

5.3.1.1 Experiment 1: varying q/K in steady state runoff

Figure 5.2 illustrates the development of potential shallow landsliding in two steep hollows of the CB-MR study area as effective steady-state precipitation increases, under the shallow subsurface flow (lateral) hydrological model. The number of predicted landslides increases with increasing precipitation, but their size and location also change. With very little precipitation, failures can only occur in steep locations where there is sufficient soil to overcome the resistive forces provided by root strength, but not so thick that the saturation ratio becomes too low. Such areas are of limited extent, and as a result landslide size is very small (figure 5.2a). As precipitation increases and the relatively saturated field expands, the extent of favorable areas also increases and landslides can become larger in size (figure 5.2b). As already seen in the artificial experiments of chapter three, in the absence of heterogeneities limiting areas favorable to landsliding, a larger size generally results in a decrease of the factor of safety. While favorable areas expand upslope in the hollow, new unstable areas develop down the hollow axis where relative saturation is higher (figure 5.2c). These trends continue as the saturation field continues to expand with increasing precipitation (figures 5.2d-e), greatly augmenting the number of overlapping predictions. While landslides become more unstable with increasing precipitation, there is an upper limit to their size set by the characteristics of the hollow: landslides cannot extend out of the hollow because of insufficient soil depth, and they cannot extend down the hollow due to insufficient slope (figure 5.2f).

The probability density functions of predicted landslide size for the entire map area (figure 5.3), show that landslide size increases with precipitation (the mode of the PDF shifts to the right). The results also indicate that while the predicted PDF's resemble the observed with high precipitation, predicted size appears smaller than observed for most precipitation scenarios. In fact, the *Kolmogorov-Smirnov* (K-S) test, which uses a measure of distance between the empirical *cumulative distribution functions* to determine if they may derive from the same distribution, confirms that only the PDF of the results of simulations having $log(q/K) = -1.9$ to -2.3 belong to the same distribution as the observations.

The probability density functions of predicted landslide topographic index (figure 5.4) illustrate the trends observed in the hollows of figure 5.2. The topographic index is essentially the ratio of drainage area and slope, thus a low index indicates landslide location to be in steep non-convergent areas, while a higher index places them further down the valley axis where drainage area increases and slope decreases.

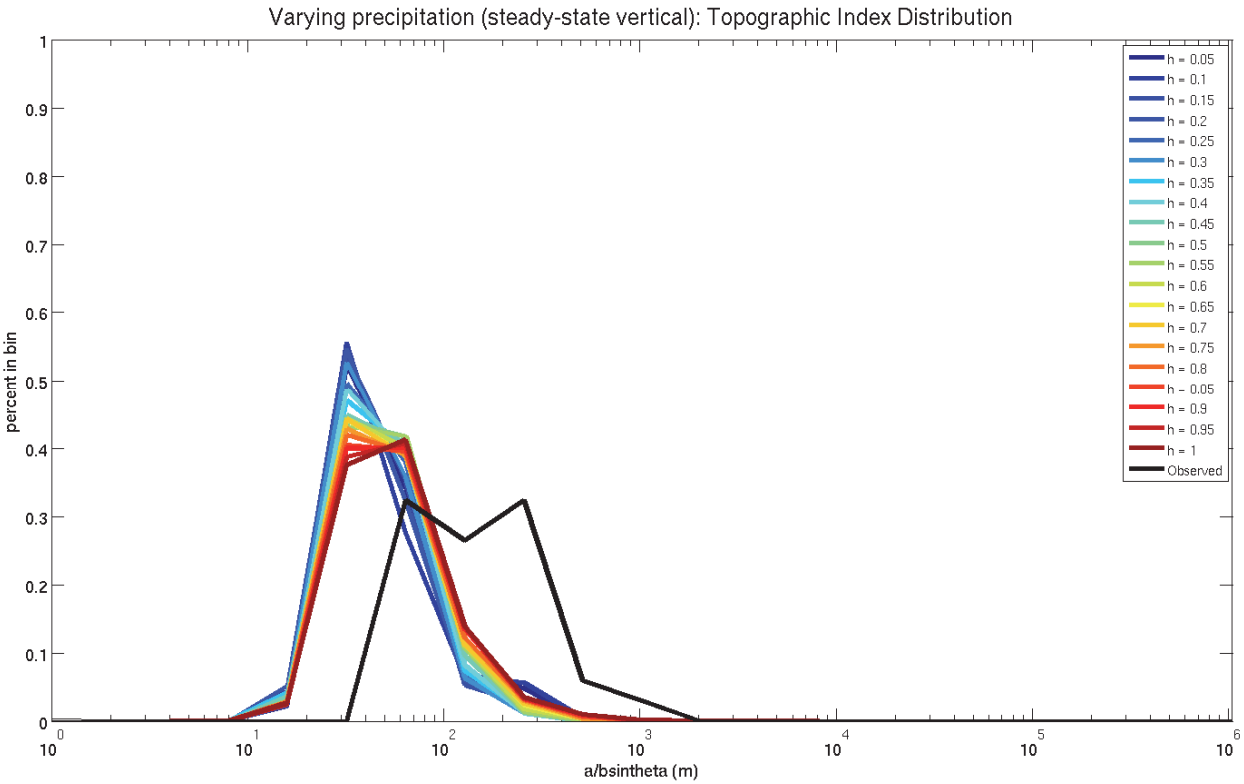

Figure 5.8. Topographic index distributions predicted using the vertical hydrological model. As precipitation increases (and the water table height *h* increases), the topographic index distribution shifts to the right (less slope, higher drainage area), but without ever reaching the distribution of the observed landslides.

Initially, with low precipitation landslides can only occur on high slopes. With moderate precipitation, the distribution is bi-modal: landslides can either occur on steep slopes or in highly convergent areas downslope. As precipitation further increases the distribution returns to a single mode centered on the observations. This is because as favorable locations become exploited and landslides expand, they become limited by the topographic setting. The landslides farthest upslope can only expand downslope and *vice versa*, and inevitably the topographic index shifts towards the middle range. Distributions arising from *log(q/K)* values of *-1.9* to *-2.3* belong to the same distribution as the observations, based on the K-S test.

The number of predicted landslides and their mean size as the ratio *q/K* is increased are shown in figure 5.5. Initially landslide number and mean size do not increase significantly, as the number and size of the landslides mostly reflects those areas of the landscape which are unstable independent of precipitation. When precipitation increases, number and size increase at a similar rate until precipitation exceeds a threshold, after which the number increases more rapidly. The threshold coincides with the value at which the distribution of locations becomes bi-modal (figure 5.4). This suggests that as favorable locations have been exploited and the extent of favorable areas increases due to the expansion of the high pore pressure field, a greater number of landslides (many of which overlapping) can be accomodated. This increase in the number of predictions is likely to be less rapid if restrictions on landslide overlap are imposed by increasing the parameter *l* of equation 3.7 (see discussion in section 4.3).

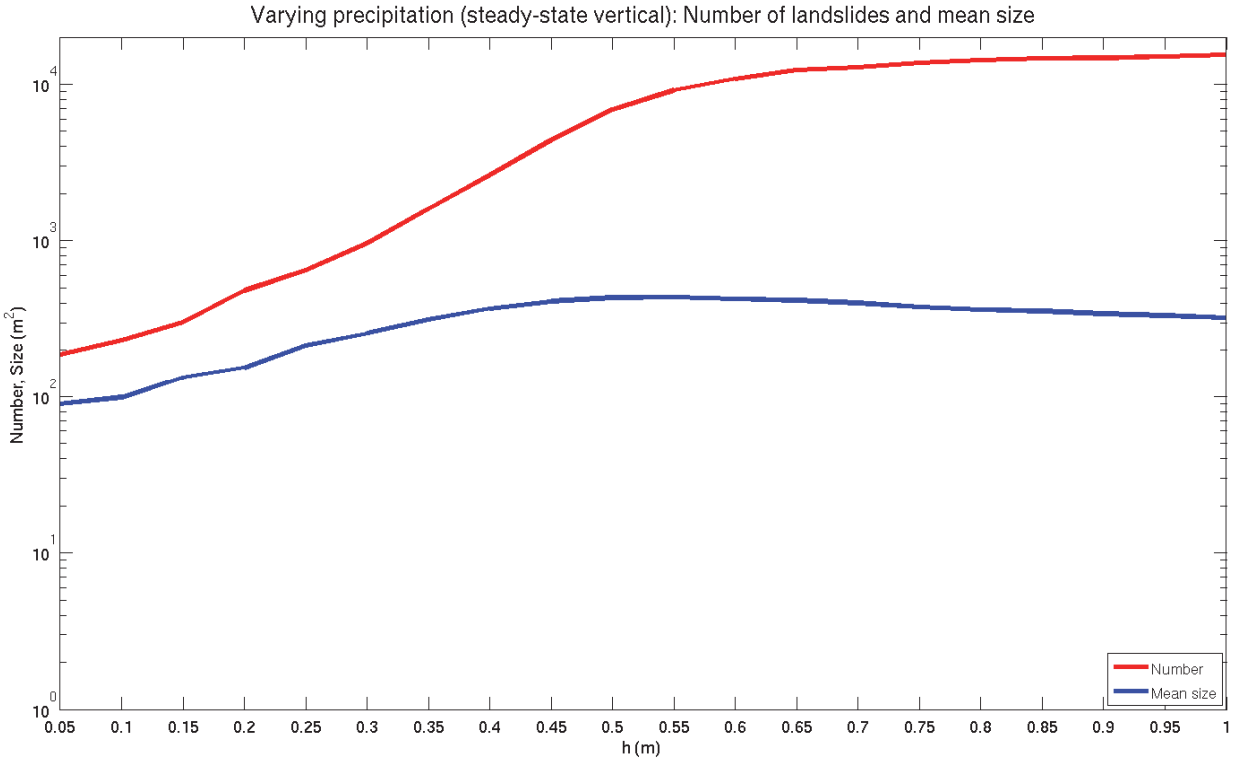

Figure 5.9. Number of shallow landslide predictions and their mean size under increasing instantaneous vertical additions to the water table height *h*. Number and size increase rapidly until *h = 0.55 m*, after which the number increases less rapidly and the mean size decreases slightly.

5.3.1.2 Experiment 2: varying p, the uniformly applied instantaneous pressure addition

Figure 5.6 illustrates the development of potential shallow landsliding in the same steep hollows of the CB-MR study area (shown in the previous experiment) as effective instantaneous precipitation increases, under the purely vertical hydrological model. Under this model, topography does not control the spatial distribution of the water table heights (they are uniform, and uniformly increased during the experiment), but still exerts a control on the saturation ratio *h/z* due the spatially varying soil depth. With very little precipitation, failures can only occur in steep locations where there is sufficient soil to overcome the resistive forces provided by root strength, but not so thick that the saturation ratio becomes too low. These areas are of limited extent, and as a result landslide size is very small (figure 5.6a). As precipitation increases the extent of these areas also increases and landslides can become larger in size (figure 5.6b-c). In contrast to the laterally-dominated scenario, they extend up and out of the hollow axis (figure 5.6d), where relative saturation is highest because of the thinner soils. At the same time new unstable areas develop where relative saturation is high but soils are sufficiently thick to overcome cohesive forces (figure 5.6e). In contrast to the topographically steered experiment, these new areas are out of the hollow axis and not in the thickest parts of the hollow as there *h/z* is too low. These trends continue as the saturation field expands with increasing precipitation (figures 5.6f), but in figure 5.6g size generally reaches a limit due to the characteristics of the hollow (e.g. soil thickness and slope), after which only smaller (and often overlapping) landslides are added (figure 5.6h-i). Only at these later stages does the significant increase of water table height allow for landslides to develop in thicker parts of the hollows. As in the

laterally-dominated case, landslides become more unstable with increasing precipitation, but are less numerous and generally exhibit a larger size than with the lateral model.

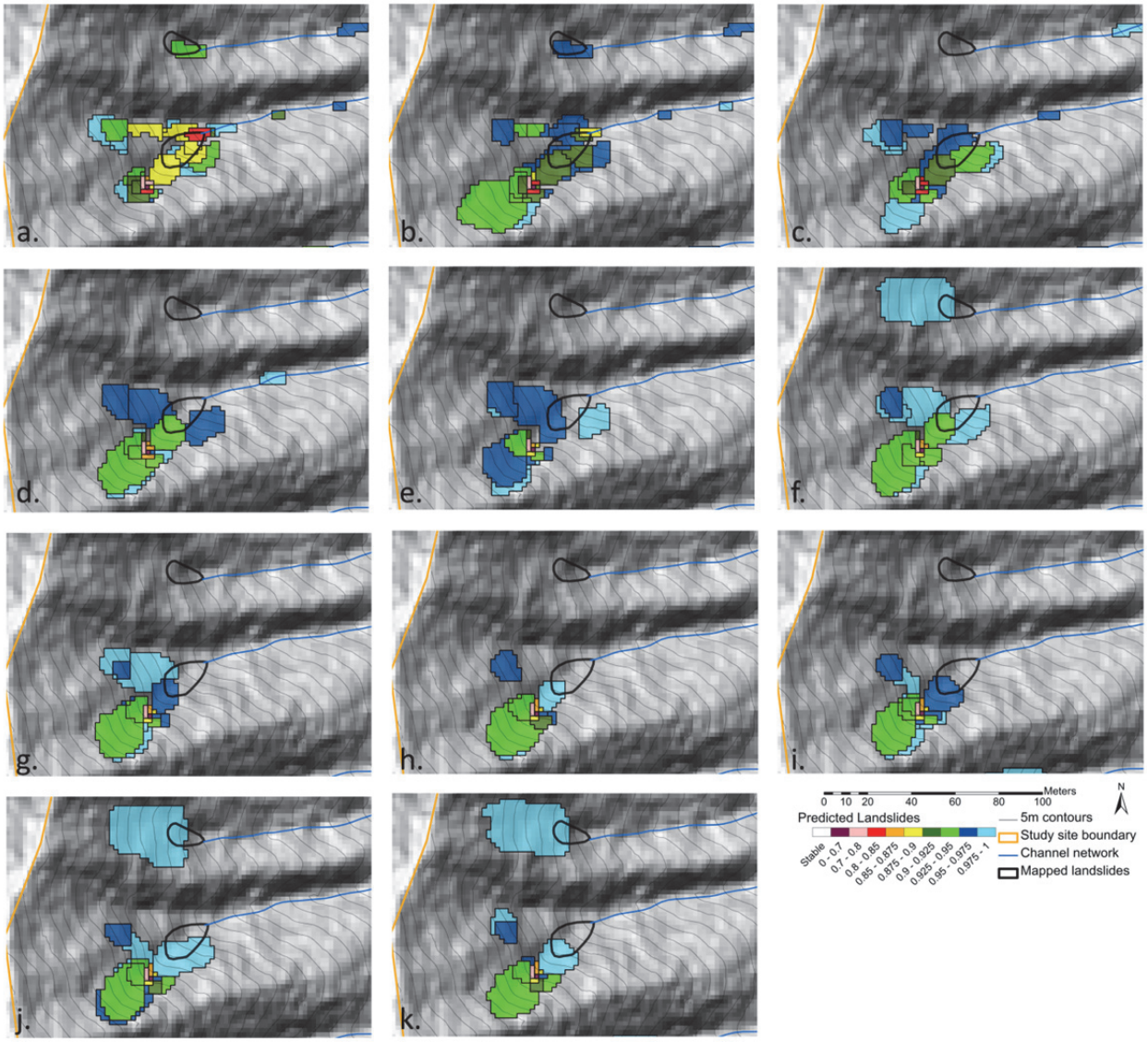

Figure 5.10. Shallow landslide predictions in two steep hollows of the CB-MR study area under increasing relative instantaneous vertical to lateral water addition, varied through the parameter *p/q*: a) *log(q/K) = -2.8*, *p = 27 mm, p/q = 0.1*; b) *log(q/K) = -2.9*, *p = 50 mm, p/q = 0.39*; c) *log(q/K) = -3.0*, *p = 67 mm, p/q = 0.75*; d) *log(q/K) = -3.1*, *p = 81 mm, p/q = 1.2*; e) *log(q/K) = -3.2*, *p = 92 mm, p/q = 1.77*; f) *log(q/K) = -3.3*, *p = 100 mm, p/q = 2.48* ; g) *log(q/K) = -3.4*, *p = 107 mm, p/q = 3.39*; h) *log(q/K) = -3.5*, *p = 113 mm, p/q = 4.52*; i) *log(q/K) = -3.6*, *p = 117 mm, p/q = 5.95*; j) *log(q/K) = -3.7*, *p = 121 mm, p/q = 7.75*; k) *log(q/K) = -3.8*, *p = 123 mm, p/q = 10.02*. When lateral contribution dominates landslides are predicted both upslope and downslope in the hollow; when vertical contribution dominates landslides are only predicted upslope in the hollow and exhibit a generally larger size.

The size distributions shown in figure 5.7 confirm the previous observations: after an initial moderate increase in size, increasing addition of water table height dramatically shifts the distributions to the right (larger size). However, a size limit is reached when *h = 0.55 m*, after which the addition of smaller landslides to the distributions results in a slight left shift. Intermediate distributions (*h = 0.3* and *0.35 m*) are statistically similar (i.e. they pass the K-S test) to the observed distribution.

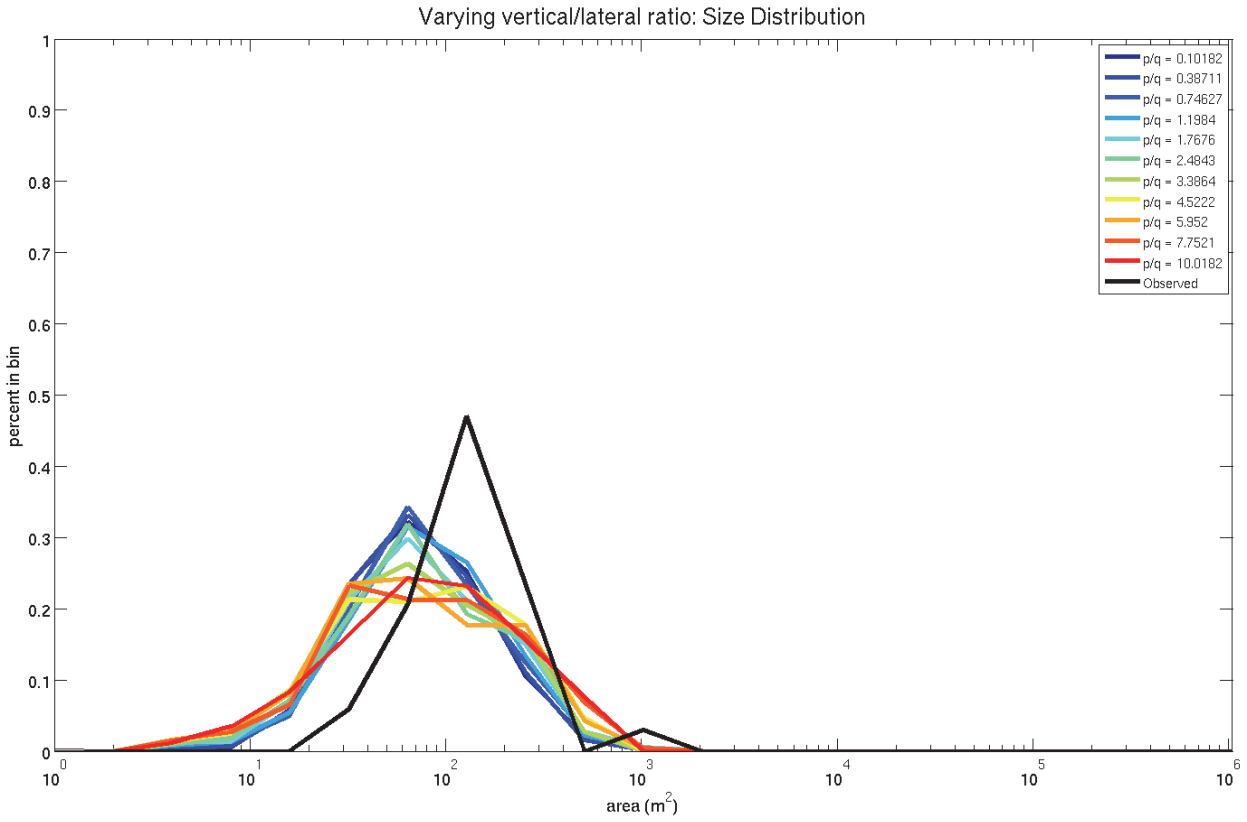

Figure 5.11. Size distributions predicted under increasing relative instantaneous vertical to lateral addition of water, varied through the parameter *p/q*. The increase of relative vertical contribution results in a slight size increase, mostly through a fatter tail on the right end of the distribution.

The topographic index distributions, shown in figure 5.8, confirm that as the water table is uniformly raised, there is a slight right shift (towards greater drainage area). This shift is however very small and the topographic index values remain in the range $< 100\ m$. Figure 5.9 shows the number and mean sizeof shallow landslide predictions under increasing instantaneous vertical additions to the water table height h. Both number and size increase rapidly until $h = 0.55\ m$, after which the number increases less rapidly and the mean size decreases slightly.

5.3.1.3 Experiment 3: lateral and vertical flow pore pressure generation

Figure 5.10 illustrates the development of potential shallow landsliding in the same steep hollows of the CB-MR study area as total precipitation (i.e. the sum of p and q) is held constant, but the relative contribution of vertical to lateral flow increases, under the mixed hydrological model. As the vertical contribution increases, the number of landslides decreases; they get larger, and move up the hollow axis (figures 5.10df), where slopes are higher and the soils are a little thinner and have higher relative saturation. This is consistent with the observations from the previous two end-member scenarios. An interesting effect can be seen in the northern most hollow: under laterally-dominated conditions a landslide is predicted in the same location as the observed landslide; as the vertical contribution increases (and the lateral decreases), the predicted landslide becomes more stable until it is no longer predicted to fail; as the vertical contribution becomes dominant, a landslide of bigger size and extending further upslope reappears. Similar behavior can be observed in other locations. This interpreted to be a result of the interplay of the soil depth and the changing relative saturation.

The size and topographic index distributions, shown in figure 5.11 and 5.12, respectively, confirm these trends: as the relative vertical contribution increases the size distribution has a modest increase (although the mode stays essentially constant, while the tails extend), and the topographic index distribution shifts from high area to high slope. The size increase and reduction in number of predicted landslides as the relative vertical contribution is increased can be also seen in figure 5.13.

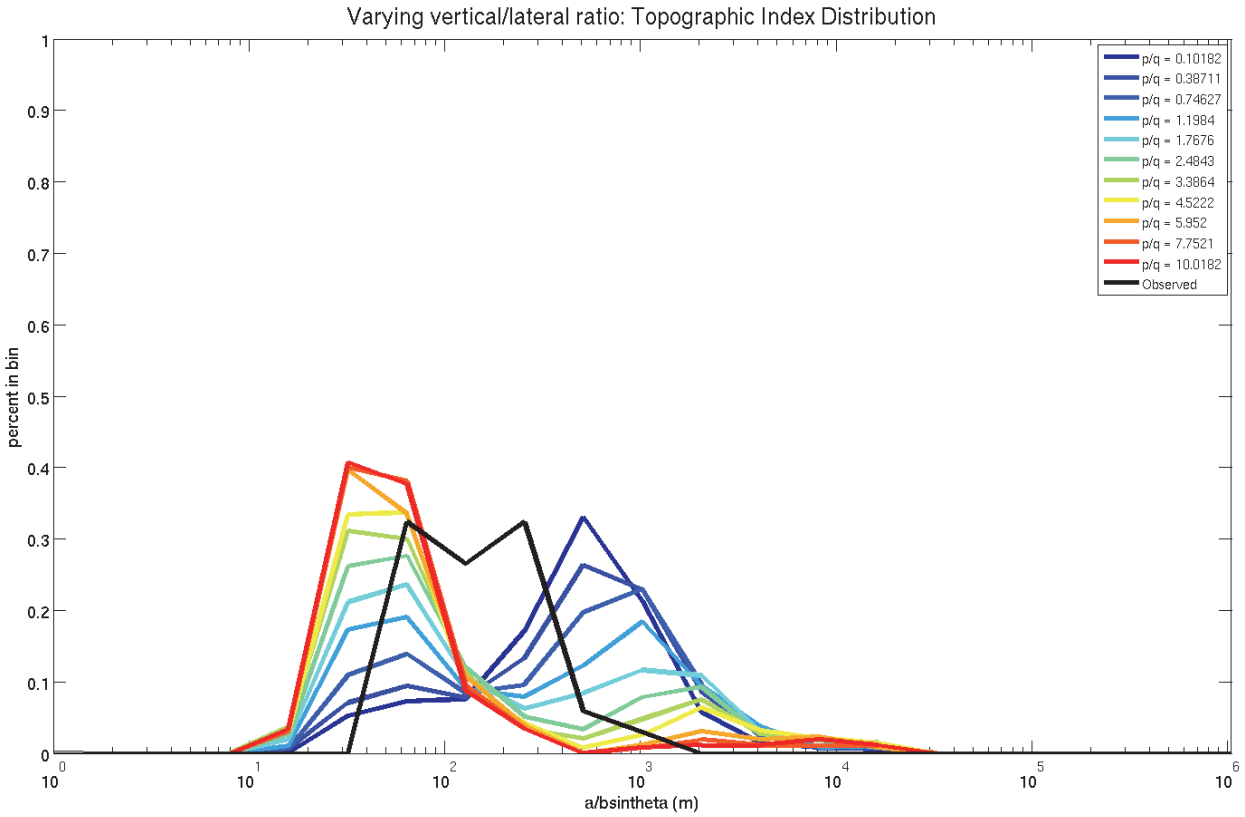

Figure 5.12. Topographic index distributions predicted under increasing relative vertical to lateral instantaneous addition of water, varied through the parameter *p/q:* the relative vertical contribution increase shifts the distributions from locations with high drainage area to locations with high slope.

5.3.2 Vegetation controls: Experiment 4

In all the experiments presented in this chapter, the root strength field parameters (C_{r0} and j, equations 2.18 – 2.20) are held spatially constant. In the reference case scenario, the values measured at the CB-1 were adopted (table 4.2). The resulting spatially varying lateral and basal root reinforcement values are shown in figure 4.9. In this experiment the effect of increased or decreased root strength on the characteristic size and location of shallow landslides at CB-MR is examined. Here root cohesion values ranging from half to double those used the reference case scenario ($C_{r0} = 21{,}666\ Pa$, and $j = 4.96\ m^{-1}$) are explored. For the CB-1 landslide, which has an average depth of almost *1 m*, this range corresponds to lateral root strength values of *1,100 Pa* to *16,500 Pa* and basal root strength values of *1 Pa* to *4,000* Pa. This range was chosen to reflect the values reported by [Schmidt et al., 2001] for industrial forests in the Oregon Coast Range.

Because of the exponential decay function used to represent the decay of root strength with depth, the total root cohesion acting on some soil depth can be changed by varying the initial value C_{r0}, or by changing the shape factor j which controls the rate of decay with depth. Figure

5.14 illustrates how both approaches produce fundamentally similar results. In figures 5.14 (a-b), j is held constant (at the reference case value), while C_{r0} is halved and doubled, respectively. In figures 5.14 (c-d), C_{r0} is held constant (at the reference case value), while j is doubled and halved (doubling j reduces cohesion), respectively. In both approaches one can observe that reducing root cohesion (figures 5.14a and 5.14c) generally results in an increased number of landslides, and a general reduction of their size. Conversely, an increase in root cohesion (figures 5.14 b and d) generally results in decreased number of landslides, and a general increase of their size. The same trends can be observed in the detail of figure 5.15. Here root cohesion is increased from left to right via the parameter C_{r0}, and from top to bottom via the parameter j (no landslides were predicted in this location when j was halved). One can also observe a greater abundance of landslides upslope in the hollows when root cohesion is reduced.

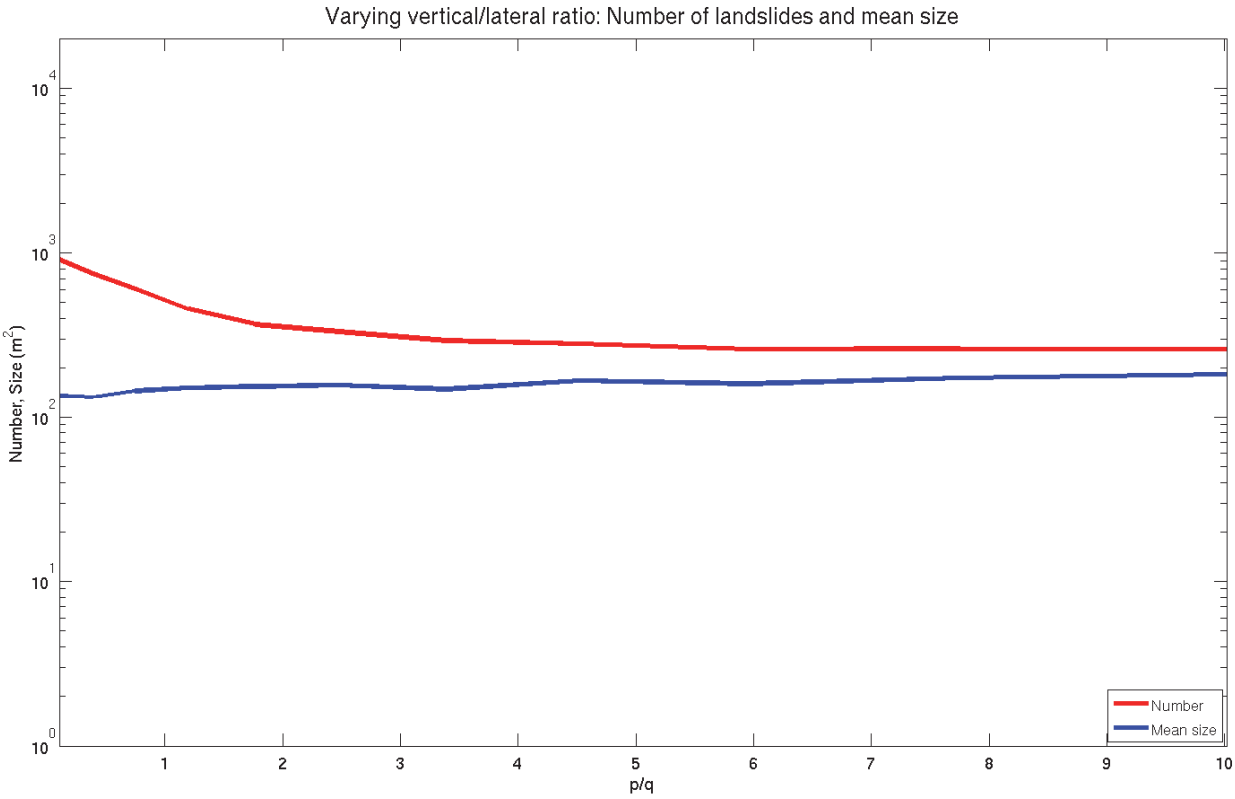

Figure 5.13. Number of shallow landslide predictions and their mean size under increasing relative vertical to lateral instantaneous addition of water, varied through the parameter *p/q:* the relative vertical contribution increase results in a slight size increase and a decline in the number of predicted landslides.

Changes in characteristic location and size are evident in the PDF's of distributions resulting from this experiment. Figures 5.16, 5.18, and 5.21 show size distributions resulting from varying C_{r0}, for j = *9.92*, *4.96*, and *2.48* m^{-1}, respectively. We can observe that sizes are generally larger with increased root strength (higher C_{r0} or lower j), and that this effect is more prominent with a lower value of j (the size distribution becomes tighter). The topographic index distributions, shown in figures 5.17, 5.20, and 5.22, illustrate that as root strength increases predicted locations are preferentially shifted to higher topographic index values (more prominently when j is lower). The general trend of increased size and decreased abundance with increased root strength is summarized in figure 5.23, where it is also observed that size increase is most significant with higher values of j and reduction in number is most significant with lower values of j.

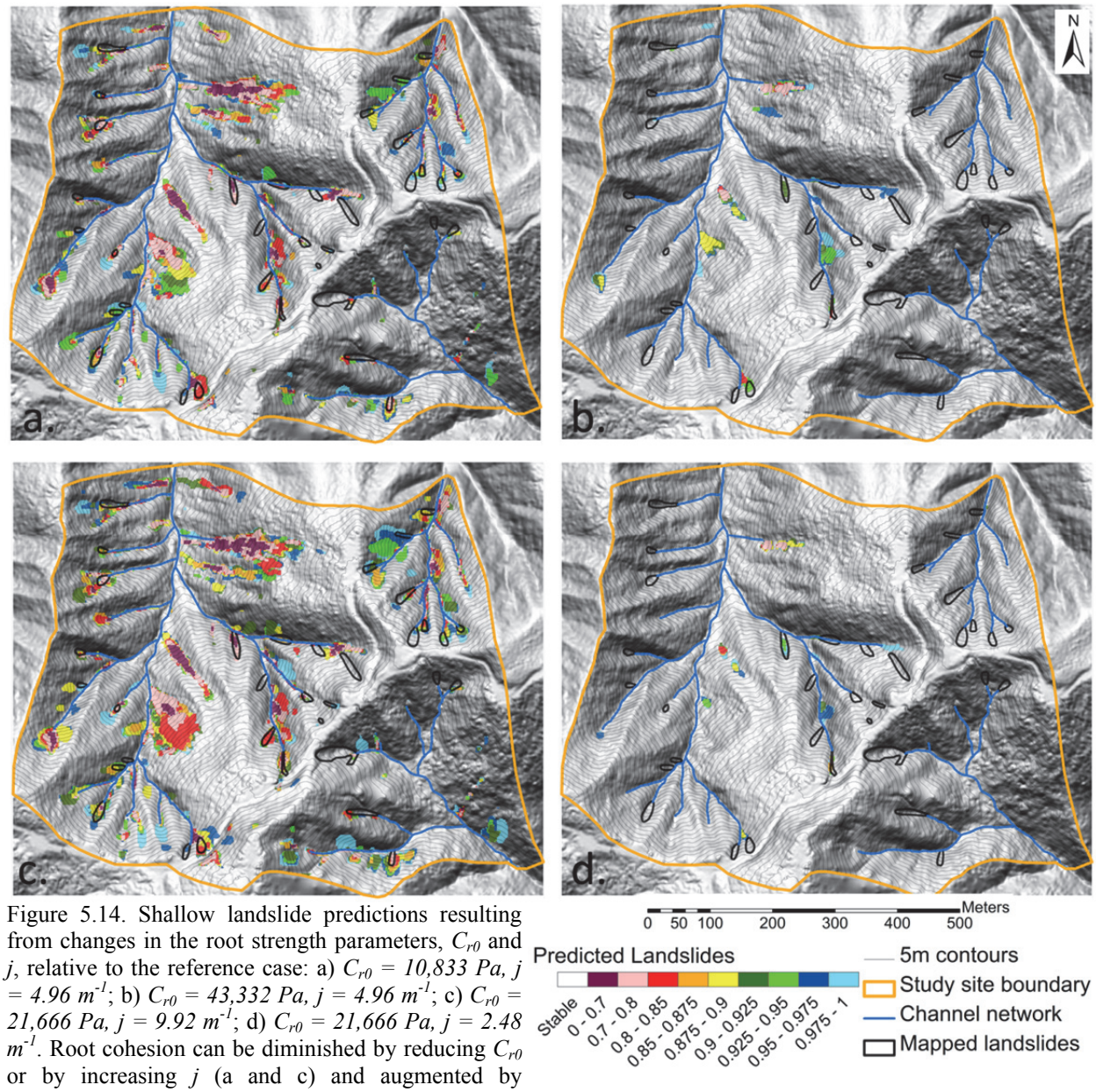

Figure 5.14. Shallow landslide predictions resulting from changes in the root strength parameters, C_{r0} and j, relative to the reference case: a) C_{r0} = *10,833 Pa*, j = *4.96* m^{-1}; b) C_{r0} = *43,332 Pa*, j = *4.96* m^{-1}; c) C_{r0} = *21,666 Pa*, j = *9.92* m^{-1}; d) C_{r0} = *21,666 Pa*, j = *2.48* m^{-1}. Root cohesion can be diminished by reducing C_{r0} or by increasing j (a and c) and augmented by increasing C_{r0} or by reducing j (b and d). Reduced cohesion generally results in more, smaller predicted landslides.

5.3.3 Material properties controls: Experiment 5

In this experiment the effect of increased or decreased shear strength of the soil on the characteristic size and location of shallow landslides at CB-MR is examined. This is performed by varying the friction angle parameter φ from *35°* to *45°*. Figure 5.24 shows the effect of the increase in friction angle, with all other parameters being held constant, on predicted landslides. It can be observed that as friction is increased, the number of predicted landslides is reduced; their size tends to decrease, and the pattern of stabilization seems to initiate upslope, with predictions preferentially found downslope in the case of high friction.

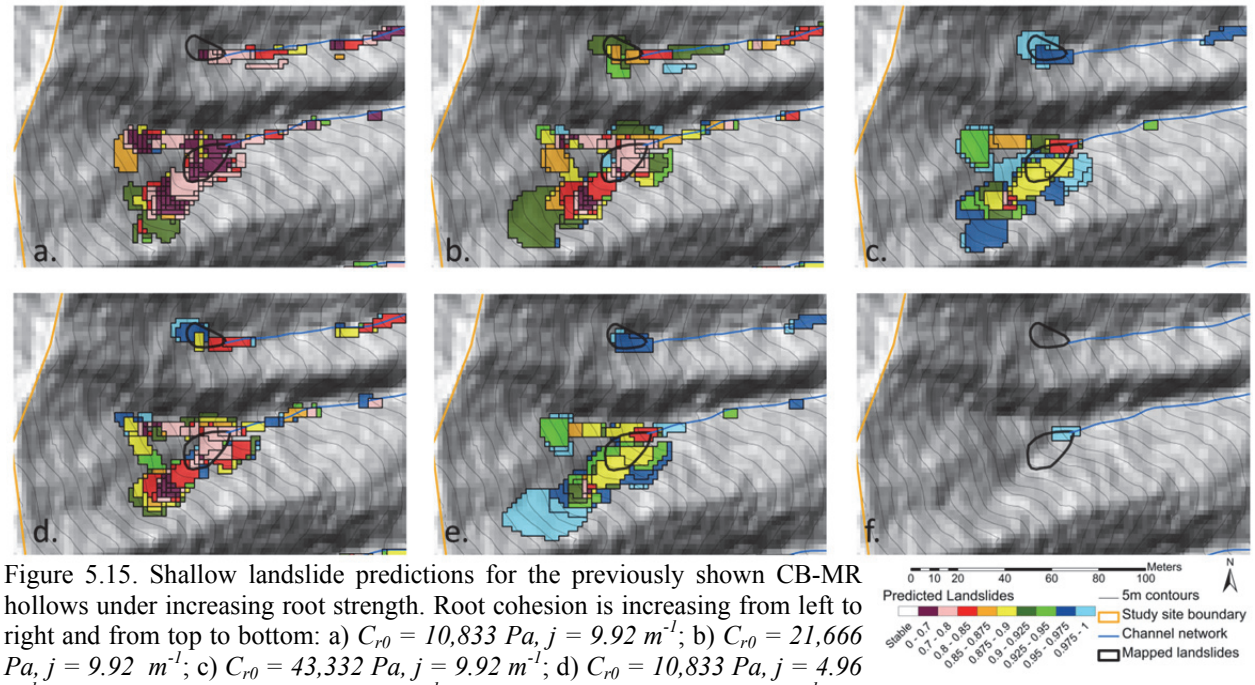

Figure 5.15. Shallow landslide predictions for the previously shown CB-MR hollows under increasing root strength. Root cohesion is increasing from left to right and from top to bottom: a) C_{r0} = *10,833 Pa, j = 9.92* m^{-1}; b) C_{r0} = *21,666 Pa, j = 9.92* m^{-1}; c) C_{r0} = *43,332 Pa, j = 9.92* m^{-1}; d) C_{r0} = *10,833 Pa, j = 4.96* m^{-1}; e) C_{r0} = *21,666 Pa, j = 4.96* m^{-1}; f) C_{r0} = *43,332 Pa, j = 4.96* m^{-1}; no landslides were predicted in this area when *j = 2.48* m^{-1}. Increasing cohesion results in fewer and generally larger predicted landslides.

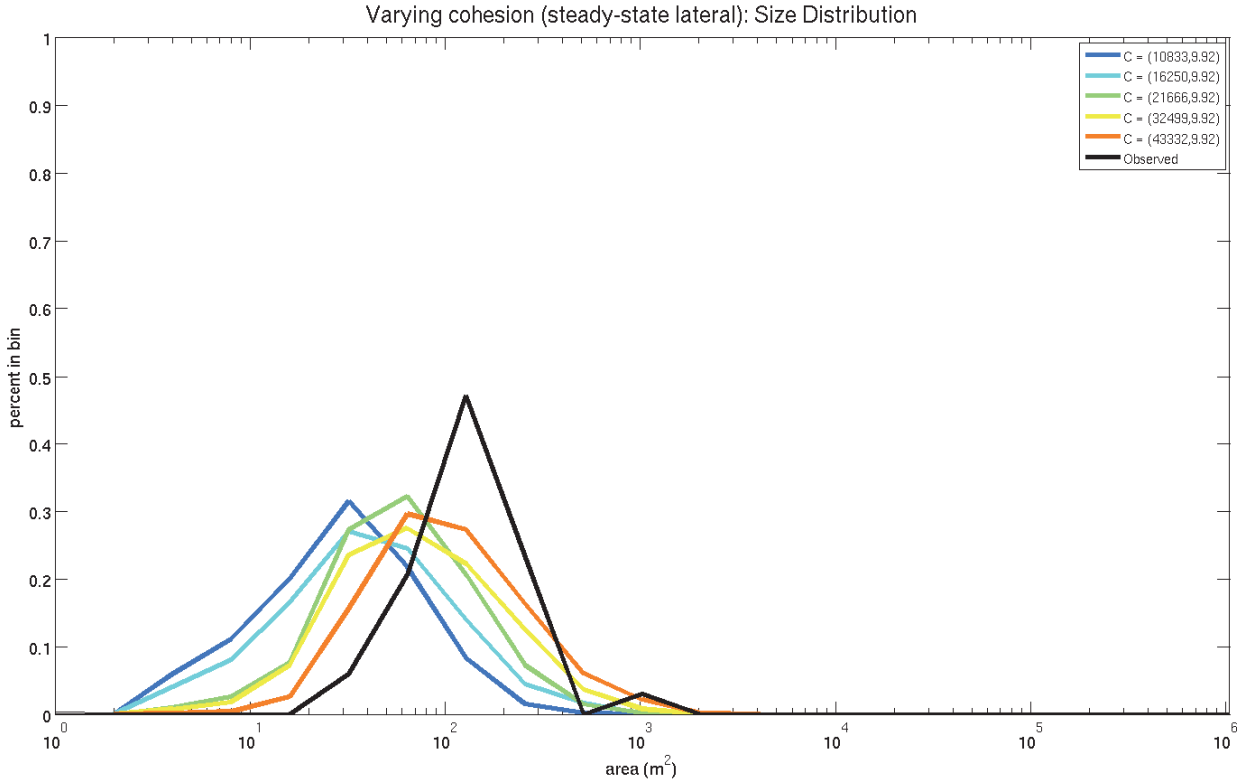

Figure 5.16. Size distributions resulting from increasing C_{r0} from *10,833 Pa* to *43,332 Pa*, for a fixed value of *j = 9.92* m^{-1}. The distribution shifts to the right (larger size) with increasing root strength.

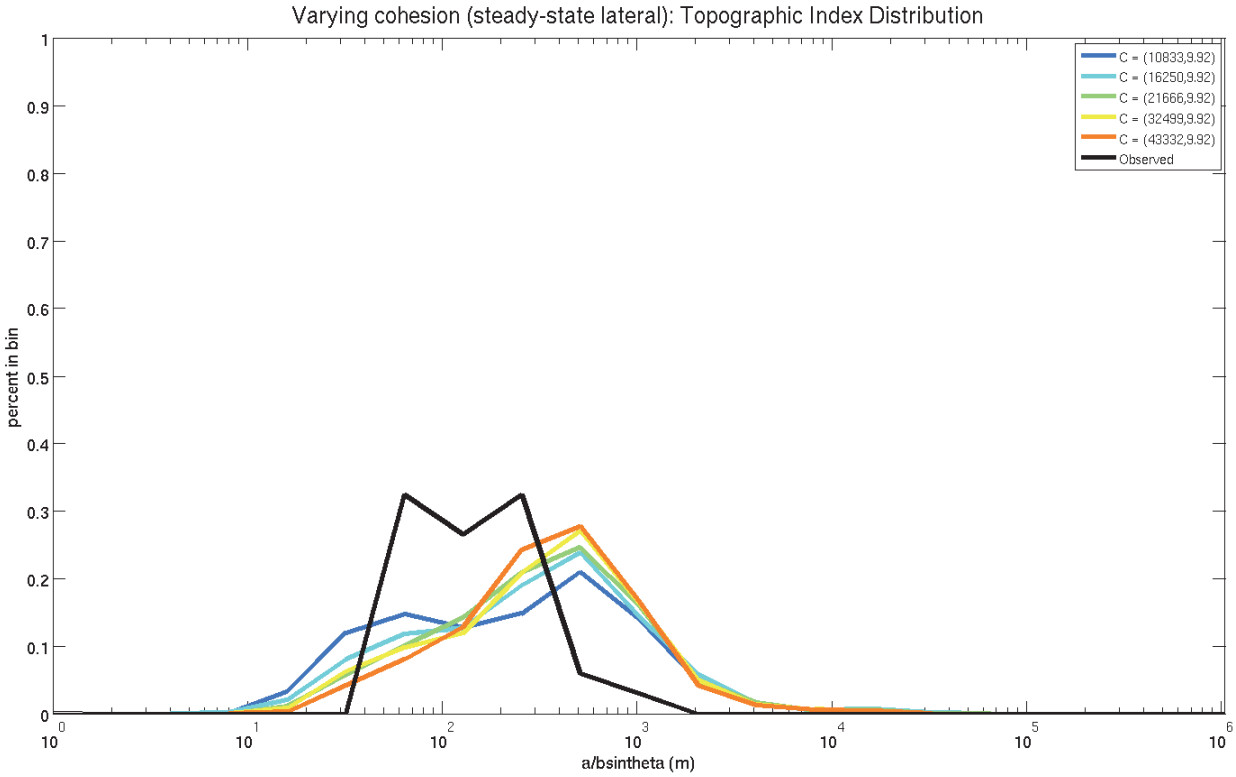

Figure 5.17. Topographic index distributions resulting from increasing C_{r0} from *10,833 Pa* to *43,332 Pa*, for a fixed value of $j = 9.92\ m^{-1}$. The distribution shifts to the right (higher drainage area) with increasing root strength.

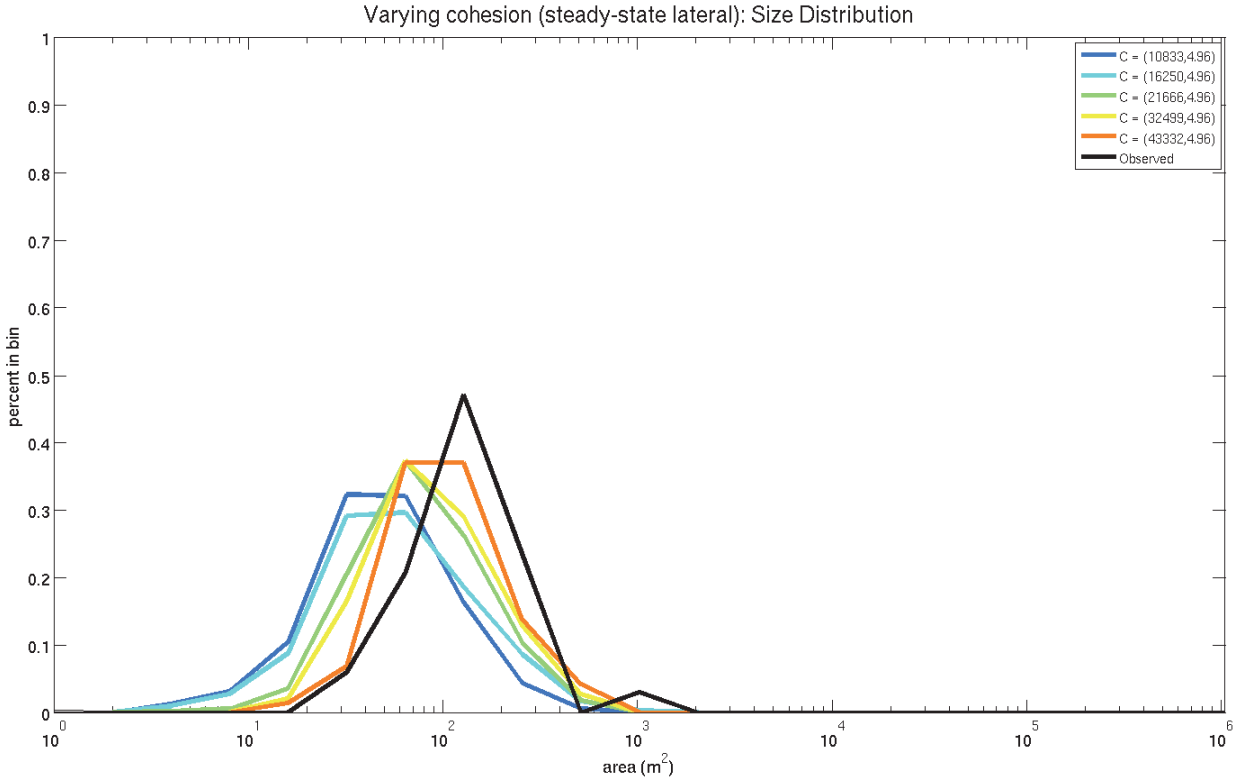

Figure 5.18. Size distributions resulting from increasing C_{r0} from *10,833 Pa* to *43,332 Pa*, for a fixed value of $j = 4.96\ m^{-1}$. The distribution shifts to the right (larger size) with increasing root strength.

All work and no play make Dino a dull boy. All work and no play make Dino a dull boy.

Figure 5.19. Shallow landslide pattern illustrating the variability of location and size emerging from an anthropometric landscape. Image: “Monique”, Y. Klein, 1960, www.yveskleinarchives.org

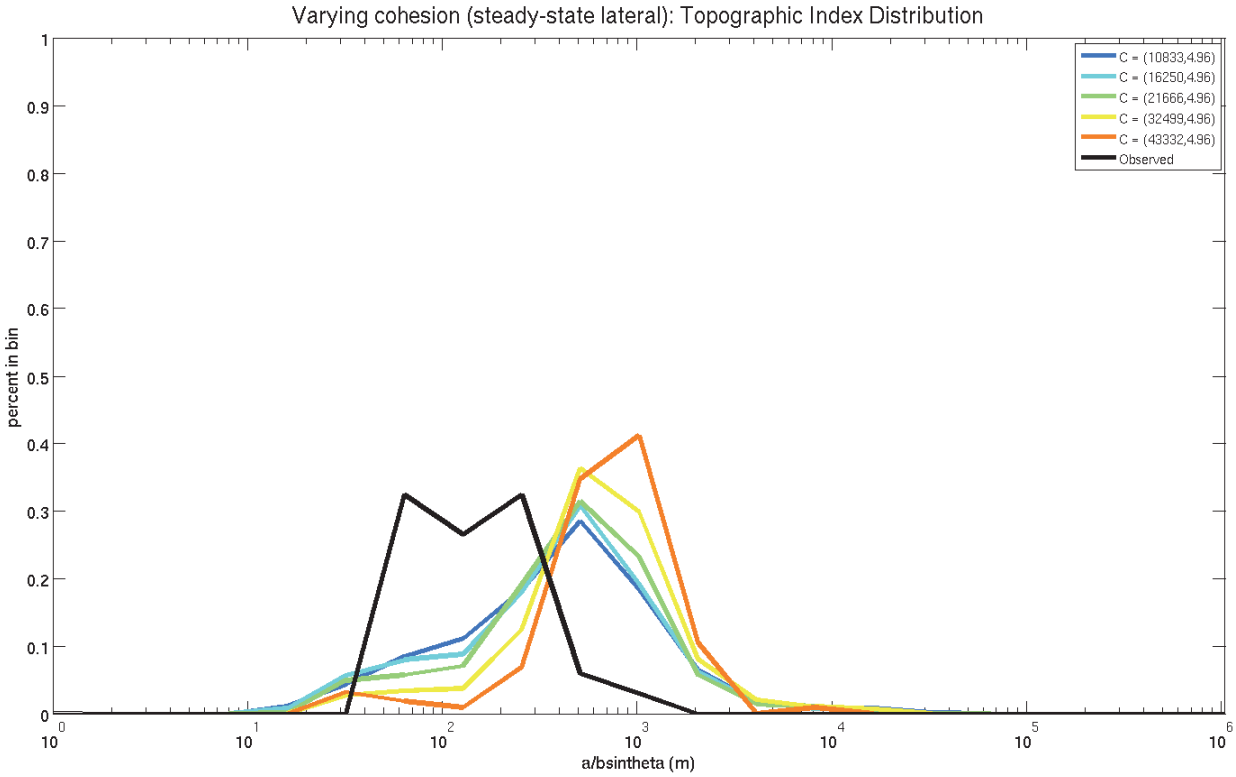

Figure 5.20. Topographic index distributions resulting from increasing C_{r0} from *10,833 Pa* to *43,332 Pa*, for a fixed value of $j = 4.96\ m^{-1}$. The distribution shifts to the right (higher drainage area) with increasing root strength.

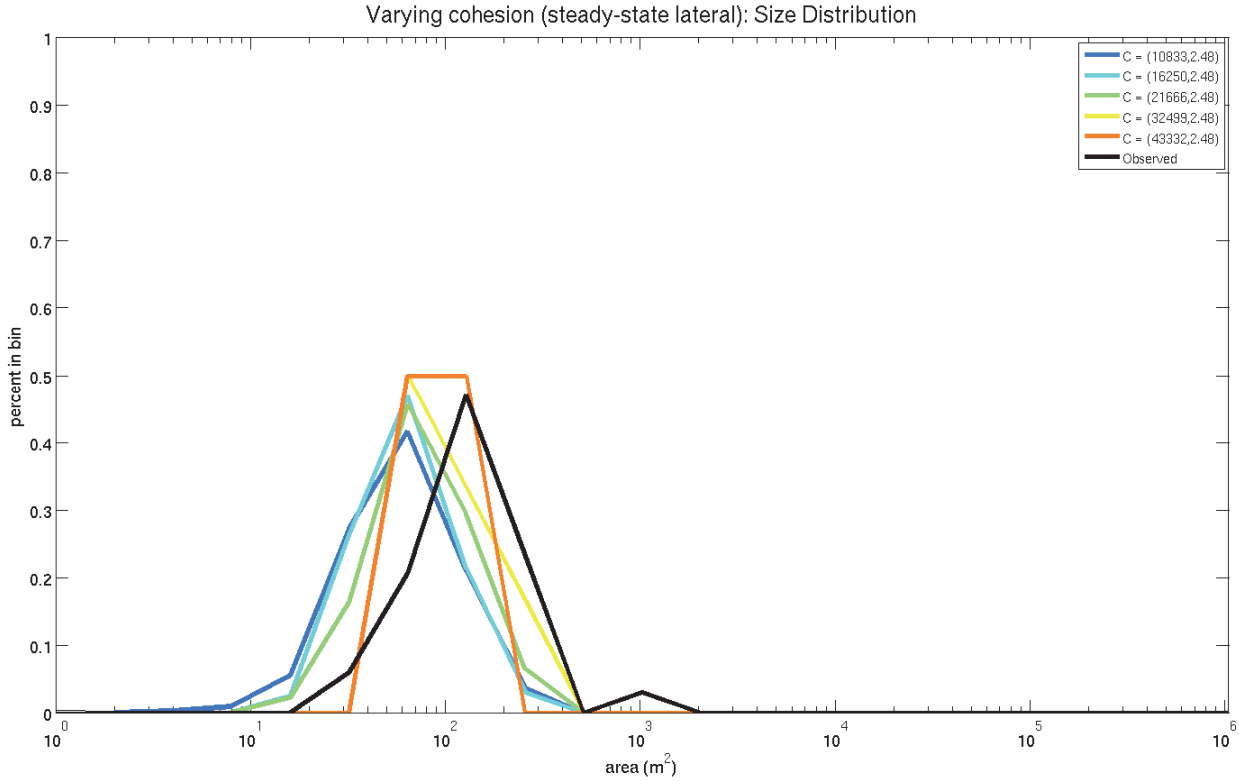

Figure 5.21. Size distributions resulting from increasing C_{r0} from *10,833 Pa* to *43,332 Pa*, for a fixed value of $j = 2.48\ m^{-1}$. The distribution shifts to the right (larger size) with increasing root strength. Only two landslides are predicted for the entire CB-MR study area in the case with highest root strength ($C_{r0} = 43{,}332\ Pa,\ j = 2.48\ m^{-1}$).

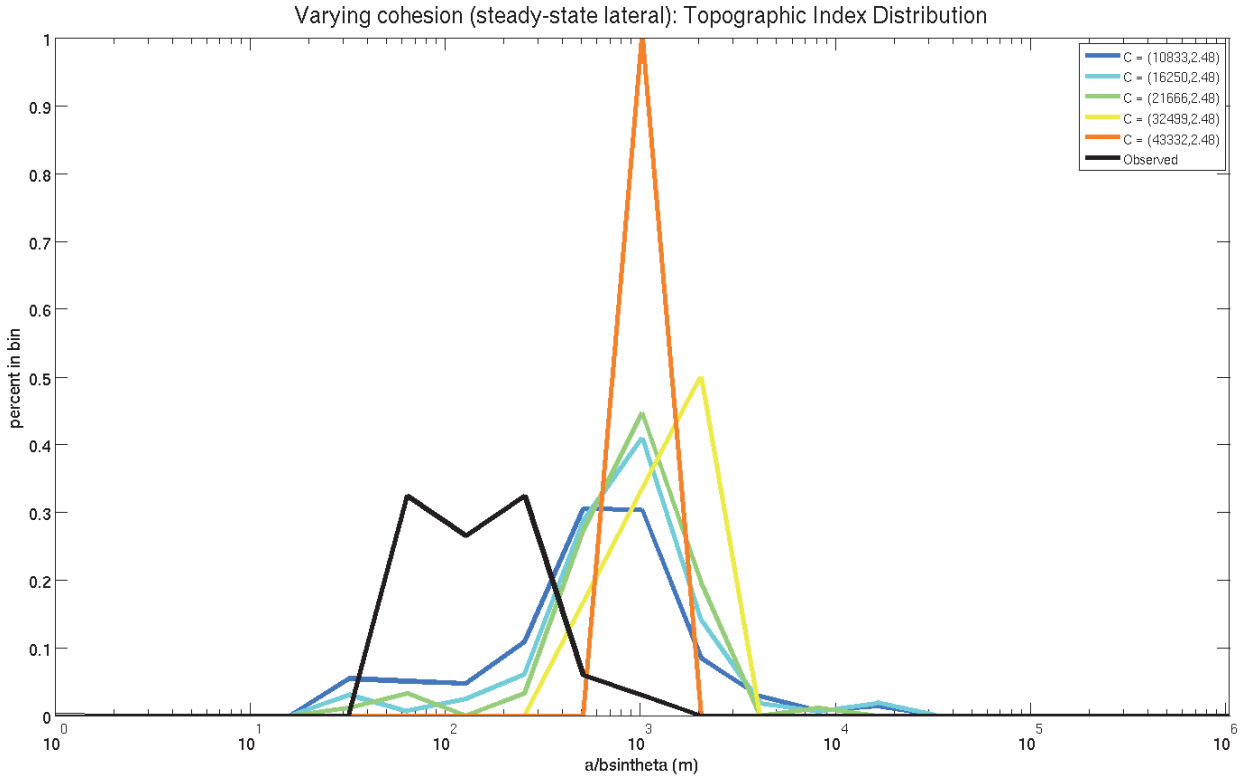

Figure 5.22. Topographic index distributions resulting from increasing C_{r0} from *10,833 Pa* to *43,332 Pa*, for a fixed value of $j = 2.48\ m^{-1}$. The distribution shifts to the right (higher drainage area) with increasing root strength, with the exception of the case with highest root strength ($C_{r0} = 43{,}332\ Pa$, $j = 2.48\ m^{-1}$), in which only 2 landslides are predicted for the entire CB-MR study area.

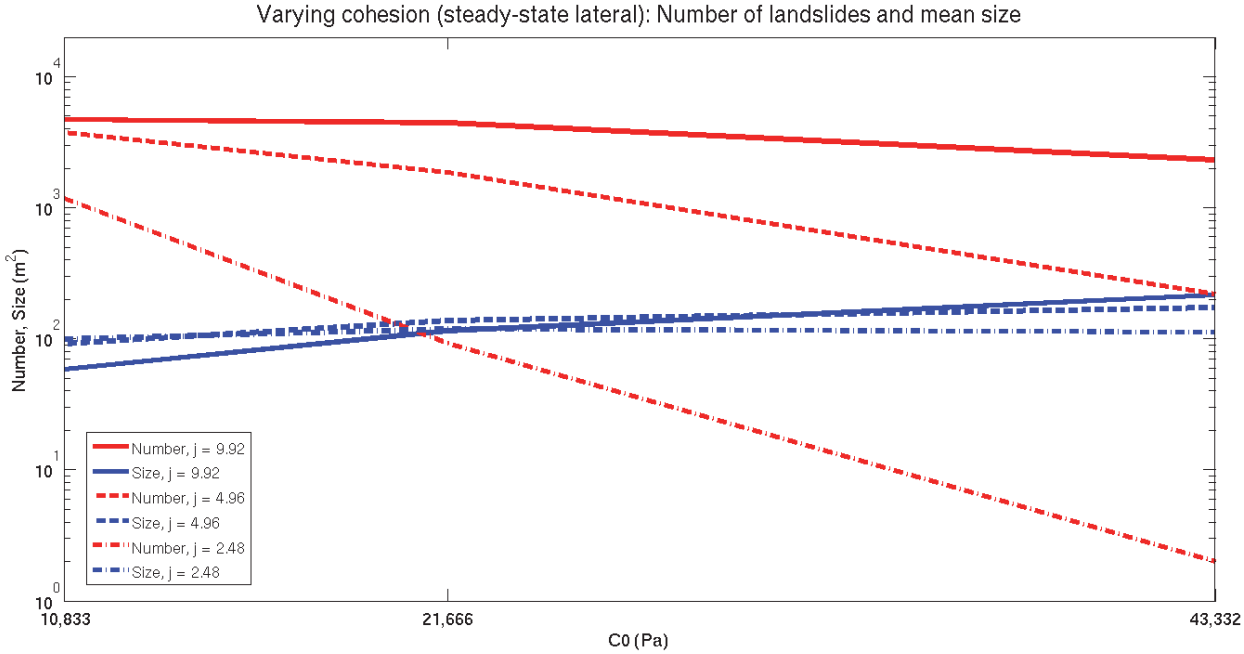

Figure 5.23. Number of shallow landslides and their mean size under increasing root strength, varied through the parameter C_{r0}, for three values of the parameter j. Increasing root strength results in a landslide size increase and a reduction in the number of predicted landslides. Size increase is most significant when root cohesion declines more rapidly with depth ($j = 9.92\ m^{-1}$). Reduction in number is most significant when root cohesion declines less rapidly with depth ($j = 2.48\ m^{-1}$).

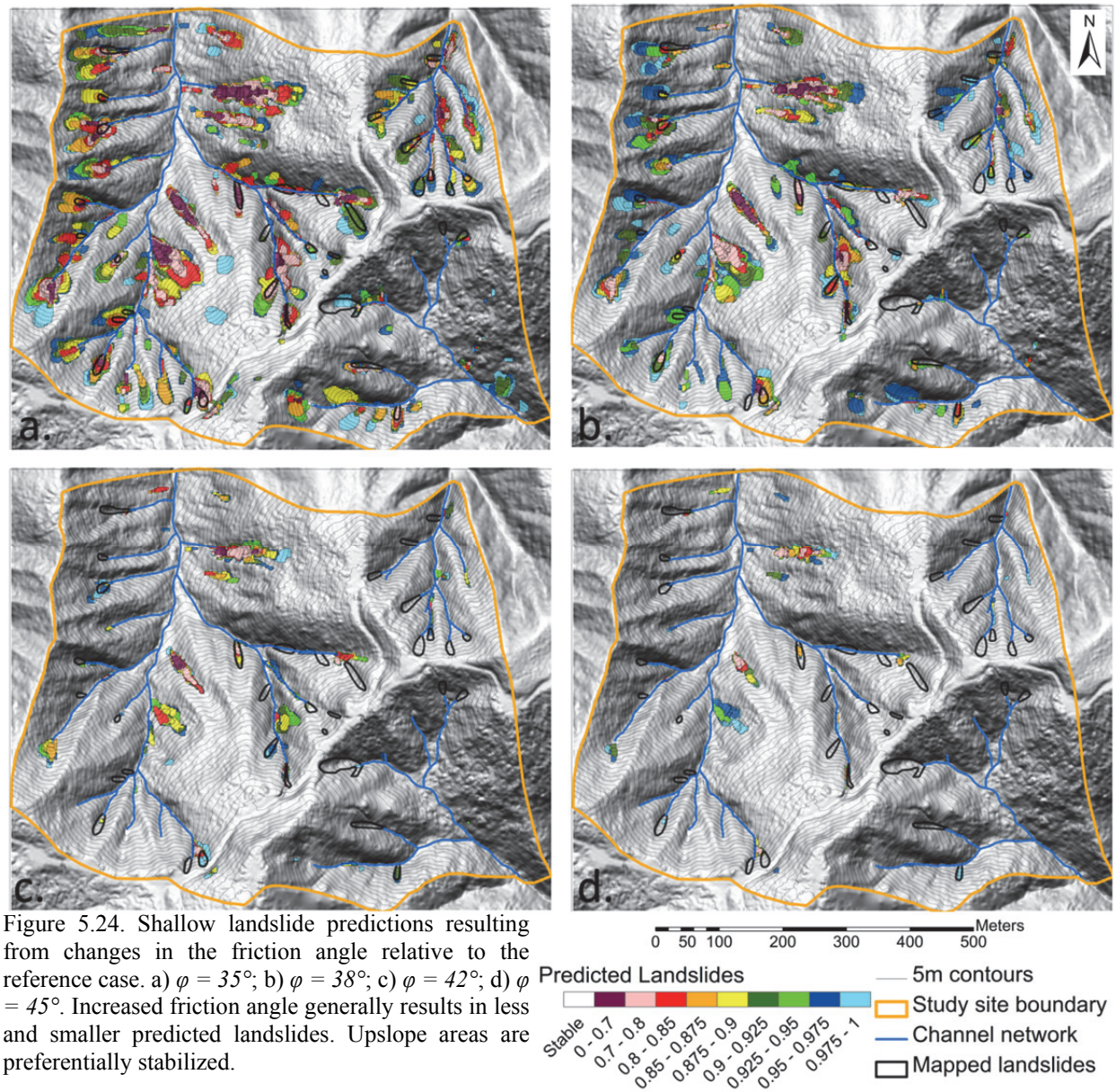

Figure 5.24. Shallow landslide predictions resulting from changes in the friction angle relative to the reference case. a) $\varphi = 35°$; b) $\varphi = 38°$; c) $\varphi = 42°$; d) $\varphi = 45°$. Increased friction angle generally results in less and smaller predicted landslides. Upslope areas are preferentially stabilized.

These observations are confirmed by the trends emerging from the PDF's of distributions resulting from this experiment. Figure 5.25 shows the size distributions obtained over a range of φ values. The distributions exhibit a moderate shift to the left (towards smaller size) when friction is increased. The topographic index distributions, shown in figure 5.26 illustrate that when friction increases predicted locations are preferentially shifted to higher topographic index values, as in the root strength experiments. The general trend of slightly decreased size and increased abundance with increased friction is summarized in figure 5.27.

5.3.4 Soil depth controls: Experiments 6 - 7

Soil depth has an important role in the stability of hillslopes as the soil mass contributes to both the driving and normal forces, and influences the effective magnitude of root cohesion, friction, and earth pressure. In this group of experiments the effect of increased or decreased soil depth on the characteristic size and location of shallow landslides at CB-MR is examined.

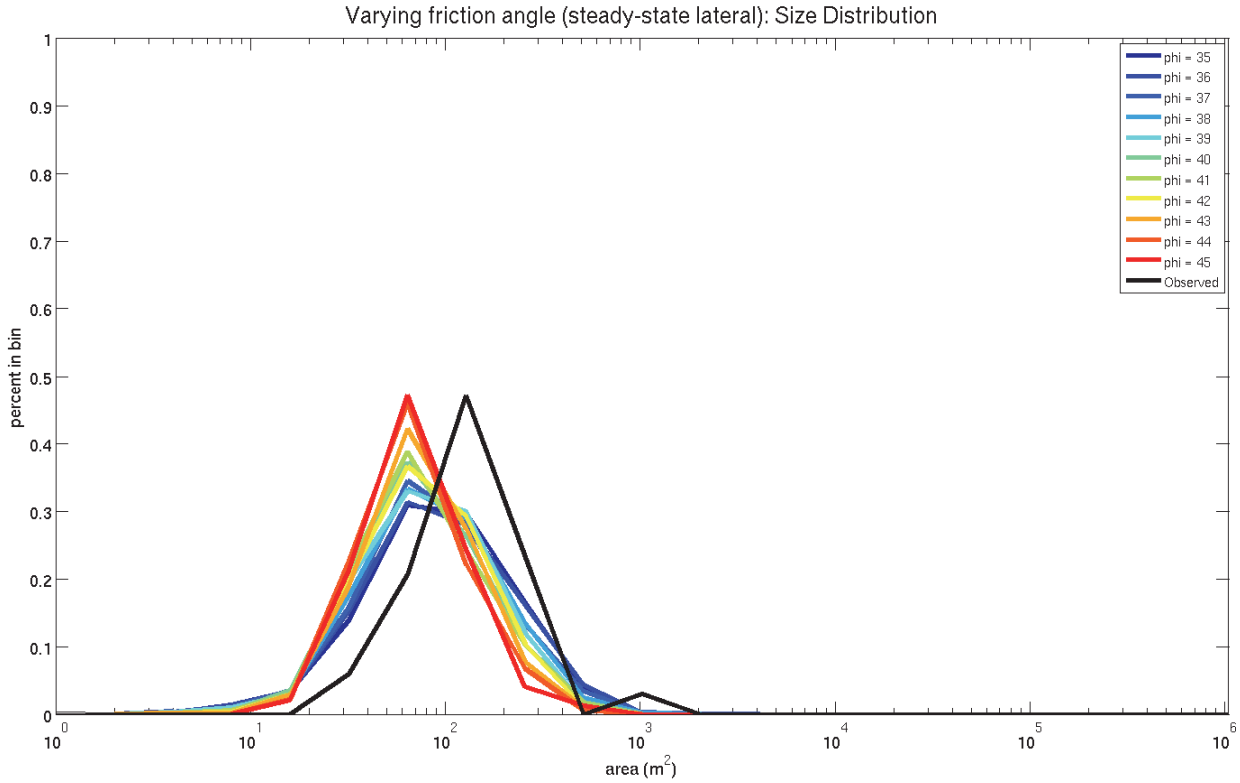

Figure 5.25. Size distributions resulting from increasing φ from *35°* to *45°*. The distribution shifts to the left (smaller size) with increasing friction.

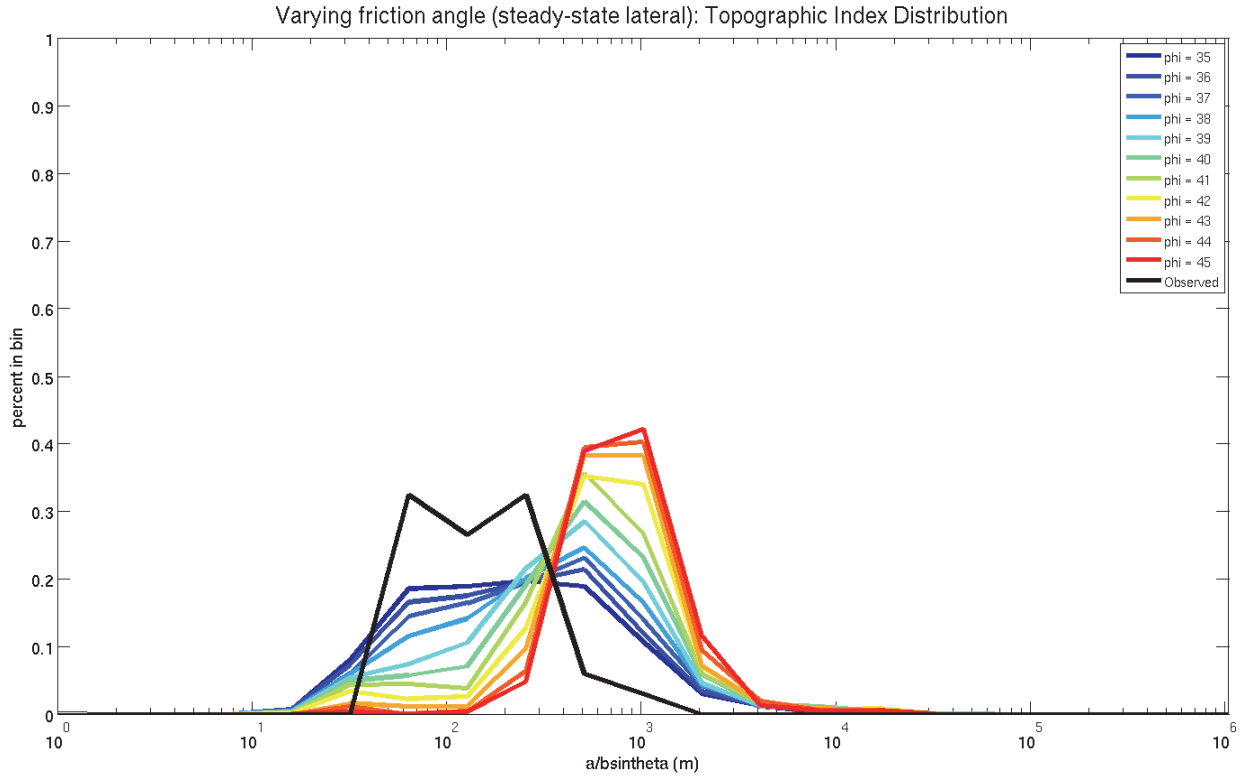

Figure 5.26. Topographic index distributions resulting from increasing φ from *35°* to *45°*. The distribution shifts to the right (higher drainage area) with increasing friction.

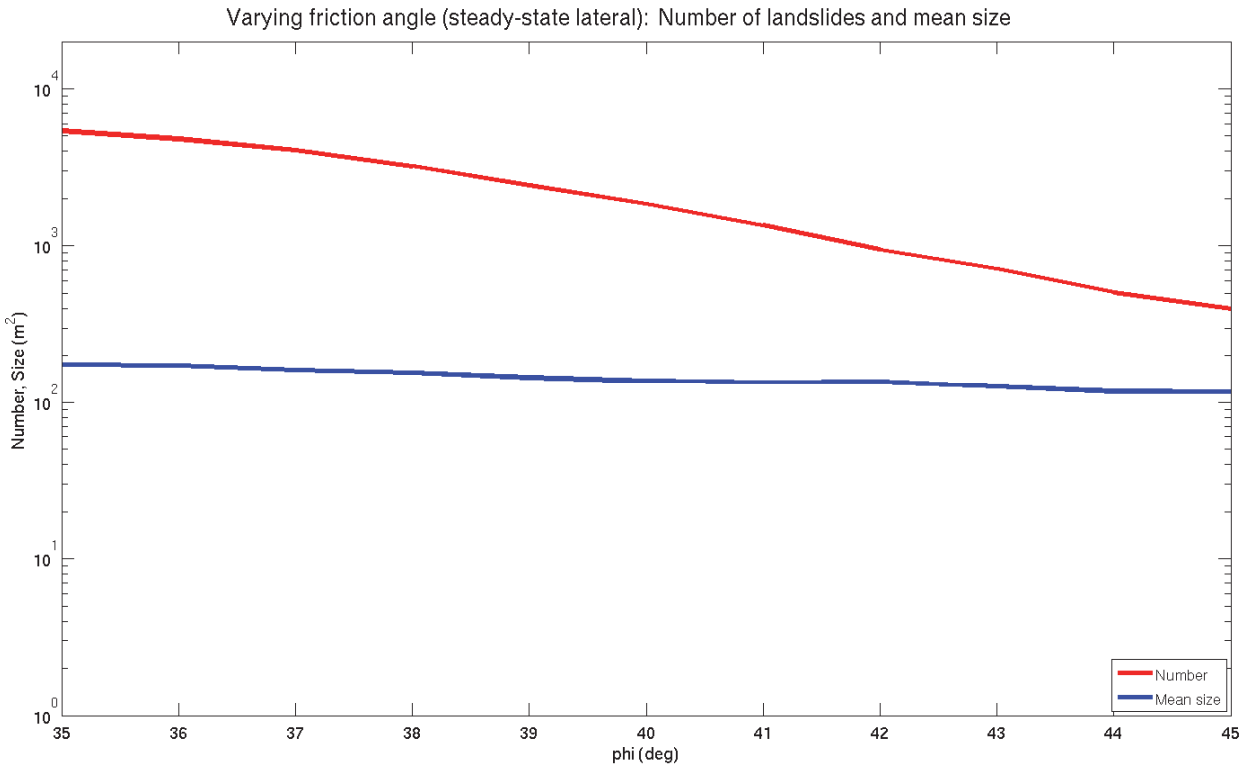

Figure 5.27. Number of shallow landslides and their mean size under increasing friction angle φ. The increase results in a slight size decrease and a decline in the number of predicted landslides.

The results of the first experiment, in which soil depth is varied proportionally relative to the reference case modeled values (see sections 2.2.3 and 4.4.1), are shown in figure 5.28. Almost no landslides are predicted when soil depth is greatly reduced. Hence, even though *h/z* is increased the dominant contribution of root strength leads to increased stability. As soil depth is increased, the number of predicted landslides and their size increases (figures 5.28a-b). As soil depth is further increased, the number of landslides remains roughly constant, and their size generally decreases (figures 5.28c-d). The size distributions resulting from this experiment are shown in figure 5.29, illustrating the increase in predicted landslide size followed by a decrease once soil depth surpasses the reference case modeled values. As soil depth is increased a shift of predicted preferential landslide locations can also be observed: when soil depth is reduced landslides are preferentially in locations with high topographic index and when soil depth is increased the moved to locations with low topographic index (figure 5.30). Figure 5.31 shows how the number and the size of predicted landslides peaks, perhaps not coincidentally, when soil thickness is the same as the values predicted by the soil depth model.

In the second experiment (experiment 7) soil depth is varied uniformly across the CB-MR study area. It is important to note that for the reference case values of root strength, friction angle and *log(q/K)* no landslides are predicted over the entire area when soil depths of *0.25 m* and *0.5 m* (figure 5.35), due to the strong effect of root cohesion in thin soils. Figure 5.32 (a-c) shows the landslide predictions for uniform soil depth values of 1, 2, and 3m, respectively. There one can observe an opposite trend from the previous experiment as the number of predicted landslides initially decreases and then increases. In fact, figure 5.35 reveals a more complex pattern: after soils are thick enough for landslides to occur (more than *0. 5 m* in this experiment, after which basal cohesion drops below *1 kPa*) there is an increase of predicted landslides; this is followed

by a decrease when depths are between *1.25* and *2.25 m*; as soil depths continue to increase, predicted landslides become more abundant but the trend ceases when soils exceed *6 m*. The average size generally decreases, but does so more rapidly after soil depths of *2.25 m*; however, this trend is reversed once depths exceed *5 m* (figure 5.35). This complex trend (quite different from the proportional soil depth experiment) is also observed in the size distributions, shown in figure 5.33.

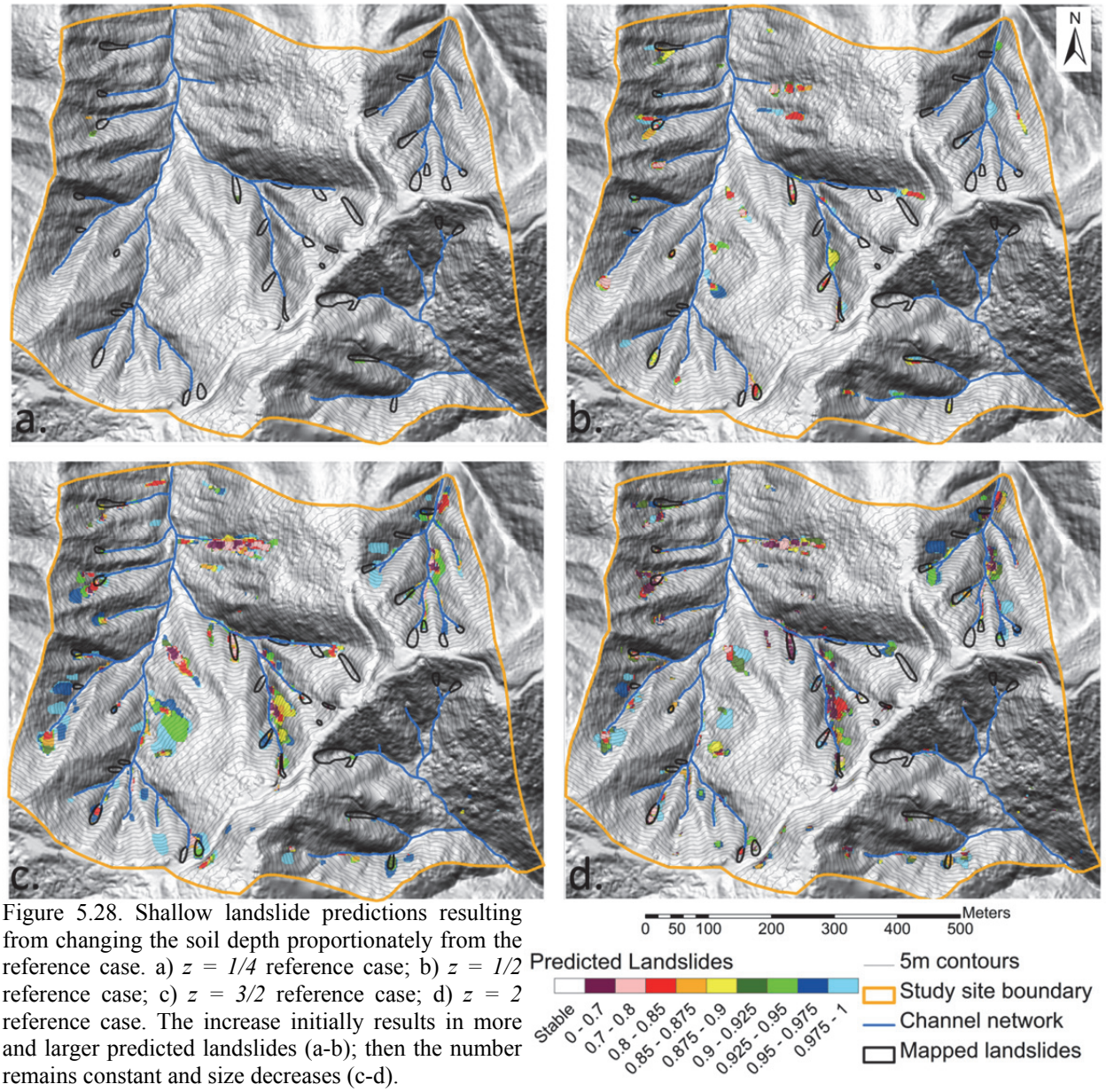

Figure 5.28. Shallow landslide predictions resulting from changing the soil depth proportionately from the reference case. a) $z = 1/4$ reference case; b) $z = 1/2$ reference case; c) $z = 3/2$ reference case; d) $z = 2$ reference case. The increase initially results in more and larger predicted landslides (a-b); then the number remains constant and size decreases (c-d).

The topographic index distribution instead shows a similar trend as in the proportional soil depth experiment: when soils are thin landslides are preferentially predicted in locations with high topographic index and when soils are thick they are preferentially predicted in low topographic index locations (figure 5.34). There is a slight difference however: this trend stops when soils exceed 3.5 m, in which case a very slight increase in the topographic index is observed (figure 5.34).

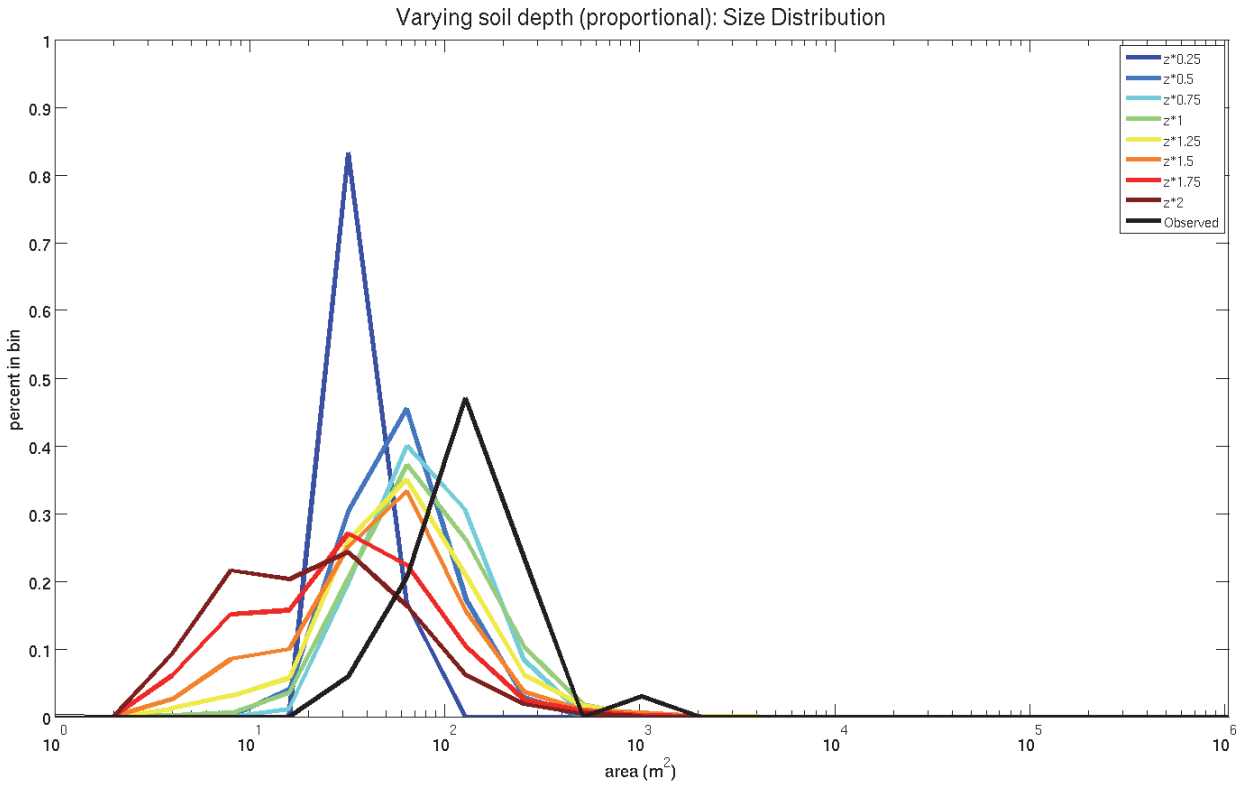

Figure 5.29. Size distributions resulting from proportionally varying soil depth from ¼ to twice the reference case modeled values. Predicted size increases until depths reach the reference case modeled values, then decreases.

5.3.5 Topographic controls: Experiment 8

In the final experiment of this chapter, the effect of varying the degree of roughness and dissection of the landscape is explored. The topography is smoothed using a Gaussian filter of size varying from *0* to *110 m*. Soil depth is re-calculated after each smoothing iteration as a different surface is produced by each filter size. Gaussian smoothing reduces both noise and detail, as can be seen in figure 5.36. Initially the structure of the topography is maintained but the fine-scale variations are removed (figure 5.36b). As the filter size is increased, adjacent hollows merge, and the topography becomes less dissected (figure 5.36c). With large filter size, the ridge and valley topography is progressively erased, resulting in a very smooth landscape with few large valleys, and generally lower slopes (figure 5.36d).

Figure 5.36 shows the effect of smoothing the landscape on predicted landslides. As the fine-scale variations are removed, predicted landslides become larger and more abundant (figure 5.36b). This trend can still be observed in figure 5.36c, but after the topography becomes less dissected and slopes decrease the number of landslides diminishes (figure 5.36d). Predicted landslide size continues to increase throughout the experiment as the landscape becomes progressively more uniform (figure 5.36a-d).

The increase of predicted landslide size is evident in the PDF's shown in figure 5.37: as the filter size increases and the landscape becomes more uniform the distributions shift to the right (larger size). The PDF's of the predicted topographic index are shown in figure 5.38. The mode of the distributions remains essentially constant but the range diminishes significantly: very few high-slope, low-area locations exist in the smoothed landscape, and locations with high drainage area are too flat to fail. Figure 5.39 shows how the average predicted landslide size increases

throughout the experiment, but also illustrates a more complex trend in landslide abundance: predicted landslides increase in number until the filter size reaches *30 m*, illustrating the effect of removing only the fine-scale variations from the landscape; with larger filter sizes landslide number generally decreases although a slight increase is observed when the filter size is between *70* and *90 m*.

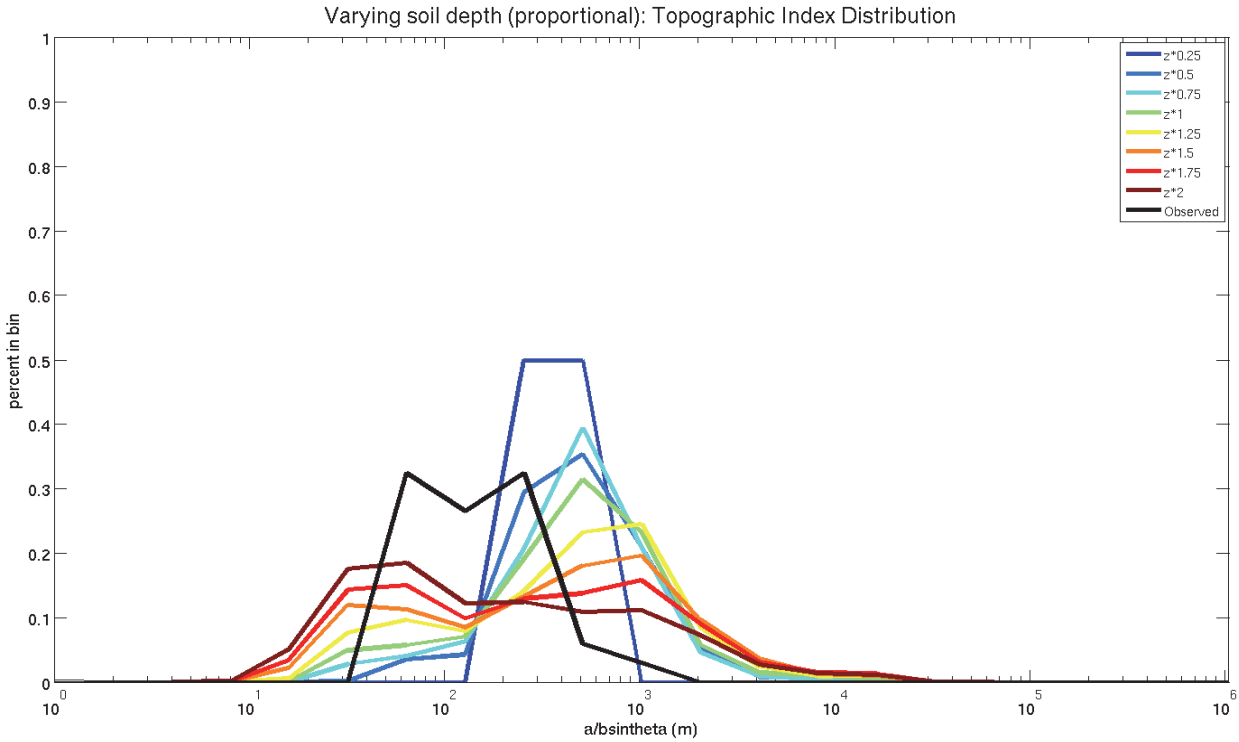

Figure 5.30. Topographic index distributions resulting from proportionally varying soil depth from ¼ to twice the reference case modeled values. As soil depth is increased, more favorable upslope areas (higher slope, lower drainage area) develop.

5.3.6 Summary of results

Table 5.2 summarizes the general trends in characteristic size, location, and abundance of predicted shallow landslides resulting from the experiments presented in this chapter. Size increases with precipitation (both p and q), root strength, and landscape smoothness increase; it decreases when friction angle or uniform soil depth increase. Location shifts towards higher drainage area when root strength or friction angle are increased, and towards higher slopes when soil depth is increased. Landslides are generally more abundant when precipitation or soil depth is increased and less abundant when root strength or friction is increased. More complex trends emerge in the other experiments: landslide size first increases then decreases as soil depth are proportionately varied (with the peak in size corresponding to the values produced by the soil depth model); with increasing precipitation, under the shallow subsurface steady-state model, landslides are initially found in locations with greater slopes, then in locations with high drainage area, and as both upslope and downslope locations expand towards each other topographic indices in the middle of the range are preferred; increasingly sooth realizations of the landscape initially lead to an increase of the number of predicted landslides, followed by a general decline.

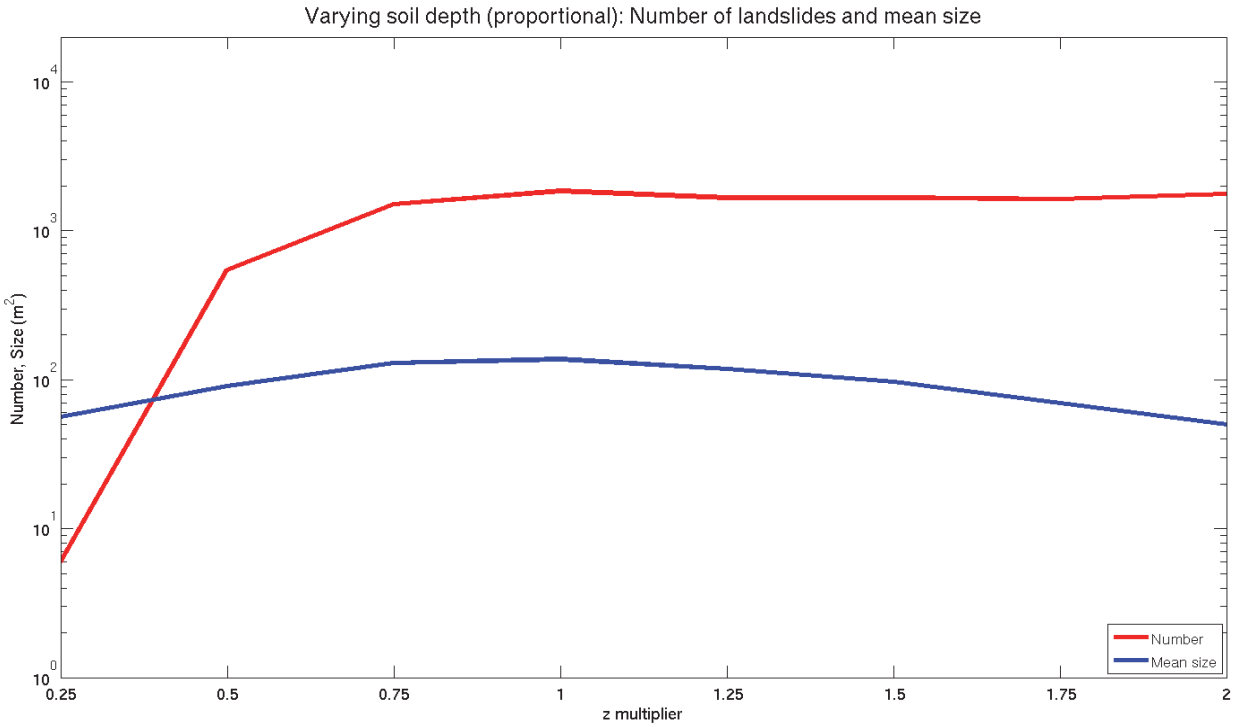

Figure 5.31. Number of shallow landslides and their mean size resulting from proportionally varying soil depth from ¼ to twice the reference case modeled values. The increase results first in a size increase (soil depth less than reference case), then decrease (soil depth greater than reference case); the number of predicted landslides increases until depths reach the reference case values, then remains roughly constant.

These results illustrate some opposing trends: as would be expected, increasing precipitation or decreasing root strength result in a greater number of predicted landslides. However in the former case an increase in characteristic size is observed, while in the latter characteristic size is reduced. This is not the case, however, if strength is decreased by reducing friction: in this case predicted landslides are more abundant, but also exhibit a larger characteristic size.

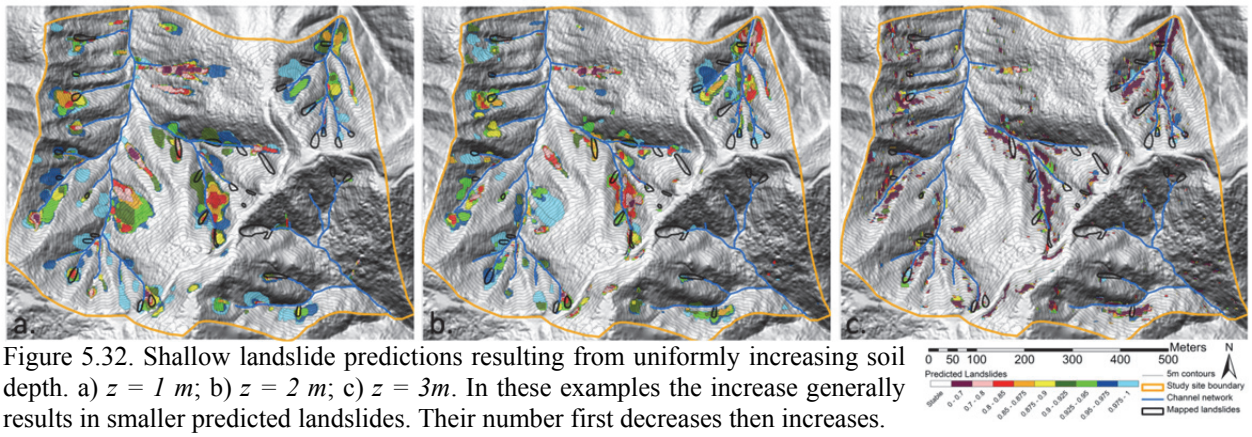

Figure 5.32. Shallow landslide predictions resulting from uniformly increasing soil depth. a) *z = 1 m*; b) *z = 2 m*; c) *z = 3m*. In these examples the increase generally results in smaller predicted landslides. Their number first decreases then increases.

Landslides mapped during the ten year of research at CB-MR, are used to evaluate the performance of the procedure in the experiments presented in this chapter. Table 5.3 presents the parameter choices resulting in the highest F-score and MCC measures (see section 3.4.5.2 for definitions). For the parameters that were best constrained in the field (root strength, and friction angle), the field measurements result in the best performance with respect to the observations. This suggests that field data can be used to calibrate less constrained parameters.

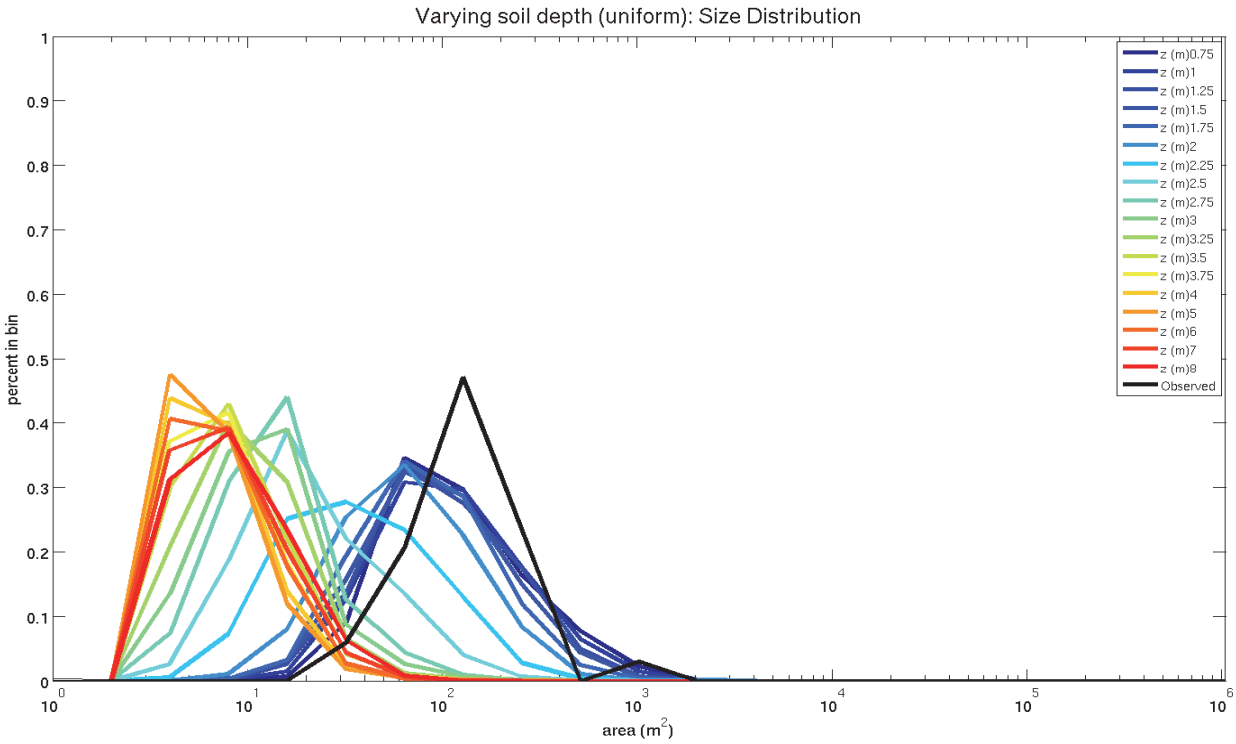

Figure 5.33. Size distributions resulting uniformly from uniformly increasing soil depth from *0.25 m* to *8 m*. Predicted size decreases drastically once soil is thicker than the rooting depth assumed by the exponential root strength decay function. When soils are extremely thick, strength is added by earth pressure and size can increase again.

5.4 Discussion

In this chapter we performed eight experiments in which properties controlling slope stability were systematically varied. Topographic induced variation in soil depth and pore pressure leads to the constant slope stability properties producing spatial structure in instability. As these properties vary across the landscape, the spatial distribution of areas favorable to landsliding changes in the landscape. This in turn affects characteristic size and location of discrete shallow landslides predicted by our procedure (represented by a PDF of size and topographic index, respectively). Varying the controlling stability properties caused landslide distributions to sample different parts of the landscape and thus to shift the PDF systematically. Four groups of experiments were performed with a focus on hydrological inputs, soil strength (through friction and root cohesion), soil depth, and topographic roughness. The parameters used for these experiments are listed in table 5.1, and a brief summary of results is given in table 5.2.

In the first group of experiments (experiments 1-3), hydrological "quickly-changing" parameters are varied while the other "slowly-changing" characteristics of the landscape (root strength, material strength, friction angle, soil depth) are held constant. In the first experiment it was assumed that the development of water table heights across the landscape is the result of topographically steered subsurface flow, resulting in higher water levels in convergent areas. Such a model is intended to represent impact of precipitation on landsliding over the long time scale (days to weeks). In the second experiment it was instead assumed that no lateral redistribution of water occurs, resulting in uniform water table heights. This model is chosen as an example of short time scale (minutes to days) effects. In the third experiment the sum of the

effective steady-state precipitation q and the uniformly applied instantaneous pressure addition p was held constant, and the relative contribution of vertical to lateral contributions to the water table was explored.

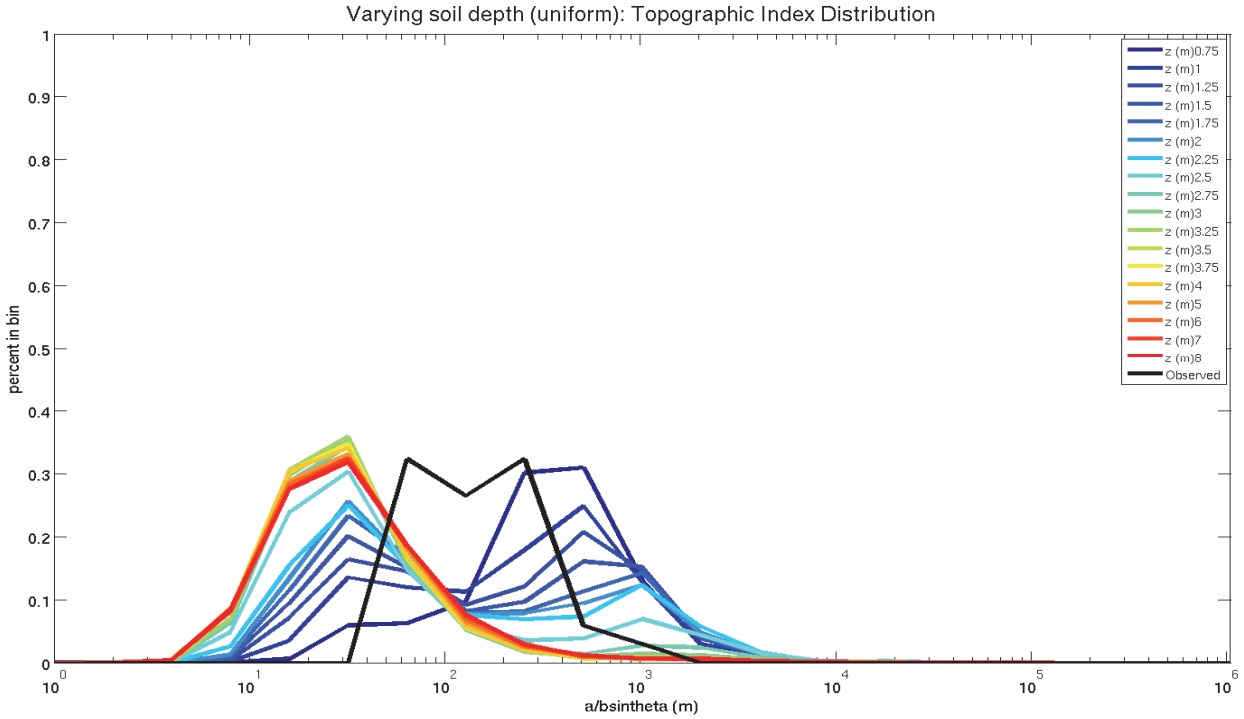

Figure 5.34. Topographic index distributions resulting uniformly from uniformly increasing soil depth from *0.25 m* to *8 m*. As soil depth is increased, more favorable upslope areas (higher slope, lower drainage area) develop.

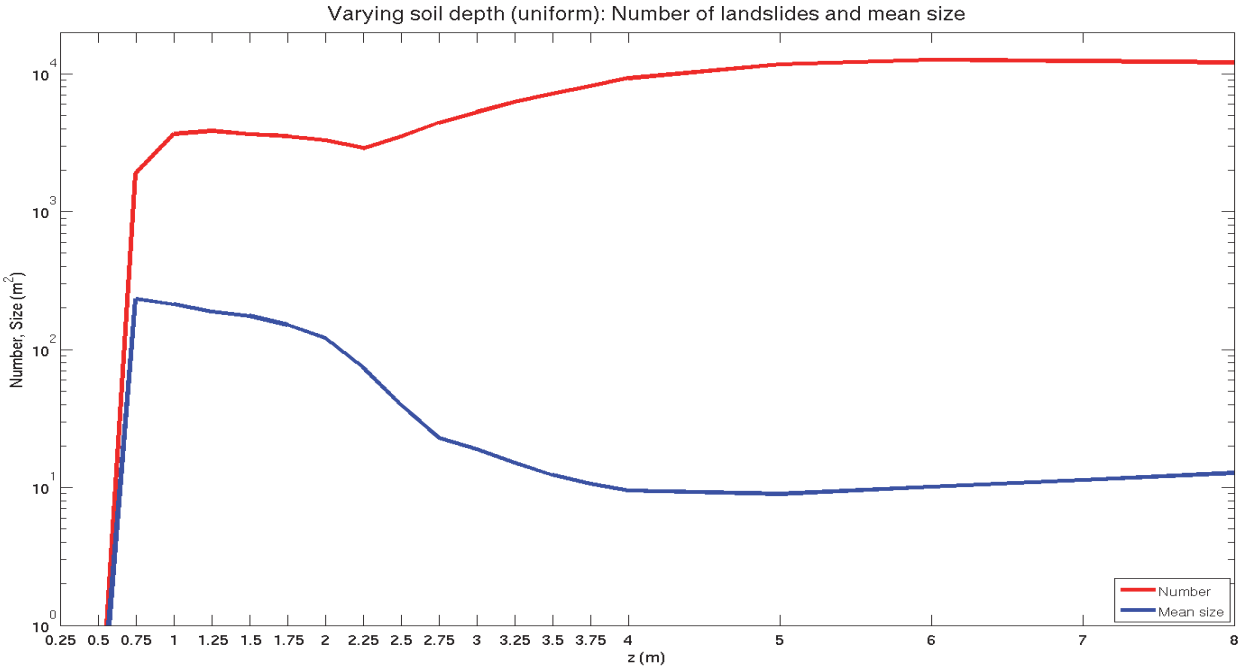

Figure 5.35. Number of shallow landslides and their mean size resulting from uniformly increasing soil depth from *0.25 m* to *8 m*. No landslides are predicted for depth less than *0.75 m*; a complex pattern emerges: the number of predicted landslides increases until $z = 1.25\ m$, then decreases until $z = 2.25\ m$; at this point the number increases again until $z = 6\ m$, after which a slight decrease is observed. Predicted landslide size decreases as soil depth increases to *5 m* (and does so more rapidly when $2\ m < z > 2.75\ m$), then increases again at a moderate rate.

As would be expected, increasing precipitation results in an increased number of predicted landslides, regardless of the hydrological model adopted (figures 5.5 and 5.9). More locations having a higher relative saturation ratio (*h/z*) results in more predicted landslides. Preferential location of landslides is affected by the different (and over-simplified) hydrological processes: while with low precipitation landslides can only occur in steep areas, with increasing precipitation the topographic index distributions take a very different form depending on whether lateral redistribution or vertical delivery of water dominate. In the former case, the saturated field expands outward from convergent areas where subsurface flow concentrates (figure 4.10), while in the latter case it expands outward from steep divergent areas where soils are thinnest (figure 4.11).

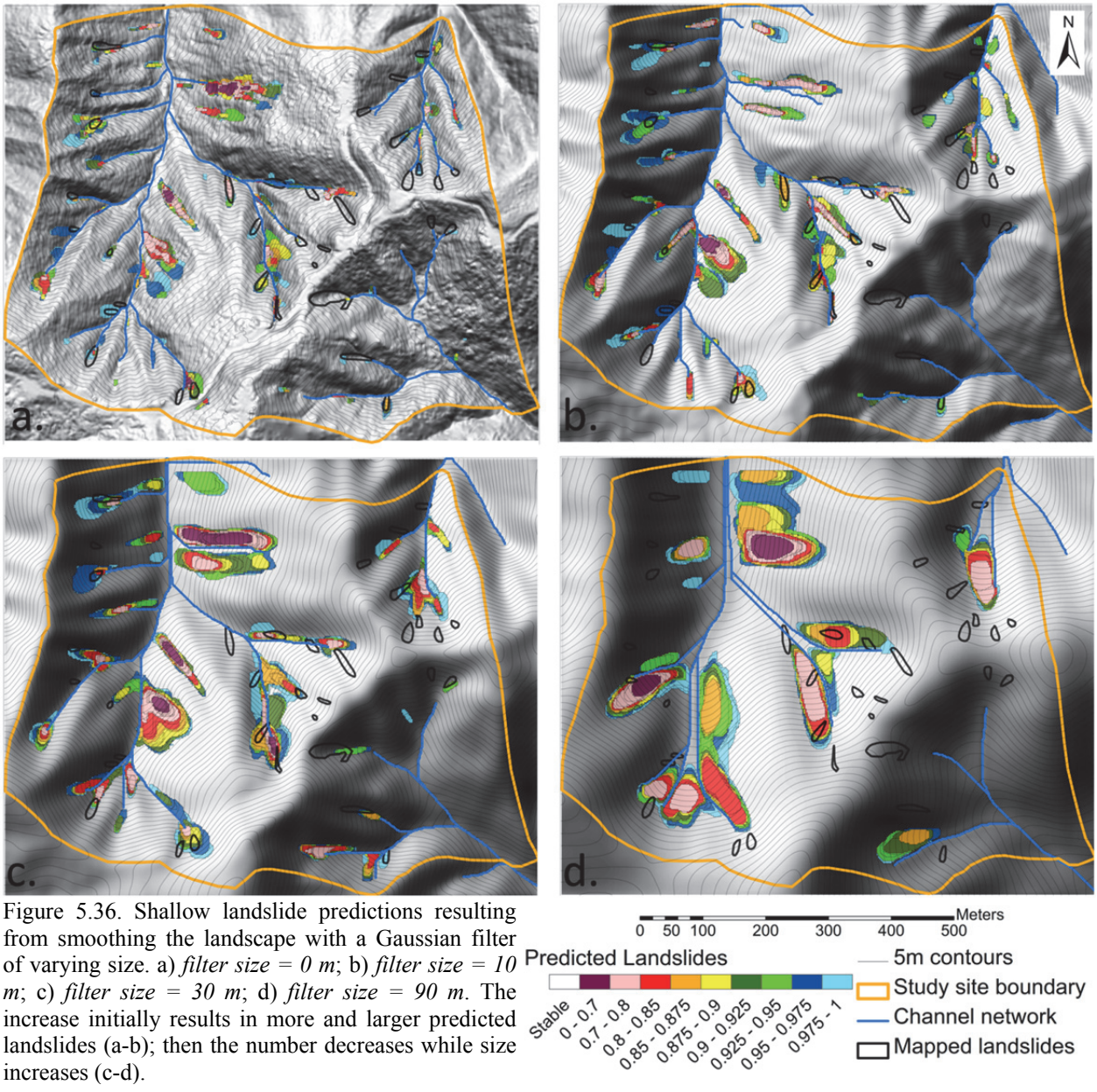

Figure 5.36. Shallow landslide predictions resulting from smoothing the landscape with a Gaussian filter of varying size. a) *filter size = 0 m*; b) *filter size = 10 m*; c) *filter size = 30 m*; d) *filter size = 90 m*. The increase initially results in more and larger predicted landslides (a-b); then the number decreases while size increases (c-d).

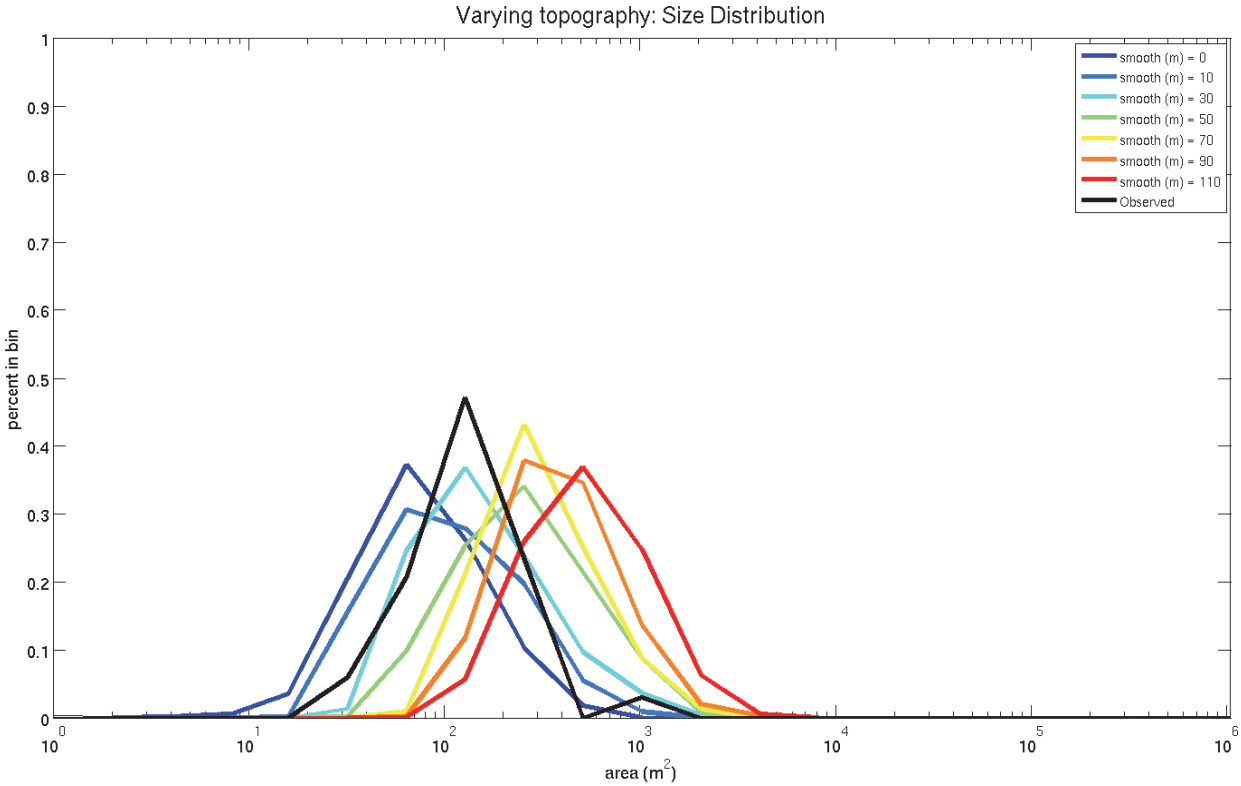

Figure 5.37. Size distributions resulting from progressive smoothing of the landscape using a Gaussian filter of size from *0 m* to *110 m*. As the landscape is smoothed (and slopes decrease) the distribution shifts to the right (larger size).

Under the lateral model and with relatively moderate precipitation (q), the distribution is bi-modal with landslides occurring in areas of high slope or high drainage area (figure 5.4). As precipitation further increases the landslides farthest upslope can only expand down the hollow axis where subsurface flow concentrates and relative saturation is higher, and the landslides farthest down the hollow axis can only expand upslope as slope is insufficient below. As a result, in the limit the topographic index assumes a mode which is in the middle of the range (figure 5.4). Perhaps not coincidentally, this limit case coincides with the topographic index distribution derived from the observed landslide dataset. In contrast, when vertical delivery of precipitation (p) to the water table dominates, the downslope expansion of landslides is strongly limited by thickening soils which decrease relative saturation. As a result the topographic index distribution changes less than in the case of lateral redistribution with increasing precipitation (figure 5.8). As with the number of predicted landslides, their size also increases independently of the hydrological model used in the experiments (figures 5.3 and 5.7). This is because as the relatively saturated field expands the extent of areas favorable to landsliding also expands, and in the absence of other limiting factors a larger size generally results in increased instability. Larger sizes are generally produced in the vertically-dominated experiments than in the latererally-dominated ones, as in this landscape the relative saturation patterns driven by p extend farther up and outside the hollow axis, resulting in a wider unstable area, particularly at the heads of the hollows (figure 5.6).

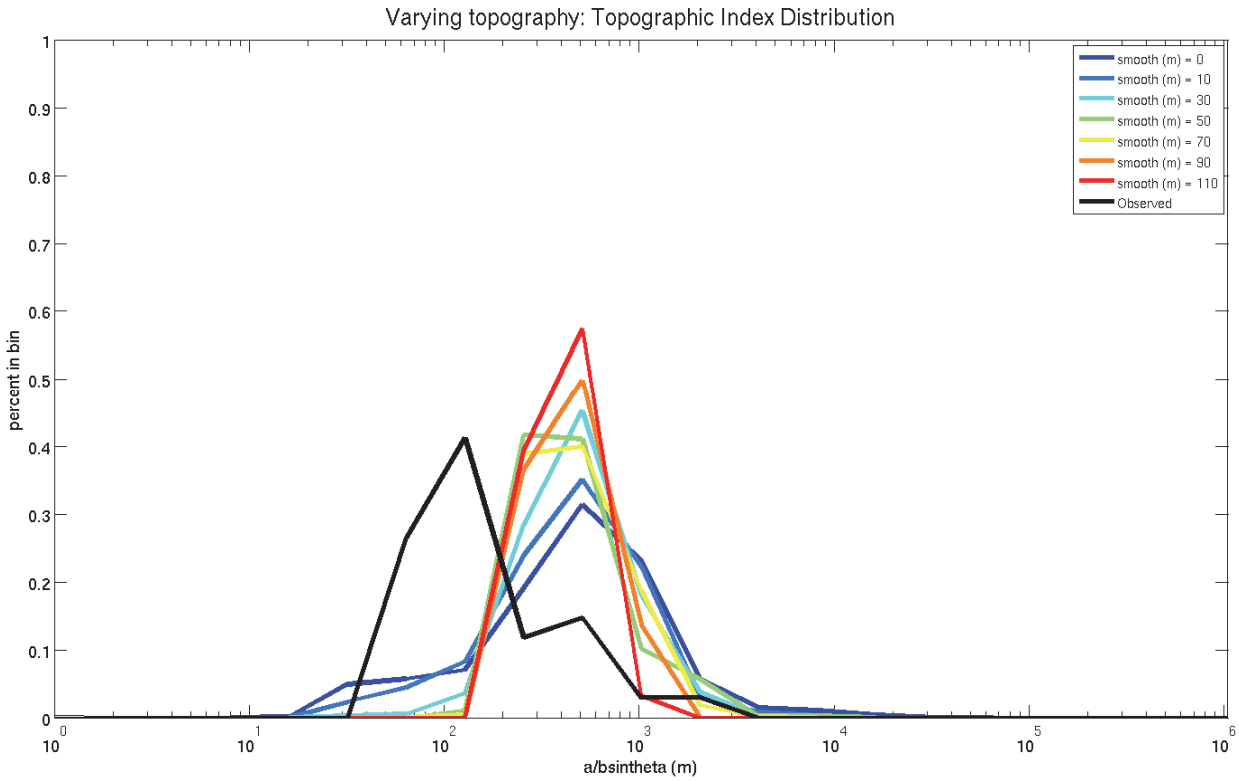

Figure 5.38. Topographic index distributions resulting from progressive smoothing of the landscape using a Gaussian filter of size from *0 m* to *110 m*. As the landscape is smoothed (and slopes decrease) the distribution tightens.

The increase in predicted landslide size resulting from an increase in precipitation (p or q) in these experiments may seem inconsistent with the results reported by Casadei et al. [2003b] who concluded that as the soil gets wetter, critical landslide size decreases. In fact, the synthetic experiments presented in chapter three show a very similar result: the wetter landslides in figures 3.14 and 3.15 are indeed the smallest. The difference lies in the fact that Casadei et al. [2003b] focus on the *critical* size (defined as the minimum size needed for the factor of safety to go below a value of 1), and do not consider that there could be a larger size with an even lower factor of safety. In contrast, here the most *probable* size (defined as the most likely as indicated by a *probability density function*) is reported. Although the non-homogeneous landscape properties of these experiments do not allow a direct comparison with the results of Casadei et al. [2003b], the fact that an expanded high-pore pressure field can cause landslides that are larger than the critical size (but less stable) is not inconsistent with their results.

In the next set of experiments (experiments 4-5), the effect of increased strength of the soils was explored. In experiment 4 the increased strength derives from root reinforcement, while in experiment 5 it derives from the shear strength of the soils (as expressed through the friction angle). Root reinforcement is modeled here by an exponential function representing the decay of root strength with depth in the soil profile (equations 2.18 – 2.20). Thus, root strength can be increased by increasing the initial value C_{r0} or by decreasing the shape factor j which controls how quickly the strength declines with depth. In both cases the number of predicted landslides decreases with increased root strength, although the reduction is most significant when root cohesion declines less rapidly with depth (figure 5.23). This result is consistent with the Reneau and Dietrich [1987] and Casadei et al. [2003] predictions that critical width increases with root

strength (they could not estimate size because they could not compute both width and length). In this case the distinction between critical and probable size is unnecessary: if the critical size increases, the probable size must increase as well.

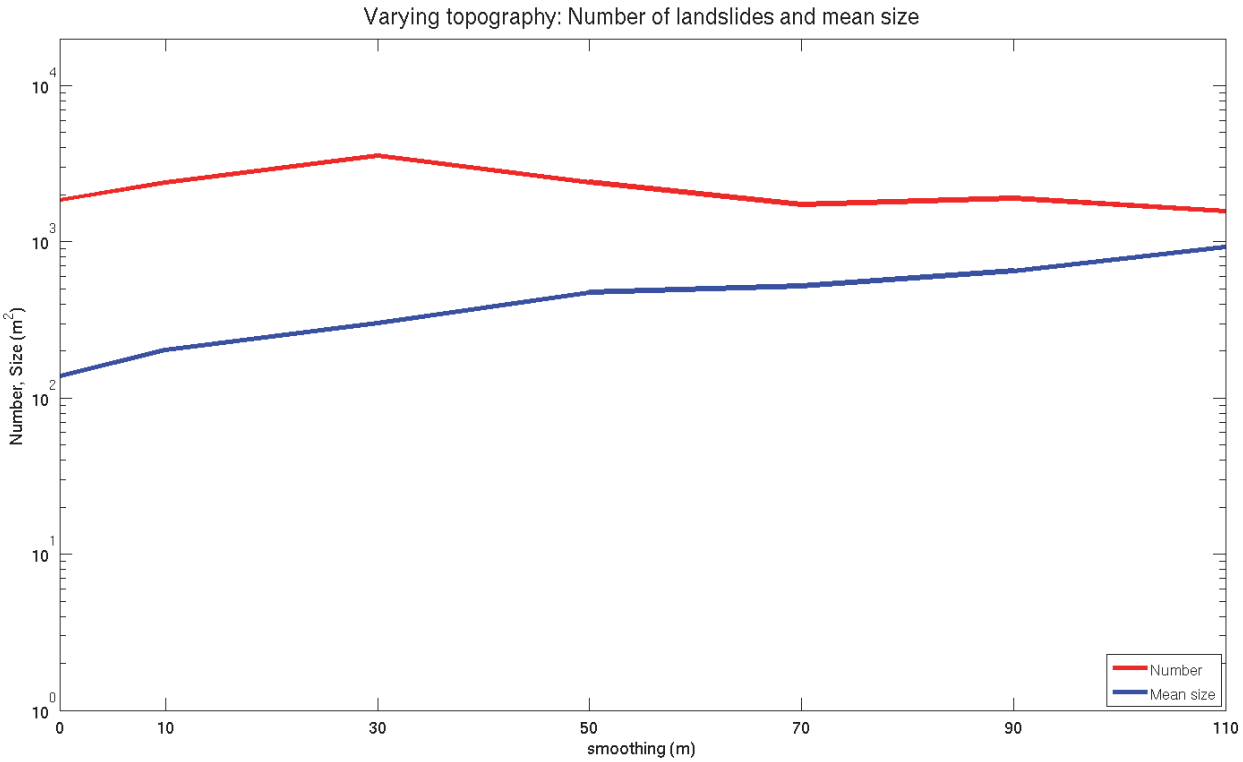

Figure 5.39. Number of shallow landslides and their mean size resulting from progressive smoothing of the landscape using a Gaussian filter of size from *0 m* to *110 m*. While the predicted size increases continuously, the number of predicted landslides reaches a peak when the filter size reaches *30 m*, then decreases.

The number of landslides is also reduced when the friction angle of the soil is increased (figure 5.27). When there is lower strength, locally favorable conditions are more numerous, resulting in an increase in the number of landslides. In general, when strength is increased (i.e. increased root strength or shear strength), landslides are preferentially found in locations having a higher topographic index (figures 5.17, 5.20, 5.22, 5.26) where higher saturation ratios but also thicker soils are found. However, the size distributions show opposite trends: increased root strength produces larger landslides (figures 5.16, 5.18, 5.20), with the size increase being most significant when root cohesion declines more rapidly with depth (figure 5.23), while increased friction angle produces slightly smaller landslides (figure 5.25). This is somewhat counter-intuitive, as the expectation is that increased strength can only be overcome by increased driving force (i.e. larger size). The difference is perhaps due to the fact that while friction always acts on all the boundaries, root strength does not contribute to the basal resistance once soils are sufficiently thick (i.e. > *1 m*). As the ratio of volume to perimeter area grows faster than the ratio of volume to surface area (i.e. perimeter area plus basal area), a larger landslide size is more beneficial when increased strength is a result of increased root reinforcement (acting mainly on the perimeter) rather than increased friction angle (acting on all the margins). In contrast, if root strength were significantly reduced, increasing the friction angle should result in larger landslide size. While the size of landslides is influenced by the friction angle, the size is still set by the extent of areas that with sufficient pore pressure and soil depth (for a given root strength) to

favor instability. The predicted decrease in landslide size with increasing friction angle shows that with increasing friction angle the areas of sufficiently high pore pressure and reduced root strength due to thick soils becomes progressively more restricted to smaller areas on the landscape. Hence, the root strength value mediated by soil depth and pore pressure strongly controls the potential extent of instability, while the friction angle sets the extent to which the potential instability is sampled.

Experiment number	Description	Landslide number	Landslide size	Landslide location
1	Increase steady-state shallow subsurface (lateral) flow, q	↑	↑	↔
2	Increase uniform instantaneous (vertical) pressure addition, p	↑	↑	→
3	Increase proportion of vertical to lateral flow contribution, p/q	↓	↑	←
4	Increase root strength base value and exponential decay function, C_{r0}, j	↓	↑	→
5	Increase soil friction angle, phi	↓	↓	→
6	Increase soil depth z (proportionately)	↑	↕	←
7	Increase soil depth z (uniformly)	↑	↓	←
8	Increase topographical smoothing filter size	↕	↑	●

↑ increase ↓ decrease ↕ Increase then decrease ● No change
← upslope → downslope ↔ downslope then upslope

Table 5.2. General trends in the size, location, and abundance of shallow landslides predicted in the experiments presented in chapter 5. Size increases when precipitation, root strength, and landscape smoothness increase; it decreases when friction angle or uniform soil depth increase. Location shifts towards higher drainage area when root strength or friction angle is increased and towards higher slopes when soil depth is increased. Landslides are generally more abundant when precipitation or soil depth is increased and less abundant when root strength or friction is increased. See text for a description of the other (more complex) trends.

In the third group of experiments (experiments 6-7), soil depth is varied across the landscape. In experiment 6, this is done by taking the spatially varying soil depth produced by the model described in section 2.2.3 and multiplying them by a coefficient ranging from *0.25 to 2* (soil depths thus increasing from ¼ of the modeled values to twice the model values). Instead in experiment 7, the soil is increased uniformly in space from *0.25 m* to *8 m*. In both cases the number of predicted landslides generally increases with increased soil depth (figures 5.31 and 5.35). In general this is because locations with sufficiently high slope but initially thin soil (where the effect of root cohesion is strong), become progressively less stable as soils are thickened (driving force increases and root strength is diminished). However, close observation reveals that this trend is more complex across a natural landscape with varying topogrpahy. In the proportional case, the number increases rapidly until soil depths reach the modeled values,

after which it essentially stays constant (figure 5.31). This implies that as new favorable locations are added due to thickening, other previously unstable regions are stabilized. The two mechanisms responsible for stabilizing these locations are earth pressure (which increases as soil thicken), and relative saturation (which decreases with soil thickness because the water table height is unchanged). These results support the concept of a "window of opportunity" for failure, suggested by Dietrich et al., [2008]: soils are stabilized by root cohesion when thin, and if they become too thick earth pressure forces can also prevent failure.

Experiment number	Description	Best performance (F-score and MCC)
1	Increase steady-state shallow subsurface (lateral) flow	log(q/k) = -2.8
2	Increase uniform instantaneous (vertical) pressure addition	p = 15 mm
3	Increase proportion of vertical to lateral flow contribution	log(q/k) = -2.8 and p = 11 mm
4	Increase root strength base value and exponential decay function	C0 = 21,666 Pa, j = 4.96 (m^{-1}) C0 = 10,833 Pa, j = 2.48 (m^{-1})
5	Increase soil friction angle	phi = 40°
6	Increase soil depth (proportionately)	Soil depth = ½ modeled values
7	Increase soil depth (uniformly)	Soil depth = 2.25 m
8	Increase topographical smoothing filter size	Filter size = 0 m (no smoothing)

Table 5.3. Best-performing parameters for the experiments presented in chapter 5. Performance is assessed using the F-score and MCC precision/recall measures in comparison to the observed landslide dataset.

In the experiment in which soil is instead increased uniformly across the landscape, no landslides are predicted until a minimum depth is reached (figure 5.35). For the chosen parameterization this depth (between *0.5* and *0.75 m*) corresponds to the depth at which root strength contribution to basal resistance is no longer significant (< *1 kPa*). Then for intermediate depths the competing effect of decreasing root strength effects due to increasing soil depth and decreasing relative saturation produce first an increase then a decrease in the number of predicted landslides. After soils are thick enough to effectively eliminate root cohesion from the balance of forces the decrease in relative saturation dominates and the number of landslides increases. When soils are extremely thick, the stabilizing effect of earth pressure becomes important and the number of landslides can no longer increase (figure 5.35).

The preferential location of predicted landslides shifts from high to low topographic index locations (from high drainage area to high slope) in both the proportional and the uniform soil experiments (figures 5.30 and 5.34). Again this is due to new locations with high slopes becoming available when soils are thickened. The difference between the two experiments is that

in the case of uniform thick soils unstable locations are almost exclusively in high slope areas, while spatially varying soils result in a wider range of locations. The size distributions instead display opposite (and complex) trends in the two experiments (figures 5.29 and 5.33). When soil is varied proportionally, size and number increase until the depths reach the modeled values (figure 5.31), as not only new locations are added but these locations expand. Conversely, further thickening of the soils results not only in locations downslope becoming more stable, but they also contract in size (as the relative saturation field shrinks and the effect of root strength is diminished). When the topographic control on soil depth is removed by the uniform treatment of soils (figure 5.35), the trend is reversed: size gets smaller as root cohesion is diminished (and does so more rapidly once the basal effects are removed), but strength added by earth pressure increases as soils get very thick, forcing size increases again (as with increased root strength, see experiment 4).

In the final group of experiments (experiment 8), the landscape is smoothed with a Gaussian filter of increasing size. With no smoothing, topography constrains the number and size of locations favorable to landslides. With modest smoothing (small filter size), only the fine scale roughness of the landscape is removed, resulting in an increase in number of predicted landslides (figure 5.39). When the filter size becomes sufficiently large, slopes generally decrease in the landscape and some hollows are lost entirely, resulting in a reduction in the number of predictions (figure 5.39). As slopes decrease and hollows diminish, the topographic index distribution tightens: the mode is essentially invariant but fewer locations are available (figure 5.38). As the landscape is smoothed it also becomes progressively more uniform, and thus more similar to the synthetic example presented in section 3.5: under uniform conditions larger size means more instability and thus lack of topographically driven constraints results in a larger size distribution (figure 5.37).

Collectively, these experiments illustrate the role of heterogeneity on landslide abundance, location, and size. Under uniform conditions larger landslide sizes are favored as they result in instability smaller factor of safety. In contrast, when the distributions of properties such as pore pressure, root strength, and soil depth vary across the landscape, a richer result is obtained: landslides sample different parts of the landscape, exhibiting specific trends in characteristic size, location, and abundance as the mean of each of these properties change. As the distribution of these landscape properties is mostly determined by topography, it can be concluded that topography exerts a first order control on shallow landslides.

5.5 Conclusion

To explore the controls on shallow landslide size and location, a sensitivity analysis was performed by applying the shallow landslide prediction procedure to the CB-MR study area in the Oregon Coast Range to obtain discrete landslide predictions. Rainfall, vegetation, soil, and topographic characteristics were systematically varied, resulting in probability density functions of predicted landslide size and location (as represented by a topographic index). We find that increasing precipitation or soil depth results in an increased number of predicted landslides. In contrast, increasing soil strength through root reinforcement or friction angle results in a decrease in the number of predicted landslides. Increasing soil depth results in predicted landslides being preferentially located in locations with steep slopes, while increasing soil strength results in predicted landslides being preferentially located in locations with high drainage area. Precipitation affects characteristic landslide location differently: if lateral re-distribution of water

is dominant, landslides are predominantly found in locations with high drainage area; in contrast, when vertical infiltration dominates they are predominantly found in areas with steep slopes. Predicted characteristic size increases with increased precipitation and with increased root strength. However, it decreases when the increased strength results from an increase of the soil friction angle. Under uniform soil thickness, characteristic size decreases with increasing soil depth. When soil thickness distributions are instead controlled by topography, increasing soil depth causes the predicted characteristic landslide size to first increase and then to decrease, after a critical value, reflecting the stabilization effect of very thick soils. Our procedure applied to a natural landscape demonstrates that as precipitation, root strength, soil depth and friction angle are varied, landslides sample different parts of the landscape, producing specific trends in characteristic landslide size, location, and abundance. Moreover, as the co-organization of these properties is mostly determined by topography, it can be concluded that topography exerts a first order control on shallow landslide location and size.

Chapter 6

Future developments and conclusion

6.1 Introduction

To address hazards posed by rainfall-triggered shallow landslides, several essential questions must be considered. These include questions such as where will landslides occur, when will they occur, how big will they be, how fast will they mobilize, and how far will they go [USGS, 2005]. The aim of my research has been principally to address the questions of "where" and, most importantly, of "how big". I have presented a slope stability method and an efficient search algorithm and combined them to search for least-stable combinations of grid cells, producing discrete shallow landslide predictions across a landscape. In order to apply this procedure at the regional scale, where required data for the slope stability model are not available, I used sub-models to estimate their spatial and temporal patterns. These sub-models extract topographic attributes, compute the spatial distributions of soils, and estimate the root reinforcement and pore pressure fields. A formal framework was defined to evaluate the performance of the procedure, based on information retrieval theory. A dataset from a study area in the Oregon Coast Range consisting of an instrumental record a rainfall-triggered shallow landslide and a complete 10-year inventory of shallow landslides allowed the procedure to be tested using field-measured and modeled physical parameters such as hydrological conditions, soil depth, and root strength. This procedure was then used in a sensitivity analysis, illustrating the important control of topography and the effect of the spatial co-organization of landscape characteristics on shallow landslide size and location. We find that the topographically induced structure of properties relevant for landsliding (e.g. soil depth and pore pressure) determines the favorable areas that can be exploited by rain storms. Varying these controlling properties changes the spatial distribution of areas favorable to landsliding in the landscape, resulting in characteristic distributions of landslide size and location, as landslides sample different parts of the landscape. For example, increased precipitation results in more and bigger landslides, while decreased root strength produces more and smaller landslides.

Many simplifying assumptions were made when modeling the distribution of properties such as root strength, soil strength, soil depth, and pore pressure. Although these properties varied spatially across the landscape in the experiments performed in this research, the parameters that were used in the submodels to predict these properties were spatially and temporally constant. In reality few, if any, of these parameters are constant across the landscape. In fact many vary significantly both in space and in time. Temporal variations in particular must be captured in order to address the question of "when" landslides may occur. Furthermore, it is expected that some of these variations may become more significant in the not so distant future, particularly as a result of climate and land use changes.

In this chapter, I will suggest methods to incorporate spatial and temporal variations in submodel parameters in the shallow landslide prediction procedure. I will discuss how the procedure that has been developed enables us to address questions about the response of the landslide regime to climate and land use change and the co-evolution of landslides and the landscape. Finally, I will give a summary of the main findings arising from my research presented in this dissertation.

6.2 Spatial variability of landslide-relevant properties

Root reinforcement across a landscape is a function of vegetation type, density, and climate (e.g. O'Loughlin, [1972]; Hathaway and Penny, [1975]; Burroughs and Thomas, [1977]; Schmidt et al., [2001]; Hales et al., [2009]; Roering et al., [2003]; Sidle and Ochiai, [2006]). Landslides tend to occur in areas of reduced root strength, at scales ranging from clear-cuts and landuse change to localized gaps in forests (e.g. Sidle et al., [1985]; Roering et al., [2003]). In order to make site-specific predictions of landslide occurrence the diversity and distribution of vegetation in potentially unstable terrain must accounted for [Roering et al., 2003]. Soil and rock strength and hydrologic properties, while varying it time much more slowly than vegetation, are nonetheless not uniform, affecting slope stability as a result of localized changes in strength (e.g. Griffiths and Fenton, [1999]; Ebel et al., [2007a,b]).

In cases where there is some understanding of the dominant processes causing this variability, one can attempt to reproduce the observed spatial variability by modeling those processes in a stochastic framework. For example, Dietrich et al. [2008] converted the exponential soil production function [Heimsath et al., 2001] to a probability distribution that was sampled according to the recurrence interval of biotic disturbances such as animal burrowing or tree throw. This resulted in a large local variability of soil depth, even on hillslopes of constant curvature.

Under the assumption that root strength variability over time is principally due to vegetation decay and regrowth processes, Sidle [1991; 1992] modeled the effects of this temporal variability on slope stability. In this exercise the spatial structure of this variability was not considered. Hales et al. [2009] proposed that the spatial variability of tensile strength provided by roots was related to topographically controlled differences in soil water potential. They introduced further variability by adding random root cohesion values to each pixel from a uniform distribution constrained by observed mean root cohesion values. Their method introduced topographically-controlled patchiness to the root strength field; however, at the fine-scale root strength variations remain uncorrelated. To address the fine-scale structure of the root strength field, Roering et al. [2003] proposed a geometrical method to estimate root network contribution from mapping of size, species, condition, and spacing of local trees. They suggest that their methodology could be combined with remote sensing techniques to quantify the spatial distribution of root strength in forested terrain. Techniques exist to determine individual tree locations from LiDAR data (e.g. Lee et al., [2010]; Li et al., [2012]), however these are yet to be applied in the context of slope stability.

In absence of such detailed data, regional-scale estimates of the length scale over which properties such as root strength are spatially correlated can be used. In section 2.25 I defined a framework that accounts for the magnitude of variability and a spatial correlation length. In this framework, a random grid is sampled from a Gaussian distribution with mean μ and standard deviation σ. A spatial correlation length is obtained by repeatedly convolving the random Gaussian field with a two-dimensional symmetric Gaussian low-pass filter for a number of iterations n.

Figure 6.1 (a-d) shows maps of lateral root strength obtained with a C_{r0} (the maximum root cohesion value at the surface) mean value of *21,666 Pa*, standard deviation equal to the mean, and number of iterations *10*, *100*, *500*, and *1000*, respectively. The correlation length increases with the square root of the number of iterations. For a pixel size of *2 m*, these correspond to

lengths of approximately *6*, *20*, *45*, and *63 m*. These lengths capture the spatial scale of variability due to tree spacing, and characteristics, reported in this region [Roering et al., 2003]. For simplicity, the shape factor and j (m^{-1}) is held constant in this experiment and only $\boldsymbol{C_{r0}}$ is varied. In contrast to the example shown in figure 2.7, here the spatial structure of root strength is mediated by the topographically controlled soil depth. As a result the pattern remains generally similar to that shown in the reference scenario (figure 4.9b). Increasing the correlation length (i.e. increasing n) creates slightly larger patches of similar root strength. In the limit, further increasing n would ultimately remove the randomized patchiness, resulting in the topographically mediated root strength of figure 4.9b.

Figure 6.2 shows the discrete landslide predictions obtained by applying the landslide prediction procedure to these four scenarios. The spatial pattern of predicted landslides is similar to those generated in the reference case scenario (figure 5.1), as it is still topographically controlled by the spatial distribution of soil depth and pore pressure, but the characteristic landslide size decreases.

The PDFs of size distributions shown in figure 6.3 illustrate how introducing local variations significantly reduces landslide size. However, with increasing number of iterations (and thus of the correlation length), the size distribution slightly shifts to the right (towards larger size) as these variations become more smooth as a result of increased Gaussian filtering. This effect is minor, however, as the pattern is mostly controlled by the initial patchiness of root strength. Introducing fine scale local variations in root strength increases the probability that a patch of a given size will include an area of high root strength. At the same time, areas of continuous low root strength susceptible to failure become smaller. As a result, increasing variability reduces landslide size. This mechanism is also responsible for the initial reduction in the number of landslides caused by introduced variability (figure 6.5). The number of predicted landslides marginally increases as the correlation length increases (figure 6.5).

The introduction of patchiness in the root strength field also causes slight changes in the topographic index PDFs (figure 6.4). While the mode of the distributions remains essentially unchanged, the distributions become progressively "fatter". This is because local reductions in root strength result in newly available locations in areas with slightly higher slope, where thinner soils previously resulted in sufficient root strength to prevent failure. In contrast, areas with deep soils are less affected since their depth averaged root cohesion is less sensitive to this variability due to the diminished root strength contribution.

These results illustrate the potential effect of the fine scale variability of root strength on slope stability. This method can be generalized to represent the impact of spatial variability of landslide-relevant parameters on landslide size, location, and abundance. As discussed above, spatial variability in soil depth is also likely to play an important role in defining landslide location and size. Here I focused on root strength variability as an example of these effects.

6.3 Temporal variability of landslide-relevant properties

In this research we adopted a simple view of landslide-relevant hydrologic processes, assuming that the pore pressure field is principally controlled by shallow subsurface saturated flow which was modeled under the steady state assumption. Steady state conditions are rarely achieved in a natural setting. Sprinkling experiments conducted by Torres et al. [1998] at our study site found that the time needed to reach steady state conditions could exceed 30 hours. Furthermore, assuming steady state conditions typically results in over-prediction of the area

affected by landsliding [Dietrich et al., 2001]. Iverson [2000] suggests that two very different timescales are relevant for landsliding: a longer scale (days to weeks) is associated with lateral subsurface redistribution of water, while at the individual storm time scale (minutes to hours), vertical infiltration is responsible for the landslide-triggering pore pressure rise. While the relative importance of these components is subject to debate (e.g. Iverson, [2004]; Montgomery and Dietrich, [2004]), it is clear that the transient nature of pore pressure development must be captured in order to predict the timing and magnitude of landsliding events. Efforts have been made to integrate the two components to account for the different time scales involved (e.g. D'Odorico et al., [2005]), but such methods are used to model landslide recurrence and not easily applied to a storm rainfall time series.

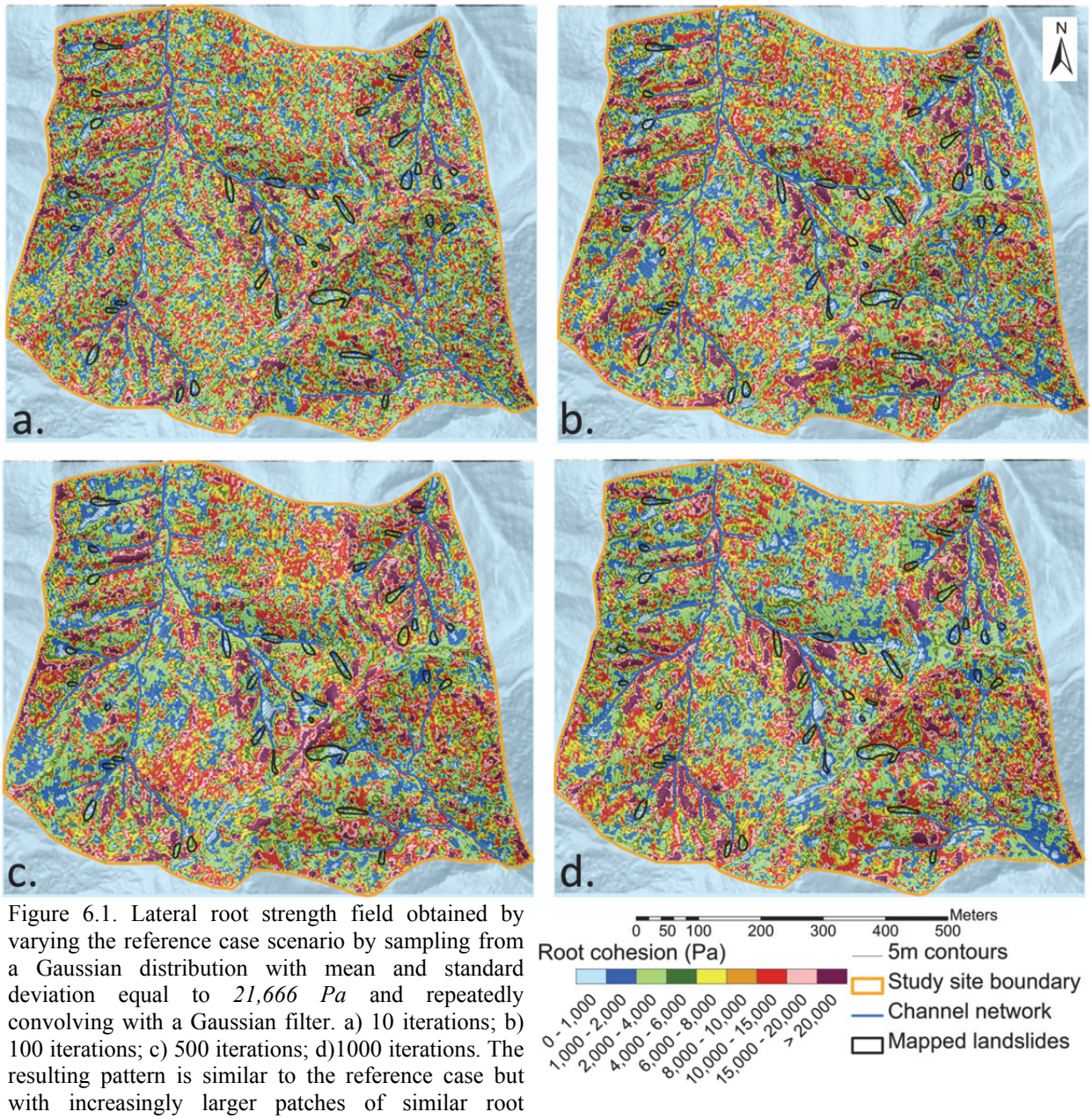

Figure 6.1. Lateral root strength field obtained by varying the reference case scenario by sampling from a Gaussian distribution with mean and standard deviation equal to *21,666 Pa* and repeatedly convolving with a Gaussian filter. a) 10 iterations; b) 100 iterations; c) 500 iterations; d)1000 iterations. The resulting pattern is similar to the reference case but with increasingly larger patches of similar root strength values.

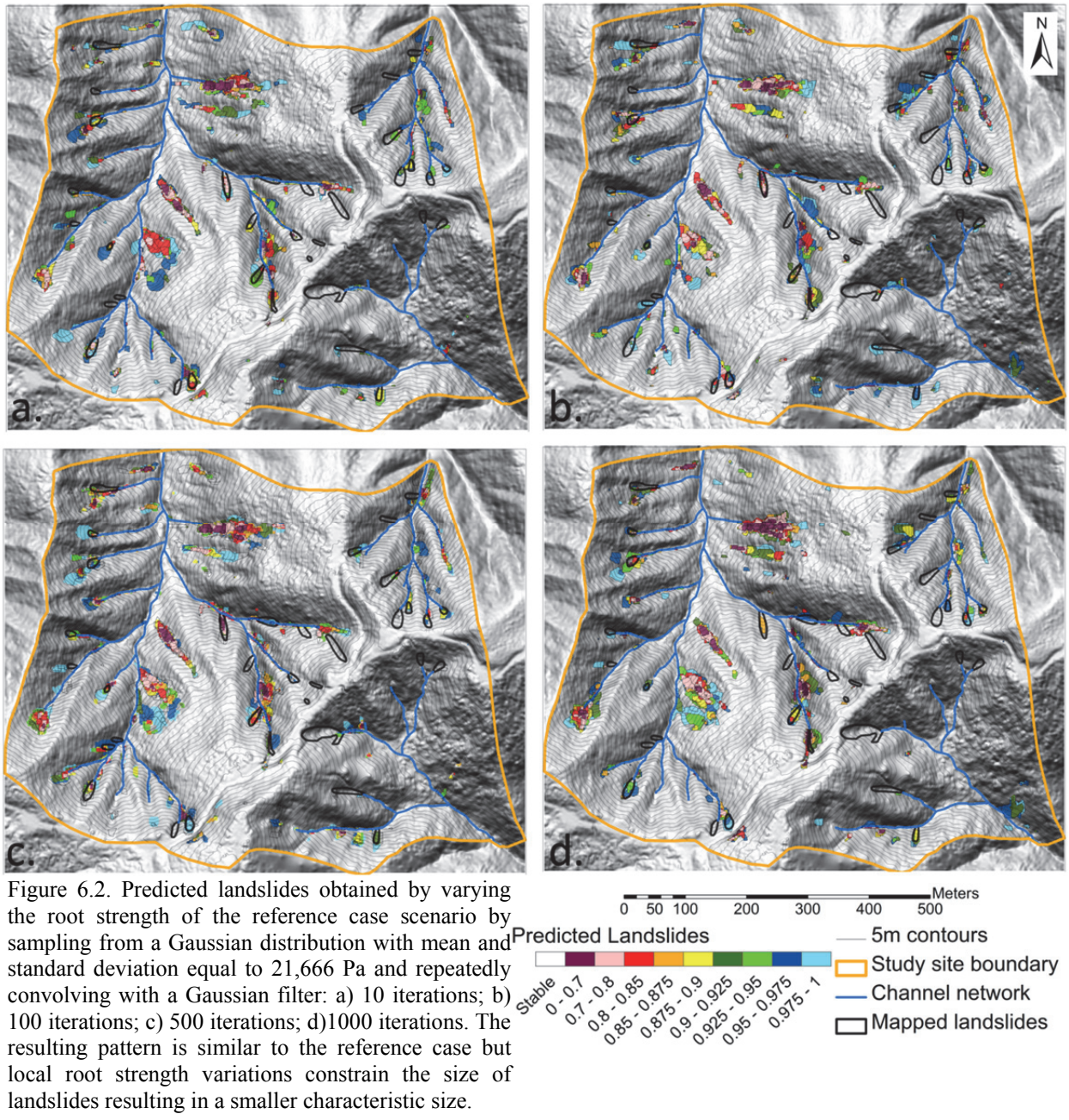

Figure 6.2. Predicted landslides obtained by varying the root strength of the reference case scenario by sampling from a Gaussian distribution with mean and standard deviation equal to 21,666 Pa and repeatedly convolving with a Gaussian filter: a) 10 iterations; b) 100 iterations; c) 500 iterations; d)1000 iterations. The resulting pattern is similar to the reference case but local root strength variations constrain the size of landslides resulting in a smaller characteristic size.

Rosso et al.'s [2006] modification of the hydrologic model underlying Shalstab, re-formulated in equation 2.17 for use in discrete time steps, is used here in combination with ten-minute rainfall intensity record of the 15–20 November 1996 recorded at CB1 [Montgomery et al., 2009]. This model represents a minimal increase of complexity with respect to the steady-state model used in the previous chapters, requiring only two additional (and easily constrained) parameters. We set the void ratio e (the volume of the voids over the volume of the solids) to *0.5* [Montgomery et al, 1997], and vary the degree of saturation of soils S_r (volume of water over the volume of voids) from *0* to *0.5*, referred to here as soil moisture. No overlapping landslide predictions are allowed (i.e. least-stable predictions are retained), as the objective is to match a single specific event.

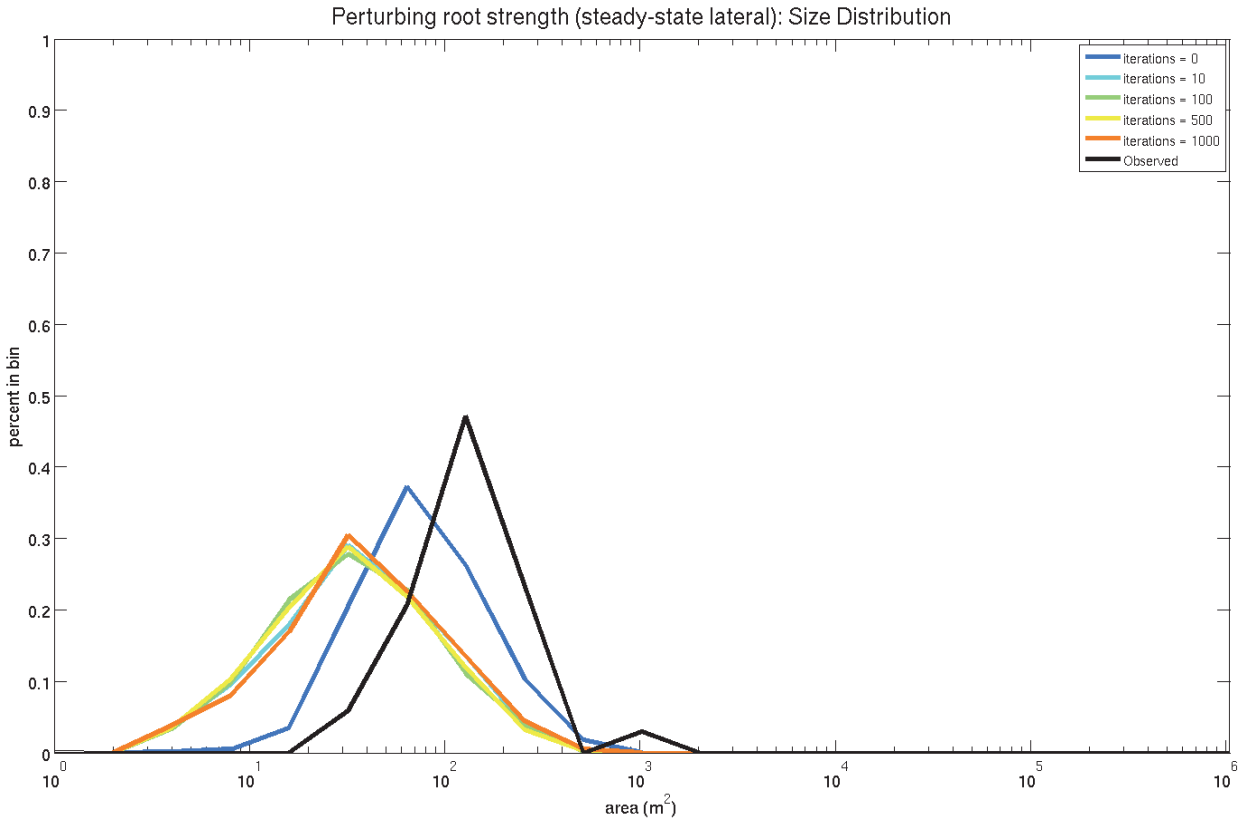

Figure 6.3. Predicted size distributions of landslides resulting from varying the reference case scenario (figure 5.1) by sampling from a Gaussian distribution for C_{r0} with mean and standard deviation equal to 21,666 Pa and repeatedly convolving with a Gaussian filter. Introducing local variations significantly reduces landslide size; as the number of iterations increases (and thus the correlation length), the size distribution slightly shifts to the right (larger size) as these variations become more smooth.

The results of the application of the procedure using the dynamic hydrological model are shown in figure 6.6. The number of predicted landslides increases with increasing soil moisture (as pore pressures are higher across the landscape), reflecting the importance of antecedent soil moisture conditions. In all scenarios, significantly fewer landslides are predicted than in the reference case using the steady-state model (figure 5.1). This does not come at the cost of performance, as a similar number of observed landslides are captured. The observed size distribution is captured (i.e. no statistical difference between predicted and observed distributions according to the K-S test) when $e = 40\%$, and the observed topographic index distributions are captured when $e = 40\%$ to 50%. These values are not unreasonable given that Torres et al. [1998] reported that values greater than 35% could be sustained in the presence of an applied flux across the ground surface.

Characteristic landslide size increases with increasing soil moisture, as shown by the PDFs in figure 6.7. This is because greater soil moisture causes the water table height h to rise more quickly in response to a rainfall rate, resulting in expanded patches of high pore pressure. As soil moisture is increased, the mode of the topographic index distribution remains fairly constant, but more landslides are predicted down the hollow axis (figure 6.8). The increased pore pressure in the convergent areas down the hollow axis enables landslides to occur in areas of lower slope. Figure 6.9 illustrates the general increase of both landslide number and average landslide size with the increase of antecedent soil moisture. It should be noted that the no-overlap condition

allows the number of predictions to temporarily diminish (for example when *e* varies from *10%* to *15%*). This can happen when a larger, more unstable shape that can result from an expanding high pore pressure field overlaps two more stable shapes. The average size also shows small decreases (for example when *e* varies from *45%* to *50%*): when landslides are added to the distribution by the increased pore pressures, they are often smaller than previously existing ones; if there is a sufficient number of them this can have the effect of reducing the average size.

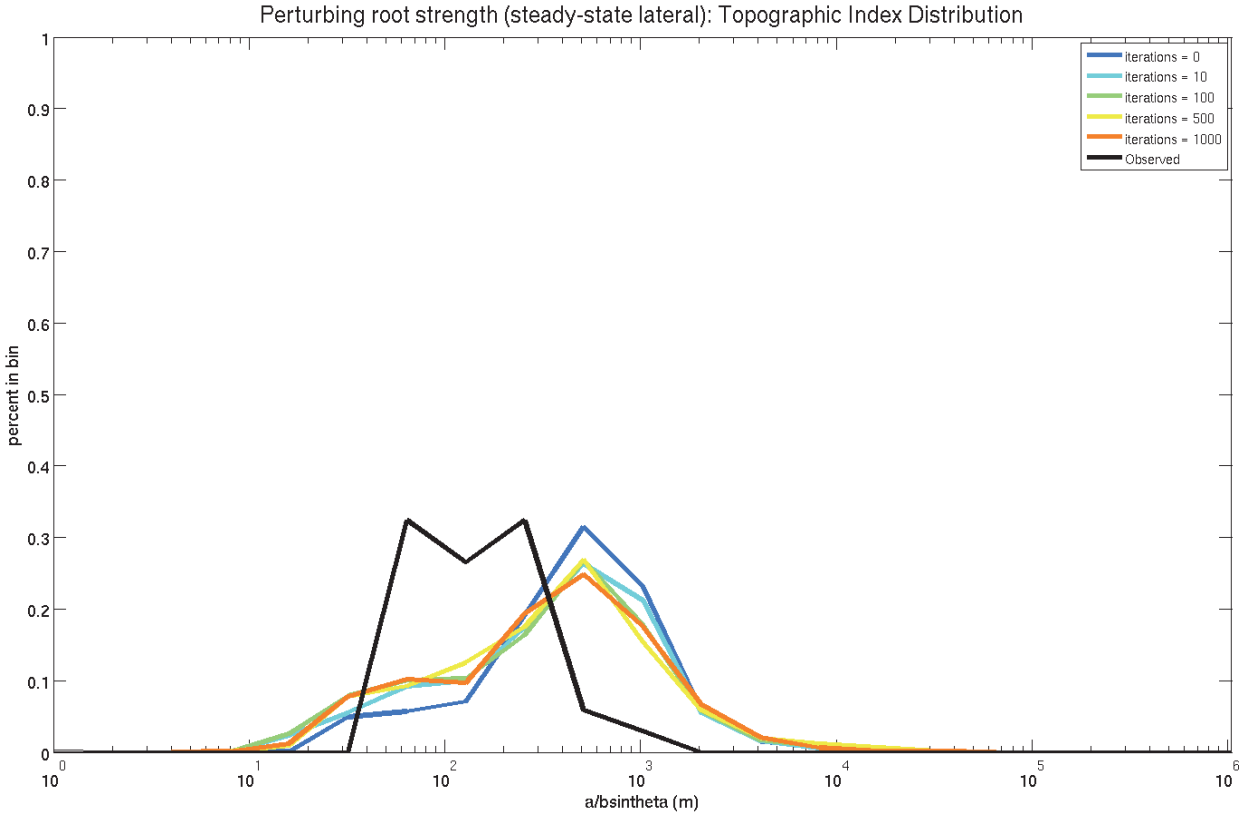

Figure 6.4. Predicted topographic index distributions of landslides resulting varying the reference case scenario (figure 5.1) by sampling from a Gaussian distribution for C_{r0} with mean and standard deviation equal to 21,666 Pa and repeatedly convolving with a Gaussian filter. Introducing local variations shifts the location towards the left (higher slope); as the number of iterations increases (and thus the correlation length), the trend oscillates around the same mode.

Figure 6.10 shows a map of debris flows that occurred at CB-MR as a result of the November 1996 storm (figure 6.10). Comparing this figure with the results of the application of the dynamic hydrological model shown in figure 6.6, shows that the procedure predicts landslides in the observed debris flow source areas. Although over-prediction is greatly reduced, there remain a considerable number of predicted landslides in areas which did not fail during this event. There are many potential reasons for the remaining over prediction: as discussed in chapter four, the soil depth sub-model does not account for prior landsliding, with the result that with the chosen parameterization all the hollows are *fully-loaded*, when in fact hollows will be at various stages of infilling. Local variations in root strength or soil depth, not represented in these scenarios may also play a role in defining landslide location. Notwithstanding these limitations, the simple, un-calibrated, dynamic hydrological model predicts the occurrence of landslides in a landslide-triggering storm, with sizes and locations consistent with observations. This is a promising result, particularly since only one storm out of all those which may have occurred during the 10 years of

landslide observations was used. This suggests that this procedure is capable of capturing the timing of landslides (as well as their size and location), given a sufficiently resolved characterization of the hydrology.

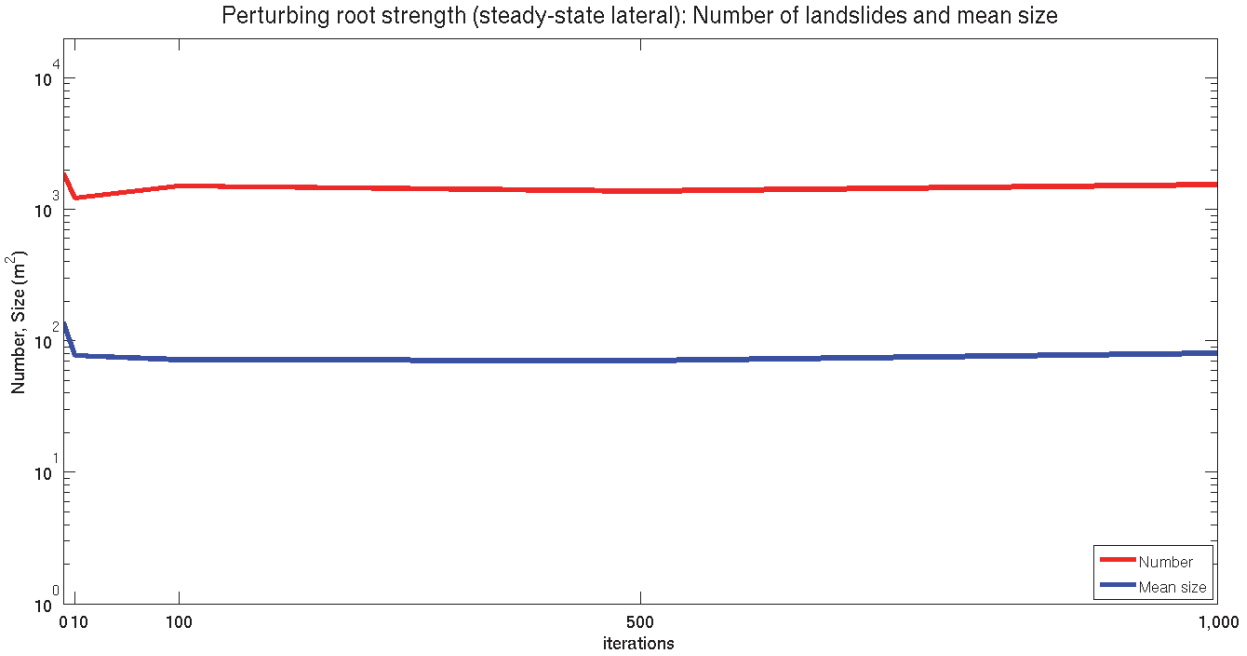

Figure 6.5. Predicted number and mean size of landslides resulting from the application of the procedure varying the reference case scenario (figure 5.1) by sampling from a Gaussian distribution for C_{r0} with mean and standard deviation equal to 21,666 Pa and repeatedly convolving with a Gaussian filter: introducing local variations significantly reduces both number and size; as the number of iterations increases (and thus the correlation length), variations are smoothed resulting in a minimal increase in both landslide number and size.

6.4 Future directions

Over time scales of years to decades, climate change can impact landsliding both through changes in the vegetation cover and through changes in the hydrologic conditions. Analyses of available precipitation records (e.g. Higgins et al., [2011]) has already documented that the frequency of extreme precipitation events has increased in the last 30 years, and this trend is expected to continue. As mean annual temperature is expected to increase and to vary significantly at the regional scale [Sokolov, et al., 2009], plant types and vegetation patterns on the landscape which are under the influence of regional climate are expected to change significantly. Furthermore, these ecosystems are likely to experience changes in their disturbance regimes, due to changes to the frequency, intensity, and duration of fires, droughts, insect and pathogen outbreaks [Dale et al., 2001]. These changes could have a profound impact on the root networks and the coupled water dynamics (e.g. ground moisture, evapotranspiration, and precipitation interception) on landslide prone hillslopes. Understanding these effects and predicting vegetation patterns and their response to climate and other environmental stressors is critical for landslide hazard assessment, particularly in light of the increased risk resulting from development into landslide-prone areas [Crozier and Glade, 2005]. In some areas, land use change may have as much (or more) impact as climate change effects on vegetation patterns [Sidle, 1991; 1992]. Climate and vegetation models (e.g. Istanbulluoglu and Bras [2006]; Ivanov et al., [2007]; Ivanov et al., [2008]; Crookston et al., [2010]; Dettinger et al., [2012]; Li et al., [2012]) can provide input data under a range of scenarios that can be used with our procedure to

predict landslide hazard (and therefore risk), and explore the impact of climate and land use change on the landsliding regime.

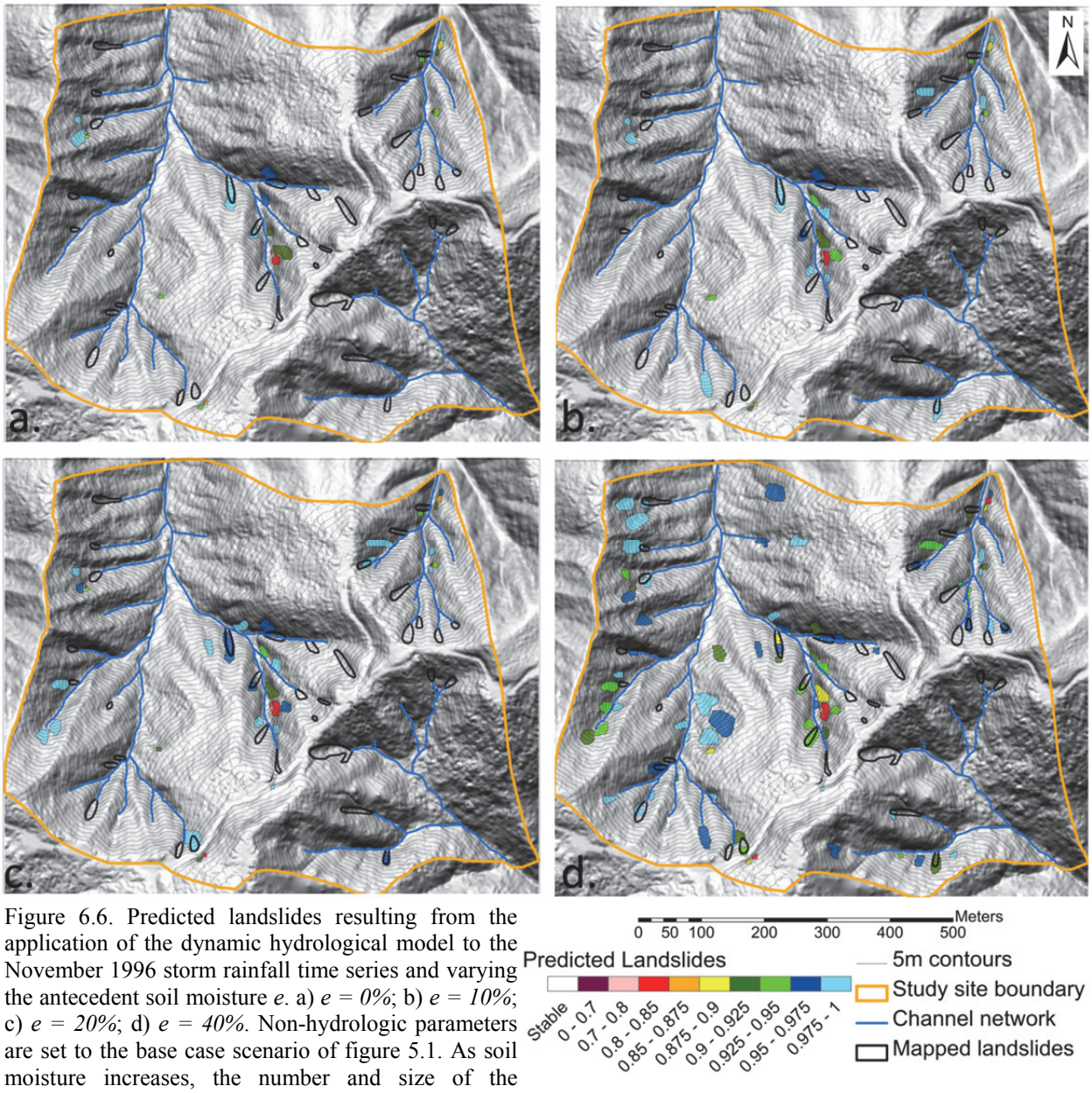

Figure 6.6. Predicted landslides resulting from the application of the dynamic hydrological model to the November 1996 storm rainfall time series and varying the antecedent soil moisture *e*. a) *e = 0%*; b) *e = 10%*; c) *e = 20%*; d) *e = 40%*. Non-hydrologic parameters are set to the base case scenario of figure 5.1. As soil moisture increases, the number and size of the landslides increases due to the expanding pore pressure field.

Over longer time scales, the topography, which has been shown in this research to exert a first-order control on landslide location and size, is itself evolving partly as a result of landsliding. This motivates the question of how do landslides shape a landscape, and what are the signatures of the landsliding regime on the landscape. Hollows in a landscape are sustained by a cycle of infilling and evacuation in which landslides play an important role [Dietrich et al., 1982; Reneau and Dietrich, 1986]. The convergence of shallow groundwater flow in these hollows combined with upstream migration of channel heads due to the periodic, small-scale landsliding, exerts a control on the fluvial network structure [Montgomery and Dietrich, 1998].

The influence of landslides on landscape form has been partly explored by coupling an infinite-slope stability model to a landscape evolution model (e.g. Tucker and Bras, [1998]; Tucker et al., [2001]; Istanbulluoglu, and Bras, [2005]). The effectiveness of these models is limited by their inability to predict discrete landslides: infinite slope calculations leads unstable grid cells to be treated as individual landslides whose size is set by the grid resolution. The procedure developed in this research presents the opportunity to integrate discrete landslide predictions in a landscape evolution model. The procedure requires high-resolution spatial data of topography, soil depth, pore pressure, and root reinforcement but is largely independent of the models which produce them, and thus could feasibly be implemented as a module within a larger framework of integrated model components such as the Community Surface Dynamics Modeling System [CSDMS, 2011].

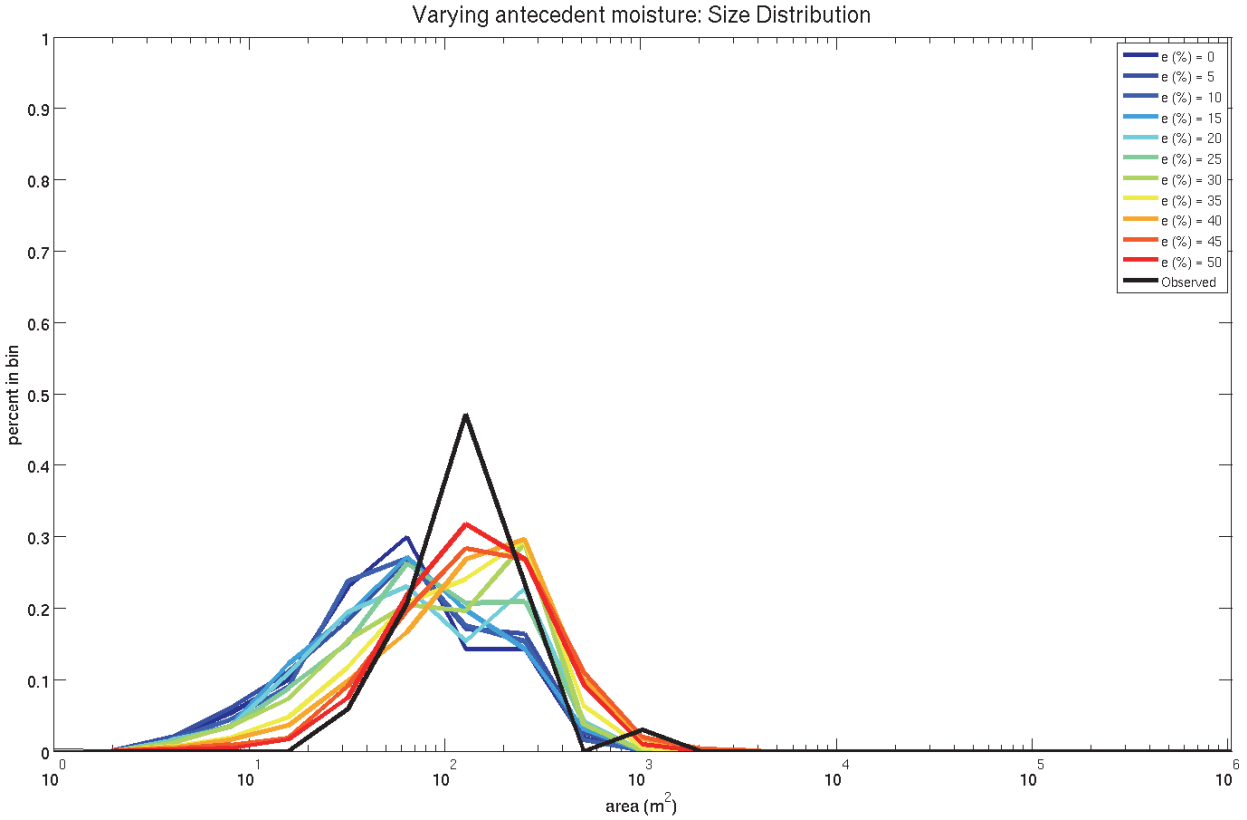

Figure 6.7. Predicted size distributions of landslides resulting from the application of the dynamic hydrological model to the November 1996 storm rainfall time series with antecedent soil moisture *e* varying from *0* to *50%*. As soil moisture increases, the size distribution shifts to the right (larger size) until it matches the observations when *e* = *40%*. Non-hydrologic parameters are set to the base case scenario of figure 5.1.

Addressing these questions over both short and long time scales remains challenging, particularly given the large degree of uncertainty in landslide predictions and in the post-failure behavior of material mobilized by landslides. While models exist to predict runoff and pore pressures, few models exist to predict colluvium thickness and root strength patterns. Field investigations are needed to map the spatial structure of colluvium thickness and root strength contribution in order to test and develop theories. Good landslide inventories, which distinguish the initial failure from the subsequent runout, are also needed for a variety of environments. These inventories should be mapped onto LiDAR quality topographic data and be as complete as possible, ideally (1) covering the entire area affected by landslides, (2) including all landslides

down to a size of 1–5 m in length, and (3) depicting landslides as polygons rather than points [Harp et al., 2011]. Such mapping efforts should be undertaken after well-documented storm events and accompanied by field work to document landslide depth and root strength attributes of landslide scars. Post-failure behavior is strongly dependent not only on the topography over which it is transported, but also on the initial size [Jakob, 2005]. The constraints on landslide size introduced here provide a first step towards these goals, but we still lack a sufficient mechanistic understanding of debris flow dynamics to effectively predict mass loss or gain across a landscape.

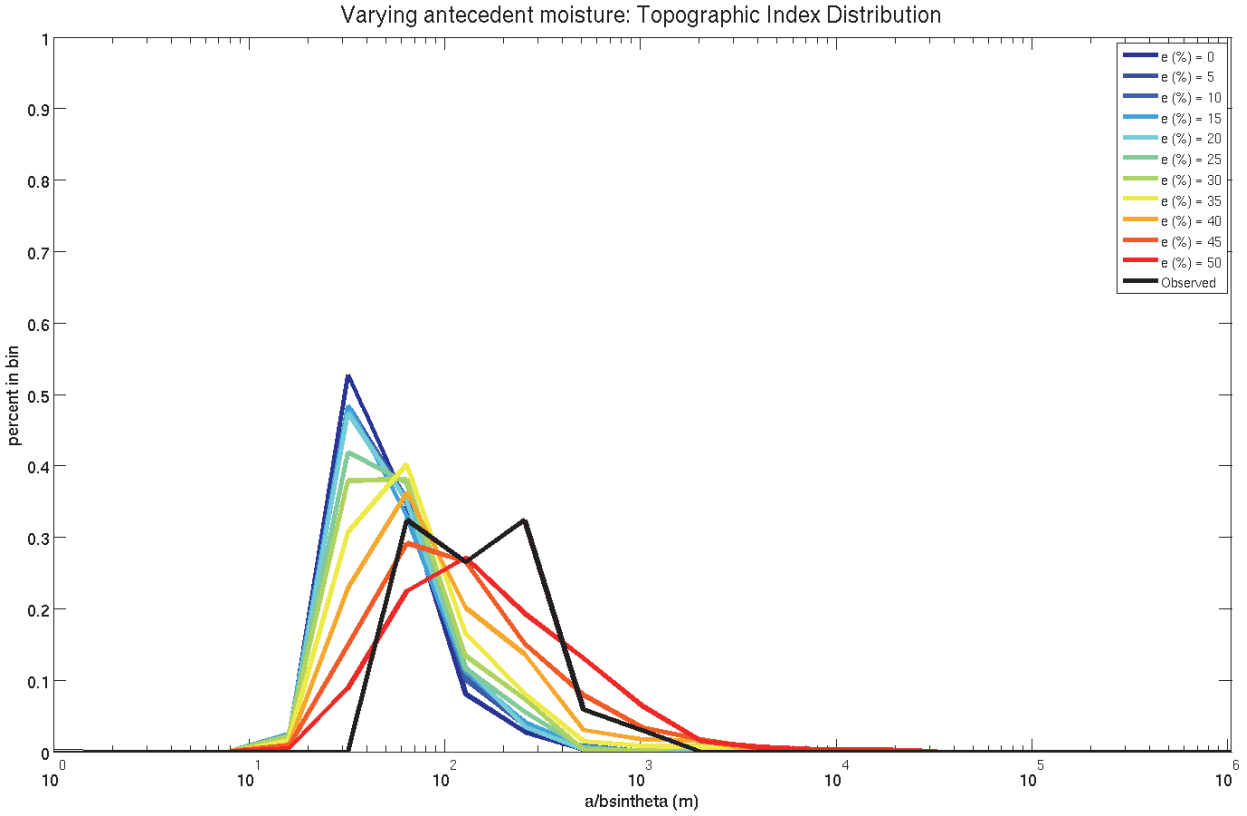

Figure 6.8. Predicted topographic index distributions of landslides resulting from the application of the dynamic hydrological model to the November 1996 storm rainfall time series with antecedent soil moisture *e* varying from *0* to *50%*. As soil moisture increases, the size distribution shifts to the right (higher drainage area) until it matches the observations when *e = 40%* to *50%*. Non-hydrologic parameters are set to the base case scenario of figure 5.1.

Complex modeling endeavors have been traditionally limited by the availability of computational resources (e.g. number of floating point operations per second or FLOPS). Recent advances in massively-parallel computing hardware now enable quadrillions of calculations per second (PetaFLOPS), approximately a million times more than an advanced desktop workstation. Similarly recent scalable parallel software frameworks have been developed for the solution of large-scale, complex multi-physics engineering and scientific problems [Heroux et al., 2005]. For example, complex solid deformation and fluid flow problems under changing boundary conditions may be simulated using software that can perform parallel adaptive mesh refinement on overlapping grids [Henshaw and Schwendeman, 2008]. These advances can now allow landscape evolution models to include more sophisticated modules and to be applied at larger scales. Recent geoscience software development paradigms have focused on developing standards and protocols for interfacing standalone applications into model components in a *plug*

and play fashion [Peckham et al., 2012]. While such interfaces permit the integration of components modeling diverse physical processes, these components are often black boxes which operate sequentially. There is thus a need for a *scalable development environment* in order to develop efficient simulation codes for future facilities with $O(10^6)$ processors as envisioned by the National Science Foundation and other organizations [Syvitski et al., 2010].

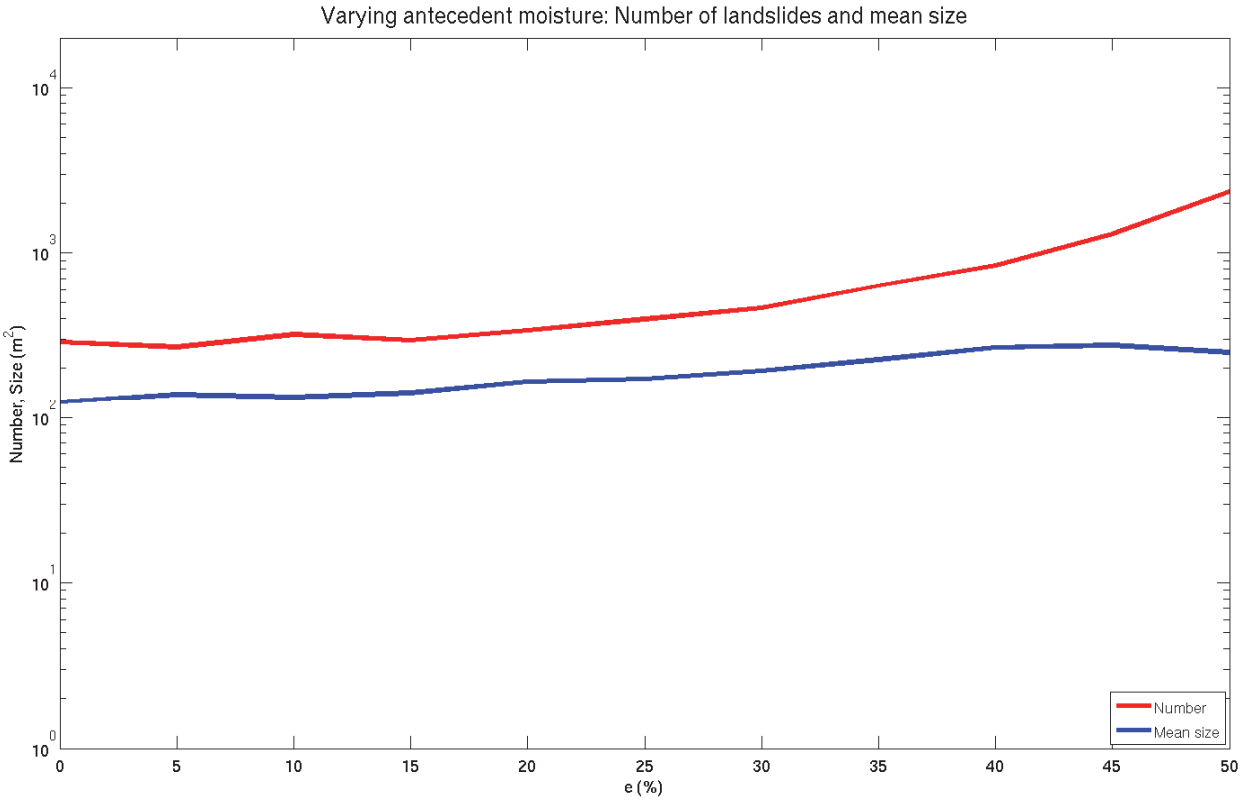

Figure 6.9. Predicted number and mean size of landslides resulting from the application of the dynamic hydrological model to the November 1996 storm rainfall time series with antecedent soil moisture *e* varying from *0* to *50%*. As soil moisture increases, both the number of landslides and their size generally increase. Non-hydrologic parameters are set to the base case scenario of figure 5.1.

6.5 Conclusions

In this research I developed a procedure that can for the first time predict discrete landslides. Its foundation is a search algorithm based on spectral graph theory that can efficiently provide a good approximation for an otherwise intractable problem. This procedure relies on a novel slope stability model, also presented here, as well as sub-models that extract topographic attributes, compute the spatial distributions of soils, and estimate the root reinforcement and pore pressure fields. A formal framework was defined to evaluate the performance of the procedure, based on information retrieval theory.

Only three fundamental assumptions were made in the development of this procedure. The first assumption was conceptual in nature: the initial landslide shape is the result of an optimization of the driving and resisting forces acting on a cluster of grid cells, locally resulting in the minimal factor of safety. This implies that landslide size is determined by the balance of the benefits associated with larger size (increased driving forces relative to resistive forces) with the costs associated with a larger size (higher probability of including areas that contribute higher

resistances). This assumption is supported by the results from the application to the study area where the procedure recovered observed landslide locations and sizes. The second assumption was algorithmically motivated: the landscape and the forces acting on it can be represented using an *undirected* graph. This allows the search problem to be re-cast as a linear eigenvector/eigenvalue problem, for which well-studied methods that provide good approximate solutions exist. The third assumption relates to definition of stability of a soil mass: an unstable cluster of grid cells fails together as rigid block. This assumption is necessary to resolve the balance of forces in a limit-equilibrium analysis and, it is consistent with the graph theoretical framework where a global optimization is sought. However, this means that the force balance is solved instantaneously and globally, thus not allowing modeling of progressive deformation in the current form of the procedure.

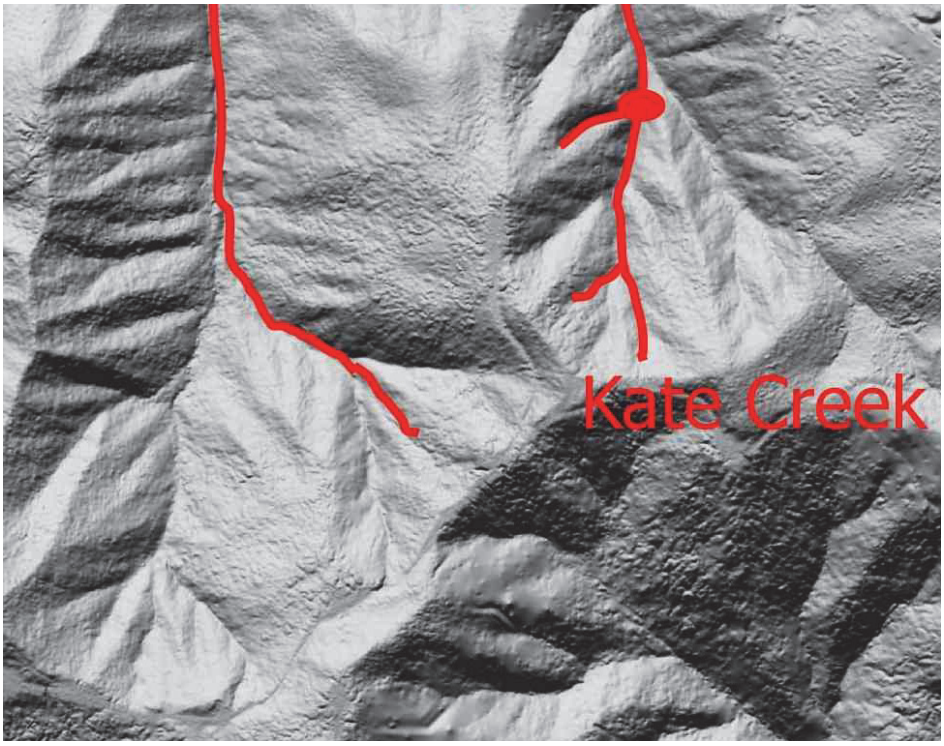

Figure 6.10. Map of debris flows observed after the November 1996 storm in the CB-MR study area. Figure courtesy of J. Stock.

The procedure requires high-resolution spatial data of topography, soil depth, pore pressure, and root reinforcement, rarely available from direct measurements at the regional scale. The sub-models used to produce these data are self-standing, and thus can be substituted as better ones emerge. Similarly, an improved stability model could be used with the search procedure. As a result, the procedure is general as long as its components conform to the assumptions above.

When the procedure is applied to a uniform synthetic landscape, it predicts that if any part of a landscape can fail, all of it can fail. Thus, in the absence of any heterogeneity landslide size and location are not very meaningful concepts. In contrast, when the procedure is applied to a natural landscape where landslide-relevant properties such as soil depth, pore pressure, and root strength vary spatially, specific trends in characteristic landslide size, location, and abundance emerge. This spatial variability is a result of the topographic control on shallow subsurface flow and soil depth. The spatial structure of these properties determines the areas favorable to landsliding that

can be exploited by rain storms, resulting in the characteristic size and location distributions of rainfall-triggered landslides. Varying these controlling properties, even uniformly, changes the spatial distribution of these areas in the landscape. This results in new characteristic distributions of landslide size and location, as landslides sample different parts of the landscape.

Numerical experiments performed in this research reveal the first-order control exerted by topography on shallow landslides. The general spatial pattern of landsliding did not fundamentally change with the introduction of stochastic variability in root strength or with variations in the mechanism of pore pressure generation. This highlights the fundamental role played by the topographically-controlled distribution of soil thickness in defining landslide location. Previous work suggested that as hollows fill with soil the influence of basal cohesion is diminished, resulting in a cycle of filling and evacuation by landsliding. Including lateral effects (root strength and earth pressure) does not alter this theory, although in this research we find that if hollows can get sufficiently deep, soil depth can have a stabilizing effect through the role of earth pressure, creating a window of opportunity in time for landsliding to occur.

Understanding hazards posed by rainfall-triggered shallow landslides requires predicting *where* landslides will occur, *when* they will occur, *how big* will they be, *how fast* they will mobilize, and *how far* will they go. This research constitutes a significant step in this direction by providing some of the first coupled predictions of where and how big landslides are, and demonstrating that capturing their timing is well within reach. By coupling this procedure with climate and vegetation models we can now explore the impact of climate and land use change on the landsliding regime. By integrating the procedure into a landscape evolution model we can then explore how, over longer time scales, landslides shape a landscape.

Bibliography

Anders, A.M., Roe, G.H., Durran, D.R., Minder, J.M., 2007, Small-scale spatial gradients in climatological precipitation on the Olympic peninsula. J. Hydrometeorol. 8: 1068–1081.

Arellano D. & Stark, T.D. 2000. Importance of three-dimensional slope stability analysis in practice. In D.V. Griffiths, G.A. Fenton & T.R. Martin (eds.), Slope Stability. ASCE Geotechnical Special Publication No. 101. New York: ASCE: : 18-32.

Arora, S., Boaz, B., 2009, Computational Complexity: A Modern Approach, Cambridge, ISBN 978-0-521-42426-4

Ashby SF, and Falgout RD., 1996, A parallel multigrid preconditioned conjugate gradient algorithm for groundwater flow simulations, Nucl Sci Eng, 124(1):145–59.

Bak, P., C. Tang, and K. Wiesenfeld, 1987, Self-organized criticality: an explanation of 1/f noise, Phys. Rev. Lett. 59, 381

Baum, R.L. and Godt, J.E., 2010, Early warning of rainfall-induced shallow landslides and debris flows in the USA, Landslides, 7(3), 259–272.

Baum, R.L., Savage, W.Z., Godt, J.W., 2008. TRIGRS — A FORTRAN program for transient rainfall infiltration and grid-based regional slope stability analysis, Version 2.0. U.S. Geological Survey Open-File Report, 2008-1159, 75 pp

Bellugi, D., Dietrich, W.E., Stock, J.D., Kazian, B., Hargrove, P., 2011, Spatially Explicit Shallow Landslide Susceptibility Mapping Over Large Areas, Proceedings of the 5th International Conference on Debris-Flow Hazards Mitigation: Mechanics, Prediction and Assessment, Italian Journal of Engineering Geology and Environment.

Benda, L., 1990, The influence of debris flows on channels and valley floors in the Oregon Coast Range, U.S.A. Earth Surf. Process. Landforms, 15: 457–466. doi: 10.1002/esp.3290150508

Benda, L.E. & Cundy, T.W. 1990, Predicting deposition of debris flows in mountain channels. Canadian Geotechnical Journal 27: 209-417.

Benda, L.E. & Dunne, T., 1997. Stochastic forcing of sediment supply to the channel network form landsliding and debris flow. Water Resources Research 33:2849–2863.

Beven, K. and P. Germann, 1982, Macropores and water flow in soils, Water Resour. Res., 18(5), 1311–1325, doi:10.1029/WR018i005p01311.

Beven, K. J., 1993, Prophecy, reality and uncertainty in distributed hydrological modelling, Adv. In Water Resourc., 16, 41-51

Beven, K. J., Lamb, R., Quinn, P., Romanowicz, R., and Freer, J., 1995, `TOPMODEL', in Singh, V. P. (Ed.), Computer Models of Watershed Hydrology. Water Resource Publications, Colorado. pp. 627-668.

Beven, K. J., 1996, A discussion of distributed modelling, in Abbott, M. B. and Refsgaard, J.-C. (Eds), Distributed Hydrological Modelling. Kluwer, Dordrecht. pp. 255-278.

Beven, K.J., 1997, TOPMODEL: a critique, Hydrol. Process., 11 (3), pp. 1069–1085

Beven, K. and Freer, J., 2001, Equifinality, data assimilation, and uncertainty estimation in mechanistic modeling of complex environmental systems using the GLUE methodology, Journal of Hydrology, 249: 11-29.

Beven, K.J., 2001, Rainfall-Runoff Modelling – The primer, Wiley, Chichester.

Bishop, A.W., 1955, The use of the slip circle in the stability analysis of slopes, Geotechnique, 5(1), 7-17.

Borga, M., Dalla Fontana, G., Gregoretti, C. and Marchi, L., 2002, Assessment of shallow landsliding by using a physically based model of hillslope stability. Hydrol. Process., 16: 2833–2851. doi: 10.1002/hyp.1074

Borja, R.I., and White, J.A., 2010, Continuum deformation and stability analyses of a steep hillside slope under rainfall infiltration, Acta Geotech., 1–14.

Borradaile, G.J., 2003. Statistics of Earth Science Data: Their Distribution in Time, Space, and Orientation. Springer Verlag, New York.

Brunetti, M. T., F. Guzzetti, and M. Rossi, 2009, Probability distributions of landslide volumes, Nonlinear Processes Geophys., 16, 179– 188.

Brunetti M.T., Peruccacci S., Rossi M., Luciani S., Valigi D., Guzzetti F., 2010, Rainfall thresholds for the possible occurrence of landslides in Italy. Nat Hazard Earth Syst Sci 10:447–458

Burrough, P.A. and McDonnell, R.A., 1998, Principles of Geographical Information Systems, Oxford, Oxford University Press, 330 pp.

Burroughs, E.R., and Thomas, B.R., 1977, Declining Root Strength in Douglas-fir after Felling as a Factor in Slope-Stability, 27 pp, Intermountain Forest and Range Experiment Station, US Forest Service, Ogden, Utah.

Burroughs, E.R.J., 1985, Landslide hazard rating for the Oregon Coast Range, In Watershed management in the eighties. Edited by E.B. Jones and T.J. Ward, American Society of Civil Engineers, New York, pp. 132–139.

Caine, N., 1980, The rainfall-intensity-duration control of shallow landslides and debris flows, Geografiska Annaler, 62, pp. 23–27

Casadei, M., Dietrich, W. E., and Miller, N. L., 2003 (a), Testing a model for predicting the timing and location of shallow landslide initiation in soil mantled landscapes, Earth Surface Processes and Landforms, 28:925-950.

Casadei, M. & Dietrich, W.E., and Miller, N. L., 2003 (b), Controls on shallow landslide width. In D. Rickermann & C.L. Chen (eds.), Debris-flow Hazards Mitigation: Mechanics, Prediction, and Assessment; Proceedings of the Third International DFHM Conference. Davos Switzerland, September 10-12, 2003: 91-102.

Chen, W.F., 1975, Limit Analysis and Soil Plasticity, Elsevier, Amsterdam.

Chen, R.H., 1981, Three-dimensional slope stability analysis, 81-17 pp, Purdue University.

Chen, W.F., and Liu, X.L., 1990, Limit Analysis in Soil Mechanics, Elsevier, Amsterdam.

Chung, F. R. K. 1997. Spectral Graph Theory. AMS Press, Providence, R.I.

Claessens, L., Heuvelink, G.B.M., Schoorl, J.M. & Veldkamp, A., 2005, DEM resolution effects on shallow landslide hazard and soil redistribution modeling. Earth Surface Processes and Landforms 30: 461-477.

Conover, W.J., 1971. Practical Nonparametric Statistics. Wiley, New York.

Cook, S. 1971. The complexity of theorem-proving procedures. In Conference Record of 3rd Annual ACM Symposium on Theory of Computing. ACM New York, pp. 151–158.

Corder, G.W., Foreman, D.I., 2009, Nonparametric Statistics for Non-Statisticians: A Step-by-Step Approach Wiley, ISBN 978-0-470-45461-9

Cormen, T.H., Leiserson, C.E., Rivest, R.L., and Stein, C., 2001, Introduction to Algorithms, MIT Press, Cambridge, MA, 2nd edition.

Coulomb, C.A., 1773, Memoir de Mathematique et de Physique, Vol. 7, Academie des Sciences, L'Imprimerie Royale, Paris, p. 343

Coulomb, C. A., 1776, Essai sur une Application des Règles de Maximis et Minimis a quelques Problèmes de Statique, relatifs a l'Architecture, Mem. Roy. des Sciences, Paris, Vol. 3, 38.
Crookston, N.L., G.E. Rehfeldt, G.E. Dixon, and A.R. Weiskittel, 2010, Addressing climate change in the forest vegetation simulator to assess impacts on landscape forest dynamics, Forest Ecology and Management 260:1198–1211.
Crozier, M.J., Glade, T., 2005. Landslide hazard and risk: Issues, Concepts and Approach. In: Glade, T., Anderson, M., Crozier, M.J. (Eds.), Landslide Hazard and Risk. Wiley, Chichester, pp. 1-40.
CSDMS, 2011, Community Surface Dynamics Modeling System (CSDMS), http://csdms.colorado.edu.
Culmann, C., 1875, Die graphische Statik, Meyer and Zeller, Zurich.
Cvetković, D., Rowlinson, P., Simić, S., 2010, An Introduction to the Theory of Graph Spectra, Cambridge University Press, Cambridge.
Dale, V.H., L.A. Joyce, S. McNulty, R.P. Neilson, M.P. Ayres, M.D. Flannigan, P.J. Hanson, L.C. Irland, A.E. Lugo, C.J. Peterson, D. Simberloff, F.J. Swanson, B.J. Stocks, B.M. Wotton, 2001, Climate change and forest disturbances, Bioscience, 51 (9), pp. 723–734.
Daniels, H.E., 1945, The statistical theory of the strength of bundles of threads: I, Proc. R. Soc. London Ser. A, 183, 405–435.
Das, B.M., 2010, Principles of Geotechnical Engineering, seventh ed., PWS-KENT, Boston, MA.
Dasgupta S., Papadimitriou C.H., and Vazirani U.V., 2006, Algorithms. McGraw-Hill Higher Education.
Davis, J., and Goadrich, M., 2006, the relationship between precision-recall and ROC curves. In Proceedings of the International Conference on Machine Learning (ICML).
Dettinger, M. D., F. M. Ralph, M. Hughes, T. D. P. Neiman, D. Cox, G. Estes, D. Reynolds, R. Hartman, D. Cayan, and L. Jones, 2012, Design of quantification of an extreme winter storm scenarios for emergency preparedness and planning exercise in California, Nat. Hazards, 60, 1085–1111, doi:10.1007/s11069-011-9894-5.
Dhakal, A.S., and Sidle, R.C., 2003, Long-term modelling of landslides for different forest management practices. Earth Surf. Process. Landforms, 28: 853–868. doi: 10.1002/esp.499
Dietrich, W. E., and T. Dunne, 1978, Sediment budget for a small catchment in mountainous terrain, Z. Geomorph. Suppl., 29, 191–206.
Dietrich, W.E., T. Dunne, N.F. Humphrey and L.M. Reid, 1982, Construction of sediment budgets for drainage basins: in Sediment Budgets and Routing in Forested Drainage Basins, F.J. Swanson, R.J. Janda, T. Dunne, and D.N. Swanston (eds.), U.S.D.A. Forest Service General Technical Report PNW-141, Pacific Northwest Forest and Range Experiment Station, Portland, Oregon, p. 5-23.
Dietrich, W. E., C. J. Wilson, D.R. Montgomery, J. McKean, and R. Bauer, 1992, Erosion thresholds and land surface morphology, Geology, v. 20, p. 675-679.
Dietrich, W. E., C. J. Wilson, D. R. Montgomery, and J. McKean, 1993, Analysis of erosion thresholds, channel networks, and landscape morphology using a digital terrain model.J. Geol. 101: 259-278.
Dietrich, W.E., Reiss, R., Hsu, M. & Montgomery, D.R., 1995, A process-based model for colluvial soil depth and shallow landsliding using digital elevation data. Hydrological Processes 9: 383-400.

Dietrich, W.E. and D.R. Montgomery, 1998, SHALSTAB: a digital terrain model for mapping shallow landslide potential, NCASI (National Council of the Paper Industry for Air and Stream Improvement) Technical Report, February 1998, 29pp.

Dietrich, W.E., Bellugi, D. & Real de Asua, R., 2001, Validation of the shallow landslide model SHALSTAB for forest management. In M.S. Wigmosta & S.J. Burges (eds.), Land Use and Watersheds: Human influence on hydrology and geomorphology in urban and forest areas. American Geophysical Union Water Science and Application 2: 195-227.

Dietrich, W.E., Bellugi, D., Heimsath, A.M., Roering, J.J., Sklar, L. and Stock, J.D., 2003, Geomorphic transport laws for predicting the form and evolution of landscapes. In P. Wilcock and R. Iverson (eds.), Prediction in Geomorphology. American Geophysical Union Monograph Series 135: 103-132.

Dietrich, W.E., J. McKean, D. Bellugi and J.T. Perron, 2008, The prediction of shallow landslide location and size using a multidimensional landslide analysis in a digital terrain model. Proceedings of the Fourth International Conference on Debris-Flow Hazards Mitigation.

D'Odorico, P., S. Fagherazzi, and R. Rigon, 2005, Potential for landsliding: Dependence on hyetograph characteristics, J. Geophys. Res., 110, F01007, doi:10.1029/2004JF000127.

Drucker, D.C., Prager, W., Greenberg, H.J., 1952, Extended limit design theorems of continuous media, Quarterly Applied Mathematics, Vol. 9, pp. 381-389.

Dunne, T., and Black, R.D., 1970a, An experimental investigation of runoff production in permeable soils, Water Resour. Res., 6(2), 478-490.

Dunne, T., and Black, R.D., 1970b, Partial area contributions to storm runoff in a small New England watershed, Water Resour. Res., 6, 1296–1311.

Dunne, T., 1991, Stochastic aspects of the relations between climate, hydrology and landform evolution, Trans. Jpn. Geomorphol. Union, 12, 1-24.

Ebel, B.A., Loague, K., Dietrich, W.E., Montgomery, D.R., Torres, R., Anderson, S.P. & Giambelluca, T.W., 2007a, Near-surface hydrologic response for a steep, unchanneled catchment near Coos Bay, Oregon: 1. Sprinkling experiments. American Journal of Science 307: 678-708.

Ebel B.A., Loague K., VanderKwaak J.E., Dietrich W.E., Montgomery, D.R., Torres, R., Anderson, S.P., 2007b, Near-surface hydrologic response for a steep, unchanneled catchment near Coos Bay, Oregon: 2. Comprehensive physics-based simulations, American Journal of Science, 07: 709–748, DOI:10-2475/04-2007-03.

Eid, H.T., Elleboudy, A.M., Elmarsafawi, H.G., Salama, A.G., 2006, Stability analysis and charts for slopes susceptible to translational failure. Canadian Geotechnical Journal 43 (12), 1374e1388.

Fanning, R.J. & Wise, M.P., 2001, An empirical-statistical model for debris flow travel distance. Canadian Geotechnical Journal 38: 982-994.

Fawcett, T., 2006, An introduction to ROC analysis, Pattern Recognition Letters, 27, 861–874.

Fellenius, W., 1927, Erdstatische Berechnungen mit Reibung und Kohasion, Ernst, Berlin (in German).

Gabet, E.J., Dunne, T., 2002, Landslides on coastal sage-scrub and grassland hillslopes in a severe El Nino winter: the effects of vegetation conversion on sediment delivery, Geological Society of America Bulletin 114 (8), 983–990.

Gerber, M., 2004, Geomorphic response to wildfire in the Oregon Coast Range [M.S. thesis]: Eugene, University of Oregon, 94 p.

Godt, J.W., Baum, R.L., Chleborad, A.F., 2006. Rainfall characteristics for shallow landsliding in Seattle, Washington, USA. Earth Surface Processes and Landforms 31, 97–110.
Godt, J.W., R.L. Baum, W.Z. Savage, D. Salciarini, W.H. Schulz, E.L. Harp, 2008, Transient deterministic shallow landslide modeling: Requirements for susceptibility and hazard assessments in a GIS framework, Engineering Geology, Volume 102, Issues 3–4, Pages 214-226, ISSN 0013-7952, 10.1016/j.enggeo.2008.03.019.
Griffiths D.V., and Lane, P.A., 1999, Slope stability analysis by finite elements, Geotechnique; 49(3):387–403.
Griffiths, D.V., and Fenton, G.A., 2004, Probabilistic slope stability analysis by finite elements Journal of the Geotechnical Engineering Division, ASCE, 130 (5) (2004), pp. 507–518.
Griffiths D.V., and Marquez, R.M., 2007, Three-dimensional slope stability analysis by elasto-plastic finite elements, Geotechnique; 57(6):537–546.
Guzzetti, F., Peruccacci, S., Rossi, M., and Stark, C.P., 2007, Rainfall thresholds for the initiation of landslides in central and southern Europe, Meteorol. Atmos. Phys., 98, 239–267.
Guzzetti F., Peruccacci S., Rossi M., Stark C.P., 2008, The rainfall intensity–duration control of shallow landslides and debris flows: an update. Landslides 5(1):3–17.
Hales, T.C., Ford, C.R., Hwang, T., Vose, J.M., and Band, L.E., 2009, Topographic and ecologic controls on root reinforcement, J. Geophys. Res., 114, F03013, doi:10.1029/2008JF001168.
Haralick, R.M., and Shapiro, L.G., 1992, Computer and Robot Vision, Addison-Wesley, Reading, Mass.
Harp, E.L., Keefer, D.K., Sato, H.P., Yagi, H., 2011, Landslide inventories: the essential part of seismic landslide hazard analyses. Eng Geol 122(1–2):9–21.
Hastie, T., Tibshirani, R. and Friedman, J. H., 2001, The elements of statistical learning: data mining, inference, and prediction. Springer.
Hathaway, R.L., and Penny, D., 1975, Root strength in some Populus and Salix clones, New Zealand Journal of Botany, 13, 333-344.
Heimsath, A.M., Dietrich, W.E., Nishiizumi, K., and Finkel, R.C., 1997, The soil production function and landscape equilibrium. Nature, 388: 358-361.
Heimsath, A.M., Dietrich, W.E., Nishiizumi, K. & Finkel, R.C. 2001. Stochastic processes of soil production and transport: erosion rates, topographic variation, and cosmogenic nuclides in the Oregon Coast Range, Earth Surface Processes and Landforms 26: 531-552.
Hemmer, P.C., and Hansen, A., 1992, The distribution of simultaneous fiber failures in fiber bundles, J. Appl. Mech., 59(4), 909–914.
Henshaw, W.D., and Schwendeman, D.W. 2008, Parallel computation of three-dimensional flows using overlapping grids with adaptive mesh refinement, J. Comput. Phys., 227, 7469.
Heroux, M.A., R.A. Bartlett, V.E. Howle, R.J. Hoekstra, J.J. Hu, T.G. Kolda, R.B. Lehoucq, K.R. Long, R.P. Pawlowski, E.T. Phipps, A.G. Salinger, H.K. Thornquist, R.S. Tuminaro, J.M. Willenbring, A. Williams, and K.S. Stanley, 2005, An overview of the Trilinos project. ACM Trans. Math. Softw., 31(3):397–423.
Higgins R. W.; Kousky V. E.; Xie P., 2011, Extreme Precipitation Events in the South-Central United States during May and June 2010: Historical Perspective, Role of ENSO, and Trends, Journal of Hydrometereology
Ho, J. ,Lee, K., Chang, T., Wang, Z., Liao, Y., 2012, Influences of spatial distribution of soil thickness on shallow landslide prediction, Engineering Geology 124, 38–46.

Horn, B.K.P., 1981, Hill Shading and the Reflectance Map, Proceedings of the IEEE, 69(1):14-47.
Hovius N., Stark C.P., Allen P.A, 1997, Sediment flux from a mountain belt derived by landslide mapping. Geology 25: 231–234.
Hovland, H.J., 1977, Three-dimensional slope stability analysis method. ASCE Journal of the Geotechnical Engineering Division 103 (GT9): 971-986.
Howard, A.D., 1994, A detachment-limited model of drainage basin evolution, Water Resources Research 30: 2261-2285.
Hungr, O., Salgado, F.M., and Byrne, P.M., 1989, Evaluation of a threedimensional method of slope stability analysis, Can. Geotech. J., 26, 679–686.
Hungr, O., McDougall, S., Wise, M., and Cullen, M., 2008, Magnitude-frequency relationships of debris flows and debris avalanches in relation to slope relief. Geomorphology, 96(3-4), 355-365.
Istanbulluoglu, E., and R. L. Bras, 2005, Vegetation-modulated landscape evolution: Effects of vegetation on landscape processes, drainage density, and topography, J. Geophys. Res., 110, F02012, doi:10.1029/2004JF000249.
Istanbulluoglu, E., and R.L. Bras, 2006, On the dynamics of soil moisture, vegetation, and erosion: Implications of climate variability and change, Water Resour. Res., 42, W06418, doi:10.1029/2005WR004113.
Itasca Consulting Group, 2000, FLAC: Fast Lagrangian Analysis of continua, Itasca Consulting Group: Minneapolis, Minnesota.
Itasca Consulting Group, 2002, FLAC3D: Fast Lagrangian Analysis of continua in 3 dimensions, Itasca Consulting Group: Minneapolis, Minnesota.
Ivanov, V.Y., R.L. Bras, and D.C. Curtis, 2007, A Weather Generator for Hydrological, Ecological, and Agricultural Applications, Water Resources Research, 43, W10406, doi: 10.1029/ 2006WR005364.
Ivanov, V.Y., R.L. Bras, and E.R. Vivoni, 2008, Vegetation-hydrology dynamics in complex terrain of semiarid areas: 1. A mechanistic approach to modeling dynamic feedbacks, Water Resour. Res., 44, W03429, doi:10.1029/2006WR005588.
Iverson R.M., 1990, Groundwater flow fields in infinite slopes. Geotechnique 40: 139–143.
Iverson, R.M., Reid, M.E., 1992, Gravity-driven groundwater flow and slope failure potential: 1. Elastic effective-stress model. Water Resources Research, v. 28: 925-938.
Iverson, R.M., Reid, M.E., and LaHusen, R.G., 1997, Debris-flow mobilization from landslides, Annual Review of Earth and Planetary Sciences, 25, 85-138.
Iverson, R.M., 2000, Landslide triggering by rain infiltration, Water Resources Research, 36 (7) (2000), pp. 1897–1910.
Iverson, R.M., 2004, Comment on ‘‘Piezometric response in shallow bedrock at CB1: Implications for runoff generation and landsliding’’ by David R. Montgomery, William E. Dietrich, and John T. Heffner, Water Resour. Res., 40, doi:10.1029/2003WR002077.
Jain, A.K., M.N. Murty, and P.J. Flynn, 1999, Data clustering: A review, ACM Comput. Surveys, 31, pp. 264–323.
Jakob, M., 2005, Debris-flow hazard analysis, In Debris-flow Hazards and Related Phenomena, Edited by M. Jakob and O. Hungr, Praxis-Springer Publishers, Heidelberg. pp. 411-443.
Jenson, S.K. and J.O. Domingue, 1988, Extracting Topographic Structure from Digital Elevation Data for Geographic Information System Analysis, Photogrammetric Engineering and Remote Sensing, 54(11): 1593-1600.

Jones J.E., and Woodward C.S., 2001, Newton–Krylov-multigrid solvers for large-scale, highly heterogeneous, variably saturated flow problems, Adv Water Resour, 24:763–74.

Kirkby, M.J., 1975, Hydrograph Modelling Strategies. In: Peel, R., Chisholm, M., Haggett, P. (Eds.), Process in Physical and Human Geography, 69–90.

Kogan, J., 2007, Introduction to Clustering Large and High-Dimensional Data, Cambridge University Press, New York, NY.

Kollet, S.J., Maxwell, R.M., 2006, Integrated surface–groundwater flow modeling: A free-surface overland flow boundary condition in a parallel groundwater flow model, Advances in Water Resources, Volume 29, Issue 7, Pages 945-958, ISSN 0309-1708, 10.1016/j.advwatres.2005.08.006.

Lee, H., K.C. Slatton, B.E. Roth, and W.P. Cropper JR, 2010, Adaptive clustering of airborne LiDAR data to segment individual tree crowns in managed pine forests, International Journal of Remote Sensing, 31(1):117–139.

Lehmann, P., and D. Or, 2012, Hydromechanical triggering of landslides: From progressive local failures to mass release, Water Resour. Res., 48, W03535, doi:10.1029/2011WR010947.

Lehoucq, R.B., D.C. Sorensen, and C. Yang, 1998, ARPACK Users Guide: Solution of Large-Scale Eigenvalue Problems with Implicitly Restarted Arnoldi Methods.

Lehre, A.K., 1982a, Sediment budget of a small coast range drainage in north-central California, Pacific Forest and Range Experimental Station General Technical Report.

Lehre, A.K., 1982b, Sediment mobilization and production from a small mountain catchment: Lone Tree Creek, Marin County, California. PhD dissertation, Univ. of California, Berkeley.

Li, F., D. Rosa, W. D. Collins, and M. F. Wehner, 2012, ‘‘Super-parameterization’’: A better way to simulate regional extreme precipitation? J. Adv. Model. Earth Syst., 4, M04002, doi:10.1029/2011MS000106.

Li, W., Guo, Q., Kelly, M., Jakubowski, M., 2012, A new method for segmenting individual trees from the lidar point cloud, Photogrammetric Engineering & Remote Sensing 78 (1), 75–84.

McKean, J.A., Dietrich, W.E., Finkel, R.C., Southon, J.R., and Caffee, M.W., 1993, Quantification of soil production and downslope creep rates from cosmogenic 10Be accumulations on a hillslope profile, Geology, v.21, p. 343-346.

Malamud, B. D., and D. L. Turcotte, 1999, Self-organized criticality applied to natural hazards, Nat. Hazards, 20, 93– 116.

Malamud, B.D., D.L. Turcotte, F. Guzzetti, and P. Reichenbach, 2004a, Landslides, earthquakes, and erosion, Earth Planet. Sci. Lett., 229, 45– 59, doi:10.1016/j.epsl.2004.10.018.

Malamud, B.D., D.L. Turcotte, F. Guzzetti, and P. Reichenbach, 2004b, Landslide inventories and their statistical properties, Earth Surf. Processes Landforms, 29(6), 687– 711, doi:10.1002/esp.1064.

Mathews, B.W., 1975, Comparison of the predicted and observed secondary structure of T4 phage lysozyme. Biochim. Biophys. Acta, 405, 442–451.

Mazindrani, Z.H., and Ganjali, M.H., 1997, Lateral Earth Pressure Problem of Cohesive Backfill with Inclined Surface, J. Geotech. Geoenviron. Eng., 123(2), 110–112. Montgomery, D. R., and W. E. Dietrich, 1994, A physically based model for the topographic control on shallow landsliding, Water Resour. Res., vol. 30, no. 4, pp. 1153-1171.

Milledge, D., Bellugi, D., McKean, J., Dietrich, W.E., in prep., Multi-Dimensional Shallow Landslide Stability Analysis Suitable for Application at the Watershed Scale.

Mohar, B., 1991, The Laplacian spectrum of graphs, in, Graph Theory, Combinatorics, and Applications, Kalamazoo, MI, 1988, vol. 2, pp. 871–898, Wiley, New York.
Montgomery, D. R., and W. E. Dietrich, 1988, Where do channels begin?, Nature, 336, 232–234, doi:10.1038/336232a0.
Montgomery, D.R. and Dietrich, W.E., 1994, A physically-based model for topographic control on shallow landsliding, Water Resources Research, vol.30, no.4, p.1153-1171.
Montgomery, D.R., Dietrich, W.E., Torres, R., Anderson, S.P., and Loague, K., 1997, Hydrologic response of a steep unchanneled valley to natural and applied rainfall, Water Resour. Res., 33(1), 91–109.
Montgomery, D.R, Schmidt, K.M., Dietrich, W.E., Greenberg, H.M., 2000, Forest clearing and regional landsliding in the Pacific Northwest, Geology v. 28, p. 311-314.
Montgomery, D.R., and W. E. Dietrich, 2002, Runoff generation in a steep, soil-mantled landscape, Water Resour. Res., 38(9), 1168, doi:10.1029/2001WR000822.
Montgomery D.R. and W. E. Dietrich, 2004, Reply to comment by Richard M. Iverson on Piezometric response in shallow bedrock at CB1: implications for runoff generation and shallow landsliding, Water Resources Research, Vol.40, W03802, doi:10.1029/2003WR002815, 3 pages.
Montgomery, D., Schmidt, K.M., Dietrich, W.E, and McKean, J, 2009, Instrumental record of debris flow initiation during natural rainfall: Implications for modeling slope stability, JGR, doi:10.1029/2008JF001078
Moore, R.J., Clarke, R.T, 1981, a distribution function approach to rainfall-runoff modeling, Water Resources Research, 17:1367-1382.
Nešetřil, J., Milková, E., Nešetřilová, H., 2001, Otakar Borůvka on minimum spanning tree problem: translation of both the 1926 papers, comments, history, Discrete Mathematics 233 (1–3): 3–36. DOI:10.1016/S0012-365X(00)00224-7. MR 1825599.
Newmark, N.M., 1965, Effects of earthquakes on dams and embankments. Geotechnique 15 2, pp. 139–160.
O'Callaghan, J.F., and D.M. Mark, 1984, The extraction of drainage networks from digital elevation data, Comput. Vision Graphics Image Process., 28, 328–344.
O'Loughlin, C.L., 1972, An investigation of the stability of the steepland forest soils in the Coast Mountains, southwest British Columbia, Ph. D. thesis, University of British Columbia,Vancouver, Canada.
Okimura, T., 1994, Prediction of the shape of a shallow failure on a mountain slope: the three-dimensional multi-planar sliding surface method., Geomorphology, v. 9: 223–233.
Papadimitriou, C., 1994, Computational Complexity (1st ed.), Addison Wesley, ISBN 0-201-53082-1.
Pearson E.S. and Hartley, H.O., ed., 1972, Biometrika Tables for Statisticians. 2. Cambridge University Press. pp. 117–123, Tables 54, 55. ISBN 0-521-06937-8.
Peckham, S.D., Hutton, E.W.H., and Norris, B., 2012, A component-based approach to integrated modeling in the geosciences: The design of CSDMS, Computers & Geosciences, http://dx.doi.org/10.1016/j.cageo.2012.04.002
Petley, D.N., T. Higuchi, D.J. Petley, M.H. Bulmer, and J. Carey, 2005, Development of progressive landslide failure in cohesive materials, Geology, 33, 201–204.
Qiu C., Esaki T., Xie M., Mitani Y., and Wang C., 2007, Spatio-temporal estimation of shallow landslide hazard triggered by rainfall using a three-dimensional model, Environmental Geology, 52(8), 1569-1579.

Quinn, P., Beaven, K., Chevallier, P., Planchon, O., 1991, The prediction of hillslope flow for distributed hydrological modeling using digital terrain models, Hydrological processes, vol. 5, pp. 59-79.

Rankine, W., 1857, On the stability of loose earth, Philosophical Transactions of the Royal Society of London, Vol. 147.

Reneau, S.L., W.E. Dietrich, C.J. Wilson, and J.D. Rogers, 1984, Colluvial deposits and associated landslides in the northern S.F. Bay Area, California, USA, Proceedings IV International Symposium on Landslides, Toronto, 1984, pp. 425-430.

Reneau, S.L., W.E. Dietrich, R.I. Dorn, C.R. Berger, and M. Rubin, 1986, Geomorphic and paleoclimatic implications of latest Pleistocene radiocarbon dates from colluvium-mantled hollows, California, Geology, v. 14, p. 655-658.

Reneau, S.L. and W.E. Dietrich, 1987, Size and location of colluvial landslides in a steep forested landscape, Proc. Int. Symp. on Erosion and Sedimentation in the Pacific Rim, 3-7 August 1987, Corvallis, Ore., Int. Assoc. Hydrological Sciences Bull., Pub. no. 165, p. 39-48.

Richardson, A., Hill, C.N., Perron, T., Scalable, massively parallel approaches to upstream drainage area computation, American Geophysical Union, Fall Meeting 2011, abstract #IN12A-05.

Robison, E.G., Mills, K., Paul, J., Dent, L., and Skaugset, A., 1999, Oregon Department of Forestry storm impacts and landslides of 1996: final report. Oregon Department of Forestry, Forest Practices Technical Report 4.

Roering, J.J., Kirchner, J.W. & Dietrich, W.E., 1999. Evidence for non-linear, diffusive sediment transport on hillslopes and implications for landscape morphology, Water Resources Research 35: 853-870.

Roering, J.J., Schmidt, K.M., Stock, J.D., Dietrich, W.E. & Montgomery, D.R., 2003, Shallow landsliding, root reinforcement, and the spatial distribution of trees in the Oregon Coast Range. Canadian Geotechnical Journal 40: 237-253.

Roering, J.J., 2008, How well can hillslope evolution models "explain" topography? Simulating soil transport and production with high resolution topographic data. Geological Society of America Bulletin 120: 1248–1262.

Rosso , R., Rulli, M.C. and G. Vannucchi, 2006, A physically based model for the hydrologic control on shallow landsliding, Water Resources Research.

Schmidt, K.M., 1999, Root strength, colluvial soil depth, and colluvial transport on landslide-prone hillslopes, Ph.D. thesis, Univ. of Wash., Seattle, Wash.

Schmidt, K.M., Roering, J.J., Stock, J.D., Dietrich, W.E., Montgomery, D.R. & Schaub, T., 2001, Root cohesion variability and shallow landslide susceptibility in the Oregon Coast Range, Canadian Geotechnical Journal 38 (1): 995-1024.

Schmidt, K.M., 2012, personal communication.

Schroeder, W.L., and Alto, J.V., 1983, Soil properties for slope stability analysis; Oregon and Washington Coastal Mountains, Forest Science, 29: 823–833.

Schwarz, M., Lehmann, P., Or, D., 2010, Quantifying lateral root reinforcement in steep slopes - from a bundle of roots to tree stand, Earth Surface Processes and Landforms 35: 354–367. DOI: 10.1002/esp.1927.

Selby, M.J., Slope Erosion due to Extreme Rainfall: A Case Study from New Zealand, 1976, Geografiska Annaler. Series A, Physical Geography , Vol. 58, No. 3, Case Studies of Rapid Mass Movements in Different Climates, pp. 131-138.

Shi, J., Malik, J., 2000, Normalized cuts and image segmentation, IEEE Transactions on Pattern Analysis and Machine Intelligence, vol.22, no.8, pp.888-905 doi: 10.1109/34.868688.
Sidle, R.C., Pearce, A.J., and O'Loughlin, C.L., 1985, Hillslope stability and land use, Water Resources Monograph Series 11, American Geophysical Union, Washington, D.C.
Sidle, R.C., 1991, A conceptual model of changes in root cohesion in response to vegetation management, Journal of Environmental Quality 20: 43–52.
Sidle, R.C., 1992, A theoretical model of the effects of timber harvesting on slope stability, Water Resour. Res., 28(7), 1897–1910, doi:10.1029/92WR00804.
Sidle, R.C., Ochiai, H., 2006, Landslides: processes, prediction, and land use. Am Geophysical Union, Water Resour Monogr No. 18, AGU, Washington, DC, p 312.
Simoni, S., Zanotti, F., Bertoldi, G., Rigon R., 2008, Modelling the probability of occurrence of shallow landslides and channelized debris flows using GEOtop-FS, Hydrological Processes 22(4): 532–545.
Sokolov A.P., Stone, P.H., Forest, C.E., Prinn, R., Sarofim, M.C., Webseter, M., and Schlosser, C.A., 2009, Probabilistic forecast for 21st century climate based on uncertainties in emissions (without policy) and climate parameters, J. Climate 22:5175–5204.
Soubra, A.H., and Macuh, B., 2002, Active and passive earth pressure coefficients by a kinematical approach, Proceedings of the Institution of Civil Engineers, Geotechnical Engineering, 155, No. 2, str. 119-131.
Spencer, E., 1967, A method of analysis of the stability of embankments assuming parallel interslice forces, Geotechnique, 17(1), 11-26.
Spowart, J.E., Maruyama, B., Miracle, D.B., 2001, Multi-Scale characterization of spatially heterogeneous systems: Implications for discontinuously reinforced metal matrix composite microstructures, Materials Science & Engineering A 307 51-66.
Stark, C.P., and Hovius N., 2001, The characterization of landslide size distributions. Geophysical Research Letters 28: 1091–1094.
Stark, C.P., and F. Guzzetti, 2009, Landslide rupture and the probability distribution of mobilized debris volumes, J. Geophys. Res., 114, F00A02, doi:10.1029/2008JF001008.
Stark, T.D., and Eid, H.T., 1998, Performance of three-dimensional slope stability analysis method in practice, J Geotech Eng ASCE, 124, pp. 1049–1060.
Stock, J.D., Bellugi, D., 2011, An empirical method to forecast the effect of storm intensity on shallow landslide abundance, Proceedings of the 5th International Conference on Debris-Flow Hazards Mitigation: Mechanics, Prediction and Assessment, Italian Journal of Engineering Geology and Environment.
Syvitski, J.P.M., Slingerland, R.L., Burgess, P., Meiburg, E., Murray, A.B., Wiberg, P., Tucker, G., Voinov, A.A., 2010, Morphodynamic Models: An Overview. In: Vionnet et al. (eds). River, Coastal and Estuarine Morphodynamics: RCEM 2009. Taylor & Francis Group, London, CRC Press, pp 3-20.
Tarboton, D. G., A new method for the determination of flow directions and upslope areas in grid digital elevation models, Water Resour. Res., 33, 309–319, 1997.
Tarolli, P. & Tarboton, D.G. 2006, A new method for determination of most likely landslide initiation points and the evaluation of digital terrain model scale in terrain stability mapping, Hydrology and Earth System Science 10: 663-377.
Terzaghi, K., 1941, General Wedge Theory of Earth Pressure, Transactions, ASCE, Vol. 106, 68–97.
Terzaghi, K., 1943, Theoretical soil mechanics: New York, John Wiley and Sons, 510 p.

Terzaghi, K., and Peck, R. B., 1967, Soil Mechanics in Engineering Practice, 2nd ed., Wiley, New York.
Torres. R., W.E. Dietrich, D.R. Montgomery, S.P. Anderson, and K. Loague, 1998, Unsaturated zone processes and the hydrologic response of a steep, unchanneled catchment, Water Resources Research, vol. 34, no. 8, pp. 1865–1879.
Tucker, G.E. & Bras, R.L., 1998, Hillslope processes, drainage density, and landscape morphology, Water Resources Research 34: 2751-2764.
Tucker, G.E., Lancaster, S.T., Gasparini, N.M., and Bras, R.L., 2001, The Channel-Hillslope Integrated Landscape Development (CHILD) Model, in Landscape Erosion and Evolution Modeling, edited by R.S. Harmon and W.W. Doe III, Kluwer Academic/Plenum Publishers, pp. 349-388.
Turcotte, D.L., 1999, Self-organized criticality, Reports on Progress in Physics 62: 1377–1429.
USGS, 2005, Landslide hazards – a national threat, USGS Fact Sheet: 2005-3156.
Van Rijsbergen, C.J., 1979, Information Retrieval, 2nd edition, London: Butterworths.
Von Luxburg, U., 2006, A tutorial on spectral clustering. Technical Report 149, Max Plank Institute for Biological Cybernetics.
Whitman, R.V., and Bailey, W.A., 1967, Use of computers for slope stability analysis, J. Soil Mech. and Found. Div., ASCE, 93(4), 475-498.
Yee, C.S., and Harr, D.R., 1977, Influence of soil aggregation on slope stability in the Oregon Coast Range. Environmental Geology, 1: 367–377.
Zevenbergen, L.W. and C.R. Thorne (1987) Quantitative Analysis of Land Surface Topography, Earth Surface Processes and Landforms, Vol. 12, pp. 12-56.